N73-12859
NASA CR-120870
TRW 14549-6001-RO-00

CASE FILE
COPY

FINAL REPORT

HYDROGEN-OXYGEN CATALYTIC IGNITION AND THRUSTER INVESTIGATION

VOLUME II
HIGH PRESSURE THRUSTER EVALUATIONS

By

R.J. JOHNSON, B. HECKERT, H.L. BURGE

PREPARED FOR

NATIONAL AERONAUTICS AND SPACE ADMINISTRATION
NASA Lewis Research Center
Contract 3-14347

P.N. HERR,
Project Manager

Requests for copies of this report should be referred to

National Aeronautics and Space Administration
Scientific and Technical Information Facility
P. O. Box 33
College Park, Maryland 20740

1. Report No. NASA CR-120870	2. Government Accession No.	3. Recipient's Catalog No.
4. Title and Subtitle HYDROGEN-OXYGEN CATALYTIC IGNITION AND THRUSTER INVESTIGATION Vol. II — High Pressure Thruster Evaluations		5. Report Date
		6. Performing Organization Code
7. Author(s) R. J. Johnson, B. Heckert, H. L. Burge		8. Performing Organization Report No.
		10. Work Unit No.
9. Performing Organization Name and Address TRW Systems Group One Space Park, Redondo Beach, California 90278		11. Contract or Grant No. NAS 3-14347
		13. Type of Report and Period Covered Final
12. Sponsoring Agency Name and Address National Aeronautics and Space Administration Washington, D.C. 20546		14. Sponsoring Agency Code

15. Supplementary Notes

Project Manager, P. N. Herr, NASA Lewis Research Center, Cleveland, Ohio

16. Abstract

The high pressure thruster effort was conducted with the major objective of demonstrating the TRW duct cooling concept with gaseous H_2/O_2 propellant in a thruster operating at nominally 300 psia (2068 kN/m^2) and 1500 lbf (6672 N). The high response catalytic igniter concept reported in Volume I of this report was incorporated into the design. The analytical design methods for the duct cooling were proven in a series of tests with both ambient and reduced temperature propellants. Long duration tests as well as pulse mode tests demonstrated the feasibility of the concept. All tests were conducted with a scaling of the raised post triplet injector design previously demonstrated at 900 lbf in NASA MSFC and MSC demonstration firings. A series of environmental conditioned firings were also conducted to determine the effects of thermal soaks, atmospheric air and high humidity. This volume presents the results of the high pressure thruster evaluations. Volume I presented the results of the catalytic igniter and low pressure thruster evaluations, NASA CR-120869.

17. Key Words (Suggested by Author(s)) Ignition, Hydrogen-Oxygen, High Pressure, Thruster, Duct Cooling	18. Distribution Statement

19. Security Classif. (of this report)	20. Security Classif. (of this page)	21. No. of Pages	22. Price*
Unclassified	Unclassified	175	

* For sale by the National Technical Information Service, Springfield, Virginia 22151

NASA-C-168 (Rev. 6-71)

NAS CR-120870
TRW 14549-6001-RO-01

FINAL REPORT

HYDROGEN-OXYGEN CATALYTIC IGNITION AND THRUSTER INVESTIGATION

VOLUME II
HIGH PRESSURE THRUSTER EVALUATIONS

by

R. J. Johnson
B. Heckert
H. L. Burge

TRW Systems Group
One Space Park
Redondo Beach, California 90278

Prepared for
NATIONAL AERONAUTICS AND SPACE ADMINISTRATION
November 14, 1972
Contract NAS 314347
NASA Lewis Research Center
Cleveland, Ohio

P. N. Herr, Project Manager
Liquid Rocket Technology Branch

TRW Systems Group
One Space Park
Redondo Beach, California 90278

FOREWORD

This report was prepared by the Applied Technology Division of the TRW Systems Group, One Space Park, Redondo Beach, California, under Contract NAS 3-14347. The contract was administered by the Lewis Research Center of the National Aeronautics and Space Administration, Cleveland, Ohio. The NASA Project Manager for the contract was Mr. P. N. Herr of the Liquid Rocket Technology Branch. This is Volume II of the final report on the subject contract and summarizes the high pressure thruster technical effort conducted during the period from March 1971 to December 1971. Volume I describes the catalytic ignition and low chamber pressure thruster evaluations, and Volume II presents the results of the high pressure thruster evaluations begun during March 1971.

ACKNOWLEDGEMENTS

The following personnel at TRW contributed to the technical accomplishments of this program: R. J. Johnson, Program Manager; B. J. Heckert, High Pressure Thruster Development and Evaluation; B. G. Morton, Igniter Evaluations; H. L. Burge and S. J. VanGrouw, Technical Advisors; E. P. Koutsoukos, M. J. Santy, and T. B. Hurst, Laboratory Investigations; H. W. Beck, K. J. Mock, and E. W. Woodell, Design; P. Y. Hsieh, Stress Analysis; F. B. Muenzer, Dynamic Analysis; F. Scott, Heat Transfer Analysis; J. T. Gardner and J. T. Fitzgerald, Engineering Liaison; J. R. Augustson, L. L. Gassert, F. E. Robinett, and R. C. Sorensen, Test Operations; D. S. Landgreen and G. P. Starr, Data Acquisition.

CONTENTS

CONTENTS (Continued)

ILLUSTRATIONS

ILLUSTRATIONS (Continued)

ILLUSTRATIONS (Continued)

ILLUSTRATIONS (Continued)

ILLUSTRATIONS (Continued)

TABLES

ABSTRACT

The high pressure thruster effort was conducted with the major objective of demonstrating the TRW duct cooling concept with gaseous H_2/O_2 propellant in a thruster operating at nominally 300 psia (2068 kN/m^2) and 1500 lbf (6672N). The high response catalytic igniter concept reported in Volume I of this report was incorporated into the design. The analytical design methods for the duct cooling were proven in a series of tests with both ambient and reduced temperature propellants. Long duration tests as well as pulse mode tests demonstrated the feasibility of the concept. All tests were conducted with a scaling of the raised post triplet injector design previously demonstrated at 900 lbf in NASA MSFC and MSC demonstration firings. A series of environmental conditioned firings were also conducted to determine the effects of thermal soaks, atmospheric air and high humidity. This volume presents the results of the high pressure thruster evaluations. Volume I presented the results of the catalytic igniter and low pressure thruster evaluations, NASA CR-120869.

1. SUMMARY

1. SUMMARY

The experimental results of the high pressure, large thruster efforts of Contract NAS 3-14347 have demonstrated the feasibility of the TRW duct cooled concept as a viable design for gaseous H_2/O_2 attitude control thrusters. In this design cooling is provided by bypassing a percentage of the GH_2 (20 to 30%) from the injector supply through a free floating cooling channel jacket around the primary combustion zone. This coolant is heated and ejected at high velocity along the nozzle walls at a contraction ratio of $\sim$ 1.5:1. The high velocity film of gas flows over the remainder of the nozzle and provides a thermal protection to the nozzle with no other cooling means. This results in a virtual adiabatic wall nozzle which requires design only for pressure loading. The 1500 lbf (6672 N) flightweight nozzle required wall thickness is on the order of 0.050 inch (0.127 cm). This results in a very lightweight thrust chamber structure

The cooling design approach results in a major reduction in thrust chamber fabrication complexity with only minimal sacrifice in performance. The resulting geometries are simple shapes and lend themselves to virtually text book analytic design with a minimum of required assumptions. As a result the predicted thrust chamber cycle life can be accepted with high confidence.

A detailed materials survey was conducted for the selection of the thrust chamber fabrication materials. A-286 was selected for the nozzle, and Berylco-10 was selected for the duct. The injector face elements were constructed from OFHC copper. All remaining external parts were fabricated from S.S.347.

The high response catalytic igniter developed earlier in the contract effort (described in Volume I) was incorporated into the design for the test firings. This unit has demonstrated the ability to repeatedly and reliably ignite the high pressure thruster in both steady state and pulse mode operation with total response times less than 50 ms.

A raised post triplet injector design was used for the experimental firings. This injector was an extrapolation from a 900 lbf (4000 N) injector developed earlier at TRW. This injector approach has proven the ability to approach 100% combustion performance over a wide range of mixture ratios. As a very high performing injector it also has a high face heat transfer rate due to the rapid, near face mixing of the propellants. The test results indicated that the pressure limit margin for the thrust chamber assembly was slightly in excess of 300 psia (2068.5 KN/m^2) with the limit being the injector's durability. The limited scope of the program did not allow for detailed investigation of the injector to improve this limit.

The demonstrated altitude delivered performance at ε = 40:1 of the thrusters at a mixture ratio of 4:1 was $\sim$432 lbf-sec/lbm (4248 N-sec/kg) with 32% of the total GH_2 flowing through the duct. This is slightly higher than the performance prediction model would give. Although the thruster experiments were not conducted with the duct at its thermal limit because of program limited hardware availability, the test data

strongly support a design point limit performance of 440 lbf-sec/lbm. At this performance level the thermal stress limits indicate a life in excess of 10^6 cycles.

The pulse mode results indicated that good pulse response could be achieved with the limiting factor being the catalytic igniter response of $\sim$ 25-30 ms. Actual thruster responses of less than 50 ms were achieved with the use of non-optimum valving.

The resulting thermal test data also confirmed the nozzle wall temperature profile predictions. The peak interior nozzle wall temperature were uniform to within 50^{o}F (10^{o}C) at any axial location in the nozzle.

The major limitation in the design approach was found to be with the high performance triplet injector as fabricated from OFHC copper. Two minor erosion problems occurred during the test effort which necessitated repairs of the unit. The high heat fluxes near the face precluded actual experimental data from being generated at pressures greater than 300 psia (2068 kN/M^2). The high response catalytic igniter performed quite well. The cold, high humidity environmental tests indicated an icing problem which precluded ignition when the catalyst surfaces were occluded. When the catalyst bed was isolated by low level purging the problem was eliminated.

The firing program as a whole was quite successful. A total of 146 tests were conducted with a number of thermal duration tests.

2. INTRODUCTION

2. INTRODUCTION

The NASA is currently planning and studying the Space Shuttle vehicle as a means of achieving low launch costs for space exploration and utilization. The orbiter vehicle of the Space Shuttle has as one of its many projected uses the direct application as a space laboratory. The direct payload weight payoff function of the orbiter is, in part, determined by its propulsion system requirements. A unit of mass in the propulsion system is essentially a unit of mass less in payload. As a consequence, in order to achieve the full potential of the vehicle it is desirable to consider the use of high energy propellants. This requirement along with the consideration of the use of the vehicle as a laboratory suggests the use of H_2/O_2 for the attitude control system, since the combination provides high energy and is the cleanest burning of all the propellants which may be considered.

The effort reported herein reflects an advanced technology which may be considered for use by such vehicles as the Space Shuttle. The effort utilizes the previously developed catalytic ignition concepts as sponsored by NASA LeRC. The thruster concept was suggested by TRW Systems as a logical concept for such application, particularly to meet long life and high cycle life requirements.

This part of the "Hydrogen-Oxygen Catalytic Ignition and Thruster Investigation" program, NASA LeRC Contract NAS 3-14347, was composed of analytical and experimental evaluations of the duct cooling concept for gaseous H_2/O_2 thrusters operating at high pressure. The high response catalytic igniter activity of the early part of the NAS 3-14347 was extended to this thruster program activity. Whereas the igniter activity began in June 1970, the high pressure thruster activity was added to the program as a limited supplemental effort and commenced in March, 1971. The entire experimental effort terminated in December, 1971.

The objectives of the high pressure thruster program effort were as follows:

- Provide a design basis for the use of the duct cooling concept.
- Evaluate the overall thruster performance, operating characteristics and durability of a cooled, near flightweight gaseous H_2/O_2 thruster.
- Determine minimum impulse bit capability of the thruster design.
- Determine the effects of environmental, humid air on the thrust chamber assembly operation.
- Evaluate the potential of the use of the igniter flow only as a minimum impulse bit device.

The following tasks were accomplished to meet the objectives:

- Thruster/Igniter Analysis and Design.
- Thruster Hardware Fabrication (one complete thruster assembly).
- Thruster/System Interaction Analysis.
- Thruster/Igniter Experimental Evaluation.

This report presents results pertaining to the high pressure thruster design. The igniter background is presented in Volume I of this report.

3. THRUSTER DESIGN AND ANALYSIS

3. THRUSTER DESIGN AND ANALYSIS

The entire emphasis in this part of the contracted effort was on the TRW duct cooled approach. No other designs were considered. The approach is described in detail in the ensuing sections of this report. To orient the reader the overall design concept is presented first.

3.1 DUCT COOLED DESIGN CONCEPT AND FEATURES

There are undoubtedly many approaches which can be taken to the design of gaseous H_2/O_2 thrusters for potential application to the Space Shuttle orbiter vehicle. Some of the more important factors to consider in the design are:

1. All propellant lead in plumbing should be integrated into the injector assembly as much as possible. This requirement eliminates external appendages around the thruster assembly which may compound variable installation geometry problems.

2. The head end assembly design should accommodate the ability to enter the propellant feed line from: (1) in-line, (2) right angle, and (3) reverse valve installation. The thrust chamber assembly should be unaffected by these installation requirements. This makes possible a common thrust chamber and injector assembly for all installations.

3. The thrust chamber cooling concept must not result in specialized nozzle designs for various degrees of scarfing and expansion ratio requirements. This eliminates nozzle regenerative cooling, if a common developed engine is to be adopted to all installations.

4. The design goal for thermal and pressure loading margin on the thruster should be an all elastic stress design. If this is achieved high cycle fatigue design approaches can be used.

5. The selected materials should be existing, well proven, and readily available materials. This eliminates the need for new materials research to satisfy the design goals.

6. The injector design should not couple adversely with the thrust chamber design. If this goal is met the injector can be optimized for performance, and the thrust chamber cooling can be optimally designed without iterative interaction design with the injector.

7. For long life the valves should be set-off from the injector by thermal stand-off plumbing and isolated struts. This prevents soak back thermal effects on the valve seats and closures.

8. For MIB control the igniter should be designed to provide both ignition functions and small bit propulsion functions. This requires a flow rate adequate for vehicle sensing and an overall

mixture ratio which results in a temperature compatible with the thrust chamber design. It also results in separate valve functions for the igniter which may be met by separate valves or integrated, two step valves.

Figure 1 illustrates the approach taken to partially meet the above goals as well as provide a flexible research tool to meet the objectives of the current contracted effort. Beginning at the head end of the thruster the main valves for the flight engine are in-line poppet valves. (TRW provided Flodyne ball and in-line poppet valves for the testing of the engine.) The main valves are pneumatically actuated by small solenoid pilot valves.

The igniter is fed by separate propellant valves. The GO_2 enters axially and the GH_2 enters radially. The igniter operates at a core combustion MR of 10:1 and an overall MR of 1:1. The igniter is centrally located in the injector. Its combustion chamber is a copper chamber with a reduced throat to provide back pressure in the igniter at startup to enhance ignition.

The injector is a 3-ring raised post triplet. The GH_2 is injected in an axial showerhead manner from the top of the posts. The GH_2 is injected as 2 impinging GO_2 jets onto the center GH_2 jet. The GO_2 orifices are recessed below the surface of the H_2 posts to minimize recirculation effects. The GO_2 manifold feeding is axially through each of the propellant rings. The GH_2 requires a larger manifold, and this requirement is met with the toroidal manifold. The H_2 to O_2 volume ratios are controlled to provide maximum pulse performance. OFHC copper was used for the experimental injector.

Cooling is achieved through the use of a duct in the combustion chamber. This Berylco-10 duct is mechanically anchored on the cold head end only. The remainder of the duct is free to float radially and fore and aft. It is designed to expand to just touch the walls of the nozzle at steady state temperature. The GH_2 flows through 90 constant width channels and exits at a contraction ratio of 1.5:1. Heat transfer analyses reveal that the controlling heat transfer resistance is always on the hot gas side. This means that the duct nearly perfectly decouples the cooling from the injector. As a consequence the injector does not have to be tailored to provide a controlled wall temperature environment.

The nozzle is a thin wall configuration. The maximum thickness is at the throat, and a continuous taper from 0.050" (0.127 cm) to 0.020" (.0508 cm) at the exit is used. (An expansion ratio of 40:1 was selected for this program.) The GH_2 film pours along the nozzle wall and provides nearly perfect thermal protection of the nozzle. The peak nozzle temperature is selected near 1800^oF (1000^oK) and usually occurs at an expansion ratio of $\sim$ 8:1. From this point on the nozzle temperature actually drops, due to internal radiation. The backwall temperature limits of 1260^oR (700^oK) are met in two ways. In the combustion chamber section the wall temperature is controlled by the coolant bulk temperature. Beyond the duct exit the surface temperature is controlled by the use of $\sim$ 0.125" (0.317 cm) of Mini-K insulation type batting.

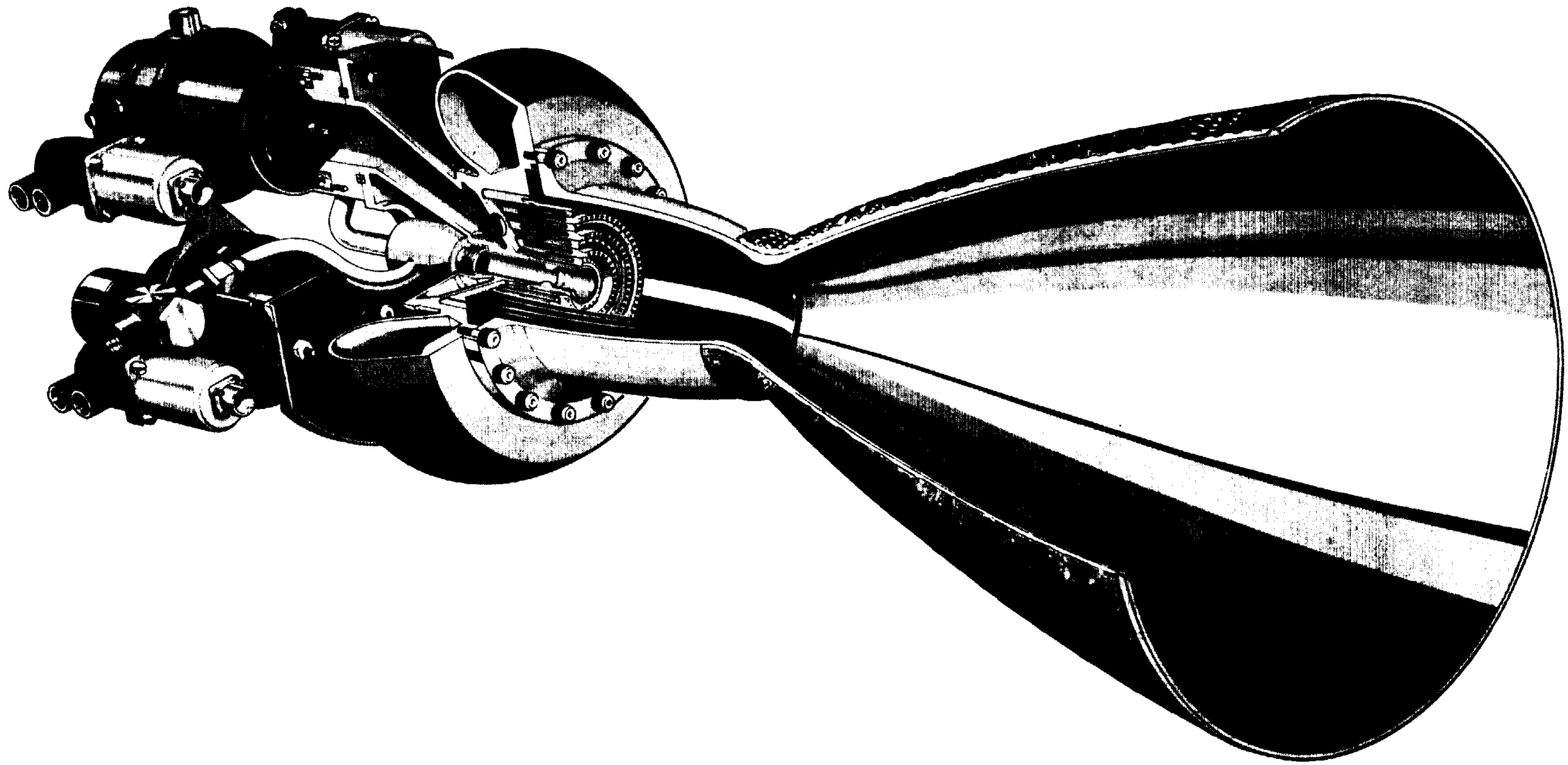

Figure 1. TRW Duct Cooled Engine Concept for H_2O_2 Thrusters

For maintainability purposes the thruster is made dissassembleable as shown. The experimental chamber assembly was designed virtually to the above description.

3.2 THRUSTER ANALYSIS AND DESIGN

The analytical design tasks encompassed both high and low pressure thruster designs for 1500 lbf (6672 N). The nominal design conditions for each case are summarized in Table 1.

Table 1. Thruster Design Conditions

	Case I	Case II
Thrust	1500 lbf (6672N)	1500 lbf (6672N)
Chamber Pressure	15 psia (103 kN/m^2)	300 psia (2086 kN/m^2)
Mixture Ratio	2.5	4.0
Nozzle Expansion Ratio	5:1	40:1
Propellant Inlet Temperatures		
Oxygen	300°R (167°K)	300°R (167°K)
Hydrogen	200°R (111°K)	200°R (111°K)
Propellant Inlet Pressures		
Oxygen	375 psia (2586 kN/m^2)	375 psia (2586 kN/m^2)
Hydrogen	375 psia (2586 kN/m^2)	375 psia (2586 kN/m^2)
C* Efficiency	98%	98%
Specific Impulse	375 $\frac{\text{lbf-sec}}{\text{lbm}}$ (3677 $\frac{\text{Nsec}}{\text{kg}}$)	435 $\frac{\text{lbf-sec}}{\text{lbm}}$ (4266 $\frac{\text{Nsec}}{\text{kg}}$)
Igniter Propellant Flow Rate	1-5% of the total flow rate	

Primary emphasis was placed on the high pressure design, although the design approach used is applicable to both the high and low pressure designs.

3.3 THERMAL DESIGN

Detailed thermal analyses were conducted on the design utilizing an approach which had been previously developed by TRW Systems for duct cooled thrusters. The specific thermal design evaluations were as follows:

- Transient and steady state temperature distributions in injector.

- Steady state temperatures in duct and chamber for several duct materials over a range of flow rates.

- For optimum choice of duct material and flow rate the effect of varying duct length was considered.

- Steady state temperatures in duct and chamber flange were determined.

- For optimum choice of duct material and flow rate the transient thermal behavior of the duct was determined.

- Insulation requirements to maintain chamber and nozzle backwall below 800°F (700.056°K) were determined.

- Transient temperature distributions in nozzle were evaluated.

3.3.1 Material Thermal Properties

A summary of the thermosphysical properties of the various candidate materials considered in the thermal analysis are summarized in Tables 2 through 7.

3.4 THERMAL ANALYSIS OF DUCT COOLED CHAMBER AND NOZZLE

3.4.1 Background

The TRW duct/film cooling approach has, experimentally and theoretically, been shown to be an effective method for cooling a wide range of rocket engine designs for H_2/F_2, N_2O_4/N_2H_4, $C_3H_8/F_2/O_2$ prior to this program. It essentially consists of fabricating a duct liner which is inserted inside the chamber shell and is cooled by propellant injection into the annular passage at the injector end of the chamber. With suitable duct sizing and flow rates the coolant side conductance will always be much greater than the gas side conductance; consequently the duct is decoupled from the combustion process.

The coolant fluid exits from the duct in the convergent position of the nozzle and will lie as a cool boundary layer close to the wall along the length of the nozzle and will effectively cool the nozzle walls.

Among the advantages of the duct cooling concept are the following:

- Unlike conventional thrusters, duct cooled thrusters are not life limited.

- Fast response and small pressure drops as well as being light and easy to build are immediate advantages of the concept.

- Cooling in throat and nozzle regions is generally more effective than for film cooling alone.

- Structural loads imposed on inner duct wall are small since the pressure differential across wall is small.

THERMOPHYSICAL PROPERTIES OF MATERIALS USED IN THERMAL ANALYSIS

Table 2

OFHC COPPER

Temp (^oF)	k(Btu/in-sec-^oF)	ρC_p(Btu/in^3-^oF)
-300.	$5.093c10^{-3}$	.0298
50.	$5.093x10^{-3}$	.0298
300.	$5.002x10^{-3}$	.0305
600.	$4.90x10^{-3}$	.0315
900.	$4.796x10^{-3}$	.0323
1100.	$4.731x10^{-3}$	.0331
1500.	$4.569x10^{-3}$	.0345

Table 4

Berylco 10

Temp (^oF)	k(Btu/in-sec-^oF)	ρC_p(Btu/in^3-^oF)
-300.	$2.48x10^{-3}$	
50.	$2.79x10^{-3}$	
250.	$3.00x10^{-3}$	
400.	$3.10x10^{-3}$	
750.	$3.41x10^{-3}$	
1100.	$3.72x10^{-3}$	.030
2000.	$3.72x10^{-3}$	

Table 3

A-286 Steel

Temp (^oF)	k(Btu/in-sec-^oF)	ρC_p(Btu/in^3-^oF)
-300.	$1.30x10^{-4}$	.0241
70.	$1.74x10^{-4}$	.0381
440.	$2.18x10^{-4}$	.0311
800.	$2.69x10^{-4}$	.0317
1160.	$3.25x10^{-4}$	.0321
1520.	$3.76x10^{-4}$	.0321

Table 5

Min K Insulation

$k = 5.78x10^{-7}$ Btu/in-sec-^oF

ρC_p = .00301 Btu/in^3-^oF

Table 6

Hydrogen at 300 psi

Temp (^oF)	C_p(Btu/lb-^oF)	k(Btu/in-sec-^oF)	μ(Lbm/in-sec)	Pr
-260	3.512	$1.345x10^{-6}$	$.258x10^{-6}$	.676
-160	3.945	$1.863x10^{-6}$	$.343x10^{-6}$	.728
- 60	3.763	$2.176x10^{-6}$	$.418x10^{-6}$	.724
70	3.567	$2.539x10^{-6}$	$.510x10^{-6}$	.716
200	3.497	$2.949x10^{-6}$	$.596x10^{-6}$	.706
500	3.481	$3.965x10^{-6}$	$.758x10^{-6}$	.666
800	3.481	$4.919x10^{-6}$	$.908x10^{-6}$	.642
1200	3.481	$6.127x10^{-6}$	$1.086x10^{-6}$	.617
1500	3.481	$6.998x10^{-6}$	$1.209x10^{-6}$	.601

Table 7

Emissivities

Inside of nozzle ϵ = .6

Outside of insulation ϵ = .9

3.4.2 Analytical Techniques

3.4.2.1 Duct Cooled Region

For thermal analysis purposes the duct is depicted as below:

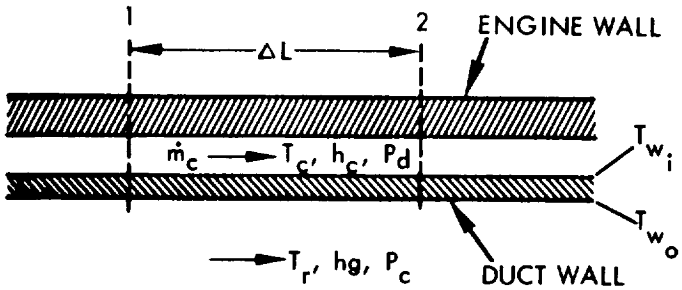

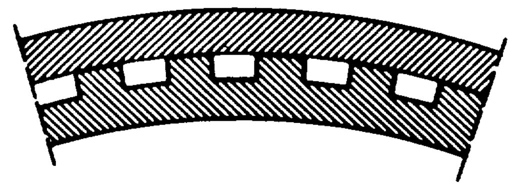

Combustion Gas Side Conditions. One dimensional Mach numbers are computed at any axial station on the basis of the following relationship

$$\frac{R_i}{R^*} = \frac{1}{M_i} \left[\left(\frac{2}{\gamma+1} \right) \left(1 + \frac{\gamma-1}{2} M_i^{\,2} \right) \right]^{\frac{\gamma+1}{2(\gamma-1)}} \tag{1}$$

where suffix i corresponds to some axial station

R = radius

R^* = throat radius

M = Mach number

γ = average gas specific heat ratio

The core mixture ratio (neglecting igniter flow) is given by

$$(O/F)_c = \frac{(O/F)_o}{1 - \frac{\dot{W}_{HD}}{\dot{W}_{HO}}} \tag{2}$$

where suffixes c,o refer to core and overall conditions, respectively

(O/F) = mixture ratio

$\dot{W}_{HD}$ = hydrogen flow in duct

$\dot{W}_{HO}$ = overall hydrogen flow

The core mixture ratio determines the core combustion gas temperature. The combustion temperature is then used to calculate the core adiabatic wall temperature

$$T_{aw} = T_c \quad \frac{1 + R\left(\frac{\gamma - 1}{2}\right) M^2}{1 + \frac{\gamma-1}{2} M^2} \tag{3}$$

where R = recovery factor = $P_r^{1/3}$

P_r = core gas Prandtl number

The film coefficient for heat transfer between the hot gas and the wall was evaluated using the Bartz simplified technique (Ref. 1) with properties evaluated at the average between the wall gas environment and the wall temperature. The Bartz equation is given by

$$h_g = .026 \left[\frac{1}{D^{*.2}} \left(\frac{\mu^{.2} C_p}{P_r{}^{.6}}\right)\left(\frac{P_c\, g}{C^*}\right)^{.8}\right] \left(\frac{A^*}{A}\right)^{.9} \sigma \tag{4}$$

where D^* = throat diameter

μ, c_p, P_r = viscosity, specific heat and Prandtl number at stagnation conditions

P_c = chamber pressure

C^* = gas characteristic velocity

σ is a correction term which accounts for property variations across the boundary layer and is given by

$$\sigma = \left[\left(\frac{1}{2}\frac{T_w}{T_c}\left(1 + \frac{\gamma-1}{2} M^2\right) + \frac{1}{2}\right)^{0.8-\frac{\omega}{5}} \left(1 + \frac{\gamma-1}{2} M^2\right)^{\frac{\omega}{5}}\right]^{-1} \tag{5}$$

where T_w = wall temperature

ω = temperature exponent of viscosity, usually given a value of 0.6

Hydrogen Coolant - Side Conditions. The coolant - side convective heat transfer established by McCarthy and Wolf (Reference 2).

$$N_{u_b} = .025\, R_{e_b}^{\;0.8}\; P_{r_b}^{\;0.4}\; (T_w/T_b)^{-.55} \tag{6}$$

where N_{u_b} = Nusselt number = $\frac{h_c k_b}{D_h}$

k_b = bulk thermal conductivity

D_h = hydraulic diameter in channel

h_c = coolant side coefficient

R_{e_b} = bulk Reynolds number

P_{r_b} = bulk Prandtl number

T_w = inside wall temperature

T_b = coolant bulk temperature

For the type of configurations under investigation, entrace, roughness and curvature effects upon heat transfer coefficients are small enough to be neglected. Any effects would only improve the cooling predictions.

A heat balance is conducted at each lateral station in the duct to evaluate temperature rise of coolant along each station.

$$\dot{q} = \frac{T_r - T_b}{\frac{1}{h_g A_h} + \frac{t_w}{k_w} + \frac{1}{h_c A_c}} \tag{7}$$

A_h = heated area per station

A_c = cooled area per station (including 'fin' effect where applicable)

t_w = duct wall thickness

k_w = wall material conductivity

For channels as shown the coolant surface consists of the width 'w' plus some fractions of the channel height 'l' to account for this 'fin effect'. The degree of this fin effect depend upon the duct material and the ratio of l to w. Analysis has shown that it is undesirable to have l/w>ℓ since the extra part of 'l' gives no additional cooling.

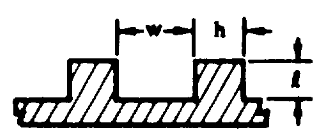

Temperature rise of fluid is given by

$$\Delta T = \dot{q}/\dot{m}_c\ C_{p_b} \tag{8}$$

$\dot{m}_c$ = coolant flow rate

c_{p_b} = bulk specific heat

Pressure drops in the duct include both momentum and friction loss and is based upon the fundamental relationship

$$-dP = \frac{\rho V}{g_c}\,dV + \frac{F_d \rho V^2}{2 g_c D_h}\,dL \tag{9}$$

ρ = density

V = velocity

F_d = friction factor

From station to station, area changes are small and velocity and density changes are linear then pressure drop per station is approximated by

$$\Delta P \quad \frac{\bar{\rho}\,(V_2^2 - V_1^2)}{2 g_c} + \frac{F_o \bar{\rho}\ \bar{V}^2}{w g_c D_r}\Delta L \tag{10}$$

where $\bar{\rho} = \dfrac{\rho_1 + \rho_2}{2}$

$\bar{V} = \dfrac{V_1 + V_2}{2}$

$\bar{V}^2 = \dfrac{V_1^2 + V_2^2}{2}$

The friction factor is given by the standard relationships for smooth tubes

$F_D = \dfrac{64}{R_{e_d}}$ for $R_{e_d} < 1600$

$F_D = .0397$ for $1600 \leq R_{e_d} < 400$

$F_D = .316$ for $R_{e_d} \leq 4000\ R_{e_d} < 100000$

3.4.2.2 Film Cooled Region

This region extends from the duct exit to the nozzle exit as shown.

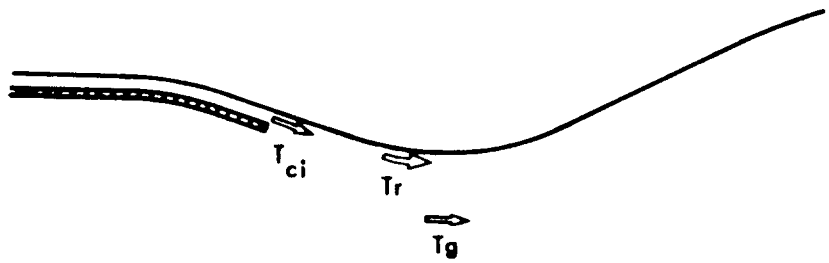

In the film cooled region the temperature acting as a driving potential to the wall is dependent upon the temperature at which the coolant exits from the duct, the hot gas temperature, and the degree to which the hot gas mixes with the cool boundary layer. The latter is described by the film coolant effectiveness η.

$$T_{r_f} = T_g - \eta \left(T_g - T_{c_i}\right) \tag{11}$$

T_{r_f} = film recovery temperature

T_g = gas temperature

T_{c_i} = duct coolant exit temperatures

Knowledge of the film effectiveness, η, as a function of axial distance from the injection point is necessary to establish the local driving temperature at the wall.

Several boundary layer mixing models are available which consider the mixing of the combustion gases with the coolant along the wall. It has been found at TRW that the most effective is the approach of Carlson and Talmor (Reference 3).

Carlson and Talmor assume that the boundary layer growth downstream of the injection is unaffected by the coolant and write the boundary layer flow equation

$$M_g = a u_e \rho_e L \left(\delta - \delta^*\right) \tag{12}$$

where M_g = hot gas flow rate in boundary layer
a = mixing coefficient

u_e & ρ_e = velocity and density at edge of boundary layer

δ = boundary layer thickness

δ^* = momentum thickness

L = axial length

δ and δ^* are calculated assuming a one-seventh power velocity profile by solving the integral momentum equation for an accelerating, compressible, turbulent boundary layer on an infinite wall. This yields

$$m_g = .329\, aL(R_{eg},x)^{4/5} (\rho_e/\rho_d)^{1/5} \left(\frac{\mu_o}{\mu_e}\right)^{1/5} \left(\frac{T_e}{T_o}\right)^{8/7} \frac{\mu_e}{x^{4/5}\, u_e^{108/35}} \left[\int_o^x u_e^{27/7} \left(\frac{T_o}{T_e}\right)^{10/7} \frac{\rho_r\, u_r}{\rho_o\, u_o}\, dx\right]^{4/5} \tag{13}$$

R_{eg},x = Reynolds number is core based upon axial distance from coolant outlet

μ,ρ,T = viscosity, density, absolute temperature

Suffixes: e = edge of boundary layer

o = stagnation conditions

r = reference temperature

A heat balance relating the boundary layer flow and core gas flow was similar to that adopted by Librizzi and Cresci (Reference 4) and yields

$$m_g = m_c \frac{C_{p_c}}{C_{p_g}} \frac{(T_c - T_{c_i})}{(T_g - T_c)} \tag{14}$$

Now
$$\frac{T_c - T_{c_i}}{T_g - T_c} = \frac{1-\eta}{\eta} \tag{15}$$

and is therefore the film <u>ineffectiveness</u> to <u>effectiveness</u> ratio denoted by Y.

Combining the boundary layer momentum thickness equation with the heat balance equation, simplifying the integral by taking $\rho_r U_r \simeq \rho_o U_o$, and expressing local velocities in terms of local Mach numbers and local density and viscosity in terms of local pressure ratios we arrive at the final form

$$Y = .329 a X_1 \tag{16}$$

where

$$X_1 = X\left[\left(\frac{P_e}{P_o}\right)^{1/4-\left(\frac{1+\omega}{4}\right)\left(\frac{\gamma-1}{\gamma}\right)} \frac{\left[1+\frac{\gamma-1}{2}M^2\right]^{1/2}}{xM^{27/7}} \int_o^x \frac{M^{27/7}}{\left[\left(1+\frac{\gamma-1}{2}M^2\right)\right]^{1/2}}dx\right]^{0.8} \tag{17}$$

where P = pressure

ω = temperature exponent of viscosity (nominally 0.6)

M = local Mach number

X represents the correlation for flat plate incompressible flow with no accelerations

$$X = \frac{R_{e_{g1}}\, x^{0.8}}{R_{e_{c,s}}}\left(\frac{\mu_e}{\mu_c}\right)\left(\frac{C_{p_e}}{C_{p_c}}\right) \tag{18}$$

where $R_{e_{c,s}}$ = Reynolds number of coolant at channel exit

The assumption of boundary layer growth being unaffected by coolant injection has been examined by Chapman (Reference 5) and found to be valid when coolant flow is less than 50% of the core flow. All cases under examination are well within this criterion and this suggests that the above approach is acceptable.

A pressure gradient correction extending flat plate incompressible correlations to accelerating flow, was also proposed by Stollery and El-Ehmany (Reference 6). The correlation substitutes

$$\left[\frac{1+\frac{\gamma-1}{2}M^2}{M}\right]^4 \int_o^x \left[\frac{M}{1+\frac{\gamma-1}{2}M^2}\right]^4 dx \tag{19}$$

for x in the X grouping.

Experimental results obtained at TRW between 1968 and 1971 showed that the experimental results were best described by a combination of these two correlations. This yields as the correlating parameter for compressible accelerating flow.

$$X_1 = X \left\{ \frac{1}{x} \left[\frac{1 + \frac{\gamma-1}{2} M^2}{M} \right]^4 \int_o^x \left[\frac{M}{1 + \frac{\gamma-1}{2} M^2} \right]^4 dx \right\}^{.8} \tag{20}$$

In addition, the mixing coefficient, based upon experiments at TRW was shown to be the form

$$a = A + \frac{B}{P_c} \int_{\substack{\text{duct} \\ \text{exit}}}^{x} \frac{\partial P}{\partial x} dx \tag{21}$$

It is noted here that this simplified form of the boundary mixing coefficient has the effect of density (or pressure level) on it as well as velocity gradient (implicit in the $\partial P/\partial X$ gradient). This is sufficient to obtain the gross detail of the film mixing coefficients. Furthermore, it takes a most complex phenomena and reduces it to an easily managed engineering solution. In a large number of TRW experiments encompassing film coolants with molecular weight of 2 to 32 it has been found that the subsonic transonic, and supersonic mixing for thrusters at 300 psia (2086 kN/m^2) is adequately described for engineering purposes with the emperical constants as

$$A \simeq 0.59, \; B \simeq 0.34$$

The viscosity of the gas at the edge of the boundary layer is found by the expression given by Bartz (Reference 1)

$$\mu_e = (46.6 \times 10^{-10}) \, (MW)^{1/2} \, (T)^{0.6} \quad \text{Lb/In-Sec} \; (\qquad) \tag{22}$$

MW = molecular weight

Equation (11) now becomes

$$T_{r_f} = T_g - \frac{1}{1 + .329aX_1} (T_g - T_{c_i})$$

This expression is used to evaluate the driving temperature in the film. The heat transfer coefficient between the film and the wall is given by the Bartz relationship.

A heat balance on the wall under steady state conditions yields

$$h_{g_f} \left(T_{r_f} - T_{w_i}\right) = \sigma\varepsilon_i F_i \left(T_{w_i}^{\ 4} - T_o^{\ 4}\right) + \sigma\varepsilon_o F_o \left(T_{w_o}^{\ 4} - T_o^{\ 4}\right) \tag{23}$$

subscripts i and o correspond to inside and outside of nozzle wall respectively.

T_w = wall temperature

σ = Stefan/Bottzman constant

ε = emissivity

F = shape factor

T_o = ambient environment temperature

3.4.3 Additional Duct Design Rationale

From past experience at TRW it has been found that the most desirable and effective design for a coolant duct is one using straight channels with a fairly large number of channels. The latter gives a high degree of cooling and also decouples the duct behavior from any injector flow maldistributions However, it will also raise duct pressure drop and so requires optimization. The choice of number of channels and preliminary dimension estimates are presented below in the design rationale.

3.4.3.1 Limiting Parameters

The key design parameters are as follows:

1) For any given duct material there is a limiting maximum temperature above which the material strength drops to too small of a value.

2) The exit velocity from the duct should equal the full stream velocity. If there is too great a disparity between the two velocities excessive turbulence will be induced in the film which results in increased mixing between the film and the core gas flow and, hence, higher downstream temperatures.

$$\therefore V_e = V_\infty \tag{24}$$

hence

$$\frac{\dot{W}}{(hw)_e \, \rho_w} = V_\infty \tag{25}$$

where $\dot{W}$ = coolant flow

$(hw)_e$ = (height x width) of each channel of duct exit

ρ = coolant density at exit

n = number of channels

$$(hw)_e = \frac{\dot{W}}{\rho n V_{oo}}$$

3. Since the duct exit pressure must equal the free stream pressure and there is a limit on the maximum duct inlet pressure this will put a ΔP limitation on the duct (nominally around 60 psi (413.7 KN/m^2)).

4. The land width between channels and the hot gas wall thickness at the duct exit should be as small as manufacturing tolerances will allow since these 'lands' will cause a 'wake' to be formed in the film. It has been found that with wide exit lands the wake can be sufficient to cause burnout of the thruster walls.

3.4.3.2 Design Approach

From limiting design parameters 2) and 4), if it is initially assumed that the exit land width were zero, then

$$W_e = \frac{2\pi R_e}{n} \tag{26}$$

where

R_e = chamber radius at exit

$$h_e = \frac{\dot{W}}{\rho \; V_{oo} 2\pi R_e} \tag{27}$$

An estimate is then made of the heat load to the duct wall and this will equal the heat absorbed by the coolant, and the coolant thermal properties at the duct exit are then determined.

Performing a heat balance at the duct exit region

$$h_c A_c \; (T_{W_i} - T_b) = h_g A_g \; (T_r - T_{W_o}) \tag{28}$$

where h_c = coolant side coefficient (McCarthy & (Wolf)

A_c = cooled area

T_{W_i} = inside wall temperature

T_b = coolant exit temperature

h_g = gas side coefficient (Bartz)

A_g = heated area

T_r = recovery temperature

T_{W_o} = outside wall temperature

Thus the required value of h_cA_c to maintain a desired duct wall temperature at the exit is known.

For high conductivity material

$$A_{c_e} = n\ (2h_e + W_e)\ \text{(Fin effect)} \quad (29a)$$

For low conductivity material

$$A_{c_e} = nW_e\ \text{(no fin effect)} \quad (29b)$$

Since h_e is already previously determined

$$A_{c_e} = \frac{2\pi R_e (2h_e + W_e)}{W_e} \quad (30a)$$

or

$$A_{c_e} = 2\pi R_e \quad (30b)$$

Since h_c = (h_e, W_e) only

then

$$h_c = (n)\ \text{only} \quad (31)$$

thus h_cA_c = (n) only (32)

Therefore the required number of channels to meet the exit heat balance criteria can be determined. From the point of view of manufacturing criteria it is desirable to have the number of channels divisable into 360. Thus the number of channels is rounded off to the nearest number divisible into 360. Another manufacturing criteria is the desirability of maintaining a constant channel width along the length of the duct, ie. The value of W_e determined will be a constant value along the length of the duct. For high conductivity materials this is a practical criteria since heat striking the 'lands' will be easily conducted into the coolant, even when the lands are fairly wide the conductivity will be sufficient to avoid excessively hot spots. With low conductivity material heat will not be conducted away so well from the lands and if these are wide enough may get hot enough to burn out and so for low conductivity materials the requirement for constant channel width may not be practical.

Based upon a specified maximum desirable wall temperature the analysis will provide a channel height distribution along the length of the duct to maintain this wall temperature. In general it will not be possible to exactly meet all the geometric, pressure drop and wall temperature requirements and so compromises are made to allow for a practical design. In general, the pressure drop and geometric restrictions are given the first consideration since these are exactly fixed beforehand. There is some latitude in duct temperature and it requires further structural analysis to adequately define the temperature limitations.

3.4.4 Verification of the Thermal Model

Prior to the start of this program a series of tests was conducted in the altitude facility at NASA MSFC on a 900 lbf (4003.2N) H_2/O_2 thruster, 40:1 area ratio thruster, operating at 300 psia (2068.5 KN/m^2) to verify the above described thermal model. In these tests the percent duct coolant was varied from 20 to 30% of the total H_2 flow. The tests ranged in length from 20 seconds to 120 seconds in duration.

The primary area of thermal interest in these tests was the correlation of behavior in the film cooled region, which was the primary region of thermal uncertainty. Therefore, the region downstream of the duct exit was thermally well instrumented. Since the duct cooled region in the combustion zone was one where standard analytical techniques apply, a much greater level of confidence in the analysis of this region was to be expected. In this thruster the duct extended to an area ratio of 1.5:1 where the coolant hydrogen was injected to become a film.

Typical temperature distribution results are shown in Figures 2 and 3 for high and low mixture ratios. It is seen that the model actually overpredicts the peak temperature and predicts this peak to occur at a location in the nozzle upstream of where it actually occurred.

The "cusp" effect is seen in all the data. The near zero gradient dT/dX in the cusp zones means the real mixing coefficient nearby went to zero in this region. To prove that this in fact is the case the NASA sponsored Mass Addition Boundary Layer (MABL) Program developed at Dynamic Sciences was used to trace the history of the "rigorous" mixing coefficient in the MABL program. The results are shown in Figure 4. This result is in consonance with the TRW results. Since the TRW program provides an excellent rapid means of design solution and so well predicts the nozzle behavior as borne out by the above results it was used exclusively to thermally design the thruster for this program.

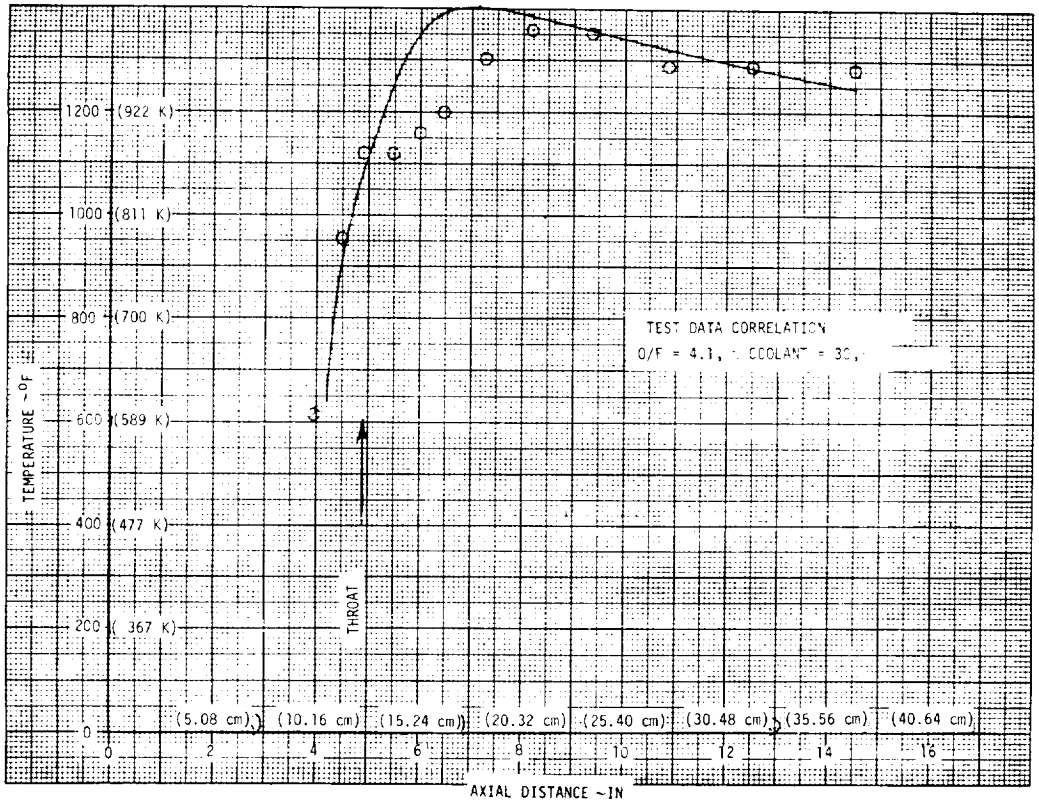

Figure 2. Thermal Model Verification Using MSFC 900 lbf (4003.2N) Results, MR = 4.1:1

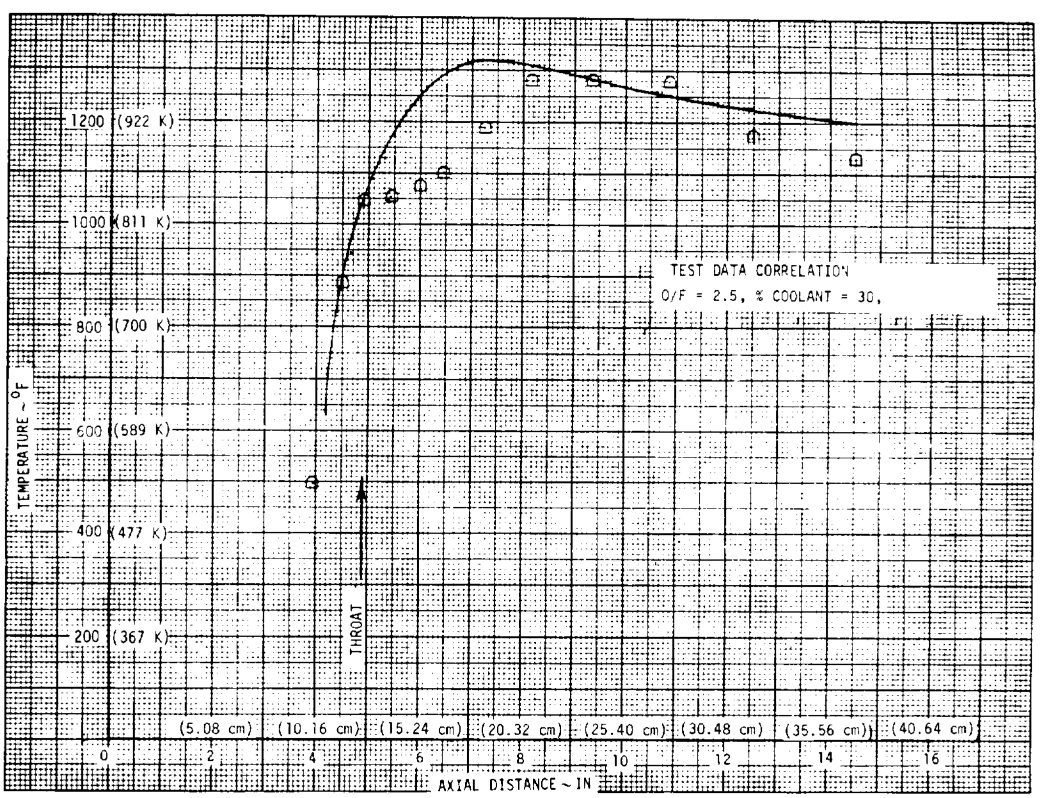

Figure 3. Thermal Model Verification Using MSFC 900 lbf (4003.2N) Results, MR = 2.5:1

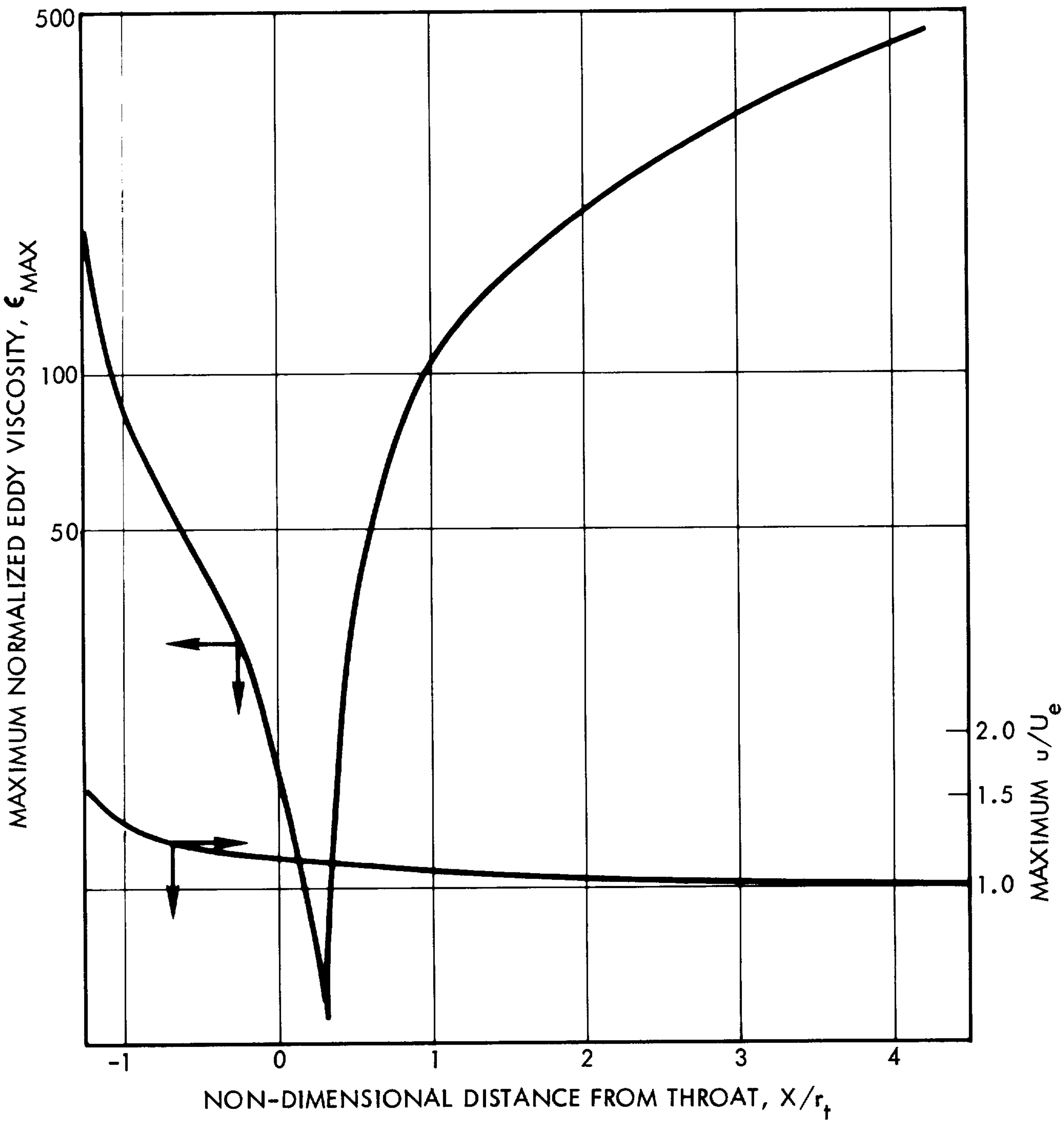

Figure 4. MABL Program Results for 900 lbf (4003.2N) MSFC Data for Mixing Effect and Velocity Ratio

3.4.5 Thermal Design Results

The thermal design results for the various duct configurations which could seriously be considered for this program are summarized below. The channel analysis showed the optimum number of channels to be ∿ 90. With this number determined the other important parameters were optimized. For the analysis the chamber and nozzle was always kept as A-286 steel.

3.4.5.1 Duct Steady State Analytical Results

Only a limited number of analyses were conducted for the ambient temperature condition and the results of this analysis using the duct cooling programs is presented in Figures 5 and 6.

Figure 5 shows the duct design parameters for a duct manufactured from OFHC copper or silver copper, with a limiting ΔP of 60 psi. The data show that for reasonable nozzle and duct temperatures the coolant flow should be around 25% of the total hydrogen flow. With a constant channel width of .076" (0.193 cm) the inlet duct height should be .46" (0.117 cm) and the exit duct height .026" (0.066 cm). The resulting temperature distribution in the duct and nozzle are presented in Figure 6.

The results of the analysis for the cold propellant condition are presented in Figure 7 through 13.

Figure 7 shows the typical results of a run conducted using the on line computer program and shows temperature distributions in duct, coolant, film and nozzle wall.

Figures 8 and 9 present the parametric design curves for OFHC, silver/copper, Berylco 10 alloy and A-286 steel. The results for the first three materials are sufficiently close to enable one design chart to be used for all three. In the case of A-286 steel the comparatively low conductivity of this material requires small land widths along the length of the duct and this results in the variable channel width as indicated.

From these design charts it was determined that the optimum coolant flow rate to maintain adequate duct and nozzle temperatures is approximately 20% of the overall hydrogen flow. Figures 10, 11 and 12 present the temperature profiles in the duct and nozzle for OFHC/silver Copper, Berylco 10 and A-286 steel respectively.

The effect of duct length is graphically presented in Figure 13 where the maximum nozzle and duct temperatures and pressure drop are presented for a Berylco 10 duct as a function of duct exit area ratio with a constant coolant flow rate in the duct using duct geometry optimized for a duct exit area ratio of 1.5:1.

Figure 14 summarizes the heat transfer coefficient at the wall along the length of the thruster for a nominal case with a hydrogen inlet temperature of $200^{o}R$ ($111^{o}K$), a coolant flow rate of 20% of the total H_2 flow and with the duct taken to an area ratio of 1.5:1.

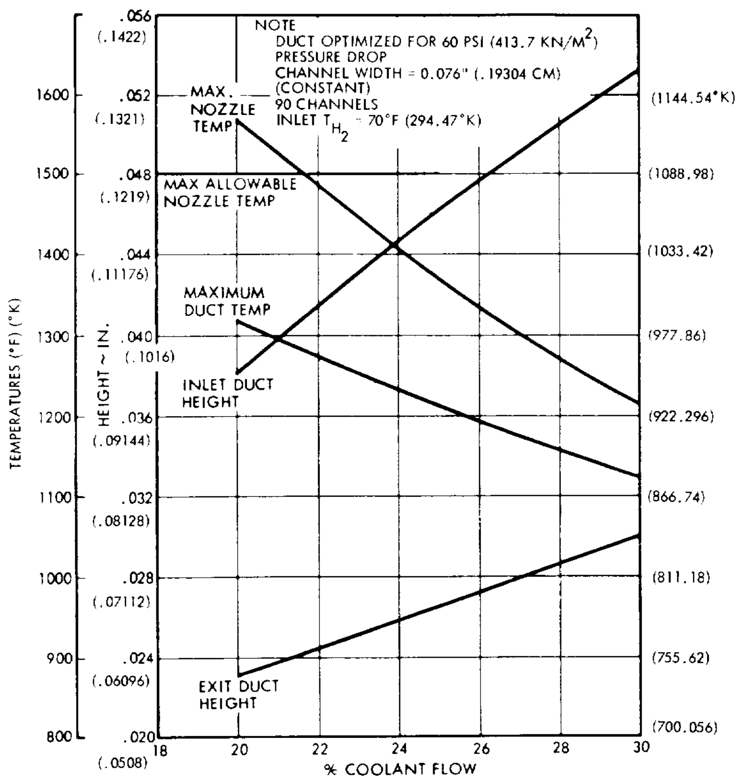

Figure 5. Duct Design Parameters for OFHC or Silver Copper, Ambient Temperature Coolant

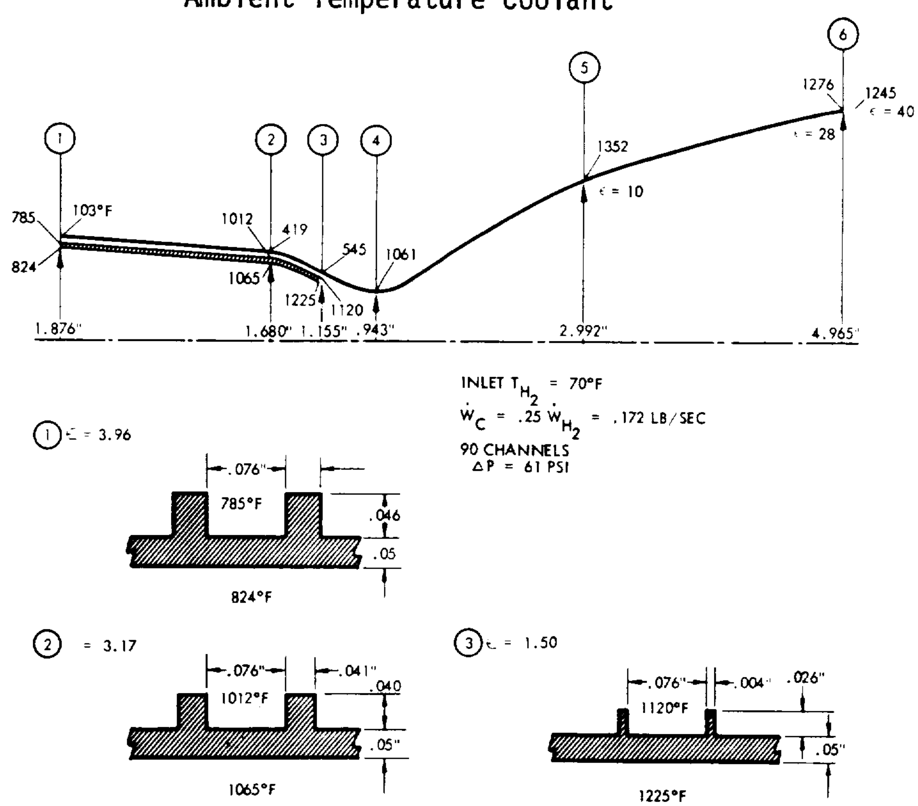

Figure 6. Temperature Distribution and Design Results for Copper Duct

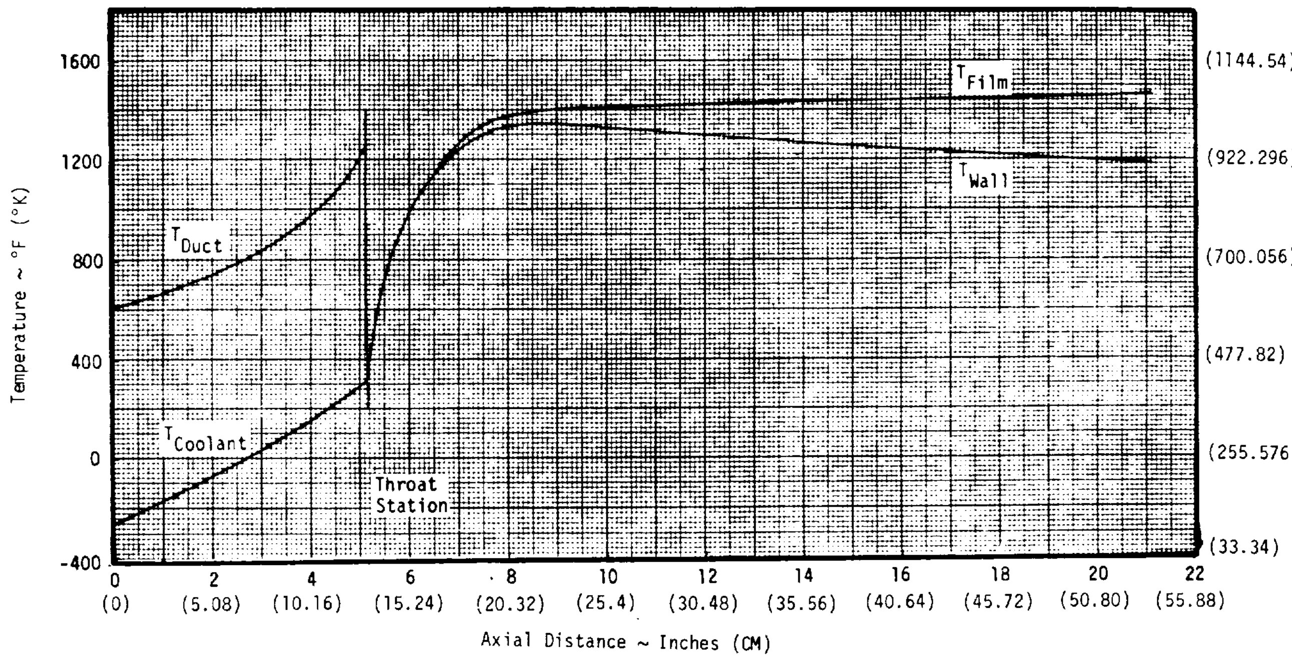

F = 1500 lbf (6672N) P_c = 300 psi (2068.5 KN/M^2) O/F = 4

No. of Channels = 90 % Coolant = 20 T_{Bulk} = 200°R (111.12°K)

Figure 7. Duct Cooled Thruster Thermal Analysis Design Results With Reduced Temperature Propellants

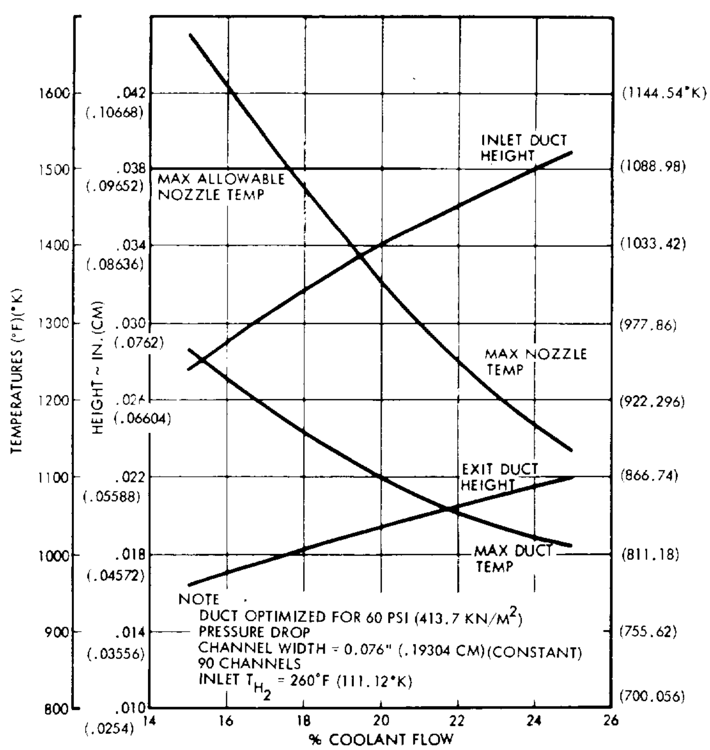

Figure 8. Duct Design Parameters for Copper, Reduced Temperature Coolant

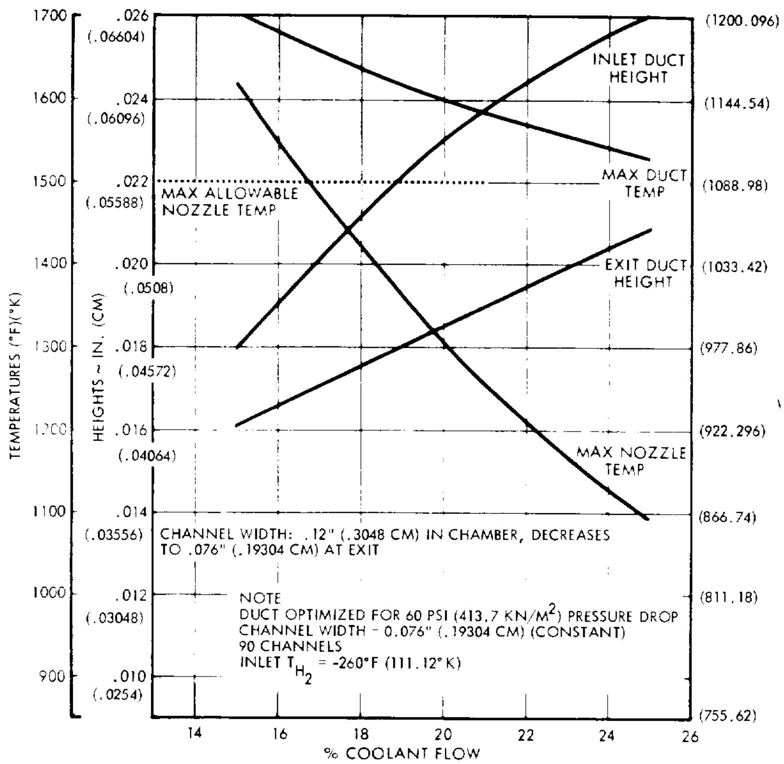

Figure 9. Duct Design Parameters for A-286 Duct

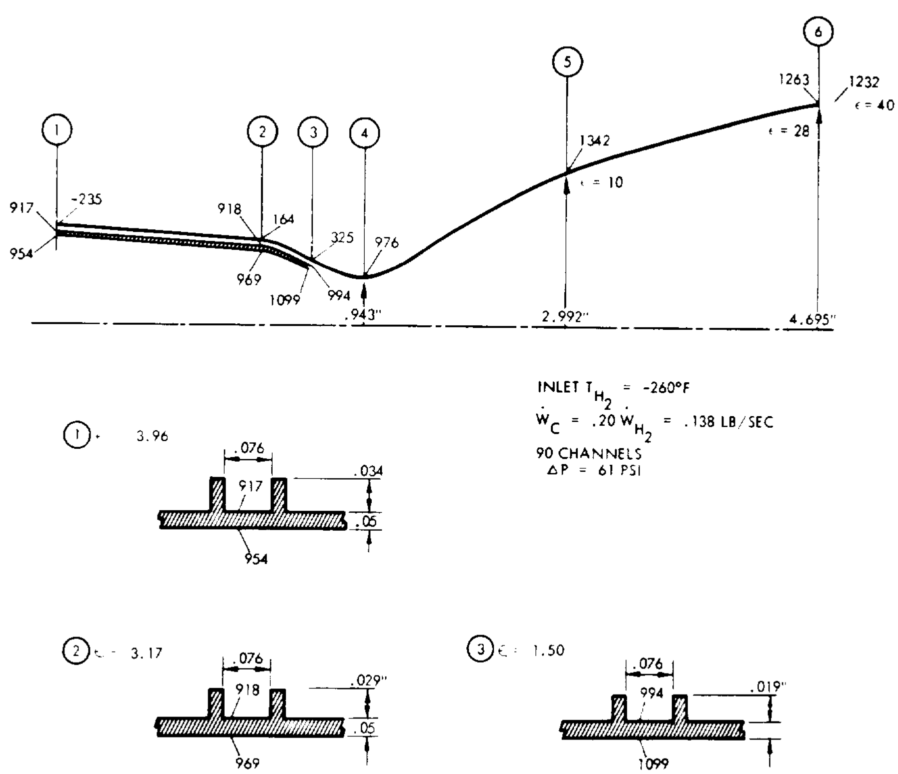

Figure 10. Thruster Thermal Design With OFHC Copper Duct, Reduced Coolant Temperature

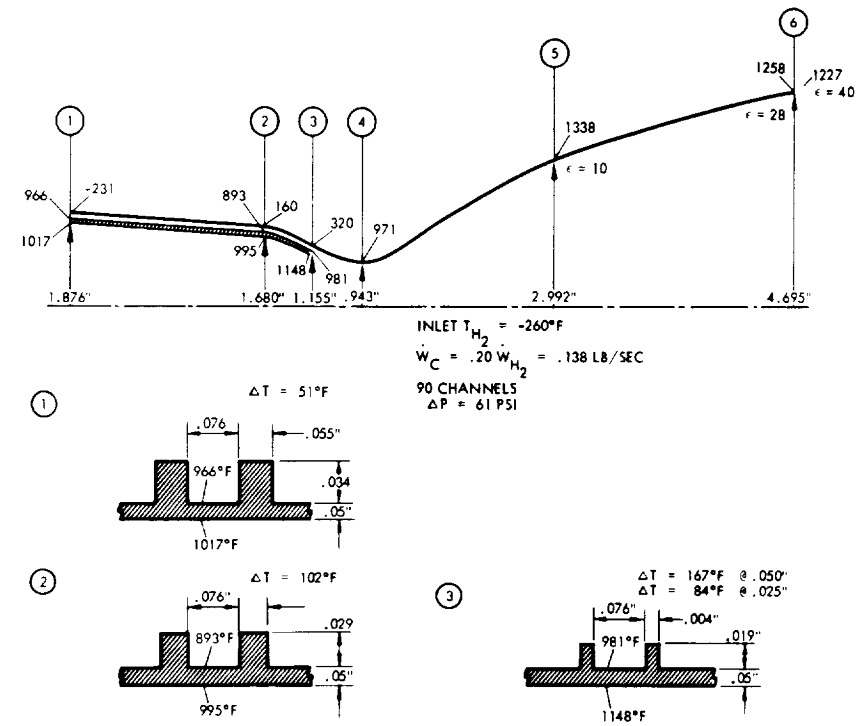

Figure 11. Thruster Thermal Design With Berylco 10 Duct, Reduced Temperature Coolant

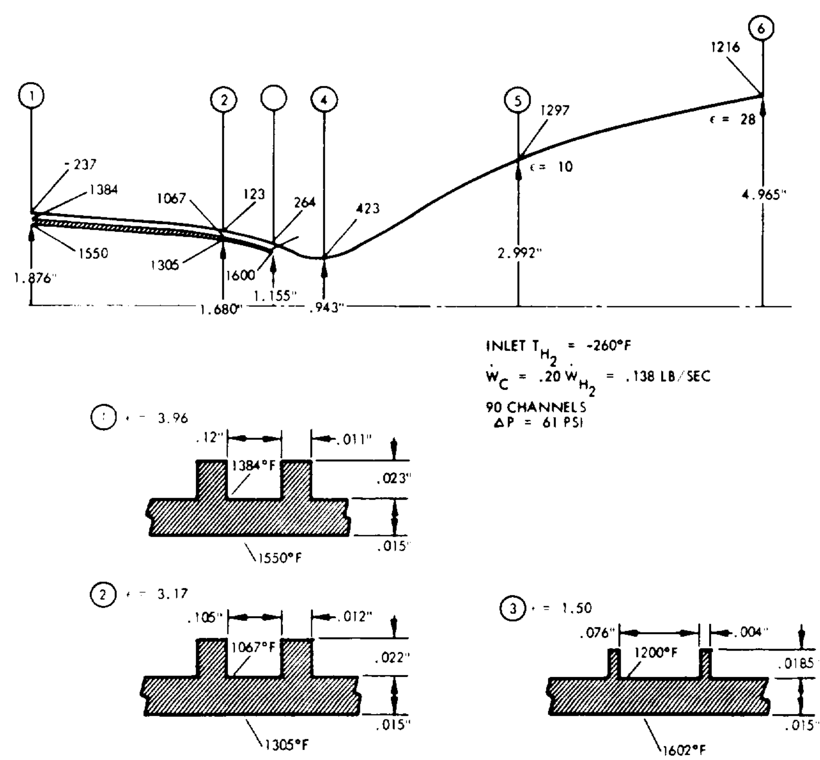

Figure 12. Thruster Thermal Design With A-286 Steel Duct, Reduced Temperatures

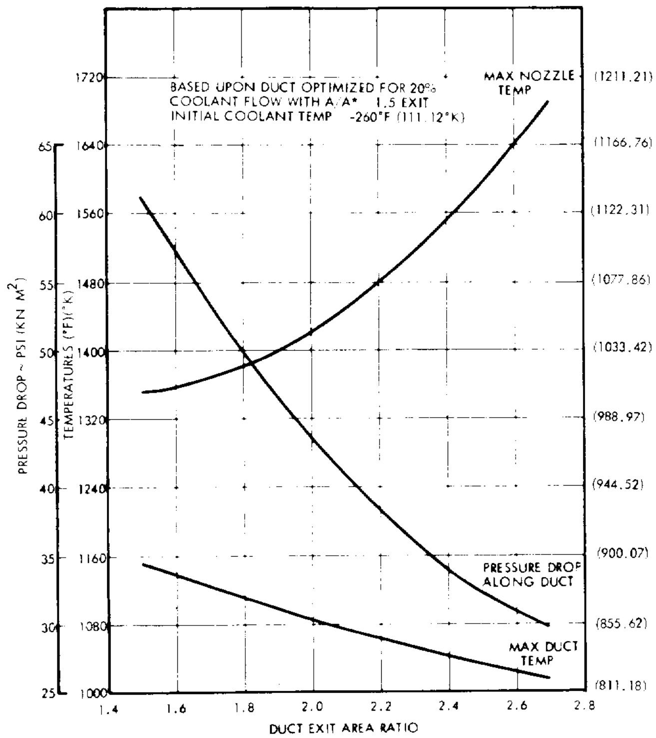

Figure 13. Effect of Changing Exit Area Ratio of Berylco 10 Duct

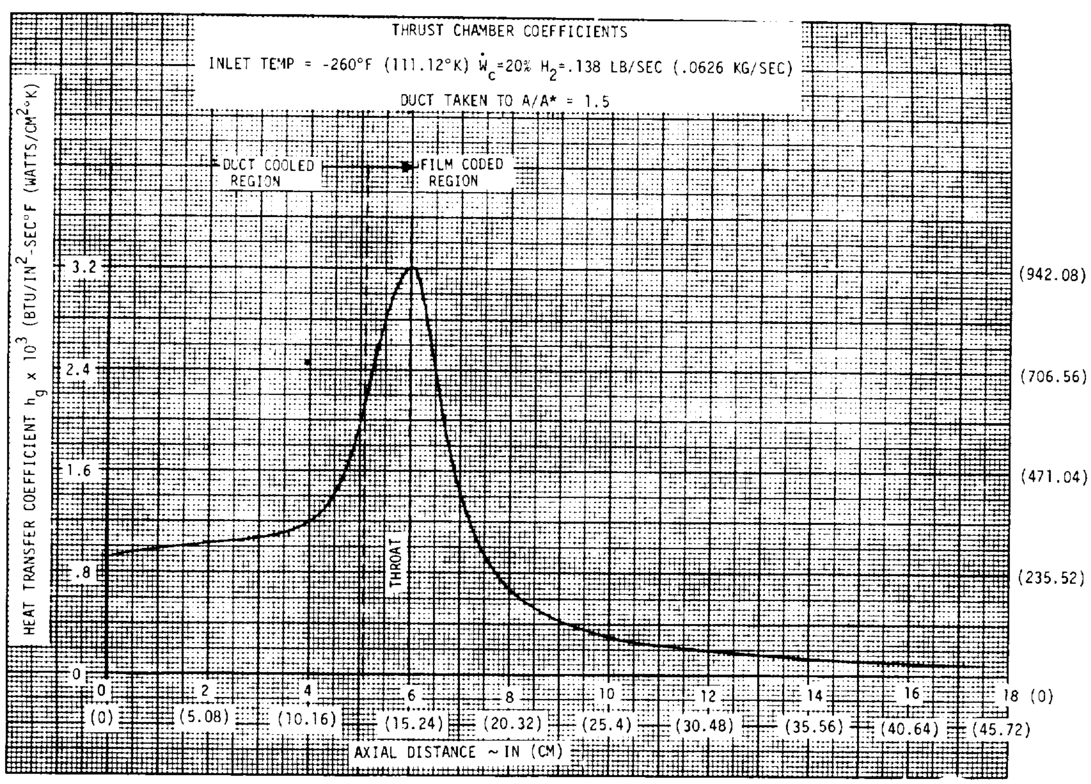

Figure 14. Nominal Gas Side Film Coefficient Distribution Used in the Thermal Analysis

3.4.6 Thermal Transient Duct and Nozzle Responses

The duct and chamber were modeled for solution on TAP. The nodal arrangement used in the combustion chamber is shown in Figure 15 with a simplified flange nodal selection. The flange zone was modelled separately as shown in Figure 16. The boundary conditions for the transient runs were derived from the previous data as input to this analysis.

Figure 17 shows the steady state duct results and Figure 18 shows the transient results for the Berylco-10 duct. As is seen the duct will operate at a temperature of approximately 1460 R (811K). It also has a startup thermal time constant of approximately two seconds. This large time constant results in a large margin of safety in the thruster for initial starting condition control. Berylco-10 was selected for the duct material.

The thermal response transients for the nozzle are shown in Figure 19. Here is it seen that the throat has a response time on the order of 6 seconds, while the exit of the nozzle takes nearly 60 seconds to respond. Such response again is indication of the thermal margin in the duct cooled design.

3.4.7 Nozzle Insulation Requirements

The nozzle beyond the duct exit must be insulated to meet thruster backwall temperature limitations. For the purpose of sizing an insulation for the thruster the previously derived temperature and heat transfer data were used. Radiation from the backwall was assumed to take place from a surface with emissivity of 0.9 to a sink at 0°R (0°K). The insulation chosen was Min K. Figure 20 presents the steady state backwall temperature at different nozzle stations for a range of insulation thickness. A thickness on the order of 0.125" (0.317 cm) will keep the wall at 800°F (700°K) in steady state.

3.4.8 Duct and Flange End Temperature Distributions

Other thermal data of interest to the design are the ΔT across the duct and the gradients along the duct and nozzle near the head end. These results are shown in Figure 21 for the various candidate duct assemblies. As is seen relatively small ΔT differences occur across the duct itself. The entire head end assembly of the unit can be expected to remain essentially at the H_2 coolant supply temperature.

3.4.9 Injector Thermal Modelling

A thermal model of the outer hydrogen and oxygen injector rings was formulated for solution on TRW's Thermal Analyzer Program (TAP). A sketch of this thermal model is presented in Figure 22 indicating the location of the nodes used in the analysis. Each node is assigned a capacitance and is connected to adjacent nodes via resistance paths as indicated in the sketch. Propellant enters the oxygen ring at 300°R (166.68°K) and the hydrogen ring at 200°R (111.12°K).

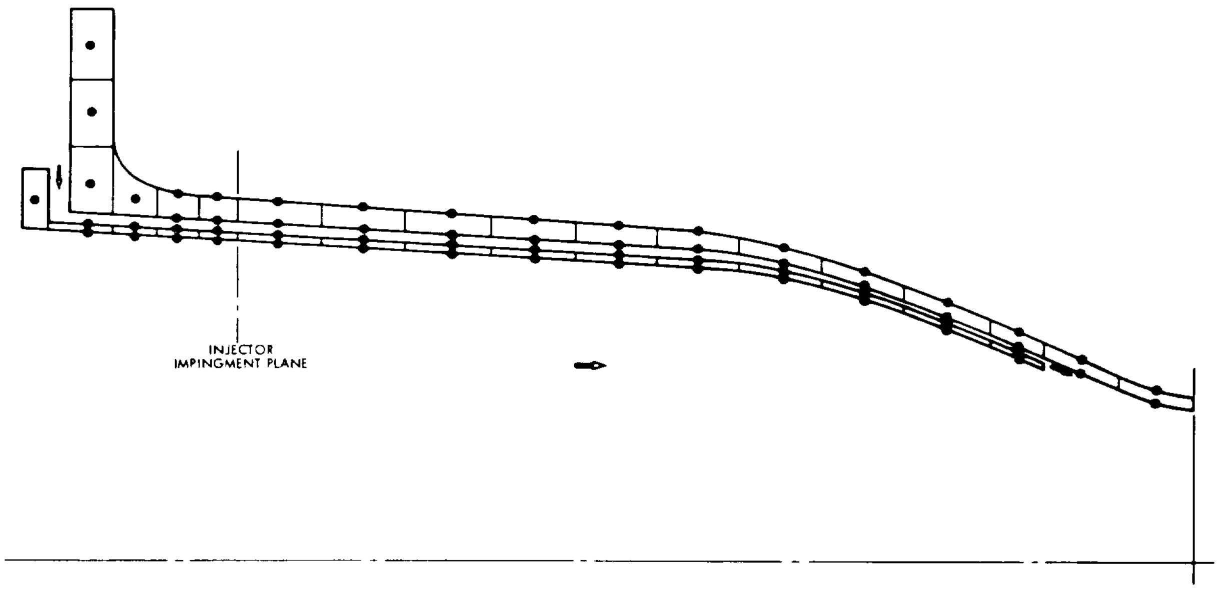

Figure 15. Duct and Chamber Thermal Nodal Model

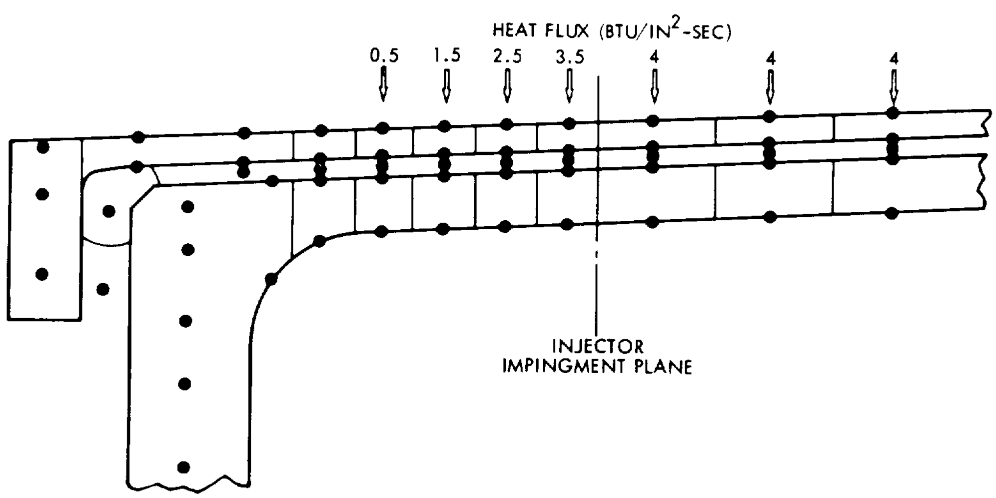

Figure 16. Flange End Nodal Model and Heat Flux Boundary Conditions.

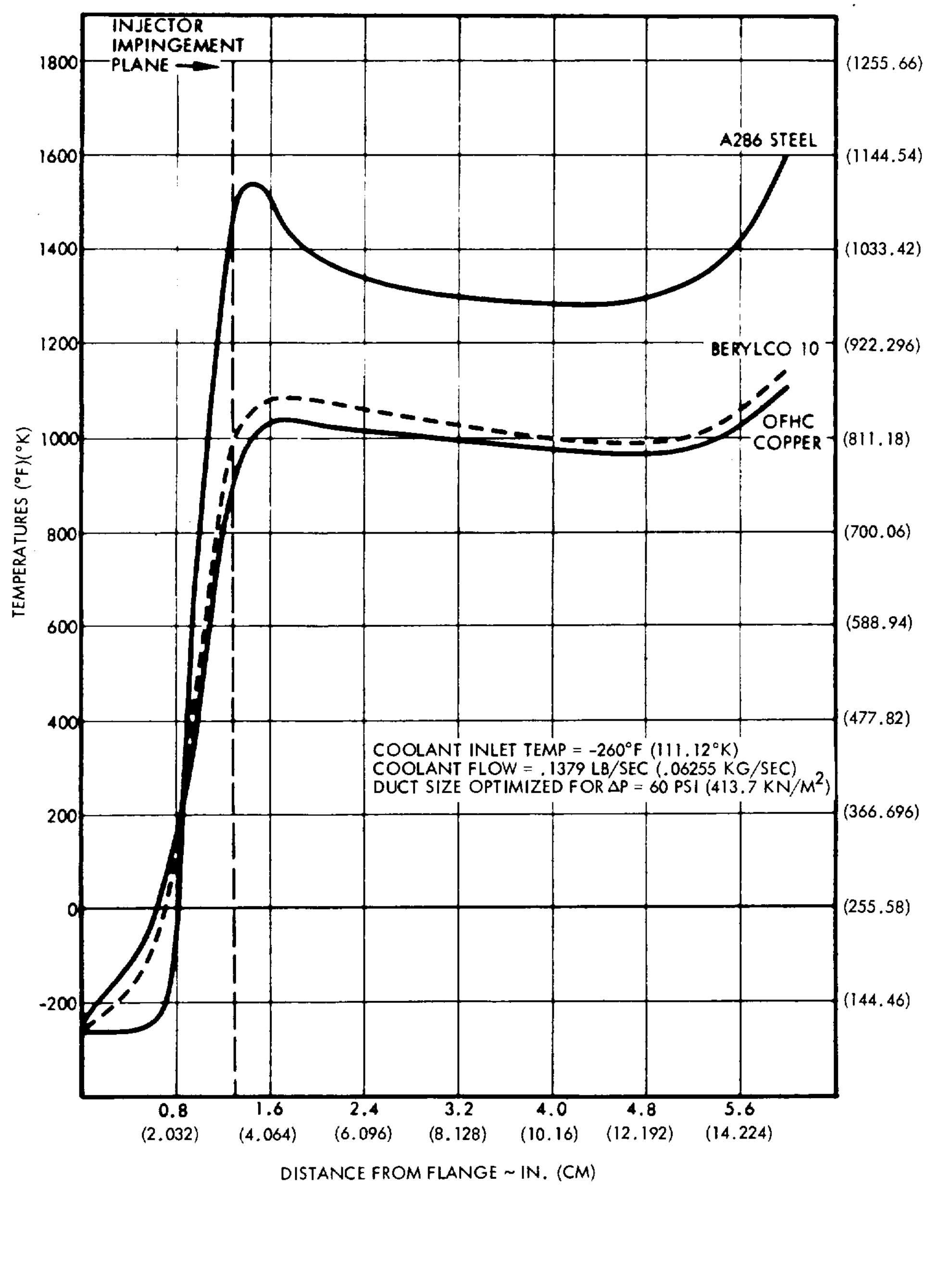

Figure 17. Steady State Duct Temperature Profile

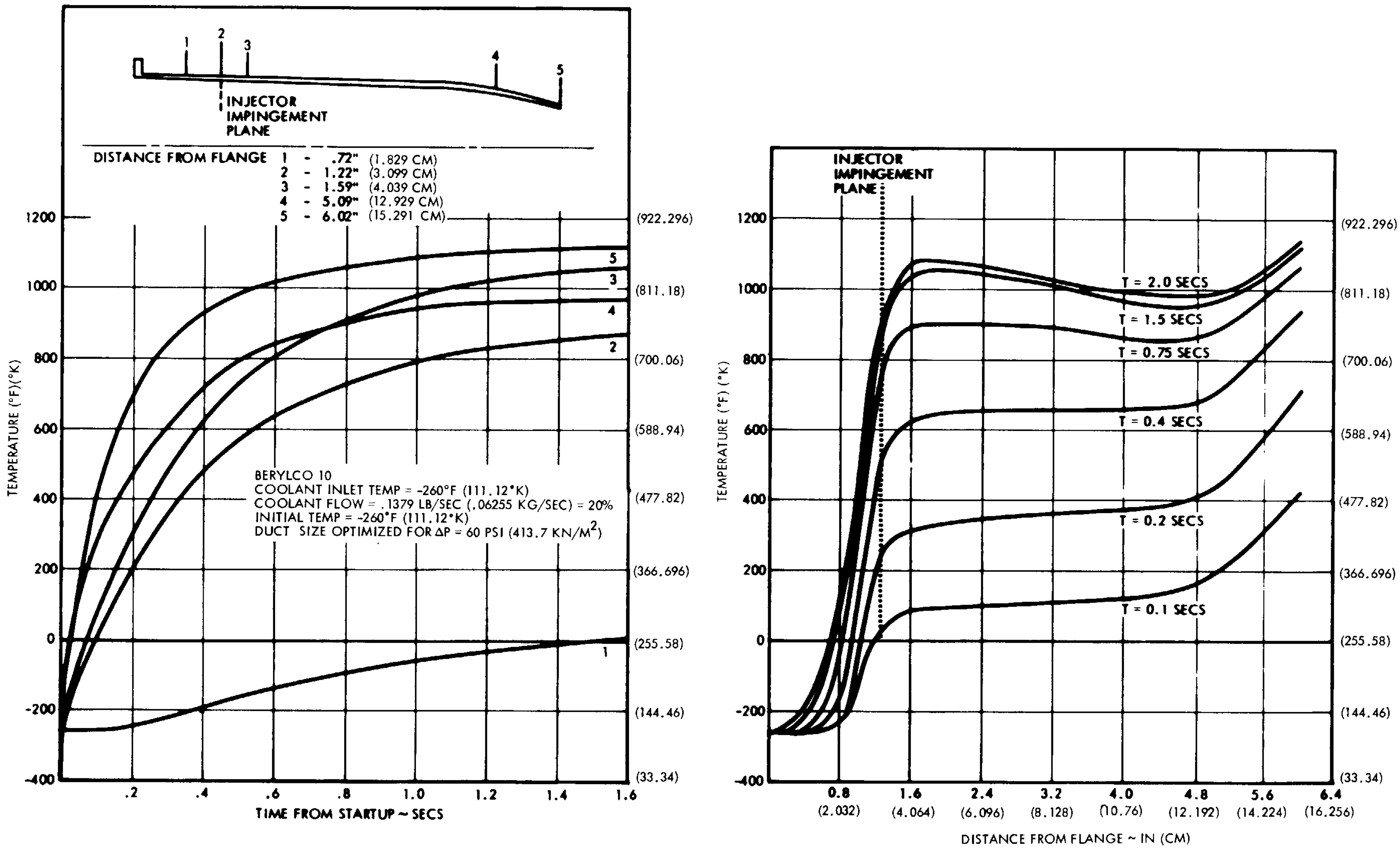

Figure 18. Duct Thermal Transients on Startup

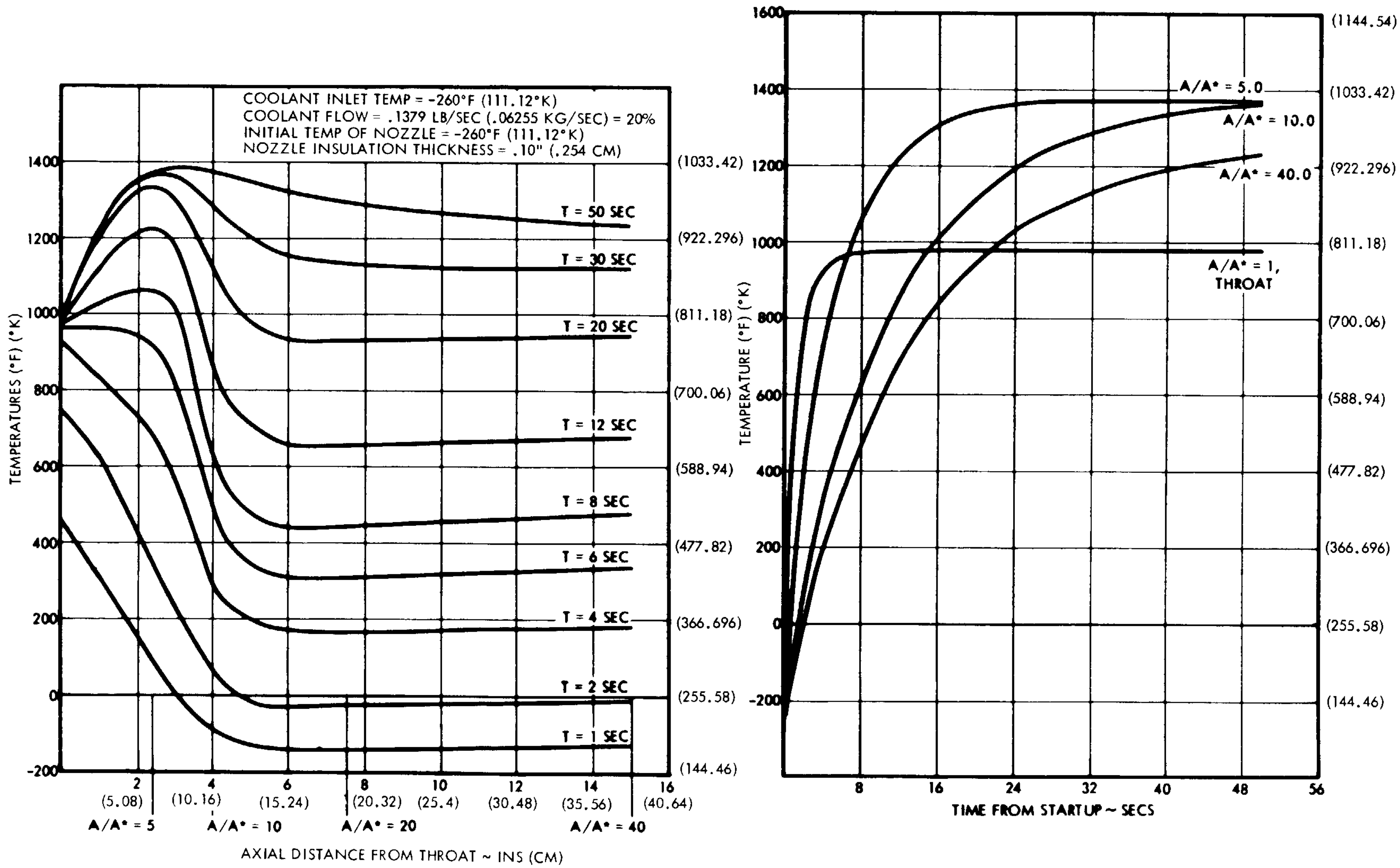

Figure 19. Nozzle Inner Wall Thermal Transients A-286 Steel

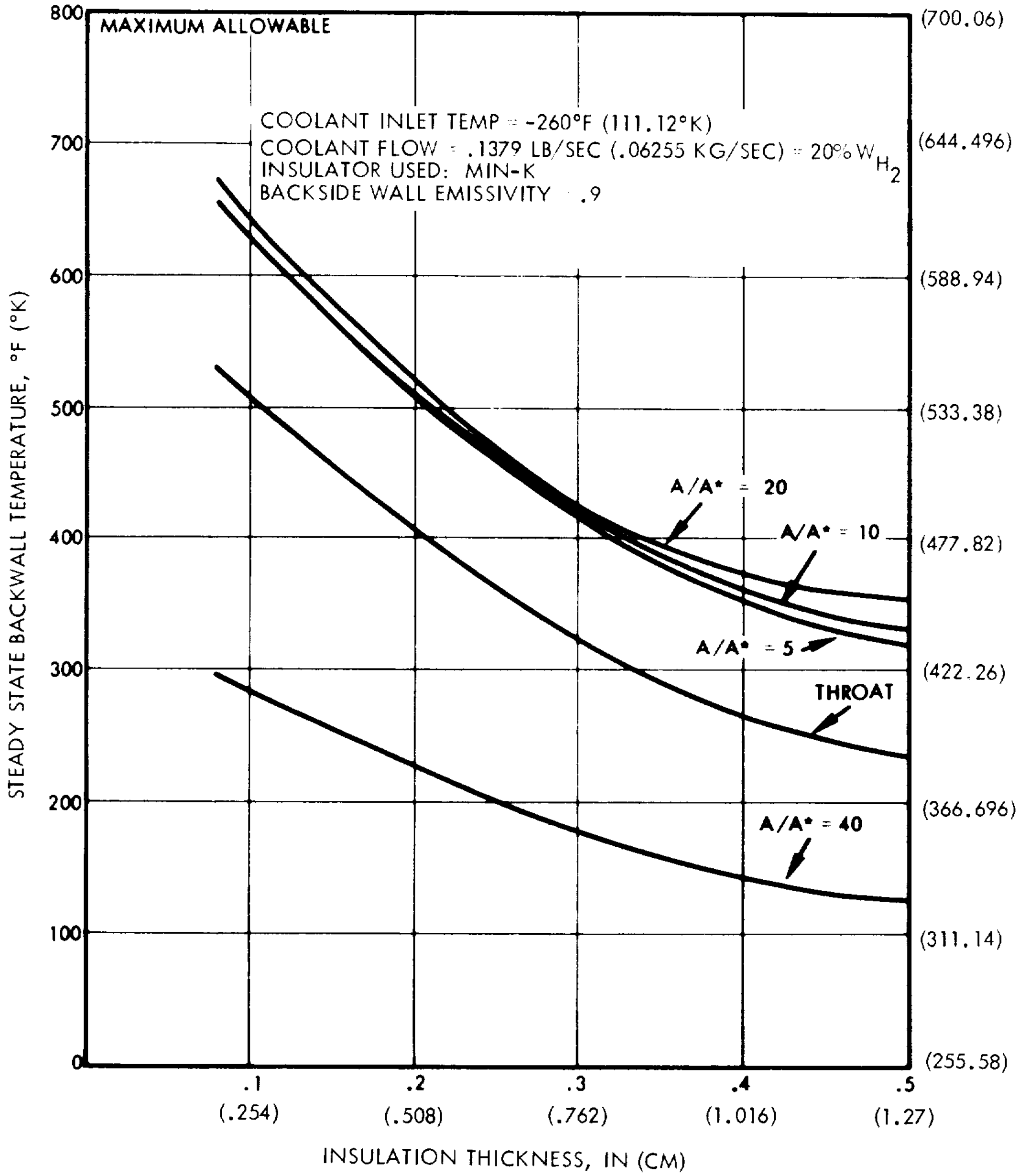

Figure 20. Backwall Insulation Requirements

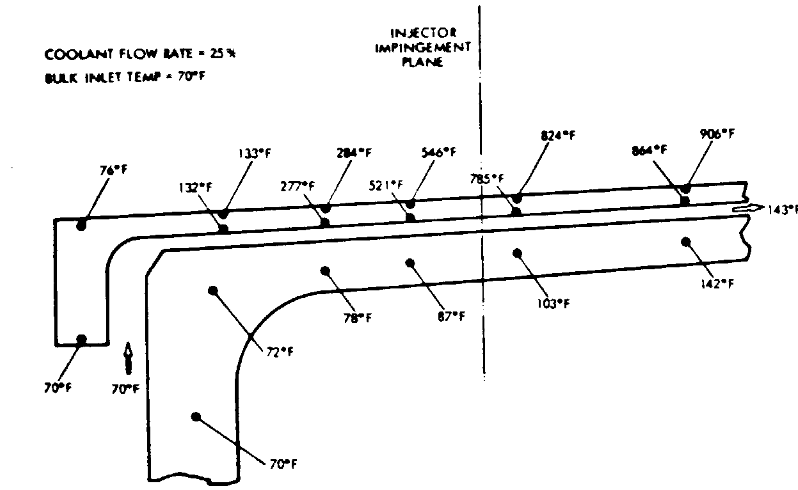

OFHC Copper or Silver Copper Duct

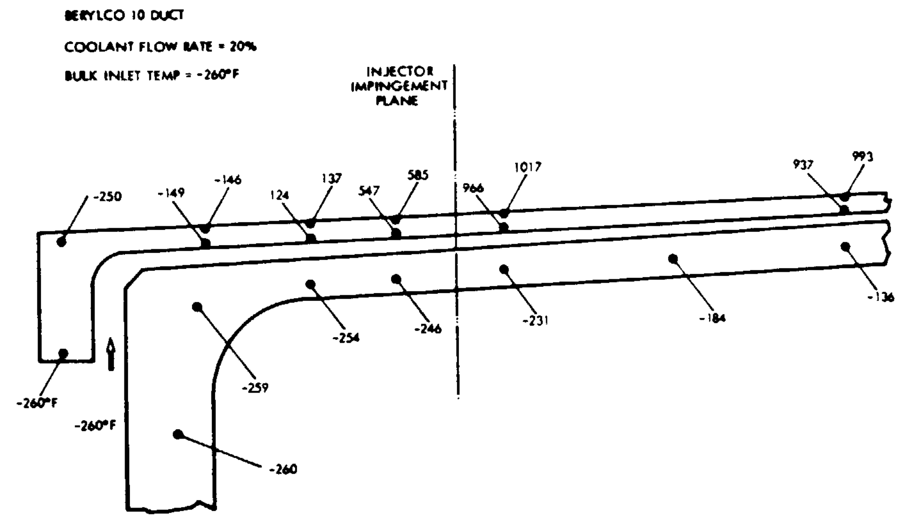

Berylco 10 Duct

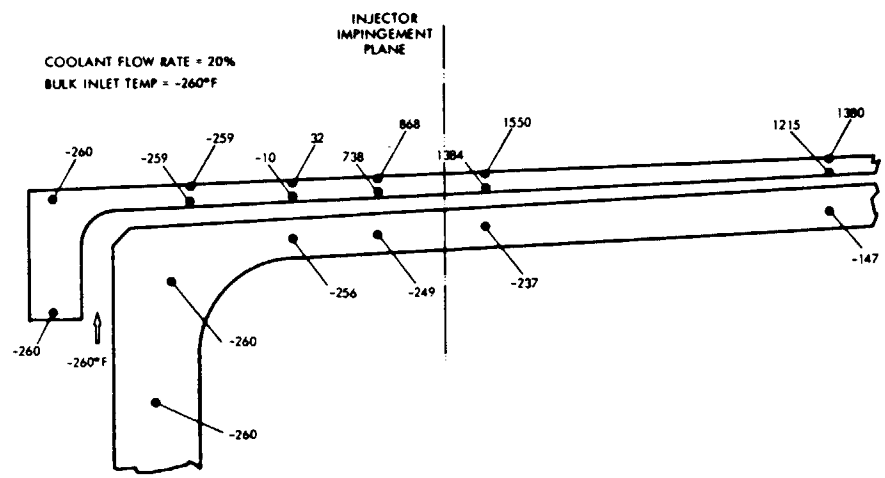

A-286 Duct

Figure 21. Duct and Chamber Flange End Temperatures

Heat Input to the injector surface could only be approximated as the complex recirculating flow pattern in the immediate vicinity of the injector, does not allow for accurate evaluation of this quantity. However, based upon previous experimental results and from the geometry of the injector the following assumptions were made for the thermal loading on the injector.

Hydrogen ring $\dot{q}/A$ = 3 BTU/in^2-sec (4.902 MWatt/m^2) over the projected exposed area

Oxygen ring $\dot{q}/A$ = 2 BTU/in^2-sec (3.268 MWatt/m^2) over the projected exposed area

The average heat transfer coefficient to the cool gas in the injector orifice is estimated by using the relationship for orifice flow with a non-fully developed boundary layer. (Reference 7)

$$\bar{N}_{u_1} = .116 \left[R_{e_d}^{2/3} - 123\right] P_r^{1/3} \left[1 + (d/x)^{2/3}\right] \left[\frac{\mu_B}{\mu_W}\right]^{.14} \tag{33}$$

where $\bar{N}_{u_1}$ = average Nusselt Number in orifice

R_e = Reynolds number in orifice

P_r = Prandtl number

d = diameter of orifice

x = length of orifice

μ_B = viscosity of propellant at bulk temperatures

μ_W = viscosity of propellant at wall temperature

In the annular manifold the coolant side coefficient is given by the relation for flow in an annulus

$$h_2 = \frac{.021\left(1+2.3\ d_{h/L}\right) C_p\ \rho\ V}{R_e^{.2}\ P_\mu^{2/3}} \tag{34}$$

d_h = hydraulic diameter of annulus

l = length of annulus

C_p = bulk specific heat

ρ = bulk density

v = fluid velocity

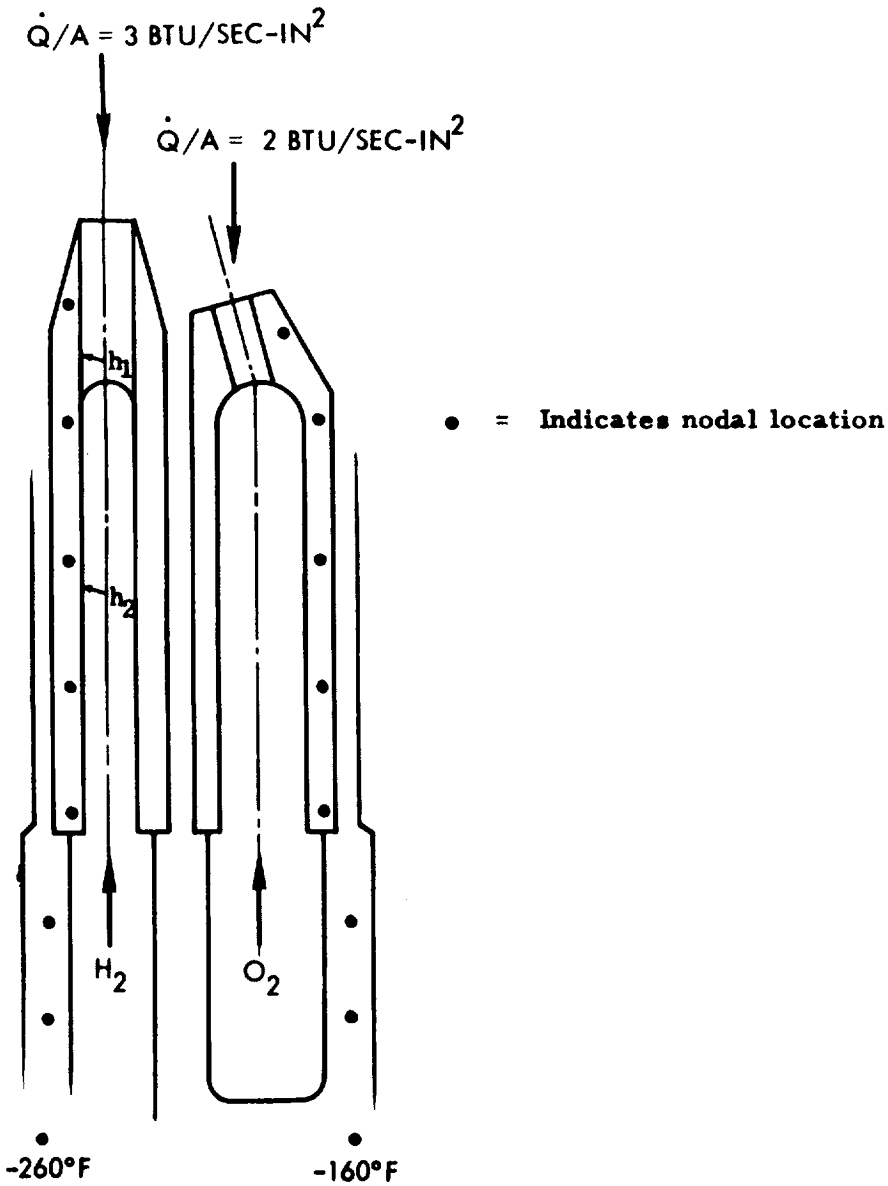

Figure 22. Injector Thermal Model

the results of the analysis are shown in Figure 23 for the 2 rings. The transient response results show the injector to have a response time of ∿ 9 seconds.

3.4.10 Stress and Life Analysis

Both the thrust chamber duct and the nozzle lend themselves quite nicely to rigorous analytical stress analysis. Thin shell theory is readily applicable and has been used exclusively in the design efforts. Final analyses were conducted using the Shell Computer Program developed in NASA Contract NAS 9-4552.

The Rhome and Hass program was used for the injector. The rudiments of the design approach are summarized here. For the purposes of the stress analysis the following was assumed.

- PRELIMINARY CHAMBER GEOMETRY SELECTION
  - L^* = 18 inches (45.72 cm)
  - Contraction Ratio = 4.0 (with tapered inner wall contour)
  - Nozzle: 80% Bell
  - Duct Exit Plane Location: $\varepsilon_c = 1.5$ to 2.5
- CHAMBER WALL
  - Thin-walled Outer Shell/Nozzle: A286
  - Duct Liner: OFHC Copper/Copper Alloy
- DUCT DESIGN APPROACH
  - Straight Channels
  - Internally Fed from Injector H_2 Manifold

Of primary interest here is the expected fatigue life. The basic starting point in the analysis is the Manson universal slope equation to find the total strain range.

$$\Delta\epsilon_t = \frac{3.5\,\sigma_u}{E} N_f^{-0.12} + D^{0.6} N_f^{-0.6} \qquad (35)$$

where

$\Delta\epsilon_t$ = total strain range

σ_u = ultimate tensile strength

E = modulus of elasticity

D = $\ln \left(\frac{100}{100-RA}\right)$

RA = reduction in area

H_2 RING

← TIME (SEC)

9	5	2	1	.6	.2
- 85	- 89	- 96	-100	-103	-123
-185	-198	-222	-238	-247	-257
-226	-239	-254	-258	-259	-260
-231	-244	-255	-258	-259	-260
-213	-225	-241	-248	-252	-255
-218	-228	-243	-250	-253	-256
-221	-225	-235	-242	-247	-254

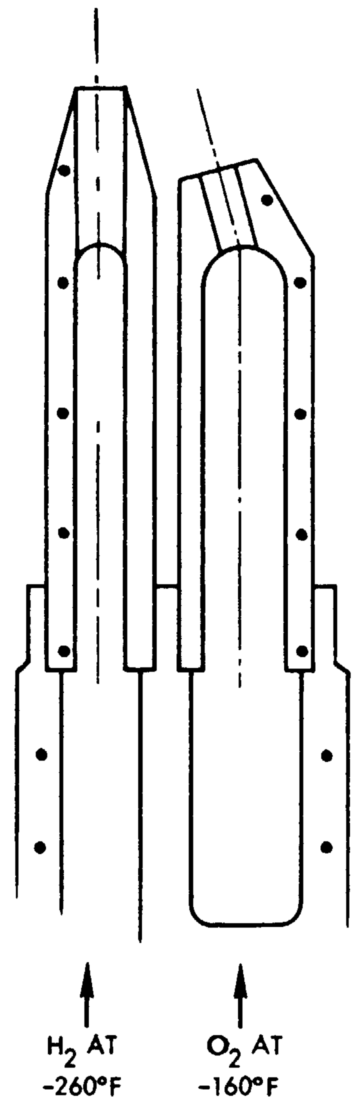

O_2 RING

TIME (SEC) →

.2	.6	1	2	5	9
- 74	- 23	- 5	9	15	20
-121	- 78	- 59	- 45	- 36	- 31
-163	-144	-129	-115	-104	- 98
-207	-205	-197	-186	-173	-164
-241	-240	-235	-227	-212	-201
-252	-250	-247	-240	-225	-216
-244	-239	-234	-227	-218	-214

Figure 23. Injector Transient Temperature Profiles

The stress analysis considered the effects of:

- Pressure Loading
- Thermal Stress
- Combined Fatigue and creep damage
- Dynamic Stress

As indicated above the duct concept lends itself to text book formulation. Prior to using the thin shell program the duct and nozzle were analytically described as illustrated in Figure 24 for the axial and meridional stresses introduced into a cylindrical element by the loads on an element. From this analysis the basic understanding of the thruster was derived and the geometry was programmed into the Shell Computer Program, as schematically illustrated in Figure 25.

At elevated temperatures where intercrystalline cracking may occur due to the effects of creep, the above rule was modified by the use of the "10% Rule." In the use of this rule the fatigue life is taken as 10% of that predicted by the universal slope method. Therefore, for 10^6 cycle life, the designer uses $N_f = 10^7$ in the universal slope equation and the permissible total strain range is determined. The calculation fatigue stress range with mean stress $\sigma_m = 0$ is found from

$$\sigma_o' = \pm \frac{1}{2} \Delta\varepsilon_t \cdot E \qquad (36)$$

From this result and available test data for the candidate materials. The fatigue stress range σ_o was obtained by proportioning the above theoretical results. Modified Goodman diagrams were used to calculate the fatigue stress σ_a as follows:

$$\frac{\sigma_a}{\sigma_o} + \frac{\sigma_m}{\sigma_u} = 1$$

$$\sigma_a = \frac{\sigma_o \sigma_u}{\sigma_o + \sigma_u}$$

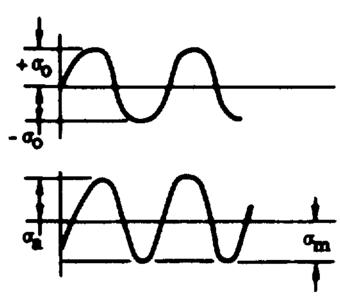

σ_o = fatigue stress range with mean stress $\sigma_m = o$

σ_a = fatigue stress range with mean stress $\sigma_m = \sigma_a$

σ_u = material ultimate strength

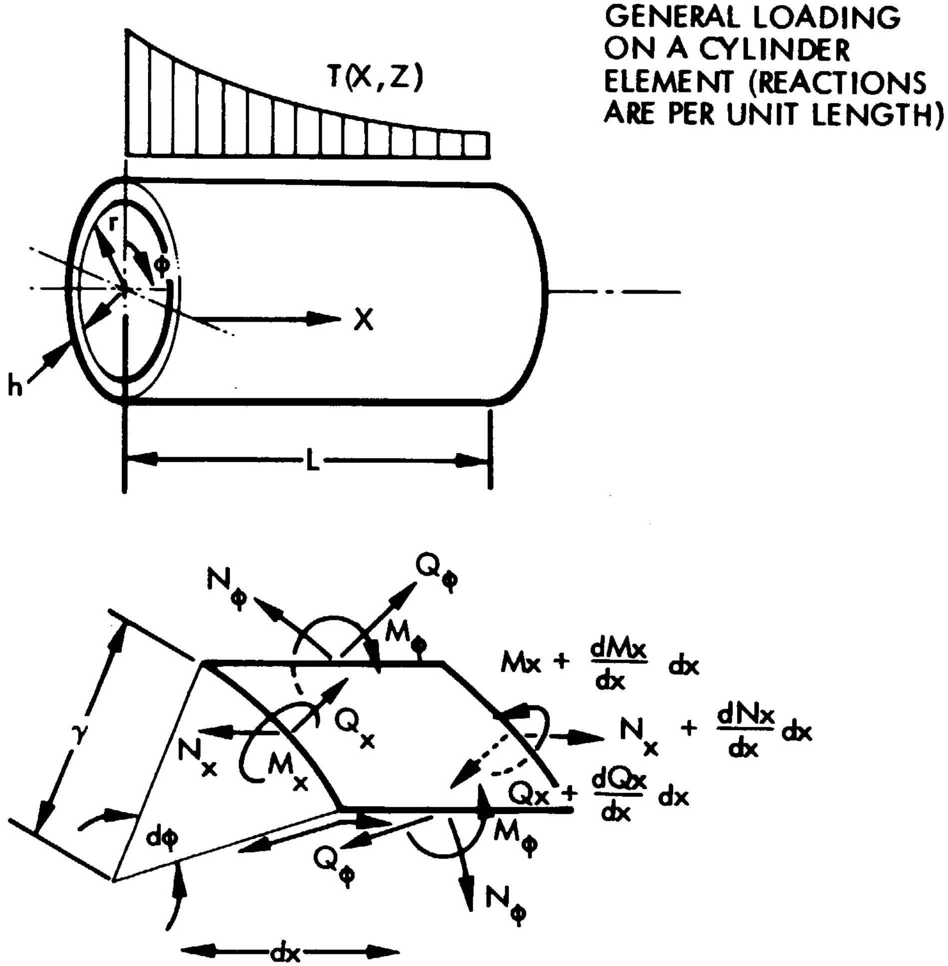

$$\sigma_x = \frac{12\ Mx\,Z}{t^3} - \frac{E\,\alpha}{(1 - v)}\left[T - \overline{T} - \Delta T\,\frac{Z}{t}\right]$$

$$= \mp\frac{6Mx}{t^2} - \frac{E\,\alpha}{(1 - v)}\left[T - \overline{T} - \Delta T\frac{Z}{t}\right]$$

$$\sigma\phi = \frac{N\phi}{t} \mp \frac{12\,v\,Mx\,Z}{t^3} - \frac{E\,\alpha}{(1 - v)}\left[T - \overline{T} - v\,\Delta T\frac{Z}{t}\right]$$

$$= -E\left(\frac{w}{r} + \alpha\,\overline{T}\right) \mp v\,\frac{6Mx}{t^2} - \frac{E\,\alpha}{(1 - v)}\left[T - \overline{T} - v\,\Delta T\frac{Z}{t}\right]$$

Figure 24. Thermal Stress Analysis Model for Duct Cooled Thruster

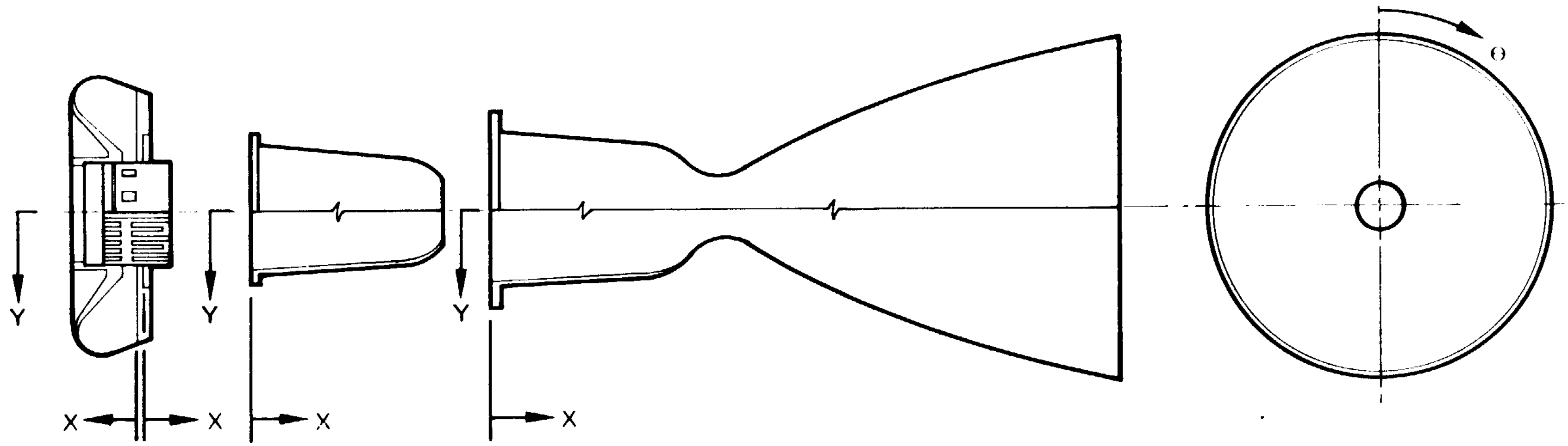

STRESS-DEFORMATION ANALYSIS OF SHELL OF REVOLUTION SUBJECT TO ARBITRARY LOADS AND TEMPERATURE DISTRIBUTIONS =

$$P = f\,(X, Y, \Theta)$$

$$T = f\,(X, Y, \Theta)$$

PROGRAM BASIS

- LINEAR - ELASTIC THIN SHELL THEORY
- FOURIER SERIES EXPANSION TECHNIQUE APPLIED
- PROGRAM WRITTEN IN FORTRAN IV
- SOLUTIONS YIELD SEPARATELY BENDING MOMENTS AND MEMBRANE FORCES SO THAT SECONDARY AND PRIMARY STRESSES COULD BE EVALUATED.

Figure 25. Shell Computer Program NASA Contract NA-S9-4552

The total fatigue stress range is given by $2\sigma_a$.

To include the combined effects of fatigue and creep the three approaches illustrated in Figure 26 were considered. The third method was selected, since it is felt to be most conservative and makes direct use of experimental data illustrated in Figure 26.

To facilitate the use of this analytical approach fatigue-temperature diagrams for the candidate materials are prepared from which one can directly determine the design stress allowables when the temperature distributions are known. Typical results are given in Figures 27 through 30.

The computer results for the A-286 nozzle are given in Figure 31 for the 10^6 cycle use without creep, 10 hrs and 50 hrs creep. The immediate observation is that the thin wall nozzle has a very large fatigue-creep margin, and no concern should be expressed over its life capabilities.

The initial results for the duct are shown in Figure 32. Here it is seen that both the analytical model and the computer model predicted an excessive stress at the beginning of the duct. To solve this potential problem a small amount of GH_2 film cooling (5%) was added to the hot gas side. This removed the duct temperature discontinuity effect, and Figure 33 shows the resultant stresses, indicating that the 10^6 fatigue cycle limit can now be met.

There also exists the possibility of destructive startup transient effects in the nozzle wall at the throat. Because of the thin wall and reduced driving temperature with the duct coolant, this problem is reduced to negligible proportions with the A-286. The results are shown in Figure 34.

The more complex triplet injector geometry was analyzed strictly by computer program. The results are given in Figures 35 and 36 for both ambient and reduced temperature propellants.

A thruster dynamic stress analysis was also conducted for the model shown in Figure 37. The analysis resulted in the conclusion that there was no problem here.

The low pressure thruster was analyzed in exactly the same manner as above. The entire results for the low pressure thruster are summarized in Figure 38.

The stress analysis conclusions were as follows:

- Fundamental theories of beams on elastic foundation, theory of elasticity, theory of plates and shells (Hetenyl and Timoshenko) are directly applicable.

- All components have margin of safety based on 10^6 cycle fatigue and 50 hours creep damage.

For combined fatigue and creep damage

- $$N_f' = \frac{N_f}{1 + \frac{k}{AF} (N_f)^{\frac{m + 0.12}{m}}}$$

  N_f = fatigue cyclic life

  k = effective fraction of each cycle for which material is subjected to maximum stress (use value of 0.3)

  F = frequency of application, cpm

  A = time to intercept of creep rupture curve

  m = slope of creep rupture line

This equation applies if $N'_f < 10\% N_f$ and if $N'_f < 10^5$ cycles.

- $\phi_f + \phi_c \leq 1$ (Rocketdyne)

  ϕ_f = damage fraction caused by fatigue

  ϕ_c = damage fraction caused by creep

- $$(2\sigma_a)' = (2\sigma_a) \frac{\sigma_u \text{ (creep rupture)}}{\sigma_u}$$

  $(2\sigma_a)$ = total fatigue stress range

  σ_u = ultimate strength of material at temperature

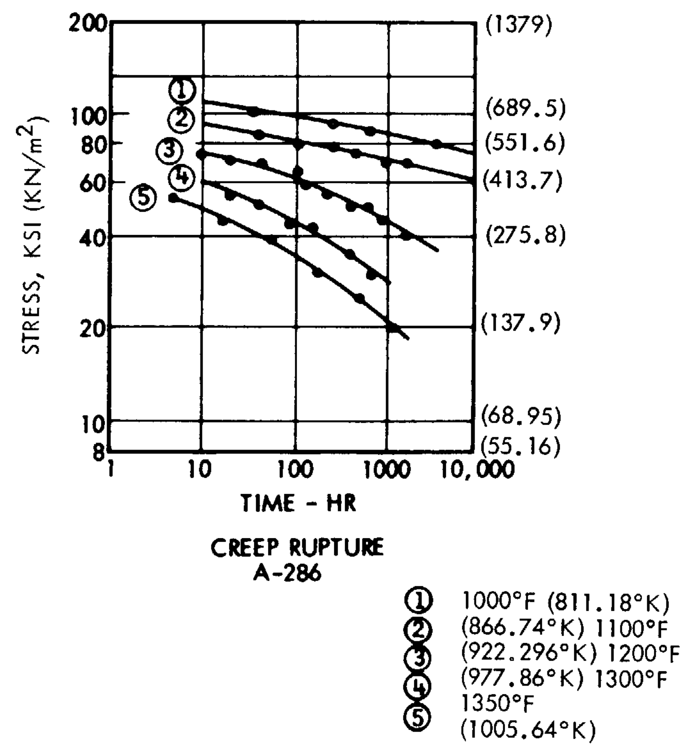

Figure 26. Combined Fatigue and Creep Analysis Approaches

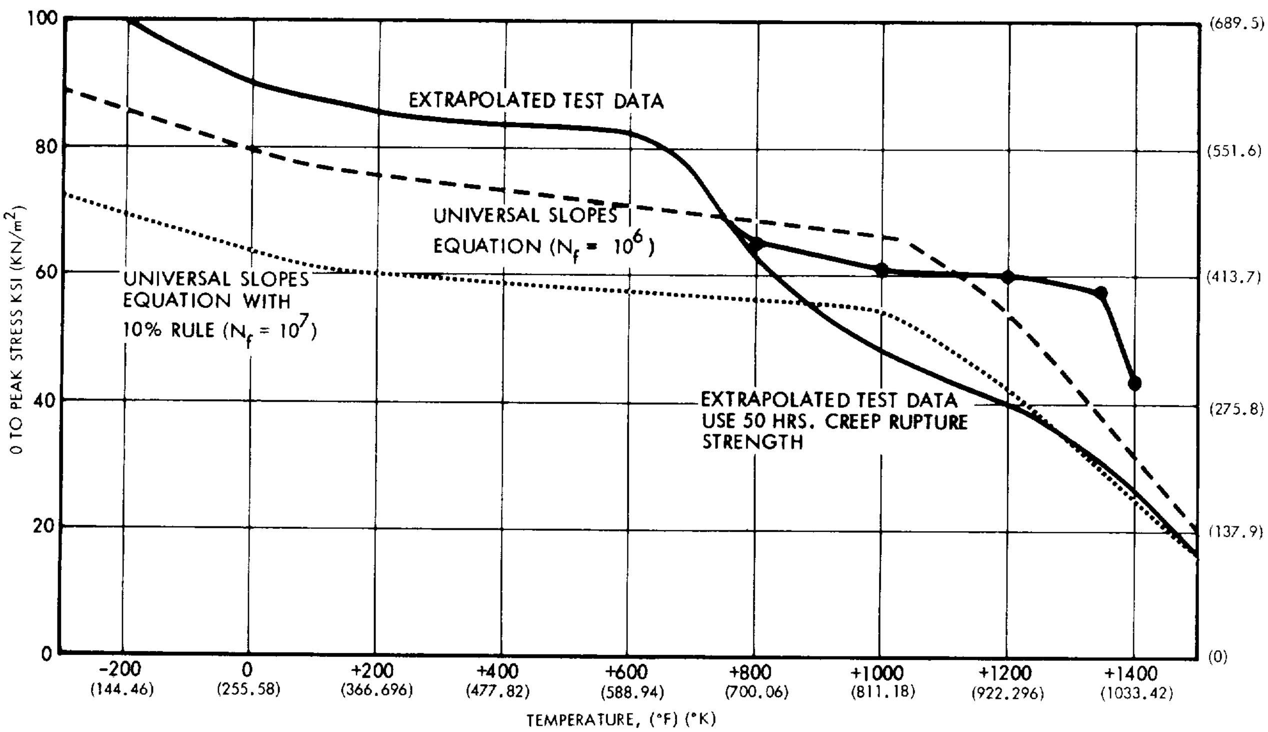

Figure 27. Unnotched Allowable Maximum Fatigue Stress for A-286 (Aged) at 10^6 Cycles

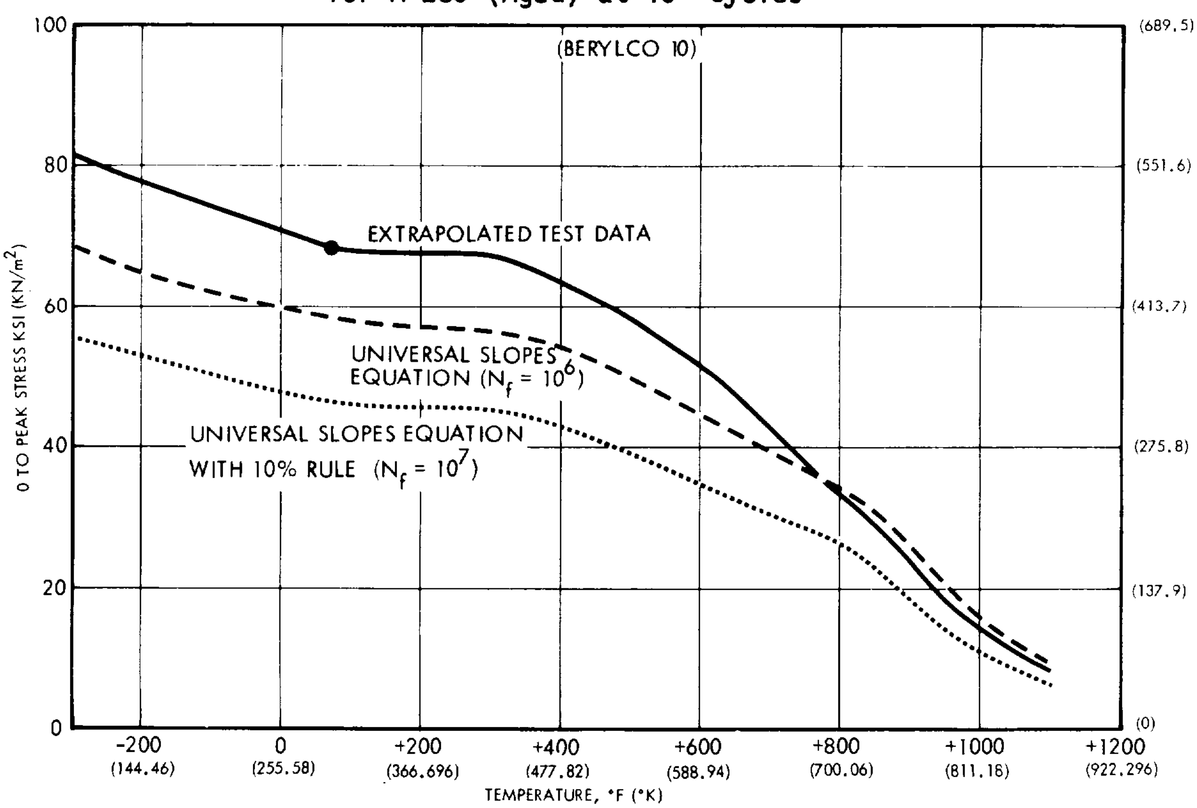

Figure 28. Unnotched Allowable Maximum Fatigue Stress for Be Cu Alloy No. 175 (Berylco 10) at 10^6 Cycles

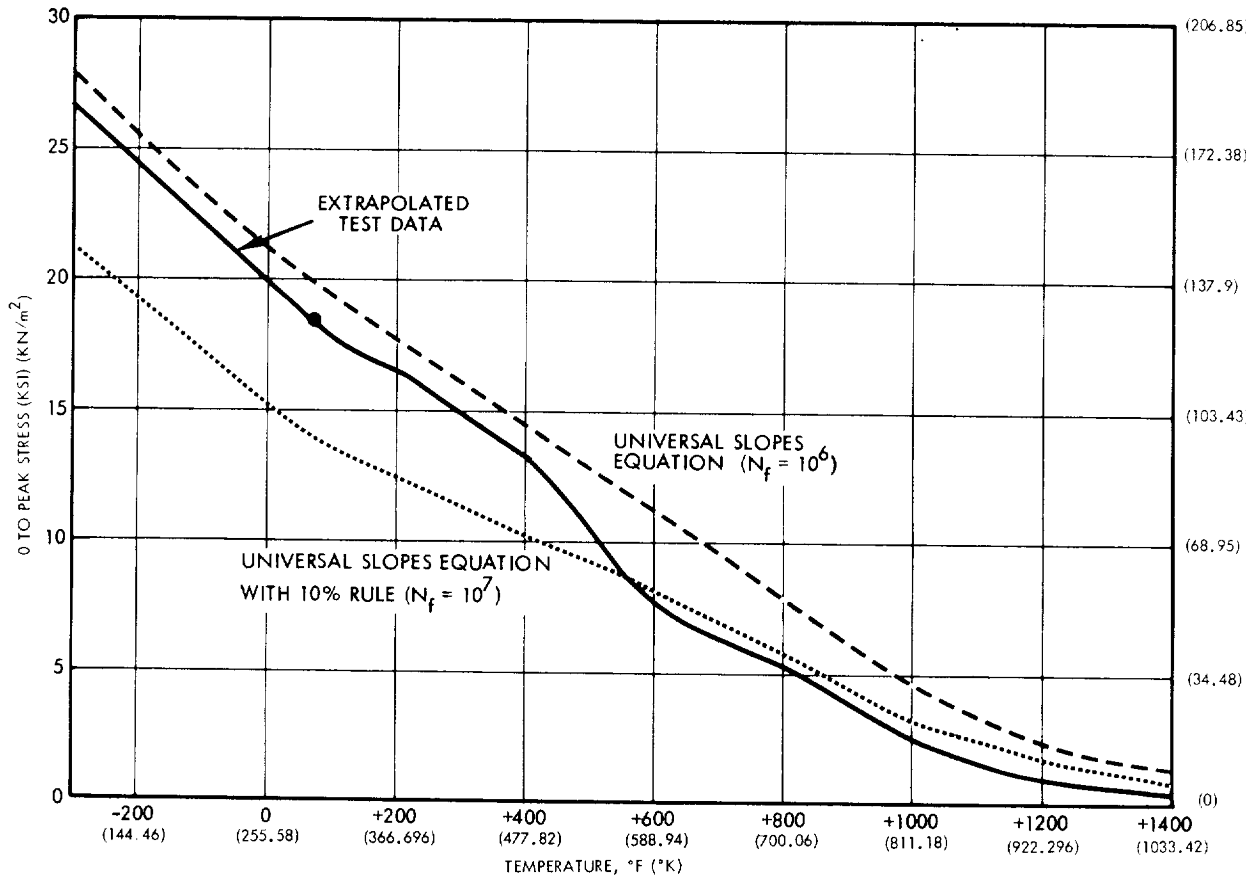

Figure 29. Unnotched Allowable Maximum Fatigue Stress for OFHC Copper (Annealed) at 10^6 Cycles

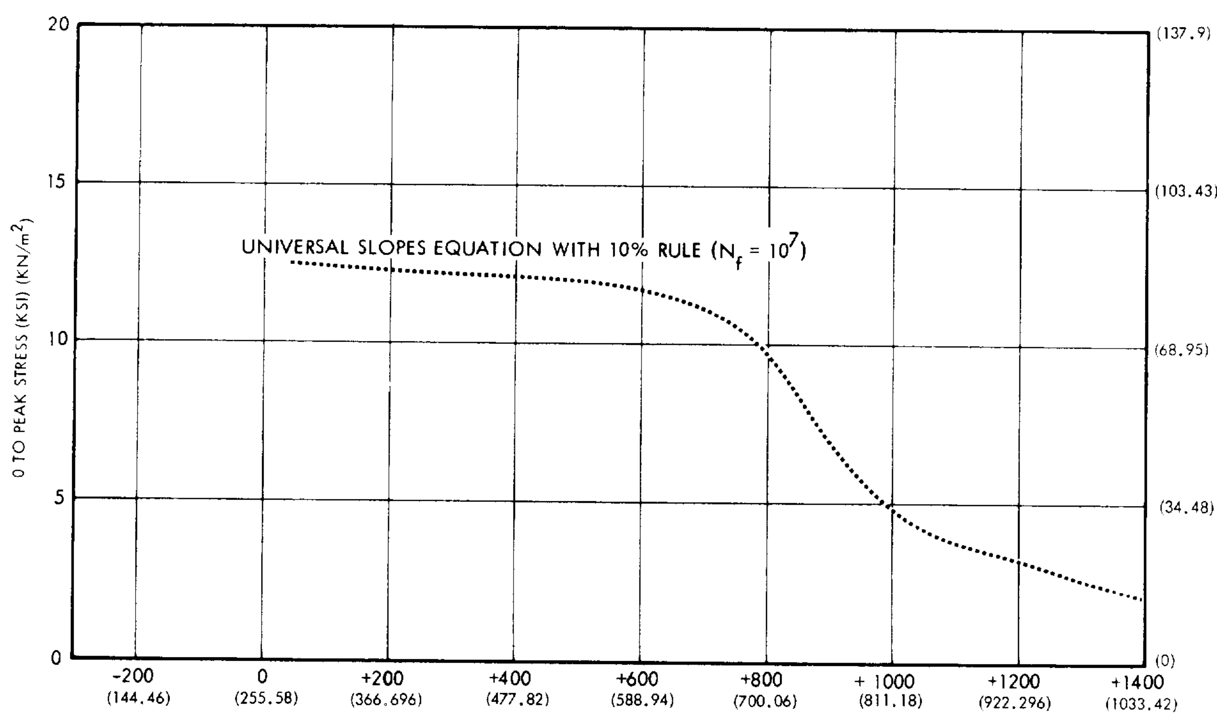

Figure 30. Unnotched Allowable Maximum Fatigue Stress for Narloy Casting Alloy at 10^6 Cycles

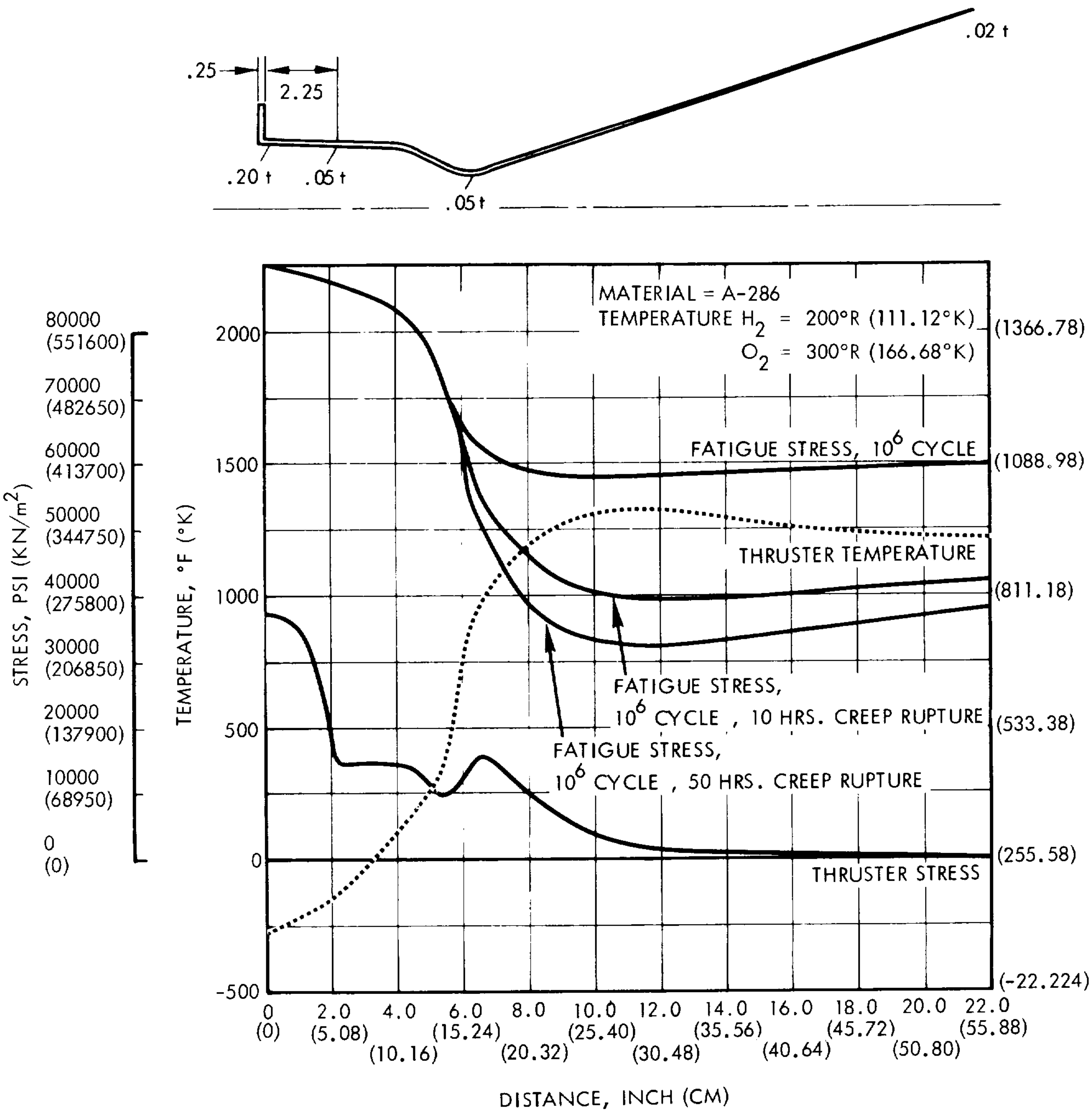

Figure 31. Thrust Chamber Stress

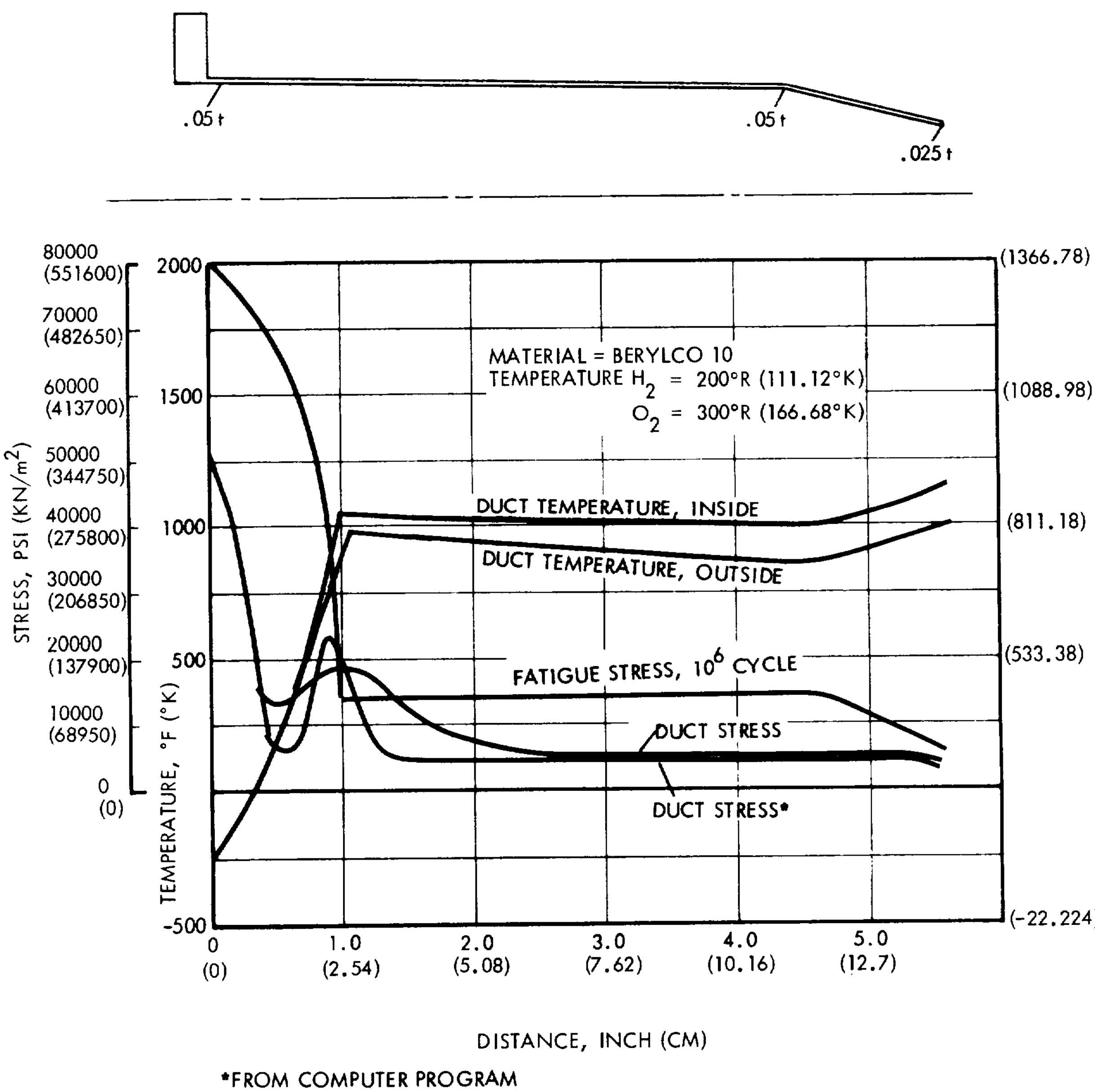

Figure 32. Duct Stress

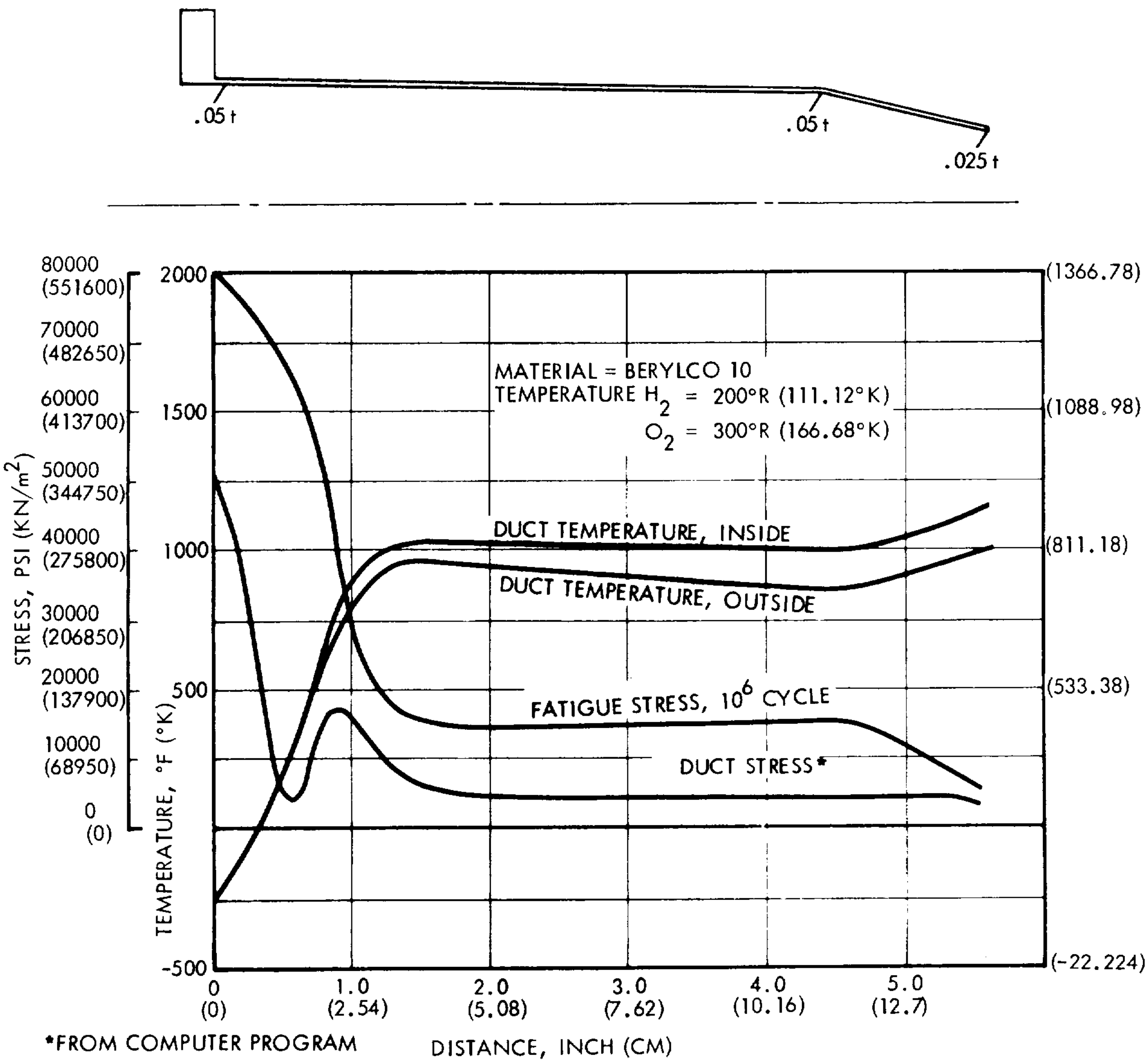

Figure 33. Duct Stress - Film Cooling Added (5%)

- IN DUCT COOLED ENGINE WORST START UP ZONE IMMEDIATELY DOWNSTREAM OF THROAT

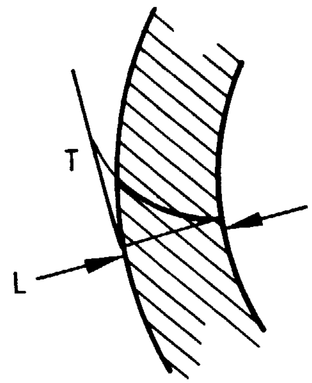

$$\frac{T_o}{T_{ad}} = \frac{\frac{1}{2}\,\frac{h}{k}\sqrt{6\,\alpha_T t}}{1 + \frac{1}{2}\,\frac{h}{k}\sqrt{6\,\alpha_T t}}$$

- MAXIMUM ΔT AT $t = L^2/6\,\alpha_T$
- TRANSIENT INDUCED STRESS $\quad \tau = \pm \dfrac{E\alpha_2\,\Delta T}{2\,(1-\Delta)}$

τ_{MAX} = 28,500 PSI (196507.5 KN/m^2)

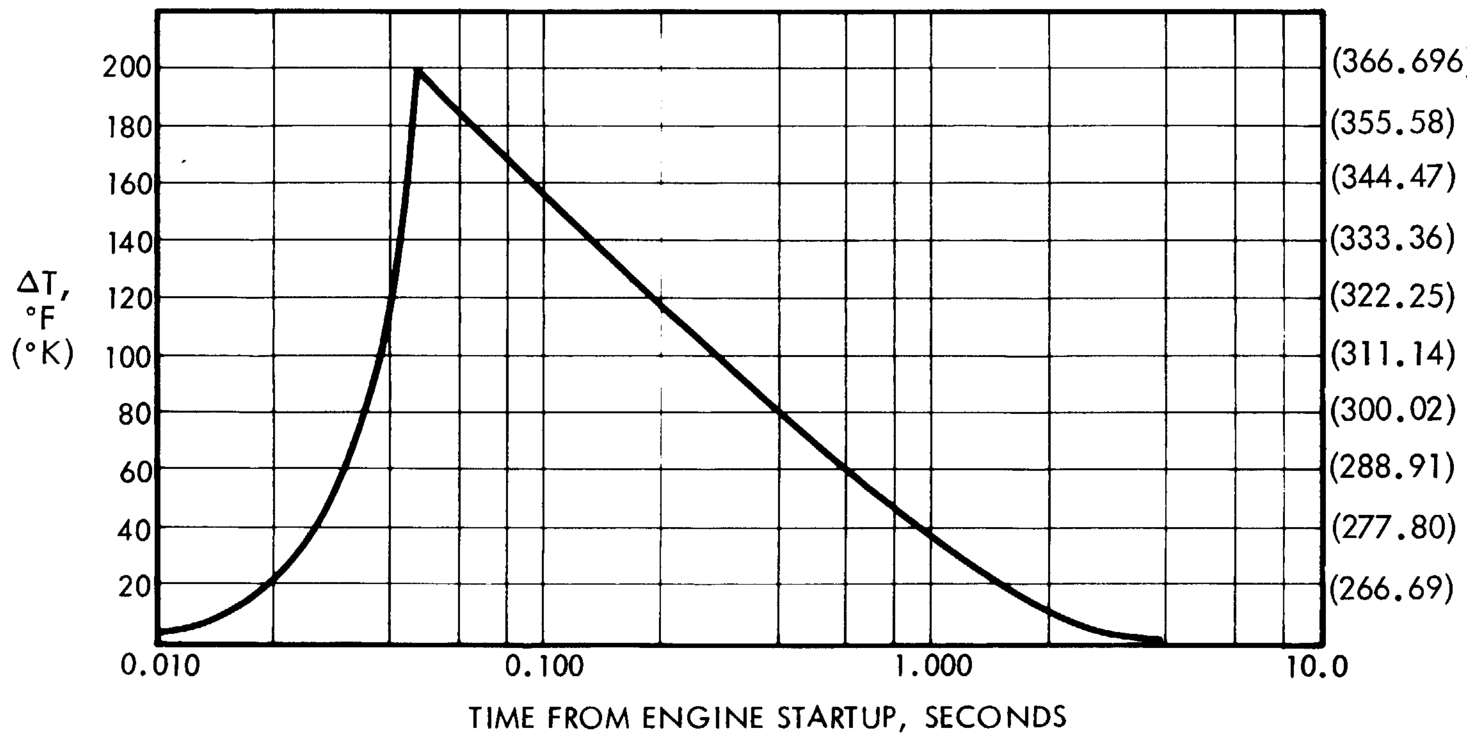

Figure 34. Start Up Transient Stresses

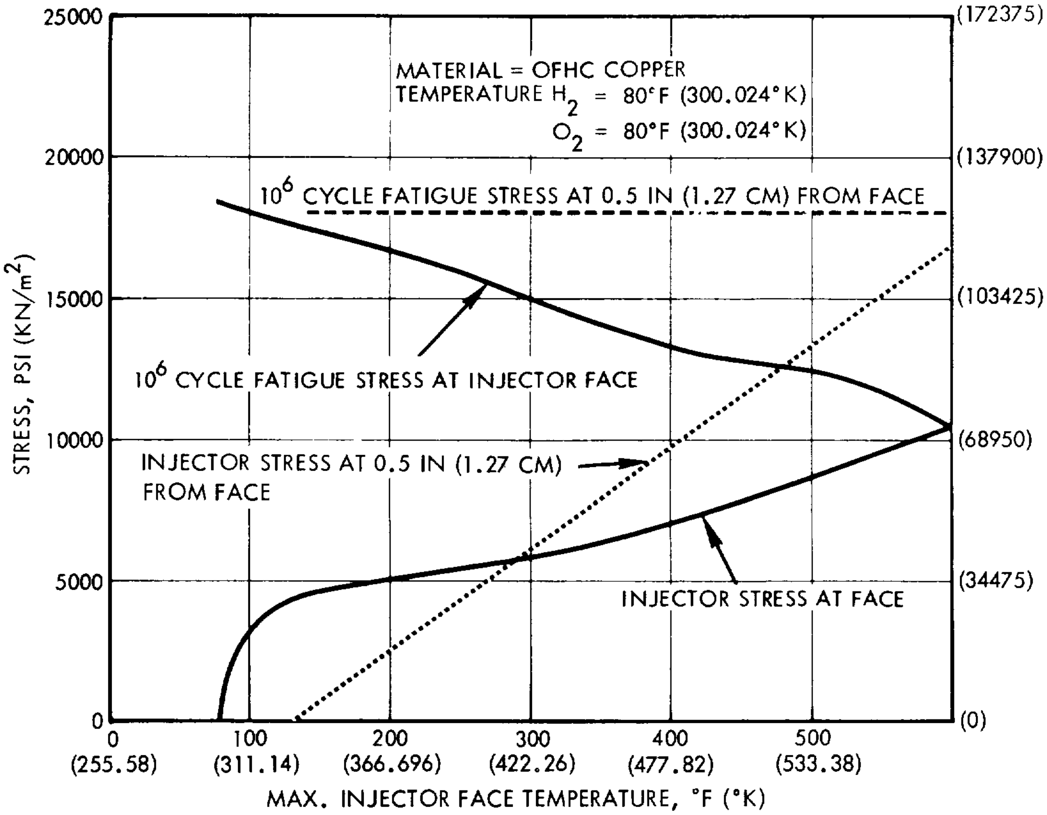

Figure 35. Maximum Injector Stresses With Ambient Propellants

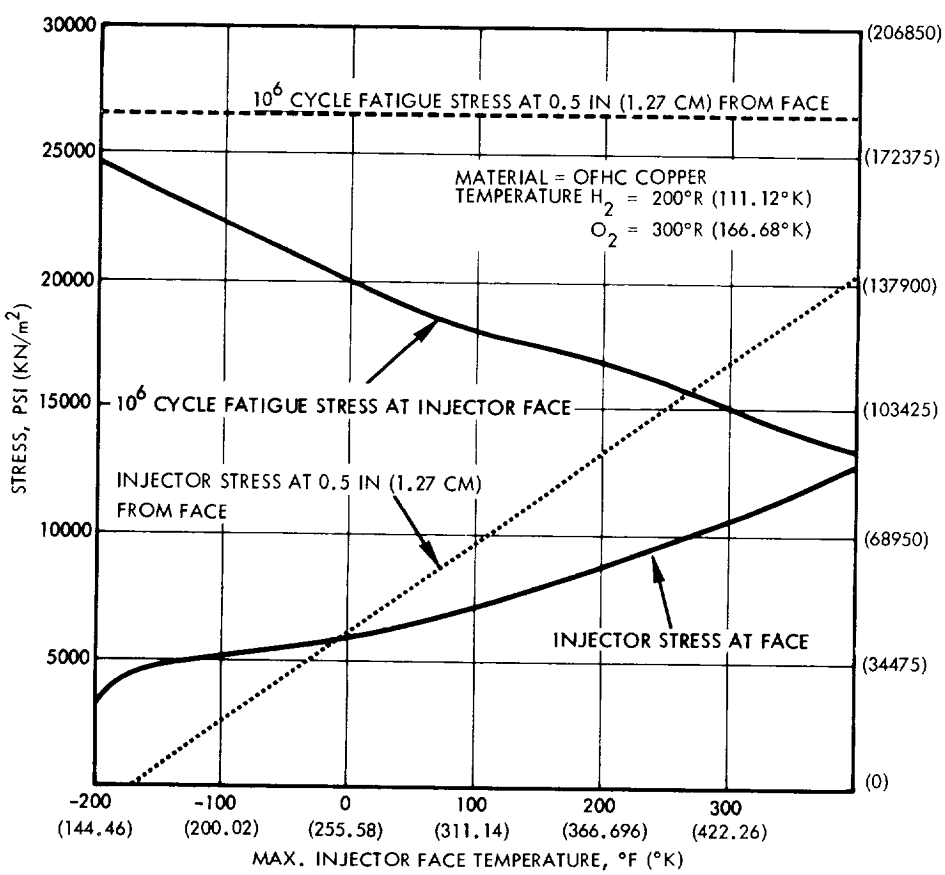

Figure 36. Maximum Injector Stresses With Reduced Temperature Propellants

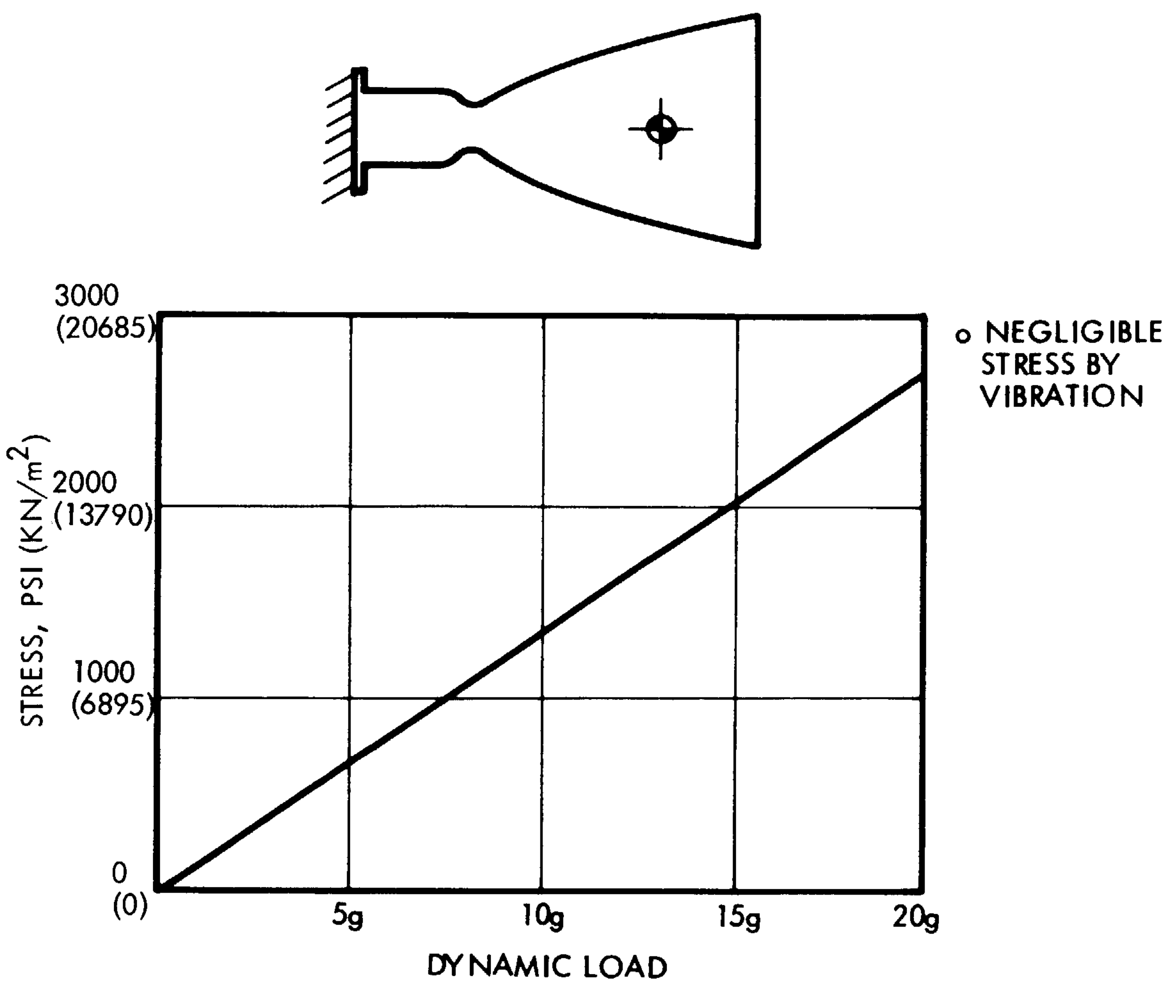

Figure 37. Dynamic Stress Magnitude at Nozzle Throat

Summary of Thermal Stress Analysis
for 15 psia (103.43 KN/m^2) Ducted Thrust Chamber Design

Location:	Chamber Duct	Nozzle
Material:	A-286	A-286
Thickness (in.) (cm)	0.05 (.127)	0.05* (.127)
Allowable Stress		
Ultimate (psi) (KN/m^2)	138,000 (951510)	64,000 (441280)
Yield (psi) (KN/m^2)	93,000 (641235)	62,000 (427490)
10^6 Cycle Fatigue (psi) (KN/m^2)	42,000 (289590)	21,000 (144795)
Temperature (^oF) (^oK)	800 (700.06)	1,400 (1033.42)
Maximum Calculated Stress (psi) (KN/m^2)	20,900 (144105.5)	0** (0)
Margin of Safety	1.01	High

*0.05 inch (.127 cm) at throat tapering to 0.02 (.0508 cm) at exit.
**Linear temperature gradients assumed for this analysis.

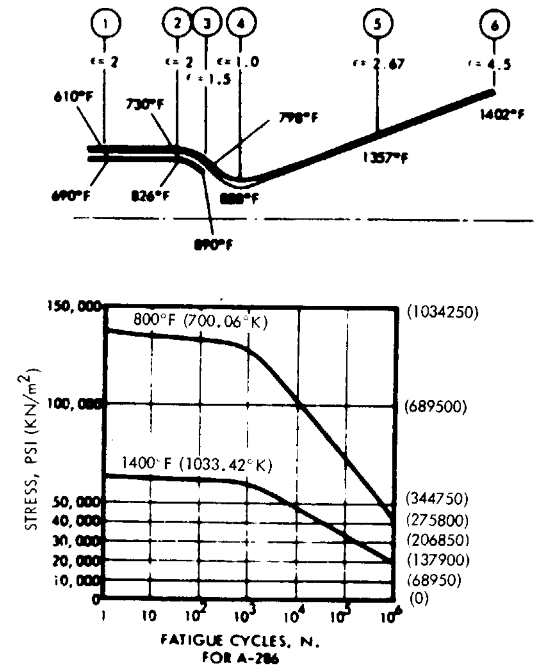

Duct-Cooled Thruster Thermal/ Structural Material Data

Figure 38. Thruster Thermal Stress Analysis Summary

- Large margin of safety for re-entry induced stress at maximum circumferential gradient of 2000°F (1366.78°K) to 1200°F (922.296°K) and maximum axial gradient of 2000°F (1366.78°K) to 1200°F (922.296°K) over initial 3 inches (7.62 cm).

3.4.11 Performance Prediction Approach

The theoretical behavior of H_2/O_2 propellants is current propulsion state-of-the-art. Consequently, this type of data is not presented here. The injector design approach from a performance point of view is of interest, and the engineering method used for gaseous propellant injectors at TRW Systems is summarized below.

Starting from the premise that combustion efficiency is governed by turbulent mixing of the two propellants after some initial mixing, an analytical expression is formulated for the combustion efficiencies as a function of the hydrogen jet radius and the distance traveled by the propellants. The axial mixing is governed by Equation (33) below (Reference (7):

$$Y_o = 1 - e^{-\left[\frac{1}{k\bar{x}\rho_e^{1/2}} - 0.70\right]} \quad (33)$$

where Y_o = centerline concentration

This expression covers the case of a gas jet in a continuum of another gas specie and relates the axial concentration (or mixing) variation. It is postulated that the combustion efficiency for this case would be related to $1 - Y_o$ or:

$$\eta_c^* = e^{-\left[\frac{1}{kx\rho_e^{1/2}} - 0.70\right]} \quad (34)$$

where: k = constant (determined experimentally)

$\bar{x}$ = x/r_j

Σ = axial distance

r_j = jet radius

ρ_e = ρ_e/ρ_j

ρ_e = density of continuum gas

ρ_j = density of jet gas

In order to more closely simulate an actual rocket engine injector, Equation (35) is modified to account forinteraction between adjacent jets caused by small inter-element spacing.

$$\eta_{C^*} = e^{-\left[\frac{c}{k\bar{x}\bar{\rho}_e^{1/2}} - 0.70\right]} \tag{35}$$

where: c = interaction parameter

This expression has been used to correlate experimental data from various sources for different injector geometries as shown in Figure 39. The constants k and c are found to have limits within which Equation (35) can be adequately used to describe the axial combustion efficiency variation. As seen the constant k varies between 0.03 and 0.10 and is related to the degree of initial mixing. Thus, for a showerhead injectors with very little initial mixing k is 0.03 with resulting greater lengths required for high performance, whereas a triplet injector has a great deal of initial mixing with corresponding shorter lengths required for good combustion efficiency. The interaction parameter, c, is a measure of the interaction between adjacent jets which can result in enhanced mixing. This constant is thus a function of the pattern fineness or inter-element spacing.

To determine the effects of other engine parameters, the expression for $\bar{x}$ can be generated as follows:

$$\bar{x} = \frac{x}{r_j} \tag{36}$$

$$\text{where } x = \frac{L^*}{\varepsilon_c} - \frac{1}{3_{\varepsilon_c}}\left(\frac{F}{\pi C_F P_c}\right)^{1/2} \cot\beta \left(\varepsilon_c^{1.5} - 1\right) \tag{37}$$

L^* = characteristic chamber length

ε_c = chamber contraction ratio

F = thrust

C_F = thrust coefficient

P_c = chamber pressure

ρ = chamber contraction angle

and

$$r_j = \left[\frac{A_j}{n_j\pi}\right]^{1/2} \tag{38}$$

A_j = total flow area of jet

n_j = number of jet orifices

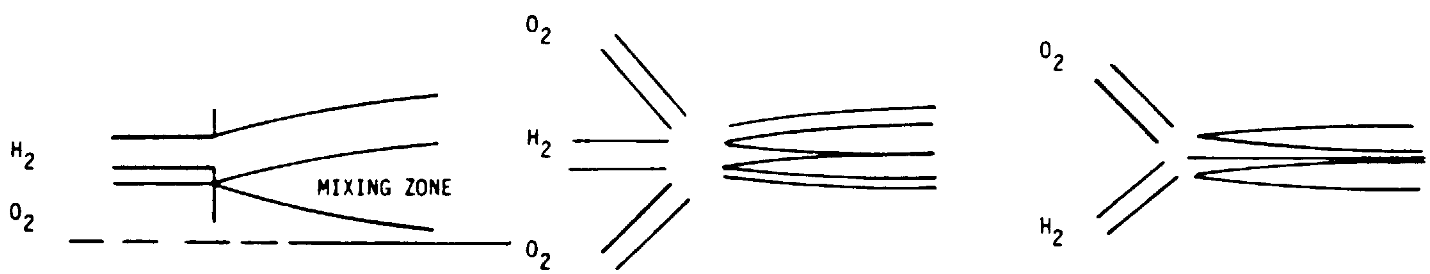

NOTE: H_2 VELOCITY ALWAYS -5-8 O_2 VELOCITY ASSUMING AXISYMMETRIC SYMMETRY, CENTER LINE CONCENTRATIONS FOLLOW FOR:

$$Y_0 = 1 - \mathrm{EXP}\left[\frac{K_0}{K_1 \, \overline{X} \, \overline{\rho_e}^{1/2} - K_2}\right]$$

COMBUSTION PERFORMANCE POSTULATED TO BE:

$$\eta_C{}^* - 1 - Y_0$$

$$\left.\begin{aligned} \overline{X} &= X/r_j \\ \overline{\rho_e} &= \rho_e/\rho_j \end{aligned}\right\} j = \text{REFERENCE JET}$$

K_0 = MEASURE OF INTERACTION BETWEEN ADJACENT ELEMENTS

K_1 = MEASURE OF LOCAL TURBULENT MIXING

K_2 = KLEINSTEIN CONSTANT (FROM BASIC THEORY)

$$\overline{X} = C \frac{L^*}{\varepsilon_C} \left(\eta_j \frac{P_C}{F}\right)^{1/2} - \eta_j{}^{1/2} \left(\frac{\varepsilon_C{}^{1.5} - 1}{\varepsilon_C}\right)$$

$$\eta_j = \eta_j \, [F, \Delta P_{INJ}/P_C]$$

EXAMINED DATA FOR TRIPLET, DOUBLET, SHOWERHEAD, COAXIAL INJECTORS. RANGE OF PARAMETERS:

$$0.5 < K_0 < 3.0$$

← SHOWERHEAD $\quad 0.03 < K_1 < 0.1 \quad$ IMPINGING JETS →

$$K_3 = 0.70$$

Figure 39. Generalized Mixing Model

Equation (37) can be written as follows for $\beta = 40^o$ and $C_F = 1.70$ since these parameters will not vary too much for different cases.

$$x = \frac{L^*}{\varepsilon_c} - .13 \left(\frac{F}{P_c}\right)^{1/2} \left[\frac{\varepsilon_c^{1.5} - 1}{\varepsilon_c}\right] \tag{39}$$

Equation (38) can be transformed by using the expression for compressible gas flow and by taking the case of: O/F = 4.0 with $M_{inj} = .6$, $C_D = .75$, $T_o = 530°F$ (550.04°K), $\gamma = 1.41$, and M = 2.016.

This results in the following:

$$r_j = .18 \left(\frac{F}{n_j P_c}\right)^{1/2} \tag{40}$$

Combining Equations (39) and (40) results in the following expression for the nondimensional axial coordinate:

$$\bar{x} = \frac{x}{r_j} = 5.6 \frac{L^*}{\varepsilon_c} \left(n_j \frac{P_c}{F}\right)^{1/2} - (n_j)^{1/2} \left(\frac{\varepsilon_c^{1.5} - 1}{\varepsilon_c}\right) \tag{41}$$

Examination of Equations (35) and (41) results in the following conclusions concerning the effects of the various engine parameters on combustion efficiencies:

1) a very fine injection pattern is desired
2) strong initial mixing is desired
3) long chamber length is desired
4) low chamber contraction ratio is desired

and

5) low ratio of thrust to chamber pressure is desired.

Substituting the appropriate engine parameters for the nominal high and low chamber pressure thruster designs into Equations (35) and (41) results in the combustion efficiency - L* curves shown in Figure 40. The required characteristic chamber length for the high chamber pressure design to achieve a combustion efficiency of 98% is about 14 inches (35.56 cm). This compares to an L* of 25 inches (63.50 cm) to achieve $\eta_{C*} = 98\%$ in the low chamber pressure design.

The basic results are then modified slightly to provide for uniform flow across the face of the injector. This results in a slight decrease in thrust/element for the inner ring elements. At no time is the thrust/element allowed to exceed the theoretically determined values. As is seen in Figure 40, the 144 element triplet for the high pressure engine is predicted to achieve 99+% combustion performance.

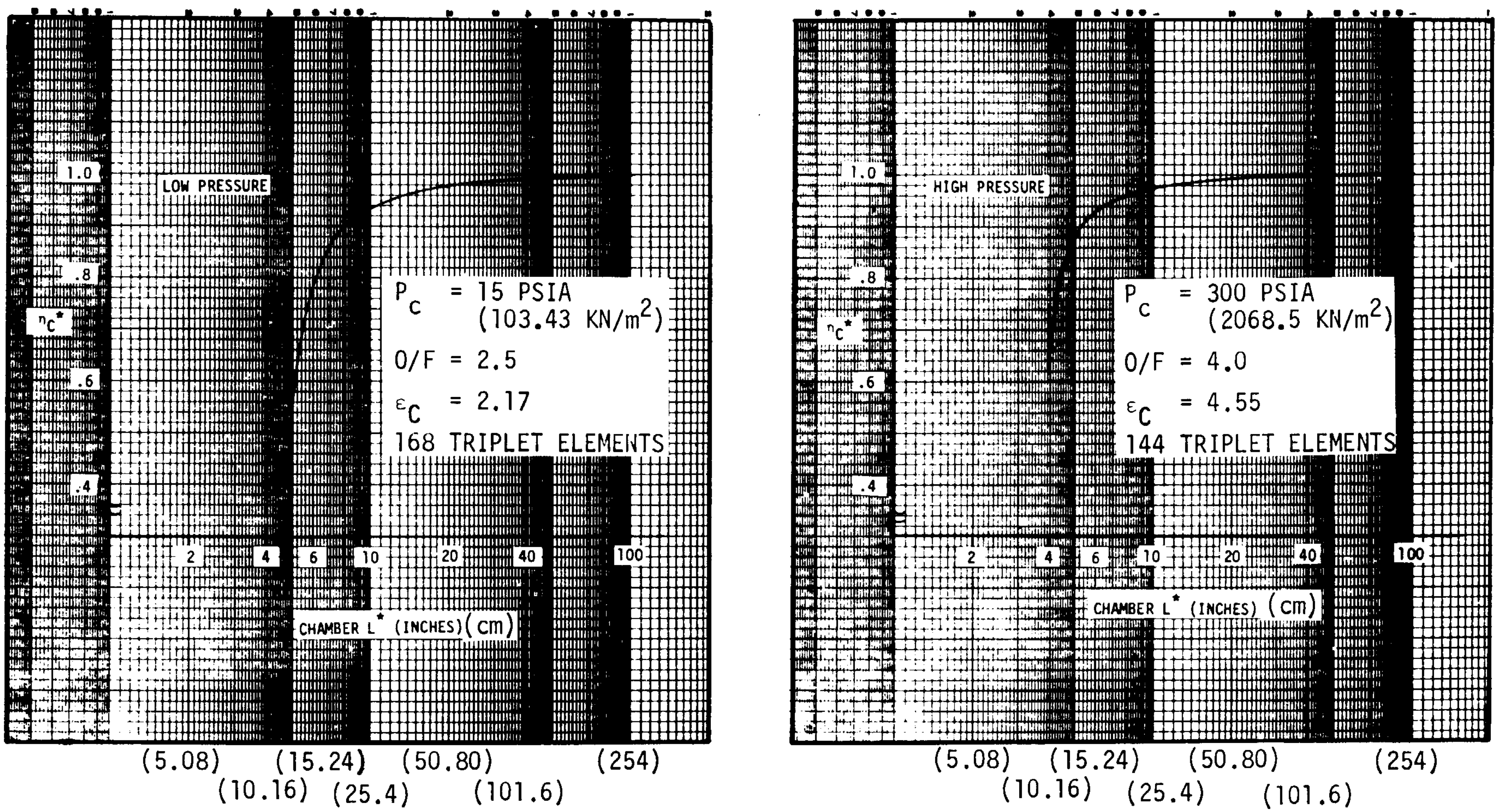

Figure 40. Predicted Gaseous H_2/O_2 Thruster Performance Trends - Thrust 1500 lbf (Thrust = 1500 lb_f, 6672 N)

Both a rigorous and an engineering performance model were utilized to predict the performance of the TRW duct cooled concept. In the ready estimating procedure, the procedures outlined in CPIA 178 were followed. The JANAF ODK reference computer program and the CPIA 178 data were used to account for all but the cooling effects. Since the former are standard industry methods, they are not repeated here. The cooling interaction method is of interest, however.

With cooling the I_{sp} of the core is degraded as follows:

$$I_{sp}' \text{ (core)} = I_{sp} \text{ (core)} \left[\frac{H_c - H_e - \Delta h}{H_c - H_e}\right]^{1/2}$$

where: H_c = chamber enthalpy at core O/F

h_e = exit enthalpy at core O/F

Δh = energy transferred from core to coolant

$X = \dot{m}_{cool}/\dot{m}_{Hz}$

$Y = \dot{m}_{igniter}/\dot{m}_T$

$$(O/F)_{CORE} = \frac{(O/F)\ (1 - Y/2) - Y/2}{1 - X - Y\ (1 + O/F)/2}$$

Enthalpy in the core is transferred to the film coolant. Treating the problem as a two-zone problem, the coolant I_{sp} contribution is:

$$I_{sp}' \text{ (coolant)} = I_{sp} \text{ (coolant)} \left[\frac{H_c - H_e + \Delta h}{H_c - H_e}\right]_{coolant}$$

Of course, the coolant loses mass and the core gains mass as given by the previously described mixing coefficient ralations. The I_{sp} of the chamber is computed from:

$$I_{sp} \text{ (TCA)} = \frac{1}{\dot{w}_T} \left[I_{sp}' \text{ (core)} \cdot \dot{w}_{core} + I_{sp} \text{ (coolant)} \cdot \dot{w}_{coolant} + I_{sp} \text{ (Ig)}\ \dot{w}_{Ig}\right]$$

The accuracy of this simplified approach with mixing properly accounted for has been verified in MSFC tests of the duct coolant concept. This correlation was then used to prepare the predicted performance map as shown in Figure 41.

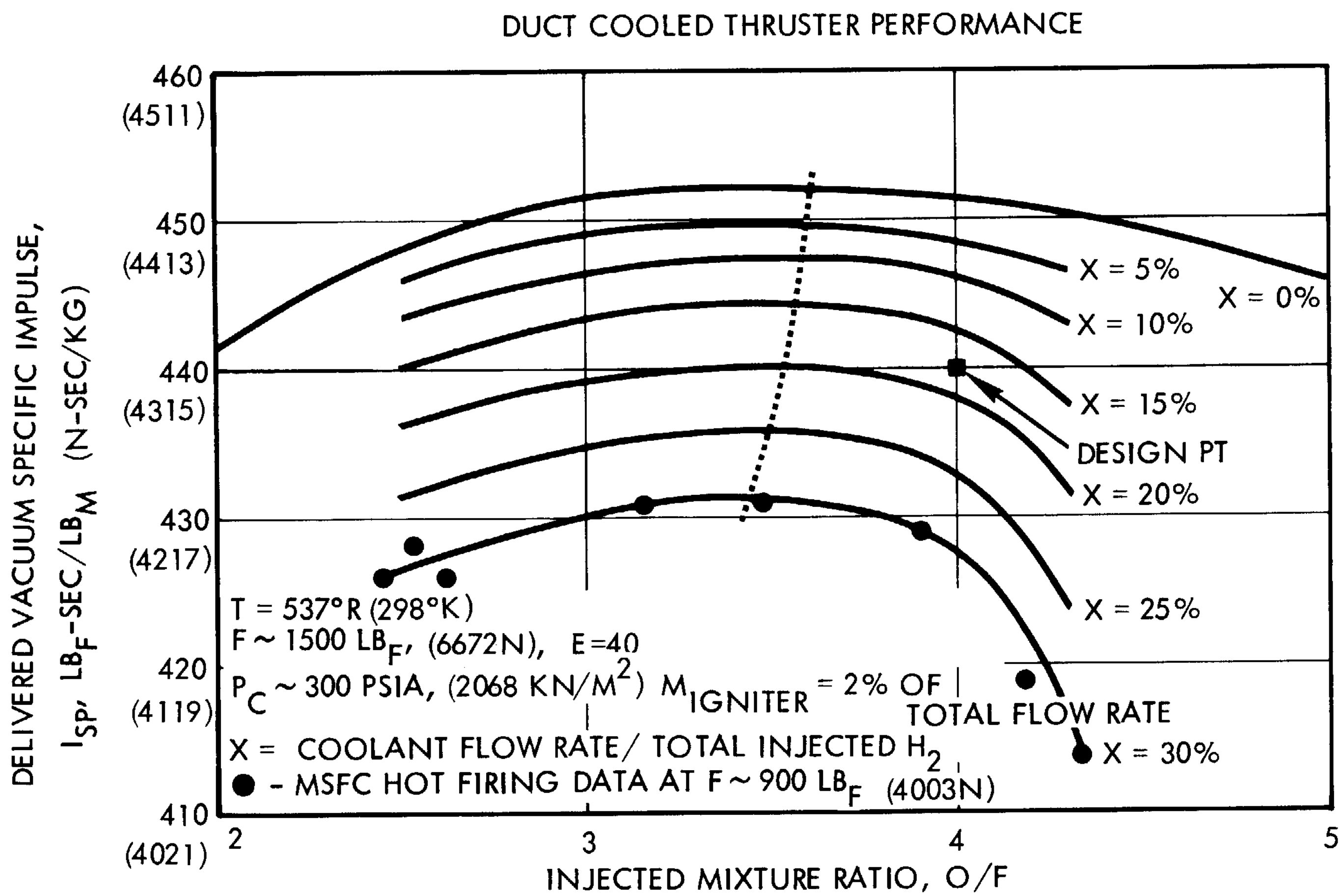

Figure 41. High Pressure Thruster Predicted Performance Map

3.5 THRUSTER MECHANICAL DESIGN AND FABRICATION

This section discribes the mechanical design of the thruster and its fabrication. The overall assembly cross-section is given in Figure 42. As seen in the cross-section the valves are shown on a stand off plate for thermal isolation. The catalytic igniter (described in detail in Volume I) is shown in the center of the triplet injector. The igniter nominal flow rate is $\sim$ 2% of the total flow, and the flow is controlled by two separate flow control valves. The duct coolant flow and the interior film coolant flow split is controlled by a replaceable flow control ring for the experimental engine. The duct is mechanically clamped in place by the nozzle flange being bolted onto the head end assembly. As shown the duct itself floats freely inside the chamber.

3.5.1 Injector Hydraulics

The triplet injector is designed with three rings of O_2-H_2-O_2 triplet elements. Forty-eight H_2 orifices and 96 O_2 orifices make up each of the three rings of triplets. The orifice diameters are varied for each ring to provide a relatively uniform mass distribution over the cross-sectional area. The injection geometry is presented in Figures 43 and 44 for the cold propellant design and for the ambient temperature design, respectively. The internal manifolding is designed for low Mach numbers to reduce circumferential flow variations. For cold propellants, the maximum Mach number at rated flow is 0.06 for the H_2 and 0.09 for the O_2, (Figure 45). With ambient temperature propellants, the maximum internal Mach numbers are 0.12 (Figure 46). The injection Mach numbers are 0.47 for the H_2 and 0.41 for the O_2, which corresponds to a pressure drop of approximately 50 psi (344.75 KN/m^2) at nominal chamber pressure. The internal manifolding is designed for a volume ratio of 4 to reduce mixture ratio transients during pulse mode operation. The dynamic response of the engine is limited by valve response rather than manifold volumes, as indicated in Figure 47.

3.5.2 Injector Design and Fabrication

As discussed earlier the injector selection was a raised post triplet with 144 elements. The design detail is given in Figures 48, 49, and 50 for the hole pattern, body, and back body. The injector rings for the experimental injector were OFHC. For the flight thrusters they would be Berylco-10.

The injector inner body assembly is a brazed assembly as shown in Figure 51. The rings are first brazed into the center body. The center body in turn is brazed into the S.S. 304L body.

The back side of the injector assembly is an all welded body, Figure 52. All of these parts were S.S. 304L.

The hole pattern is EDM into the assembly after its final braze and pressure check. The final injector assembly is shown in Figure 53.

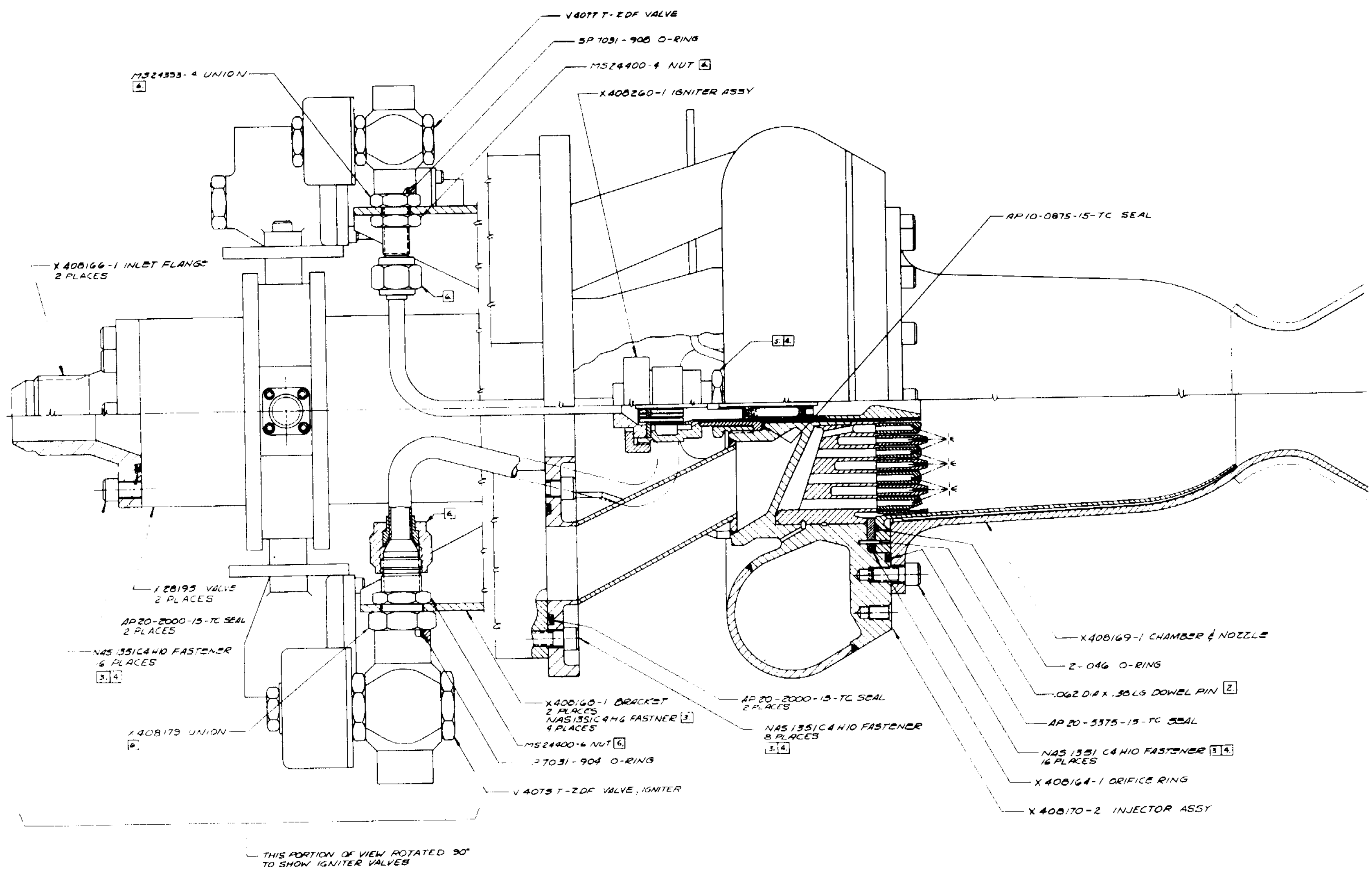

High Pressure TCA

Figure 42. Duct Cooled Thruster Assembly Cross-Section

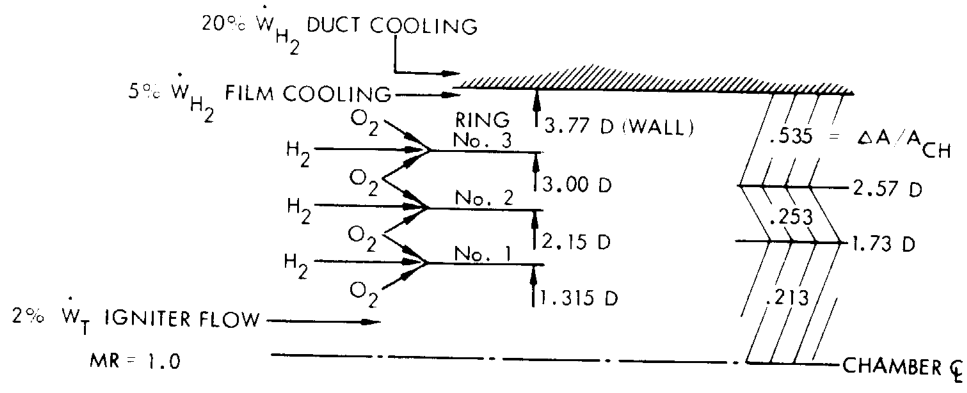

T_{H_2} = 200°R (111°K)

T_{O_2} = 300°R (167°K)

RING NO.	% $\frac{W}{W_T - W_{H_2}}$ FC + DC	INJ. MR	NO. OF ORIFICES O_2/H_2	ΔA_{H_2} $(IN^2)(CM^2)$	ΔA_{O2} $(IN^2)(CM^2)$	D_{H_2} $(IN^2\ (CM^2)$	D_{O_2} $(IN^2)(CM^2)$	W_{H_2} (LB/SEC)	W_{O_2} (LB/SEC)
1	*25	6.90 (5.34*)	96/48	.0418 (0.270)	.090 (.580)	.033 (.213)	.035 (.226)	.095 (.043)	.655 (.297)
2	25	5.34	96/48	.0567 (.366)	.094 (.606)	.039 (.252)	.036 (.232)	.129 (.058)	.690 (.313)
3	50	5.34	96/48	.114 (.735)	.189 (1.219)	.055 (0.355)	.050 (.322)	.259 (.118)	1.380 (.626)
				Σ = .213 (1.371)	.373 (2.405)			.483 (.219)	2.725 (1.237)

*INCLUDING IGNITER FLOW

O_2/H_2 IMPINGEMENT ANGLE = 20°

$\dot{W}_{H_2}$ = 0.69 LB/SEC (0.313 KG/SEC)

$\dot{W}_{O_2}$ = 2.76 LB/SEC (1.253 KG/SEC)

OVERALL $\dot{W}_{O_2}/\dot{W}_{H_2}$ = 4.0 (1.816 KG/SEC)

CORE $\dot{W}_{O_2}/\dot{W}_{H_1}$ (IN CL. IGNITER) = 5.34 (2.424 KG/ SEC)

$\dot{W}_{IGN\ H_2} = \dot{W}_{IGN\ O_2}$ = 0.0345 LB/SEC (0.0157 KG/SEC)

$\dot{W}_{H_2}$ FC + DC = 0.173 LB/SEC (0.078 KG/SEC)

$\dot{W}_T$ = 3.45 LB/SEC (1.566 KG/SEC)

Figure 43. Triplet Injection Parameters (COLD) X408170

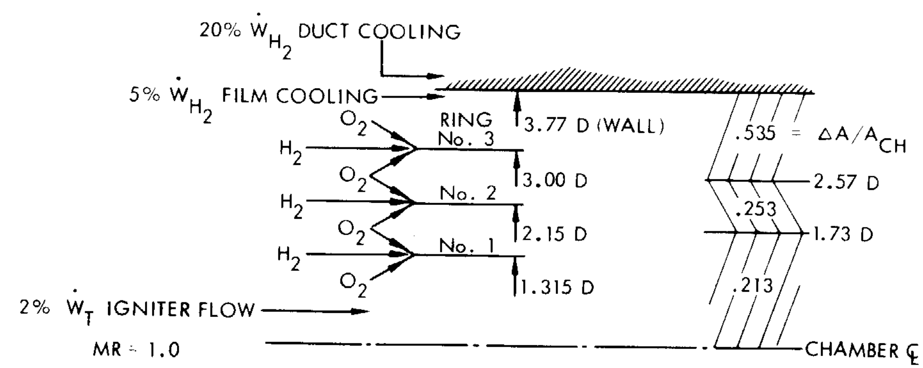

T_{H_2} = 540°R (300°K)

T_{O_2} = 540°R (300°K)

RING NO.	% W W_T-W_{H_2} FC + DC	INJ. MR	NO. OF ORIFICES O_2/H_2	ΔA_{H_2} (IN^2)(CM^2)	ΔA_{O_2} (IN^2)(CM^2)	D_{H_2} (IN^2)(CM^2)	D_{O_2} (IN^2)(CM^2)	W_{H_2} (LB/SEC)(KG/SEC)	W_{O_2} (LB/SEC)(KG/SEC)
1	*25	6.90 (5.34*)	96/48	.0697 (0.450)	.133 (0.858)	.043 (.271)	.042 (.271)	.095 (.043)	.655 (.297)
2	25	5.34	96/48	.0948 (0.611)	.141 (0.909)	.050 (.322)	.043 (.277)	.129 (.058)	.690 (.313)
3	50	5.34	96/48	.190 (1.276)	.281 (1.812)	.071 (.458)	.061 (.393)	.259 (.118)	1.380 (.626)
			Σ =	.355 (2.287)	.555 (3.579)			.483 (.219)	2.725 (1.237)

*INCLUDING IGNITER FLOW

O_2/H_2 IMPINGEMENT ANGLE = 20°

$\dot{W}_{H_2}$ = 0.69 LB/SEC (0.313 KG/SEC)

$\dot{W}_{O_2}$ = 2.76 LB/SEC (1.253 KG/SEC)

OVERALL $\dot{W}_{O_2}/\dot{W}_{H_2}$ = 4.0 (1.816 KG/SEC)

CORE $\dot{W}_{O_2}/\dot{W}_{H_1}$ (INCL. IGNITER) = 5.34 (2.424 KG/SEC)

$\dot{W}_{IGN\,H_2} = \dot{W}_{IGN\,O_2}$ = 0.0345 LB/SEC (0.0157 KG/SEC)

$\dot{W}_{H_2}$ FC + DC = 0.173 LB/SEC (0.078 KG/SEC)

$\dot{W}_T$ = 3.45 LB/SEC (1.566 KG/SEC)

Figure 44. Triplet Injection Parameters (AMBIENT) X408170

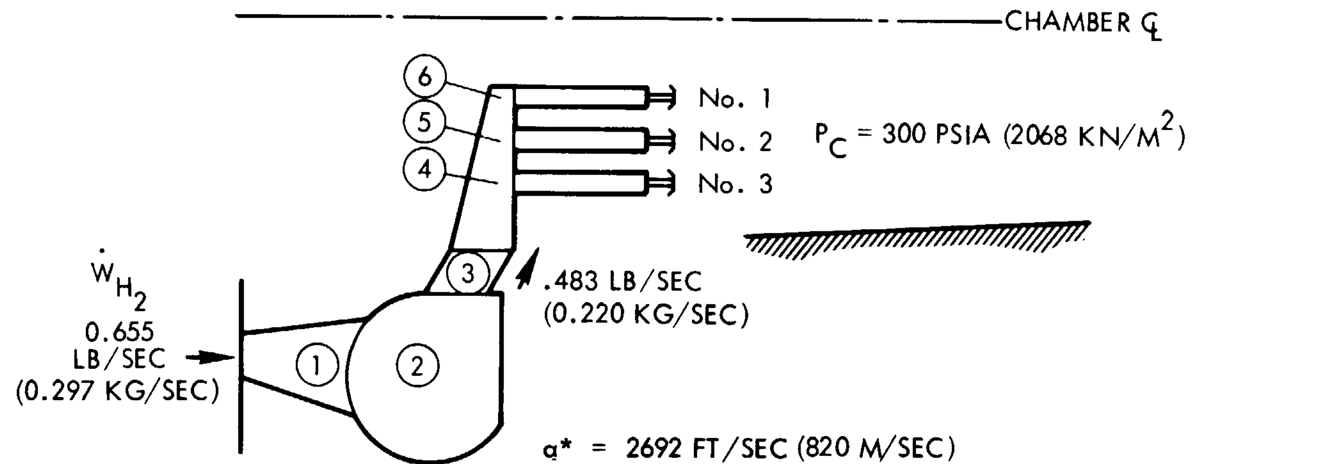

a* = 2692 FT/SEC (820 M/SEC)
VOLUME FROM VALVE EXIT TO INJECTION ORIFICES = 80 IN^3 (1312 CM^3)

REGION	MACH NO.	NOM. FLOW AREA (IN^2)	(CM^2)	ΔP (PSI)	(KN/M^2)	$\dot{W}_{H_2}$ (LB/SEC)	(KG/SEC)
INLET (1) TO MANIFOLD (2)	0.055	2.0	(12.9)	0.7	(4.8)	.655	(0.297)
MANIFOLD (2)	0.017	3.3X 2	(43)	-		.655	(0.297)
ENTRANCE TO 8 (3) PORTS	0.046	1.78	(11.5)	0.3	(2.1)	.483	(0.219)
(4) 8 PORTS AT No. 3 H_2 RING	0.061	1.30	(8.38)			.483	(0.219)
(5) 8 PORTS AT No. 2 H_2 RING	0.049	0.745	(4.805)	2	(13.8)	.224	(0.101)
(6) 8 PORTS AT No. 3 H_2 RING	0.067	0.230	(1.484)			.095	(0.043)
No. 3 RING	0.054	0.790	(5.095)	-		.259	(0.118)
No. 2 RING	0.037	0.567	(3.657)			.129	(0.059)
No. 1 RING	0.045	0.347	(2.238)	-		.095	(0.043)
INJECTION ORIFICES, No. 3 RING	0.47	0.114	(0.735)	60	(414)	.259	(0.118)
INJECTION ORIFICES, No. 2 RING	0.47	0.0567	(0.365)	60	(414)	.129	(0.059)
INJECTION ORIFICES, No. 1 RING	0.47	0.0418	(0.270)	60	(414)	.095	(0.043)

Figure 45a. Triplet Injector Manifold Parameters X408170
Hydrogen Side, TH_2 = 200°R (111°K)

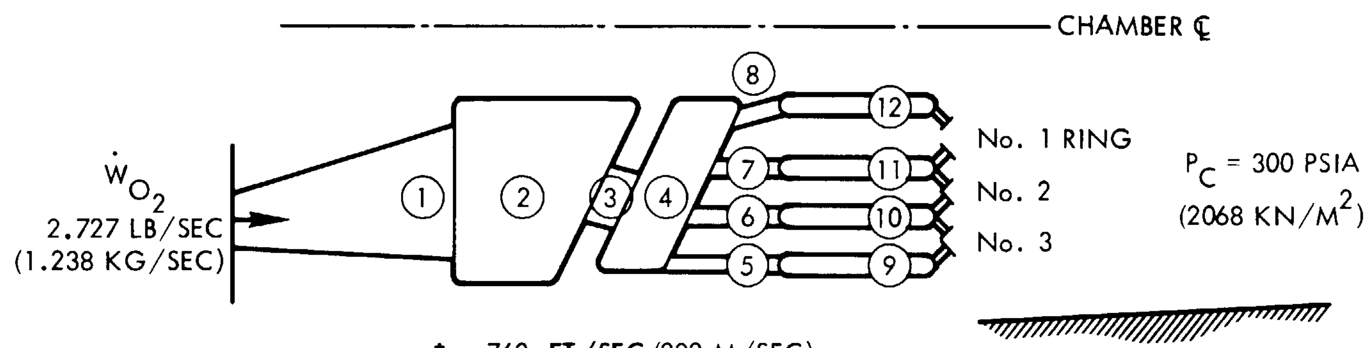

a* = 762 FT/SEC (232 M/SEC)
VOLUME FROM VALVE EXIT
TO INJECTION ORIFICES = 20 IN^3 (328 CM^3)

REGION	MACH No.	NOM. FLOW AREA (IN^2)	(CM^2)	ΔP (PSI)	(KN/M^2)	$\dot{W}_{O_2}$ (LB/SEC)	(KG/SEC)
INLET (1) TO MANIFOLD (2)	0.09	1.5	(9.7)	2.1	(14.5)	2.726	(1.238)
MANIFOLD (2)	0.07	1.0 X 2		-		2.726	(1.238)
DISTRIBUTION PLATE (3)	0.07	2.0	(12.9)	1.7	(11.7)	2.726	(1.238)
MANIFOLD (4)				-		2.726	(1.238)
(5) 8 PORTS	0.04	0.867	(5.59)			0.691	(0.314)
(6) 8 PORTS	0.085	0.62	(4.00)	2.7	(18.6)	1.032	(0.468)
(7) 8 PORTS	0.075	0.45	(2.90)			0.674	(0.306)
(8) 18 ORIFICES	0.075	0.232	(1.50)			0.328	(0.149)
(9)	0.028	1.22	(7.87)	-		0.691	(0.314)
(10)	0.060	0.88	(5.68)	-		1.032	(0.468)
(11)	0.063	0.55	(3.55)	-		0.674	(0.306)
(12)	0.082	0.214	(1.38)	-		0.328	(0.149)
INJECTION ORIFICES No. 3 RING	0.41	0.090	(0.580)	45	(310)	1.381	(0.627)
INJECTION ORIFICES No. 2 RING	0.41	0.094	(0.606)	45	(310)	0.691	(0.314)
INJECTION ORIFICES No. 1 RING	0.41	0.139	(0.897)	45	(310)	0.655	(0.297)

Figure 45b. Triplet Injector Manifold Parameters X408170
Oxygen Side, $TO_2 = 300^oR$ (167^oK)

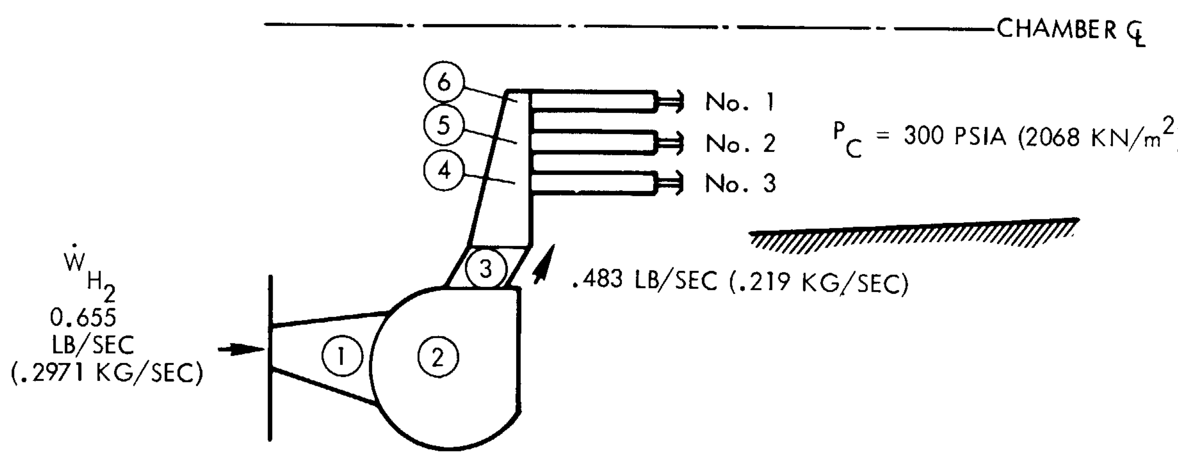

α^* = 4350 FT/SEC (1325.88 M/SEC)
VOLUME FROM VALVE EXIT TO
INJECTION ORIFICES = 80 IN^3 (1311.2 CM^3)

REGION	MACH NO.	NOM. FLOW AREA (IN^2) (CM^2)	ΔP (PSI) (KN/m^2)	$\dot{W}_{H_2}$ (LB/SEC) (KG/SEC)
INLET ① TO MANIFOLD ②	0.090	2.0 (12.90)	2 (13.79	.655 (.29711)
MANIFOLD ②	0.028	3.3 X 2 (21.29) X 2	-	.655 (.29711)
ENTRANCE TO 8 ③ PORTS	0.075	1.78 (11.48)	0.7 (4.83)	.483 (.2191)
④ 8 PORTS AT No. 3 H_2 RING	0.10	1.30 (8.39)		.483 (.2191)
⑤ 8 PORTS AT No. 2 H_2 RING	0.081	0.745 (4.81)	5 (34.48)	.224 (.1016)
⑥ 8 PORTS AT No. 3 H_2 RING	0.11	0.230 (1.48)		.095 (.0431)
No. 3 RING	0.088	0.790 (5.10)	-	.259 (.1175)
No. 2 RING	0.061	0.567 (3.66)		.129 (.0585)
No. 1 RING	0.073	0.347 (2.24)	-	.095 (.0431)
INJECTION ORIFICES, No. 3 RING	0.47	0.190 (1.23)	60 (413.7)	.259 (.1175)
INJECTION ORIFICES, No. 2 RING	0.47	0.0948 (.6116)	60 (413.7)	.129 (.0585)
INJECTION ORIFICES, No. 1 RING	0.47	0.0967 (.6239)	60 (413.7)	.095 (.0431)

Figure 46a. Triplet Injector Manifold Parameters X408170
Hydrogen Side, TH_2 = 540°R (300.02°K)

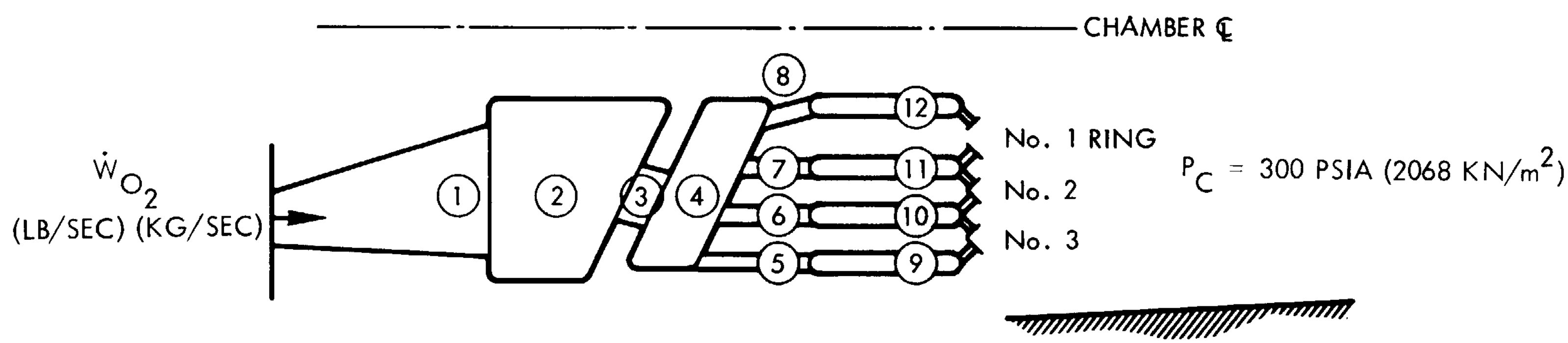

α^* = 1084 FT/SEC (330.403 M/SEC)
VOLUME FROM VALVE EXIT TO
INJECTION ORIFICES = 20 IN^3 (327.8 CM^3)

	REGION	MACH NO.	NOM. FLOW AREA (IN^2) (CM^2)	ΔP (PSI) (KN/m^2)	$\dot{W}_{O_2}$ 2.727 LB/SEC (1.237 KG/SEC)
	INLET 1 TO MANIFOLD 2	0.12	1.5 (9.7)	3.7 (25.51)	2.726 (1.238)
	MANIFOLD 2	0.09	1.0 X 2 (2.54) X 2	-	2.726 (1.238)
	DISTRIBUTION PLATE 3	0.09	2.0 (12.9)	3.1 (21.37)	2.726 (1.238)
	MANIFOLD 4			-	2.726 (1.238)
5	8 PORTS	0.053	0.867 (5.59)		0.691 (.314)
6	8 PORTS	0.114	0.62 (4.00)	5 (34.43)	1.032 (.468)
7	8 PORTS	0.102	0.45 (2.90)		0.674 (.306)
8	18 ORIFICES	0.10	0.232 (1.50)		0.328 (.149)
9		0.038	1.22 (7.87)	-	0.691 (.314)
10		0.081	0.88 (5.68)	-	1.032 (.468)
11		0.084	0.55 (3.55)	-	0.674 (.306)
12		0.11	0.214 (1.38)	-	0.328 (.149)
	INJECTION ORIFICES No. 3 RING	0.41	0.281 (1.81)	45 (310)	1.381 (.627)
	INJECTION ORIFICES No. 2 RING	0.41	0.141 (.9097	45 (310)	0.691 (.314)
	INJECTION ORIFICES No. 1 RING	0.41	0.133 (.858)	45 (310)	0.655 (.297)

Figure 46b. Triplet Injector Manifold Parameters X408170
Oxygen Side, TO_2 = 540°R (300.02°K)

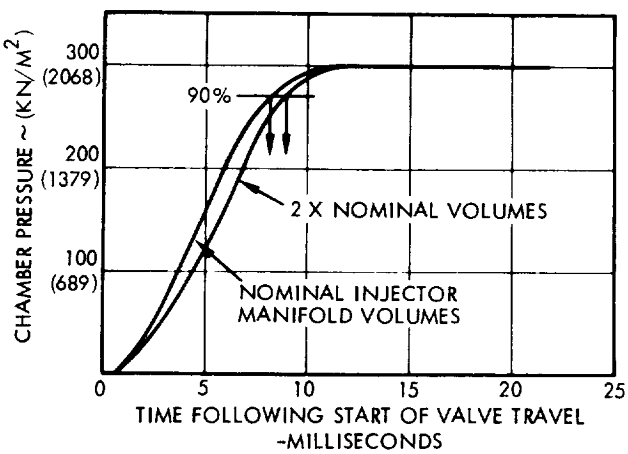

HIGH PRESSURE

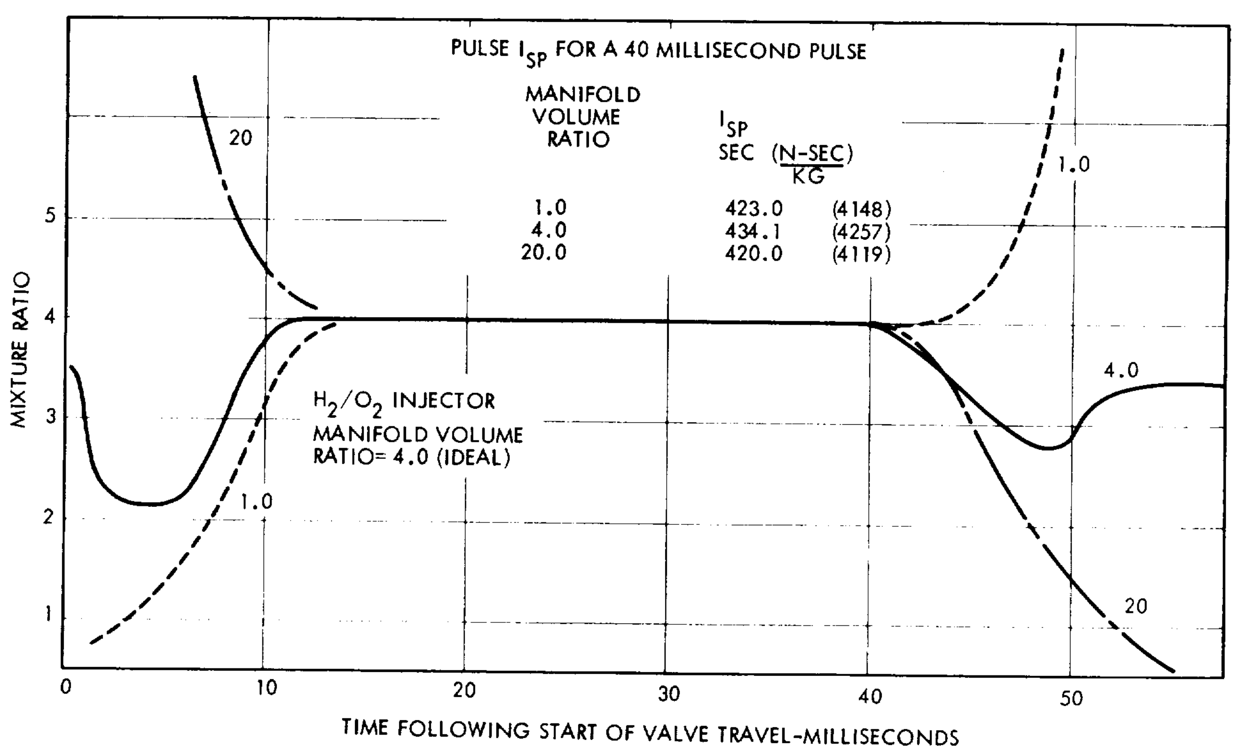

Figure 47. Variation in Pulse Mode Mixture Ratio with Injector Manifold Volume Ratio High Chamber Pressure Thruster

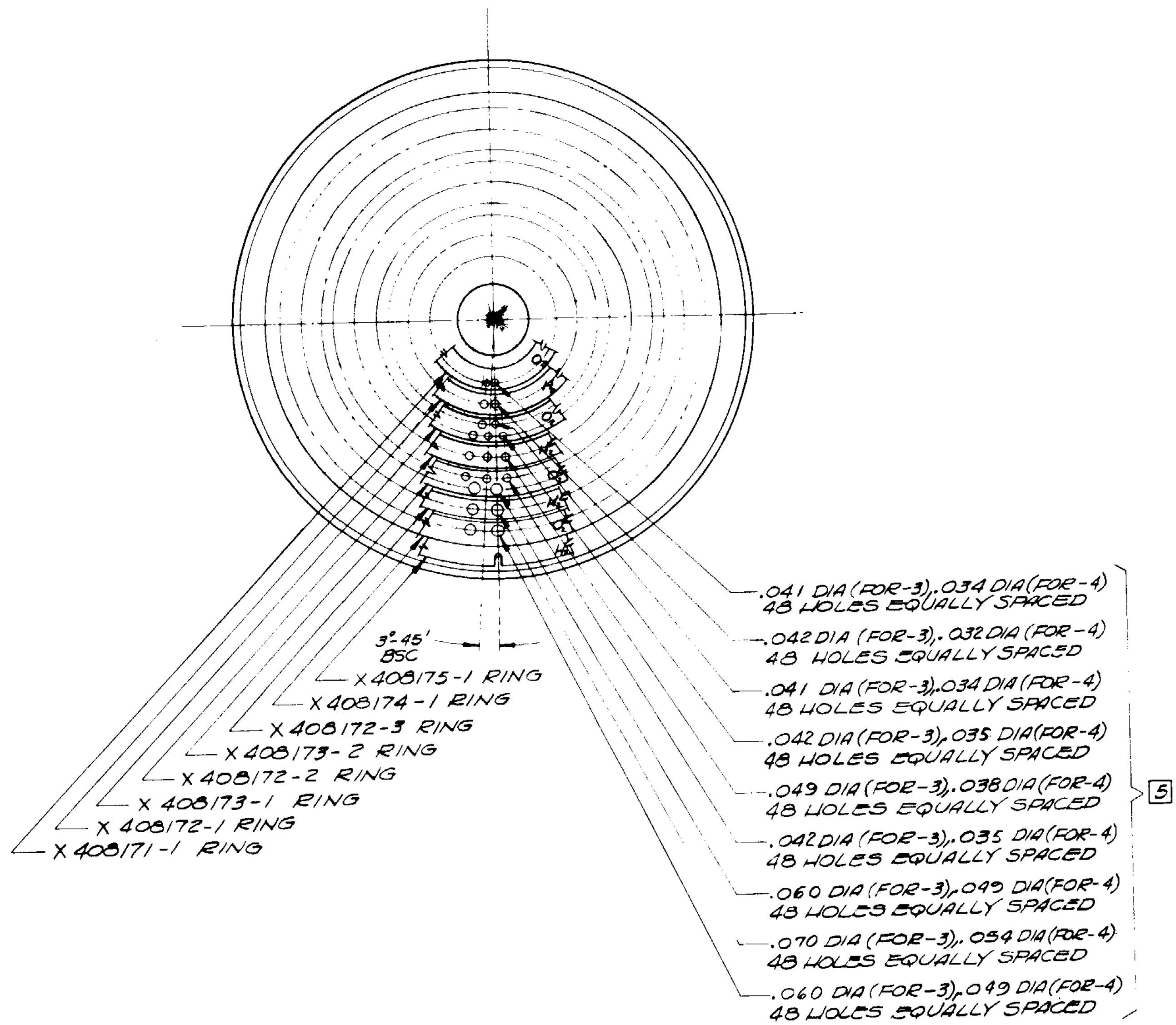

Figure 48. Triplet Hole Pattern

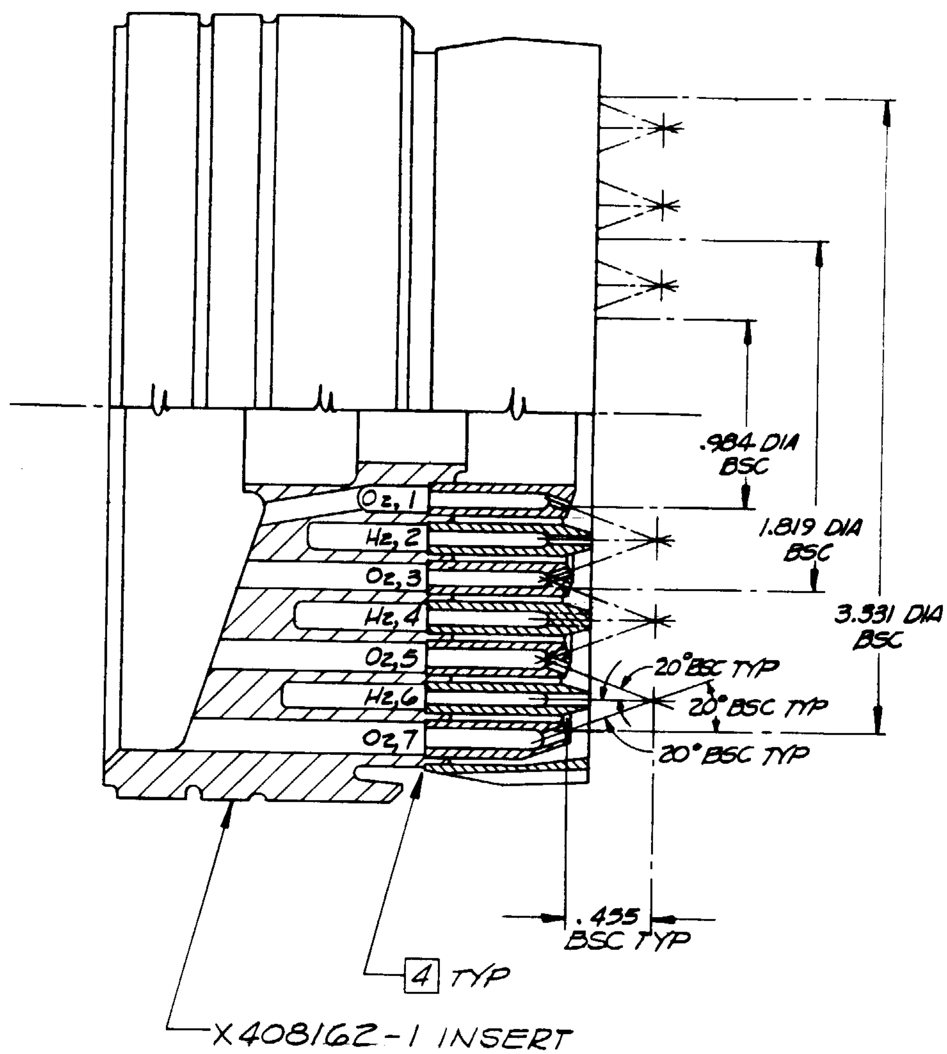

Figure 49. Triplet Body Insert With Rings

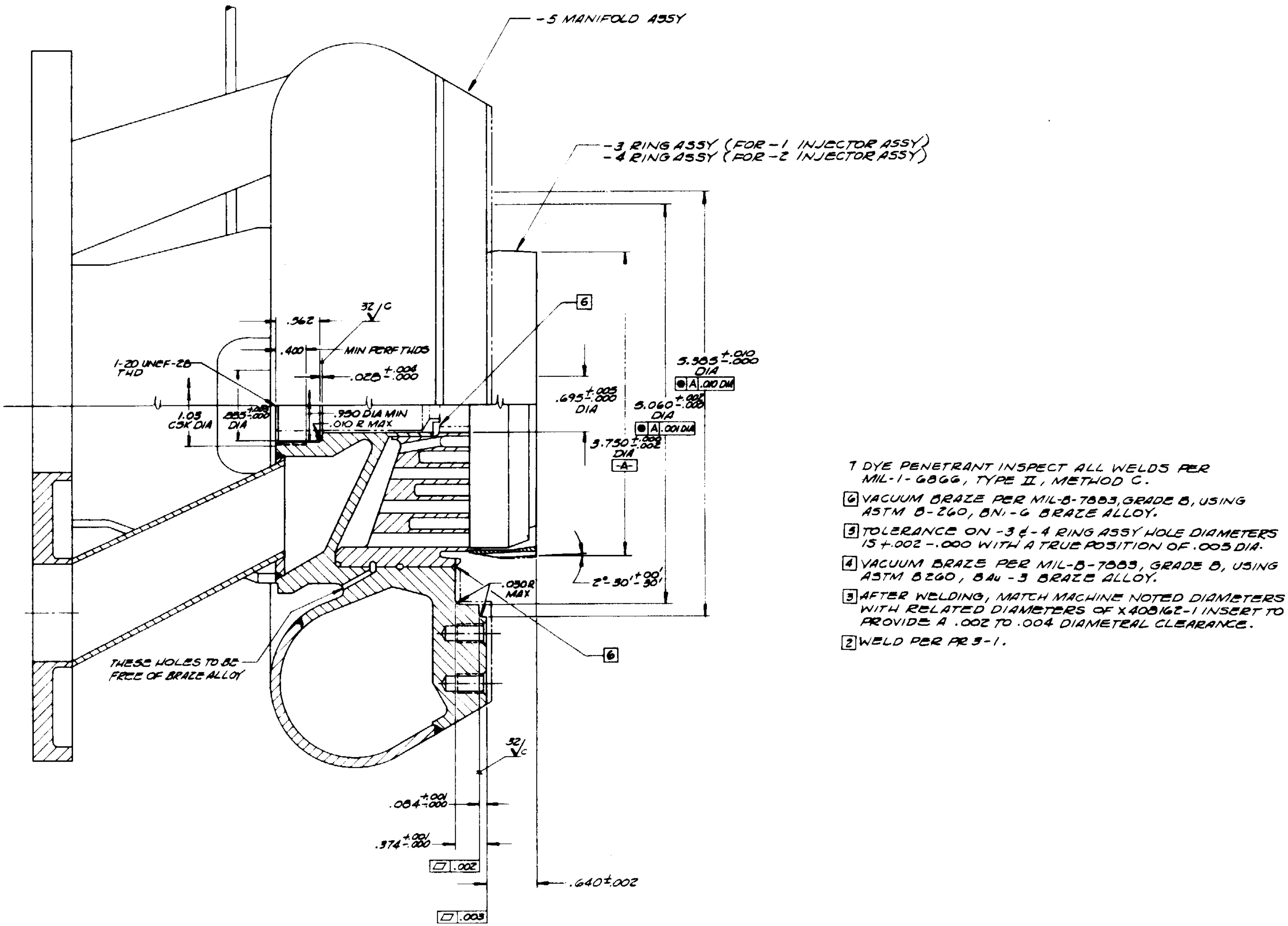

Figure 50. Triplet Manifolding

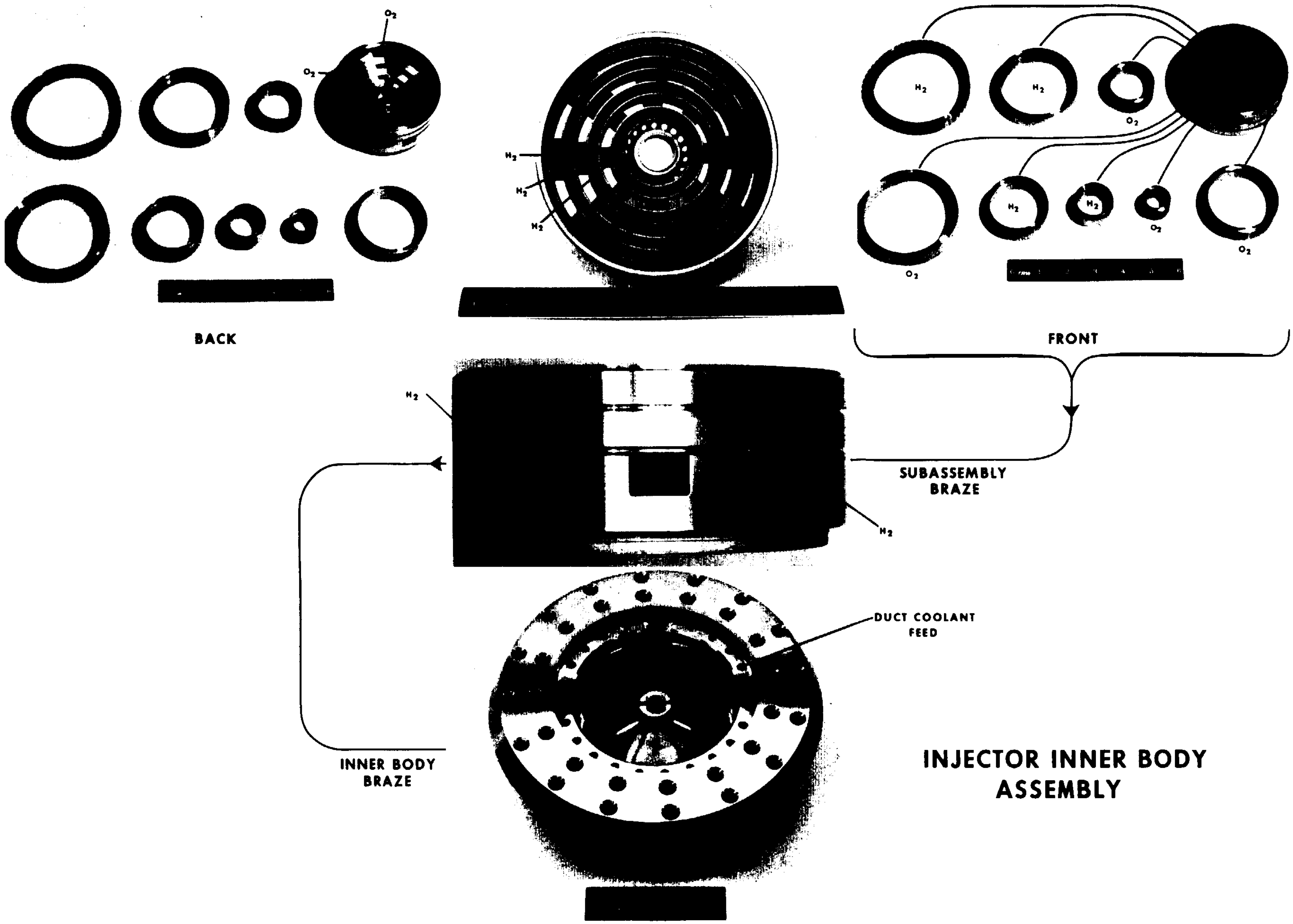

Figure 51. Injector Center Body Assembly

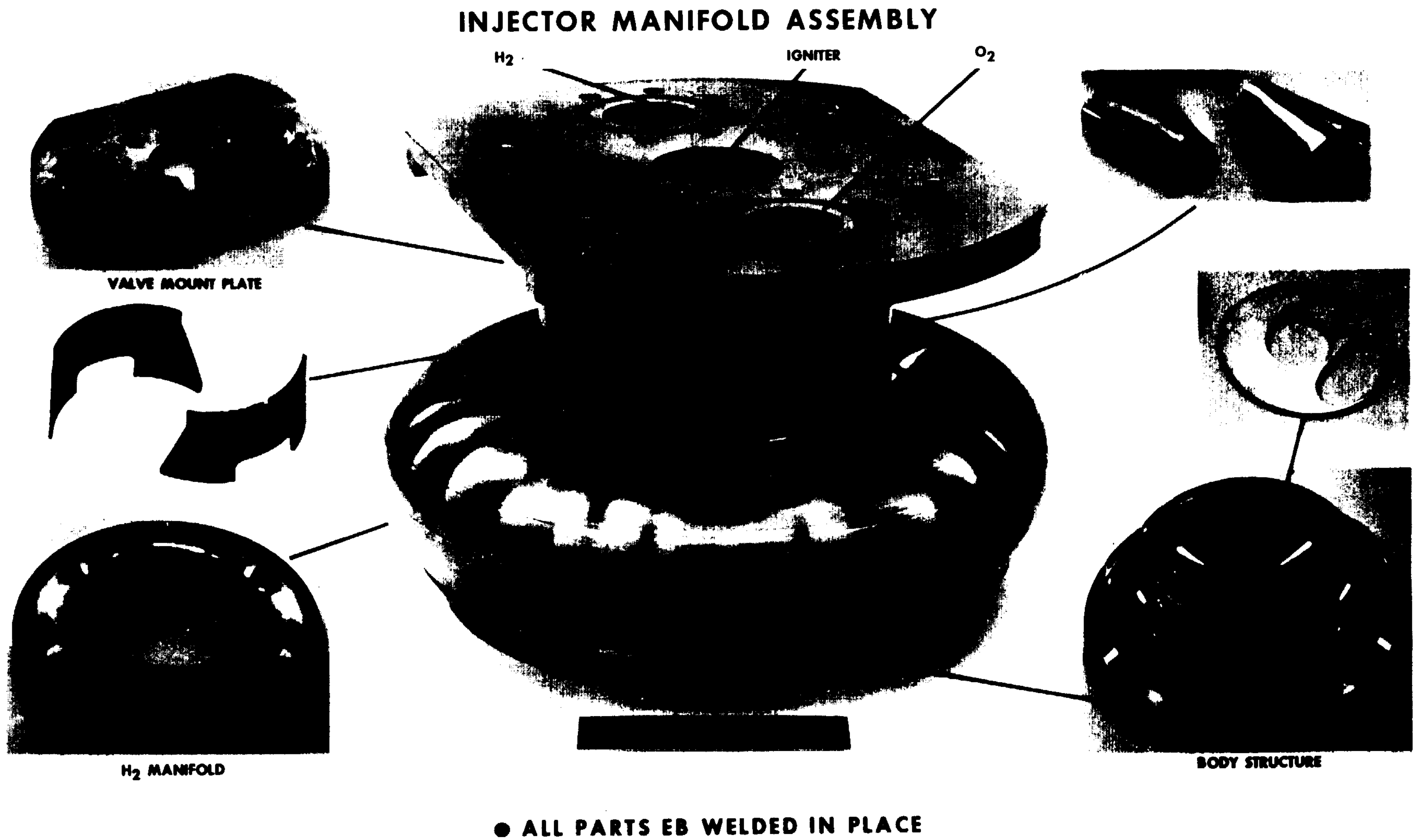

Figure 52. Injector Manifold Assembly

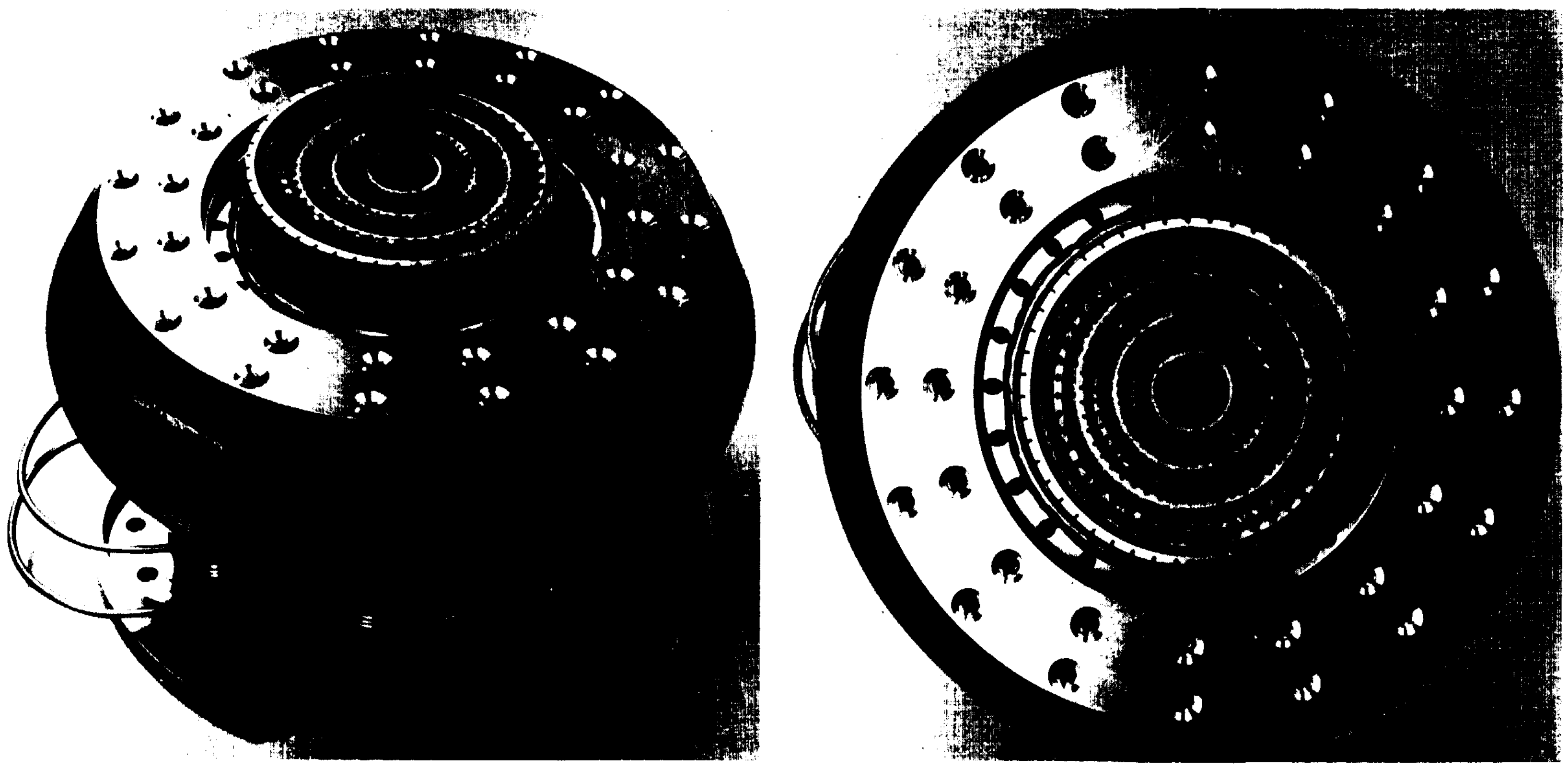

Figure 53. Triplet Injector Assembly

3.5.3 Duct Design and Fabrication

The duct is a single piece Berylco-10 configuration with 90 channels The design detail is shown in Figure 54 and the finished product is shown in Figure 55.

3.5.4 Nozzle Design and Fabrication

The nozzle is a single piece A-286, 40:1 nozzle for the altitude firings. Its design is shown in Figure 56. The nozzle is an 80% bell contour. The chamber has a nearly 3^{o} taper in it to provide a guiding surface for the duct. The Section B is at an area ratio of 12:1. Short S.S. nozzles of 12:1 were used for sea level checkout firings. The nozzles were machined from pierced billets. A finished nozzle is shown in Figure 57.

3.5.5 Catalytic Igniter

The high pressure catalytic igniter selection was based upon design guidelines established during the igniter scaling analysis described in Volume I of this contract report. The downstream O_2 injection technique was incorporated to minimize overall igniter response time, as experimentally determined during the response enhancement investigation (Section 3.2.2., Volume I).

The high Pc igniter design is shown schematically in Figure 58. The volumes and flow resistances were selected to allow O_2 to pulse through the system and diffuse backwards through the downstream end of the catalyst bed, this O_2 being intercepted by the low MR (less than 1:1) H_2-O_2 mixture from the upstream end. The pneumatic design of the unit was investigated by analog modeling of the results from the igniter scaling analysis. Overall mixture ratio is 1:1, with 90 percent of the total H_2 flow utilized for cooling the reactor combustion chamber.

Ten percent of the igniter H_2 and O_2 passes through the catalyst bed at a MR of 1:1 or lower. The remaining 90 percent of the O_2 is injected downstream of the catalyst bed to provide high response ignition and to raise the local MR to 10 O/F to provide a high temperature effluent for reliable main thruster ignition.

3.5.6 Overall Thruster Assembly

The overall assembly drawing is shown in Figure 59. This figure gives all major dimensions. The actual thruster assembly is shown in Figure 60.

3.5.7 Thruster Material Tradeoff Summary

The material selection philosophy for the thruster assembly nozzle was based on a philosophy which would not allow any new material development requirements. The pro and con factors considered are given in Table 8. Effects of H_2 are shown in Figure 61. From these results the primary material selection were taken as A-286 for the nozzle and Berylco-10 for the duct.

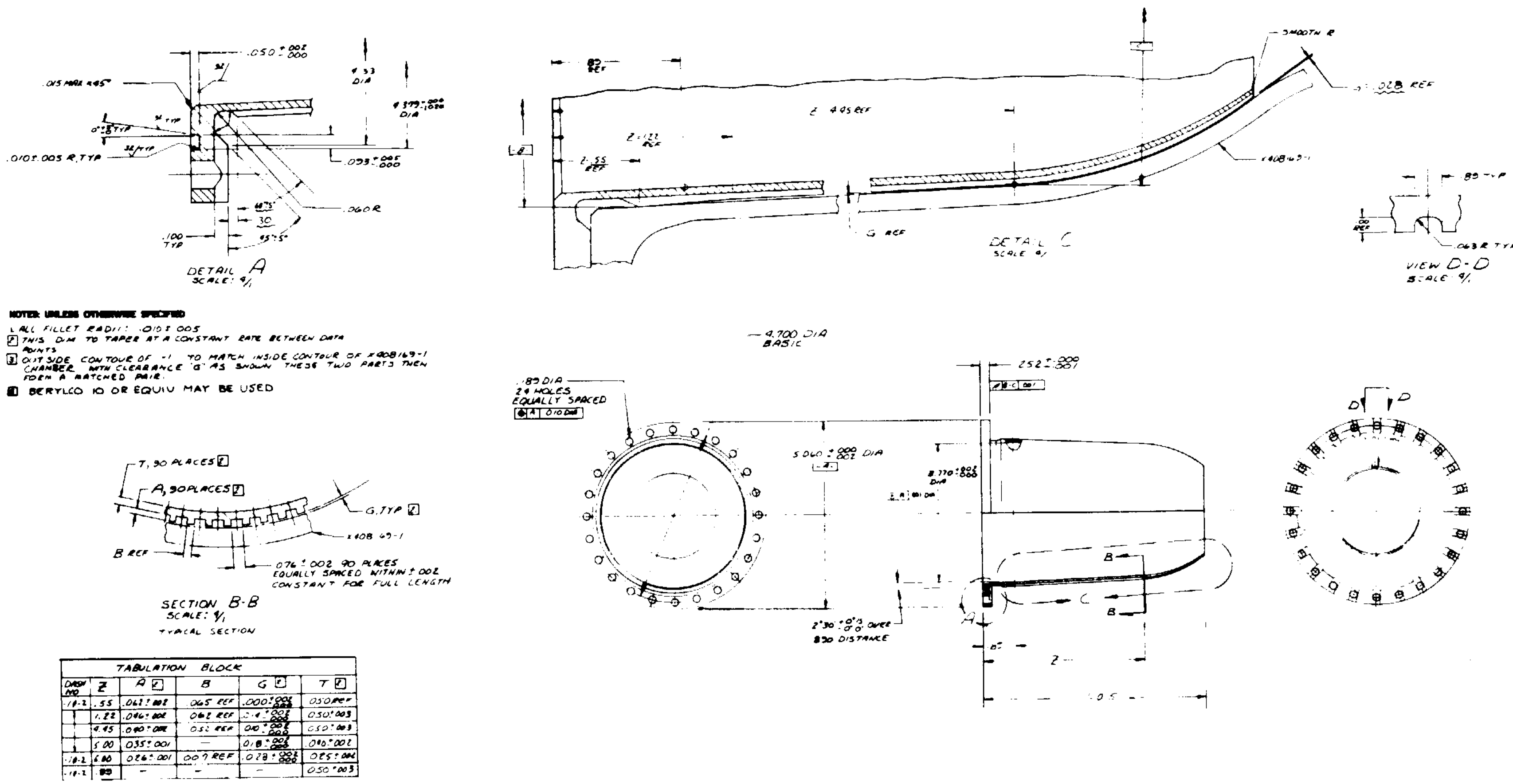

Figure 54. Duct Design Details

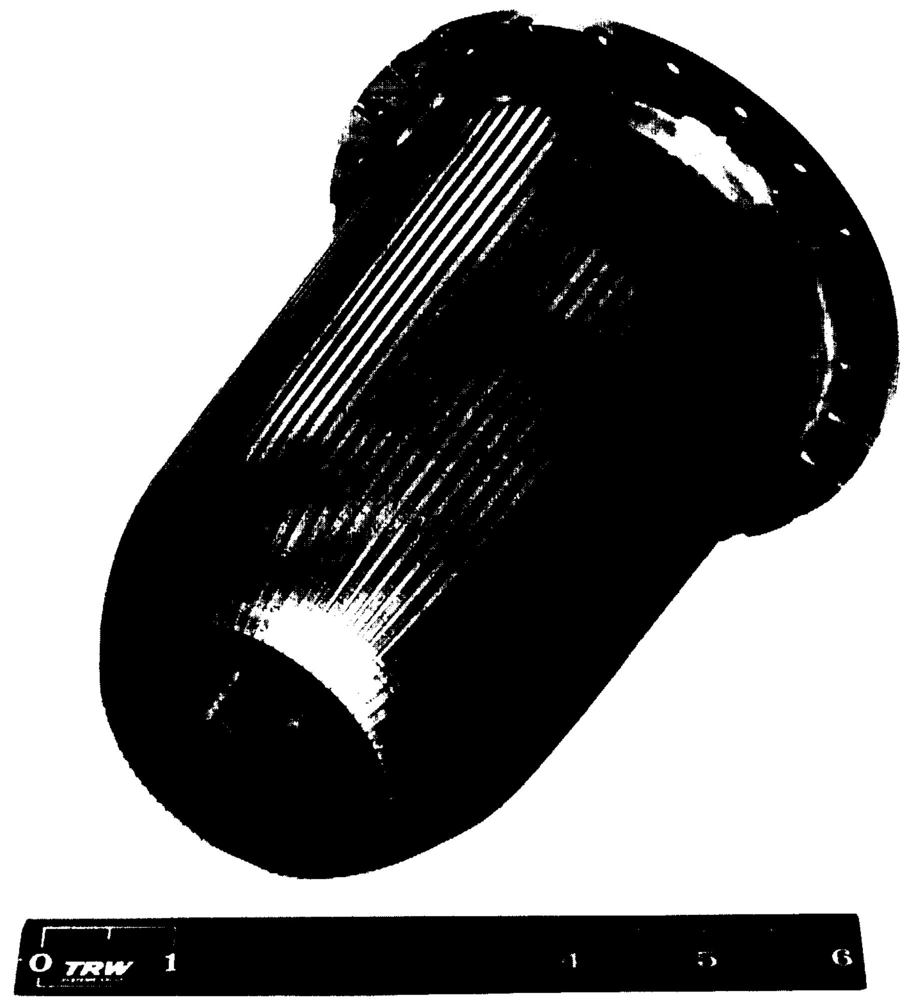

Figure 55. Finished Berylco-10 Duct (Weight 1.90 lb)

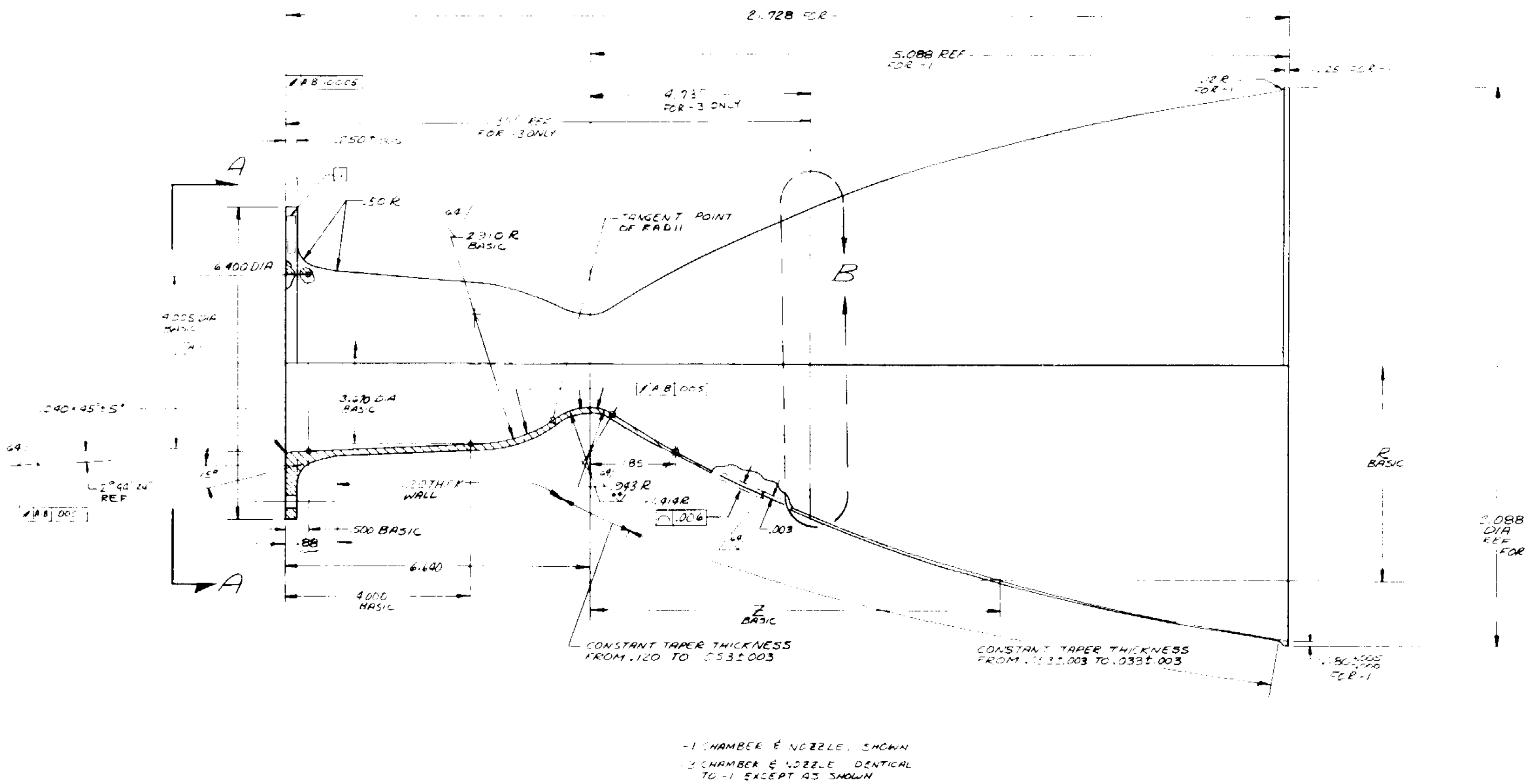

Chamber

Figure 56. 1500 lb_f (6672 N) Nozzle and Chamber Design

- FLIGHT ENGINE NOZZLE ΔX_{thrust} = 0.050" (.127 cm)
  ΔX_{exit} = 0.020" (.0508 cm) - 0.030" (.0762 cm)
- WEIGHT 9.4 lbs (41.81 N)

Figure 57. Finished A-286 Single Piece Nozzle

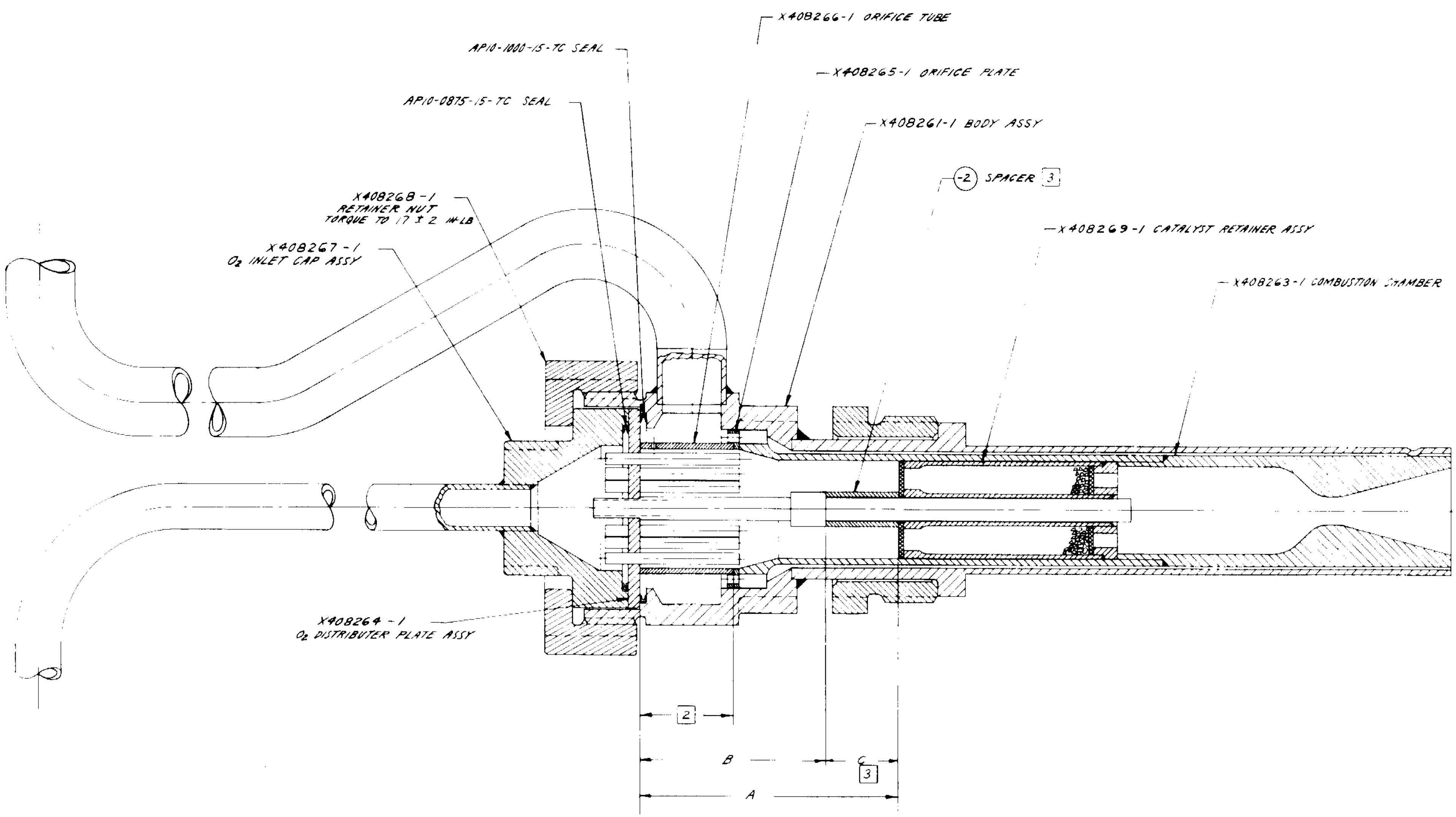

Figure 58. Catalytic Reactor - Downstream O_2 Injection

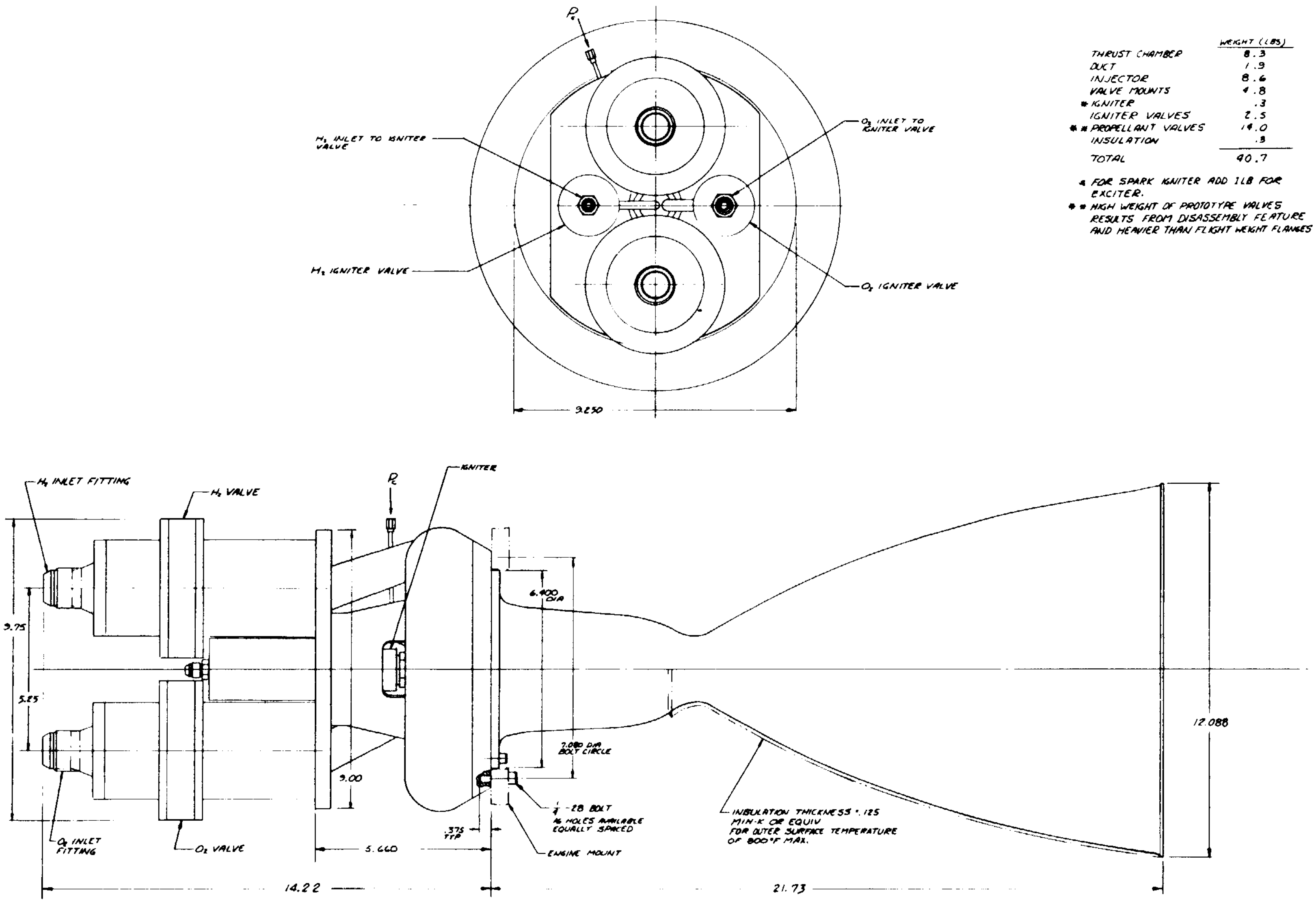

Figure 59. Overall Experimental TCA, With the Experimental Weights Included.

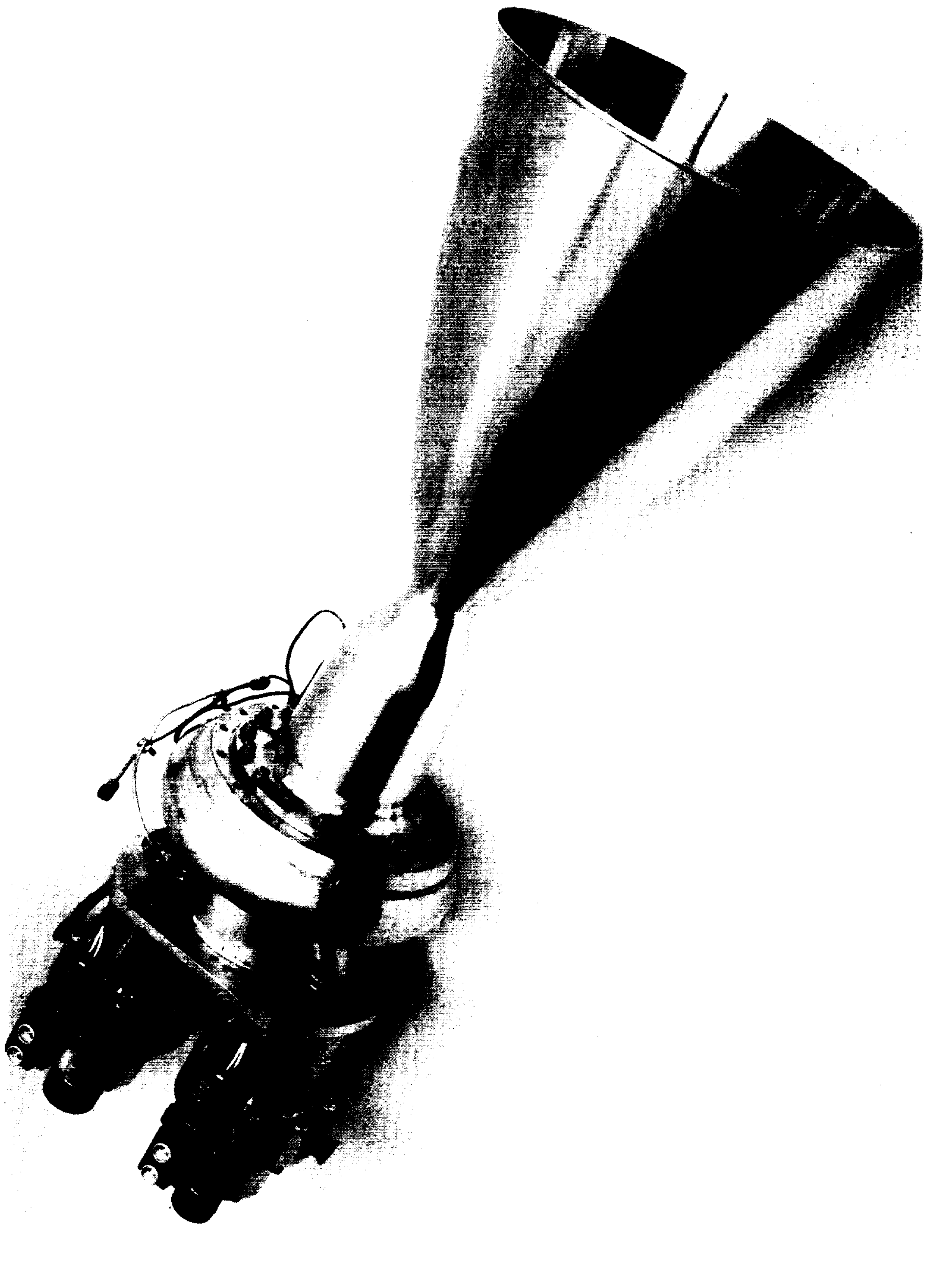

Table 8. Thruster Material Tradeoff Summary

	PRO	CON
A-286	• READILY FORMABLE AND WELDABLE • NOT SENSITIVE TO O_2, H_2 • RESISTANT TO CORROSION • EXCELLENT MECH. PROP. TO 1350°F(1005.64°K) FTY 60 KSI (413.7 KN/m^2) • READILY AVAILABLE IN BAR, SHEET, WIRE, PLATE • THERMAL-PHYSICAL PROPERTIES EXTENSIVELY STUDIED • CONSIDERABLE CASE STUDY INFORMATION	• STRENGTH IS REDUCED WITH USE ABOVE 1350°F (1005.64°K) • THERMAL CONDUCTIVITY IS ONLY FAIR
L-605	• READILY FORMABLE AND WELDABLE • RESISTANT TO CORROSION • GOOD HIGH TEMP. PROP. 30 KSI (206.85 KN/m^2) AT 1350°F(1005.64°K) • READILY AVAILABLE IN SHEET, BAR, WIRE • THERMAL PHYSICAL PROP. WELL CHARACTERIZED • WIDE USAGE IN HIGH TEMP. STRUCTURES	• SCANT DATA ON EFFECT OF H_2 ENVIRONMENTS, PARTICULARLY IN WELDS AND HAZ • FATIGUE STRENGTH IS REDUCED IN H_2 ENVIRONMENT, NOT SENSITIVITY PROBABLY INCREASED • THERMAL CONDUCTIVITY IS ONLY FAIR
ELECTROFORMED NICKEL	• CORROSION RESISTANT • FORM COMPLEX STRUCTURES READILY • GOOD THERMAL CONDUCTIVITY • EXCELLENT DUCTILITY (IN AIR)	• POOR HIGH TEMP. STRENGTH 5 KSI (34.48 KN/m^2) AT 1350°F (1005.64°K) • SENSITIVE TO H_2 ENVIRONMENT • PROCESS SENSITIVE, WIDE SPREAD IN MECH. PROPERTIES • LITTLE HISTORICAL DATA IN CRITICAL APPLICATIONS
TD NICKEL	• CORROSION RESISTANT • GOOD HIGH TEMP. PROP. 32 KSI (220.64 KN/m^2) AT 1350°F (1005.64°K) • GOOD THERMAL CONDUCTIVITY • APPEARS INSENSITIVE TO H_2	• PROPERTIES AND USAGE NOT WELL CHARACTERIZED • LIMITED AVAILABILITY • JOINING PROBLEMS

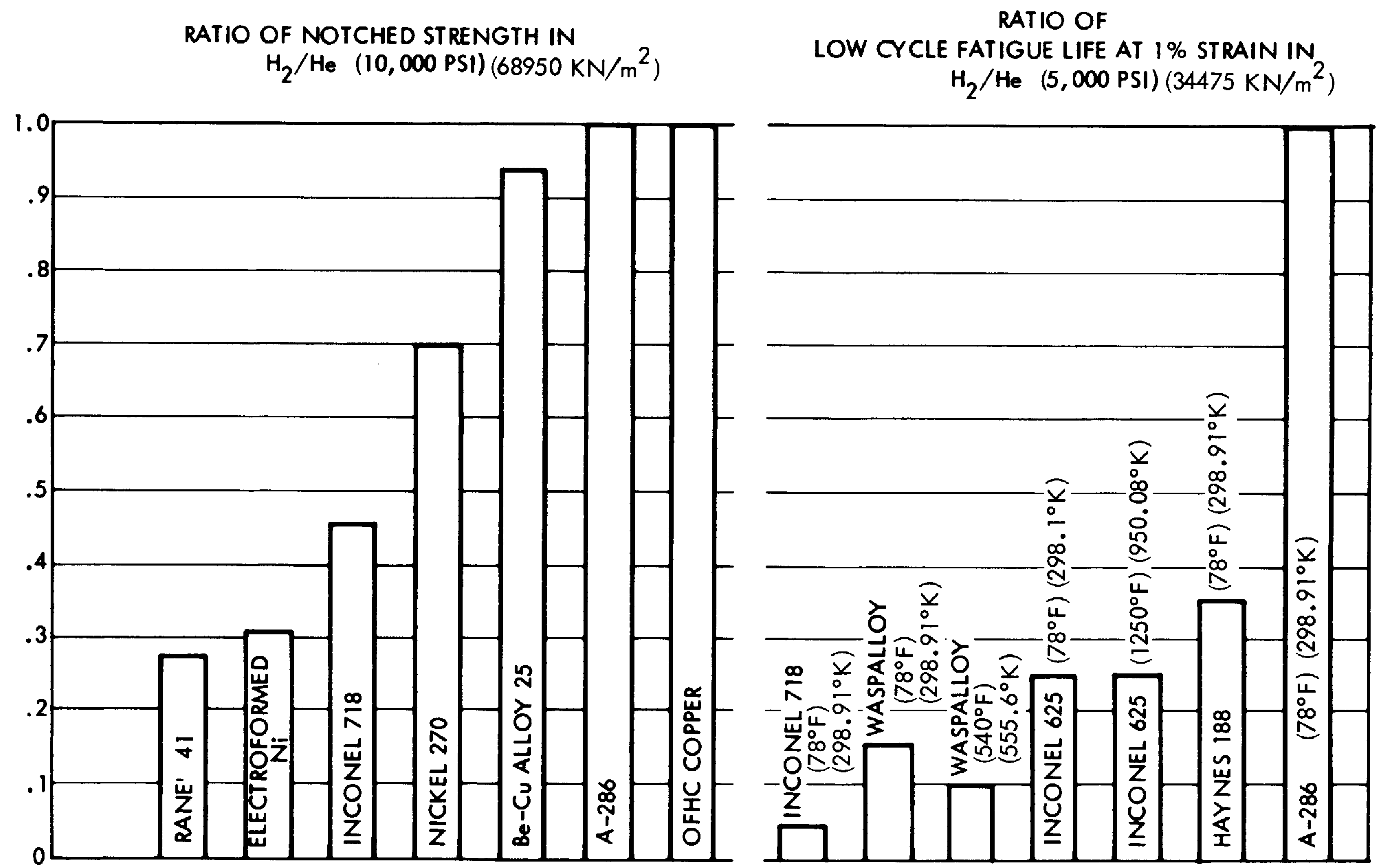

Figure 61. Effect of Hydrogen on Selected Properties of Some Candidate Thruster Materials

3.5.8 Low Pressure Thruster Design

The low pressure thruster design cross-section is included here for reference purposes. It is shown in Figure 62.

3.6 THRUSTER/SYSTEM INTERACTION ANALYSIS

Analysis of the pulse mode operation of the 1500 lbf (6672 N) thrusters was performed for each set of operating conditions previously specified in Table 1. The minimum impulse bit (MIB) capability of the complete thruster/igniter assembly (including igniter-only operation) was determined analytically, and the environmental effects on MIB and steady-state performance were also evaluated, as described in the following sections.

3.6.1 Thruster/Igniter MIB Analysis

MIB analyses were conducted using lumped parameter dynamic computer models developed to simulate flow rates, pressures, and propellant reactions throughout the actual thruster, igniter, and propellant feed system volumes. Comparison of these model outputs with test firing data has shown good correlation.

Figure 63 presents typical computer data comparing igniter-only and full thruster pulse-mode operation. Response times of 10 milliseconds for the igniter valves and 25 milliseconds for thruster valves were selected for this particular computer run. Data from a simulated full thruster firing without and with feed systems are presented in Figures 64 and 65, respectively, indicating the increase in MIB caused by feed line volumes.

The results of the full thruster MIB analyses are summarized in Figure 66 for the high pressure, 1500 lbf (6672 N) thruster. Although propellant supply pressure and temperatures have some effect, thruster MIB is mainly a function of valve response time, as indicated in Figure 66.

Igniter-only MIB analyses are presented in Figure 67. MIB is obviously a direct function of igniter flow rate, expressed as a function of nominal overall thruster flow rate in Figure 67. Igniter valve response effects are indicated in Figure 67. The results in Figure 67 indicate that manifold volumes have little effect on MIB. Igniter-only MIB is affected mainly by valve response time and, of course, by igniter flow rate.

MIB analyses were also performed for the 1500 lbf (6672 N), 15 psia (103 kN/m^2) thruster. Design and analysis only were conducted for this thruster; no hardware fabrication or testing was performed during this program.

The results of the MIB analyses for the high thrust, low Pc thruster are summarized in Figure 68. Again, one of the major factors affecting thruster and igniter MIB is valve response time, as shown in Figure 68.

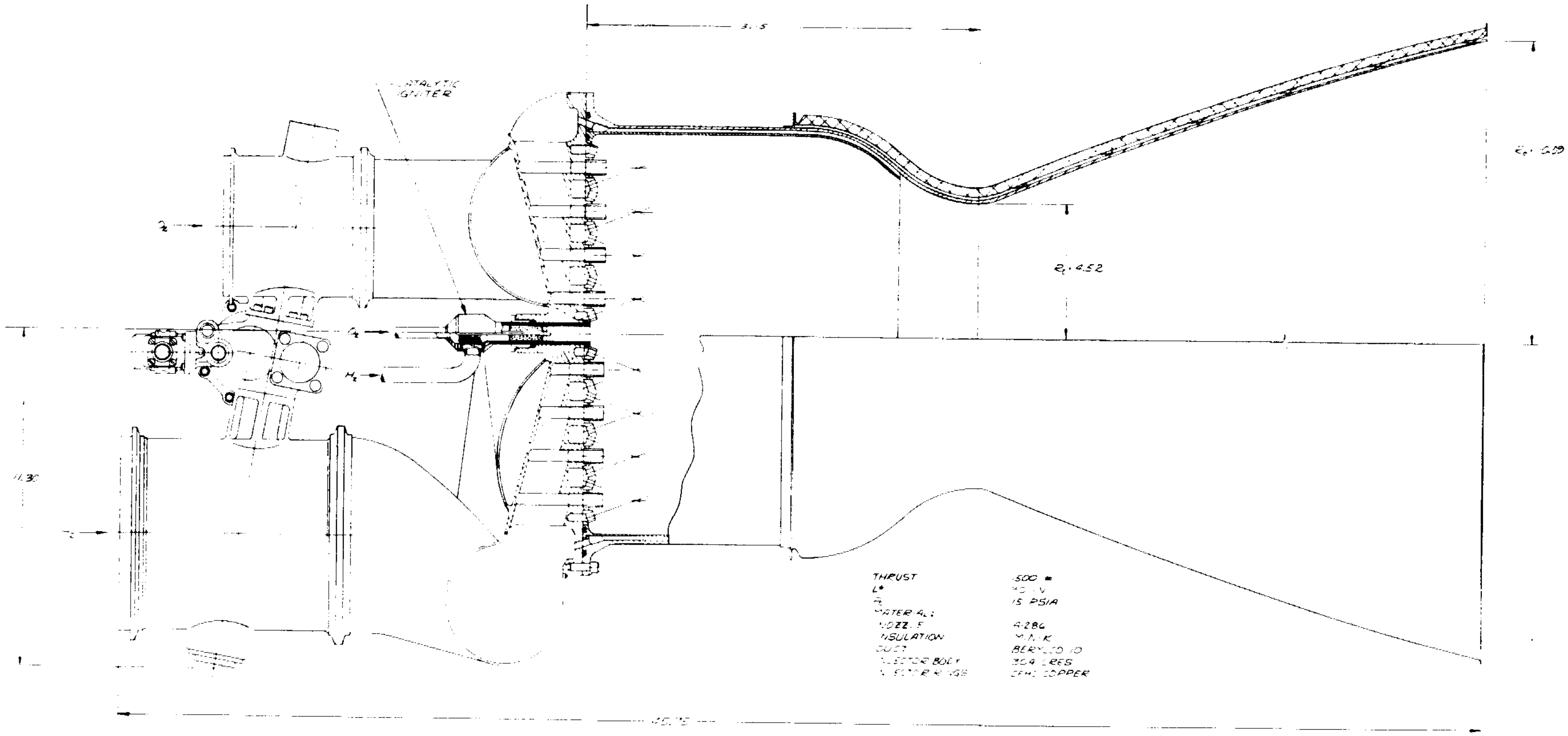

Figure 62. Low Chamber Pressure Thruster Design

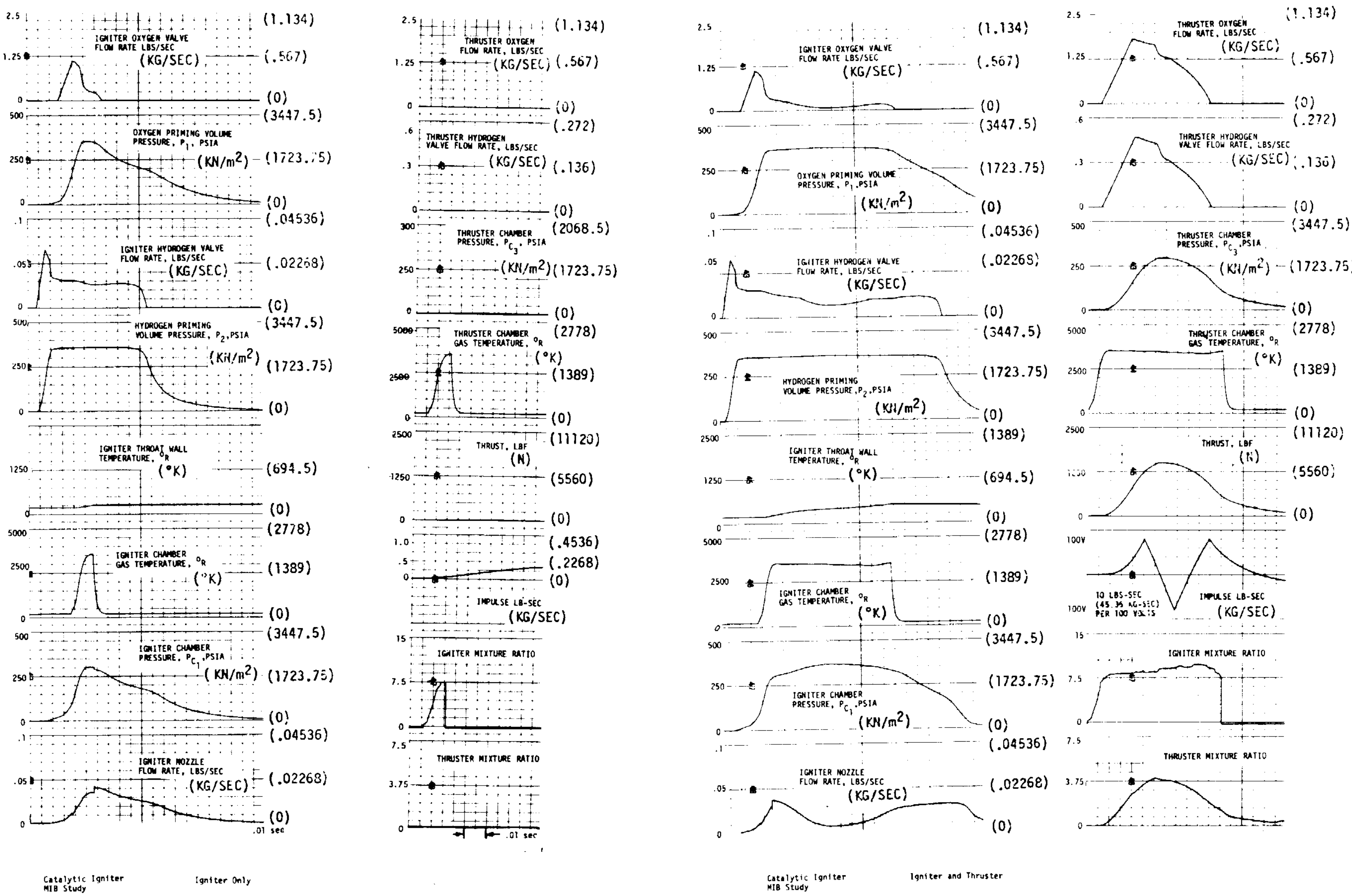

Figure 63. Computer MIB Prediction - Igniter-Only Operation Compared to Full Thruster

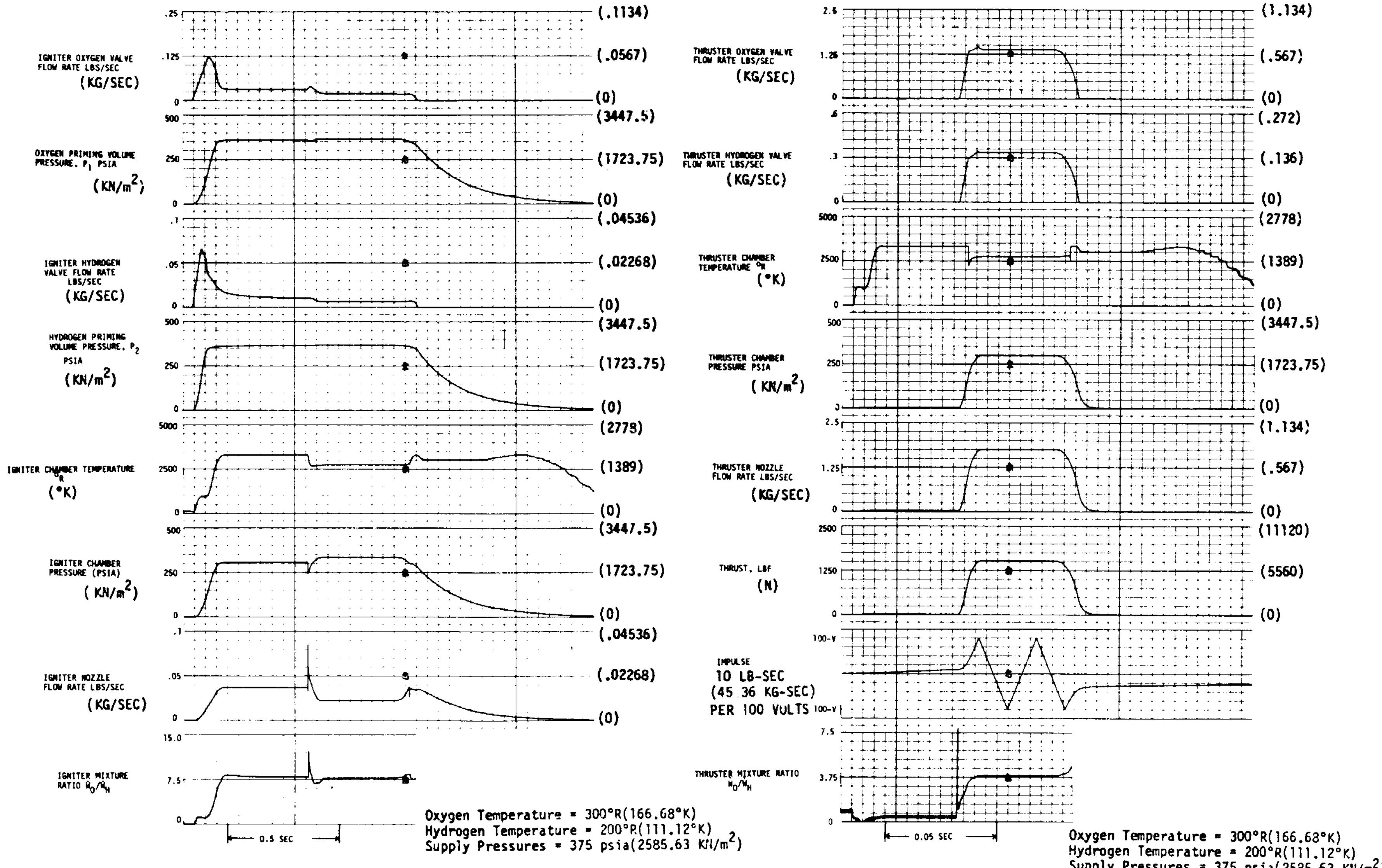

Figure 64. Computer MIB Prediction Data - Long Pulse Without Feed Line

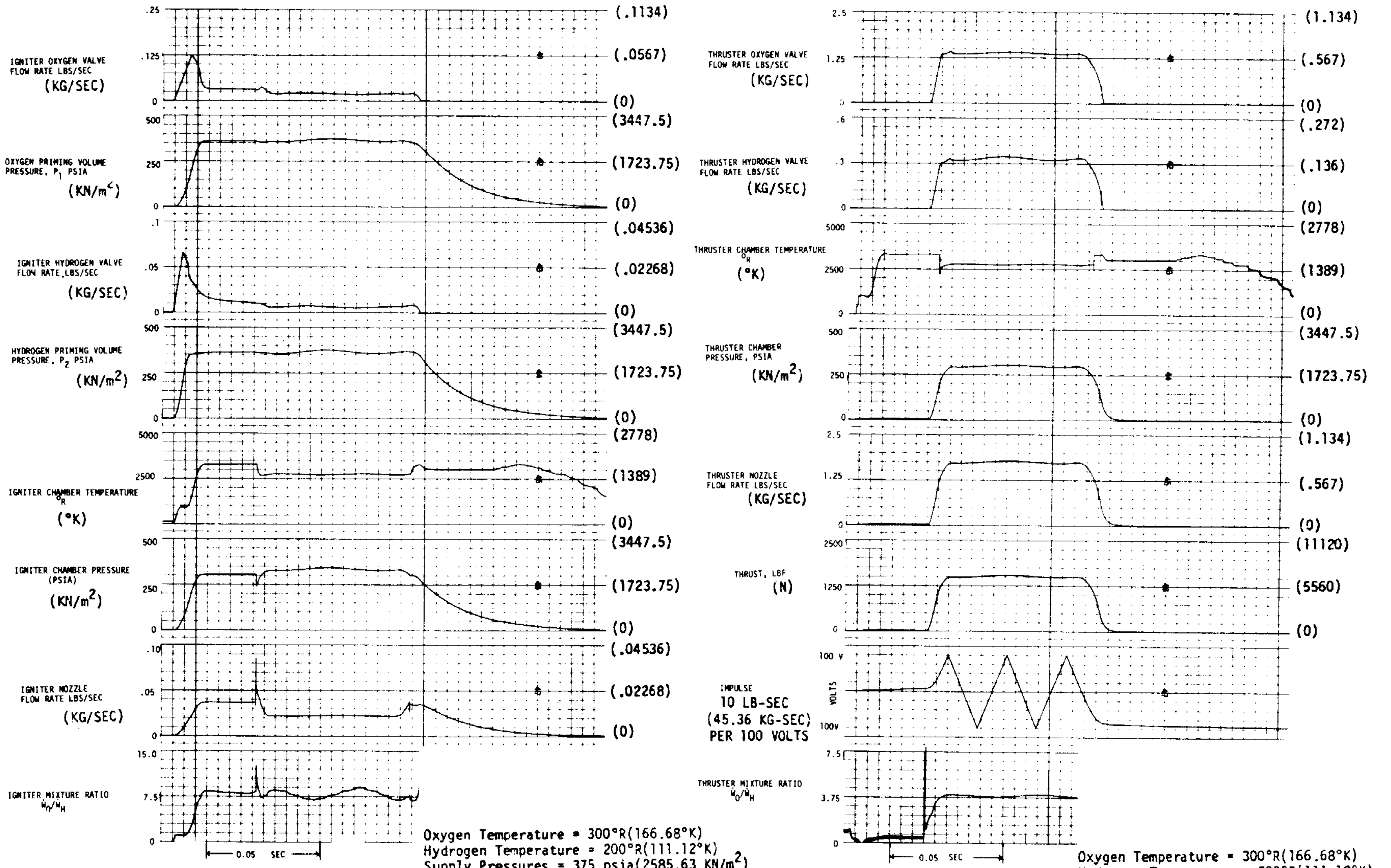

Figure 65. Computer MIB Prediction Data - Long Pulse with Feed Line

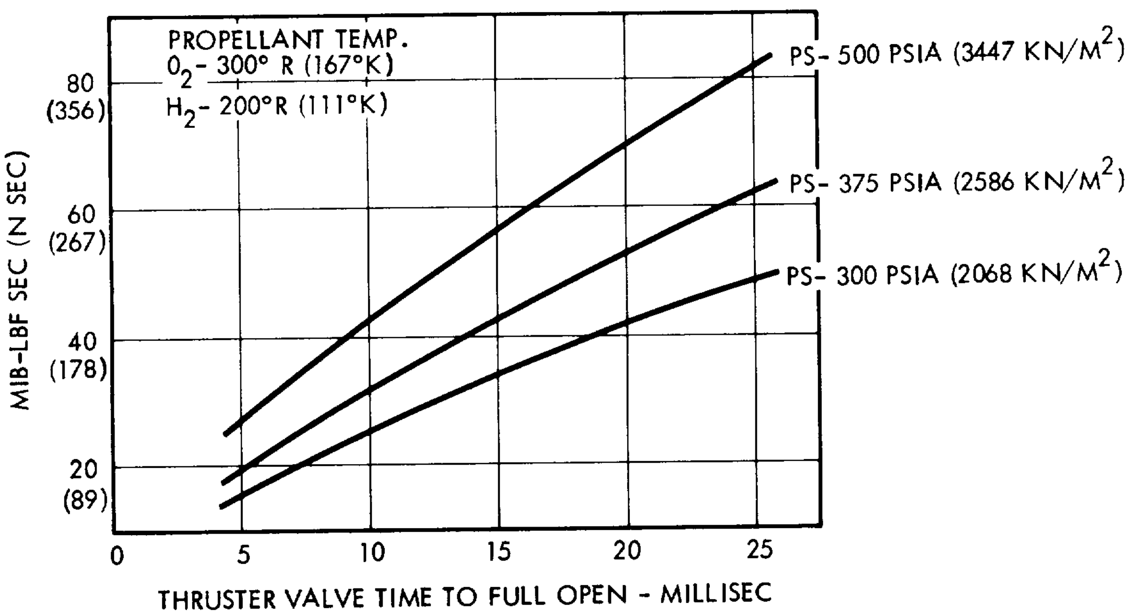

(a) THRUSTER MIB VERSUS VALVE RESPONSE AND SUPPLY PRESSURE

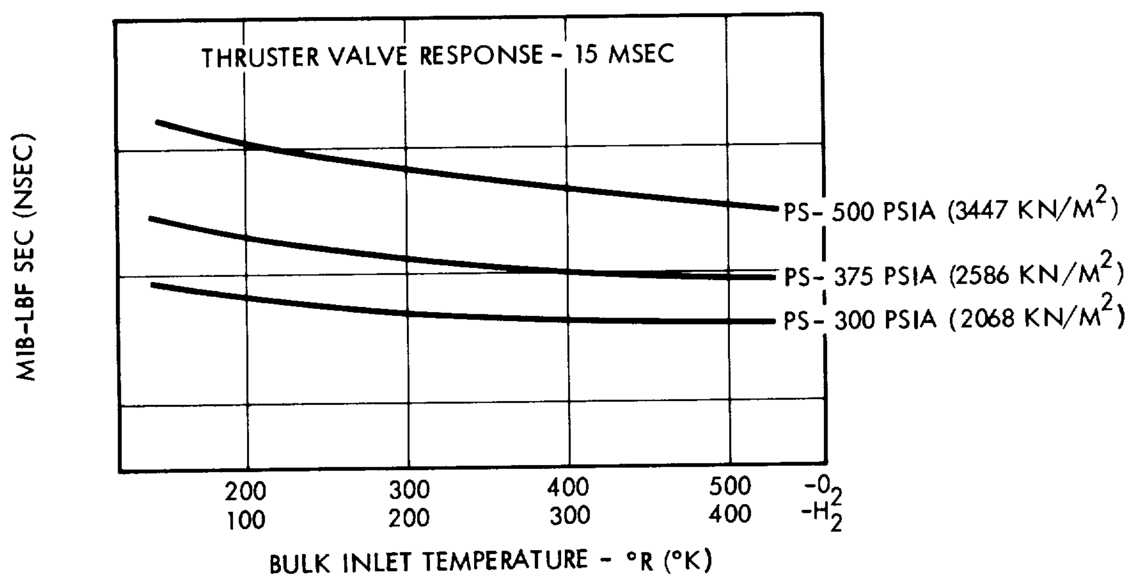

(b) THRUSTER MIB VERSUS PROPELLANT TEMPERATURE AND SUPPLY PRESSURE

Figure 66. Thruster MIB Analysis - High Pc

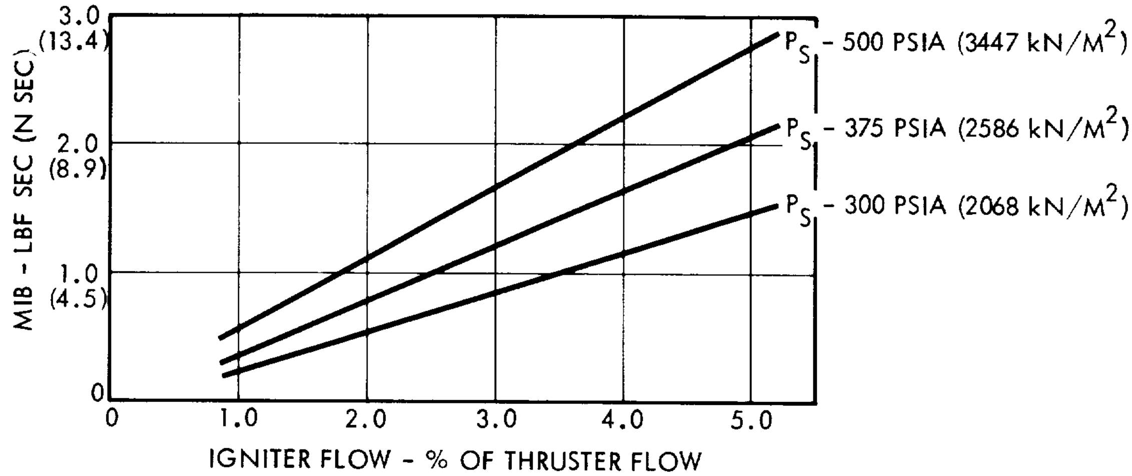

(a) IGNITER MIB VERSUS FLOW RATE AND SUPPLY PRESSURE

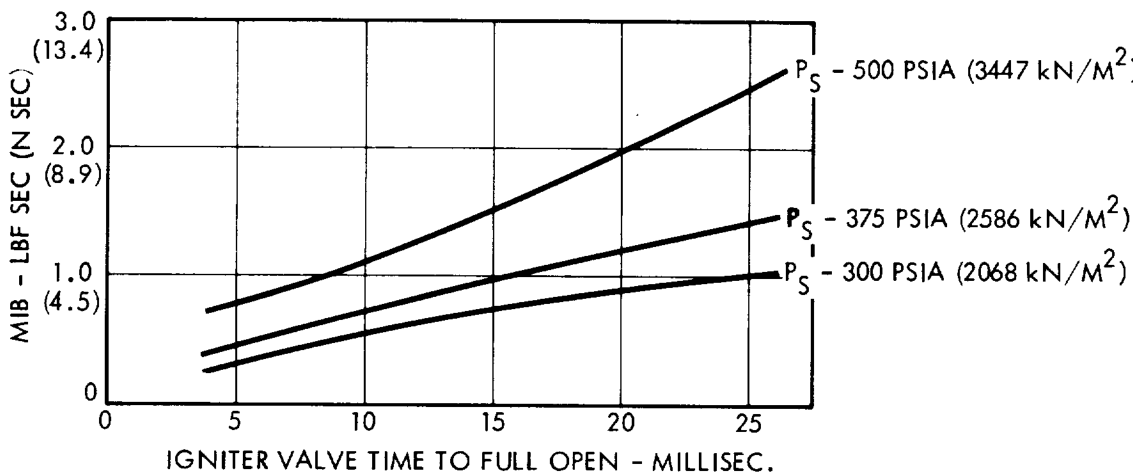

(b) IGNITER MIB VERSUS VALVE RESPONSE AND SUPPLY PRESSURE

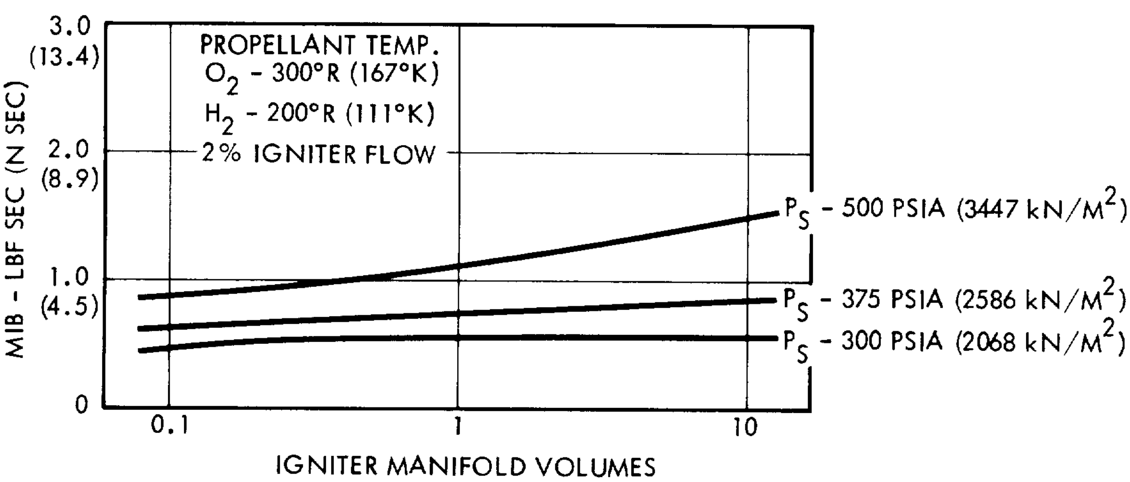

(c) IGNITOR MIB VERSUS MANIFOLD VOLUMES AND SUPPLY PRESSURE

Figure 67. Igniter-Only MIB Analysis - High Pc

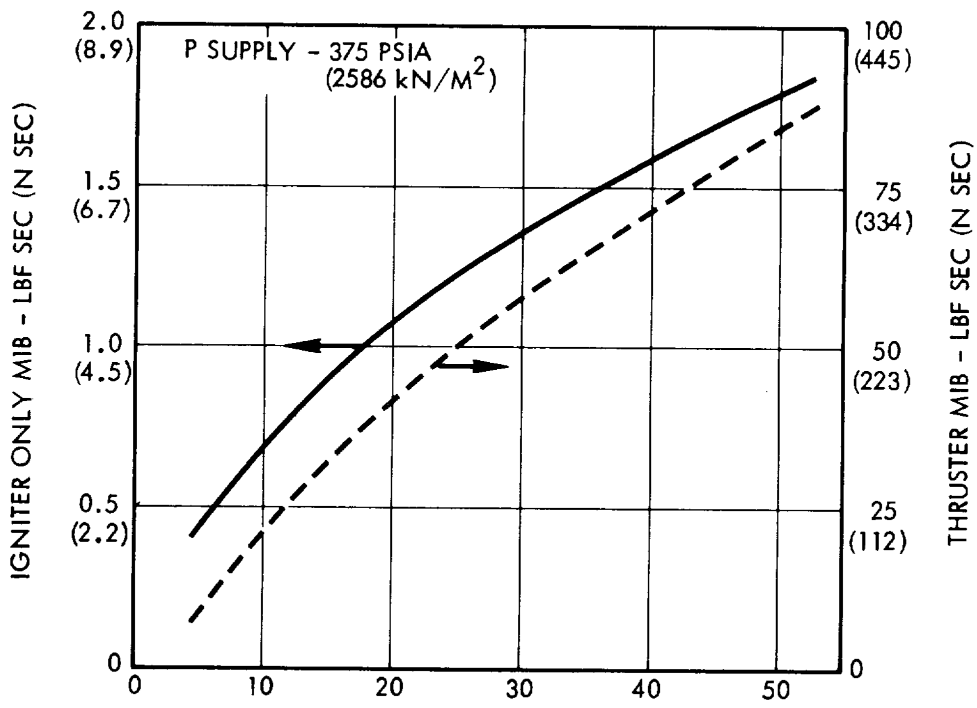

(a) THRUSTER AND IGNITER MIB VERSUS VALVE RESPONSE

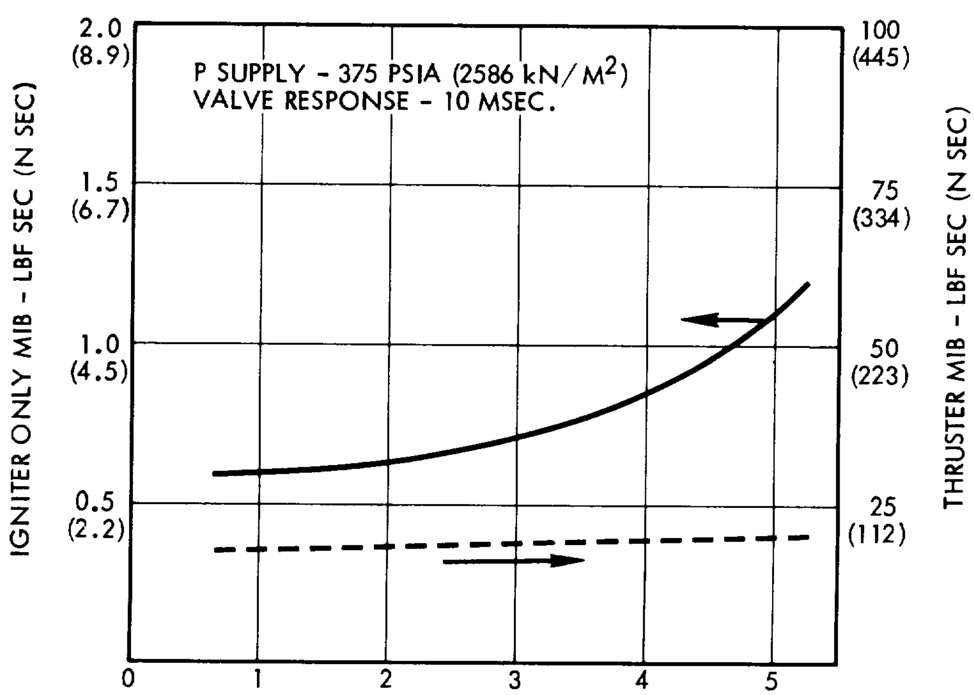

(b) THRUSTER AND IGNITER MIB VERSUS IGNITER FLOW RATE

Figure 68. Thruster/Igniter MIB Analysis - Low Pc

Figure 68 indicates that igniter flow rates have a significant effect on igniter-only MIB but have a negligible effect on MIB if the full thruster is fired, as expected.

The overall thruster/igniter MIB analysis results indicate that thruster or igniter MIB is largely a function of valve response time. Extremely low MIB values for thrusters of this size (less than 1.0 lbf sec [4.448 N/sec]) were shown to be attainable by firing the igniter only. These MIB predictions were later verified by full thruster and igniter-only test firings, as described in Section 4.

4. HIGH PRESSURE THRUSTER EVALUATION TESTS

4. HIGH PRESSURE THRUSTER EVALUATION TESTS

The following test series were conducted.

- Injector performance tests with a copper heat sink chamber, with no duct installed, at sea level conditions to document core c* performance and heat transfer to the chamber walls over the mixture ratio range with ambient temperature propellants.

- Combustion performance tests with a duct cooled stainless steel chamber at sea level conditions to document c* performance at different duct flow levels over the mixture ratio range.

- Altitude tests with ambient temperature propellants and with cold propellants to document specific impulse performance and thrust chamber temperatures at different duct cooling flow levels over the mixture ratio range.

- Pulse mode tests to document minimum impulse bit performance and duct cooling characteristics.

- Igniter-only tests to document minimum impulse bit performance and cooling requirements.

Test description and test results are presented in the following sections.

4.1 PERFORMANCE TESTS

4.1.1 Injector Performance and Uncooled Thrust Chamber Heat Flux Determination

4.1.1.1 Test Description

Tests were conducted in the TRW Vertical Engine Test Stand VA1, which was used for both sea level and altitude tests (Figure 69). The engine installation with the heat sink chamber is shown in Figure 70. Engine instrumentation is shown in Figure 71. The primary flow measurement consisted of sonic orifices, with close coupled upstream pressure and temperature measurement. The sonic orifices were calibrated in the test stand using an NBS calibrated Quantum Dynamics flowmeter with the pressure and temperature instrumentation used for the engine tests. Heat flux was determined using temperature measurement of the external surface of thermal isolation plugs. Heat flux measurement location and Photocon installation location are indicated in Figure 72. Igniter flow and main propellant flow were controlled by Circle Seal valves and Flowdyne valves, respectively. A photograph of the valves mounted on the injector is presented in Figure 73. A spark igniter installation, used for the injector performance tests, is shown in the photograph. Close-up photographs of the igniter and main propellant valves are shown in Figure 74.

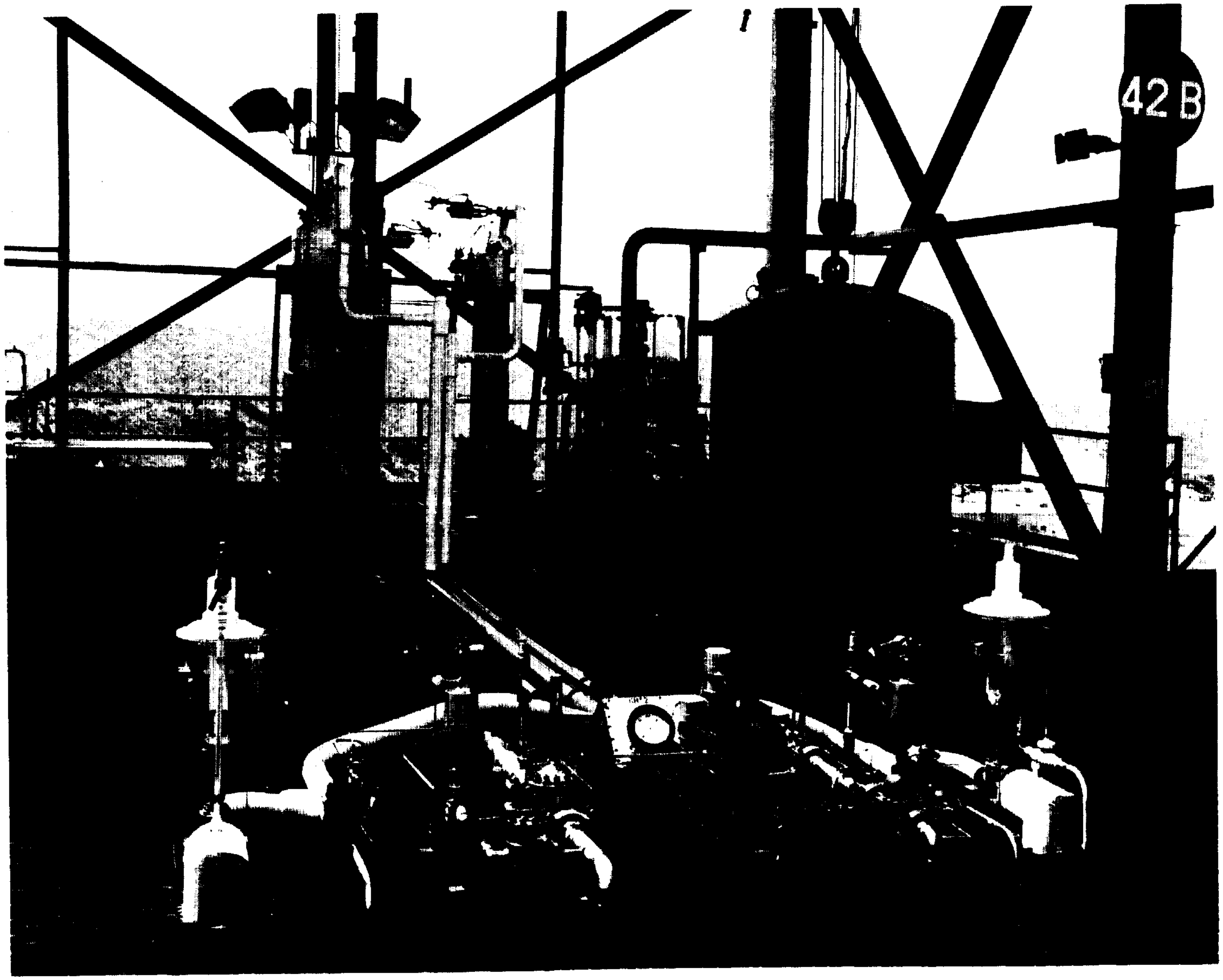

Figure 69. Overall View of High Thrust Engine Stand

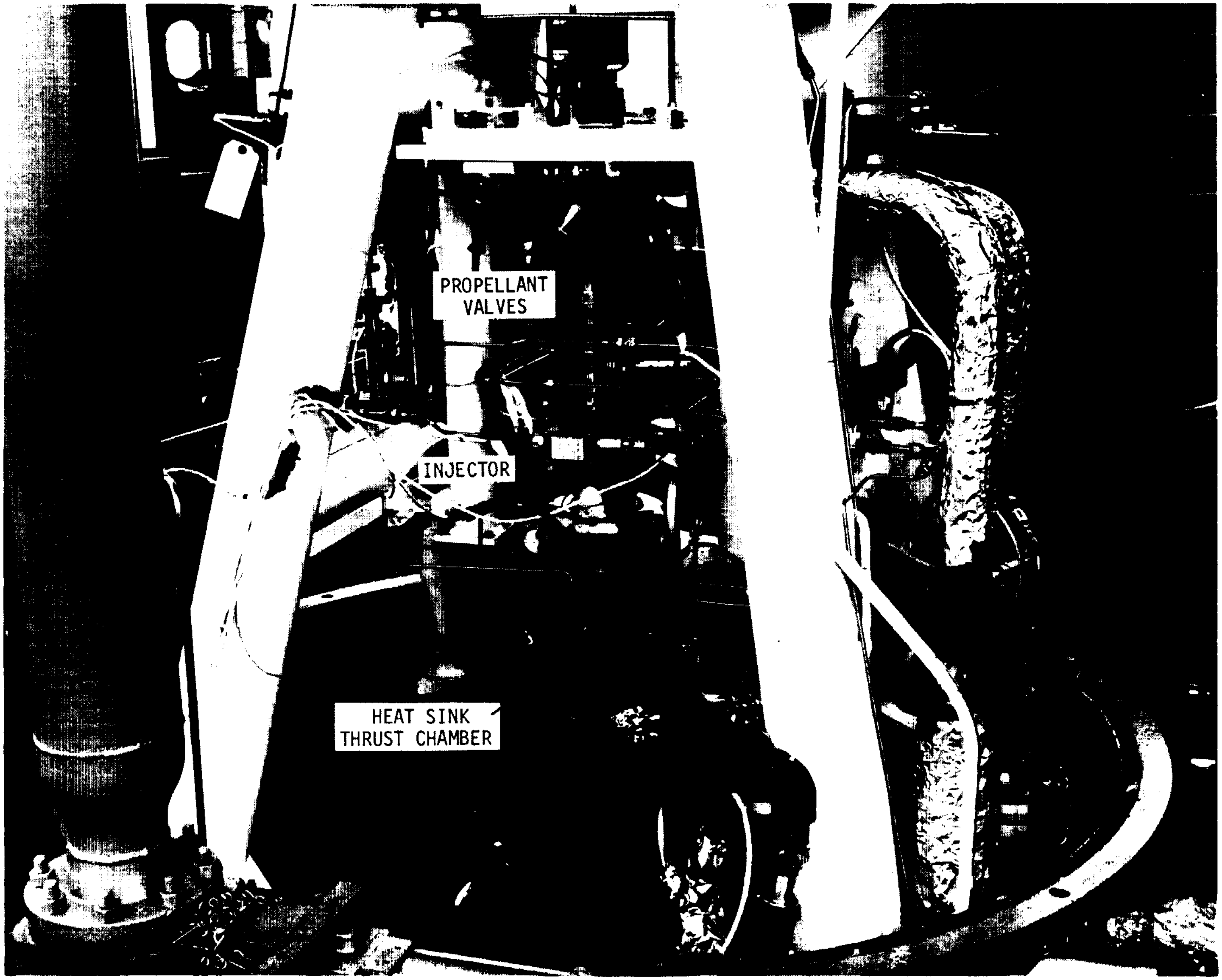

Figure 70. Test Installation of Heat Sink Thrust Chamber

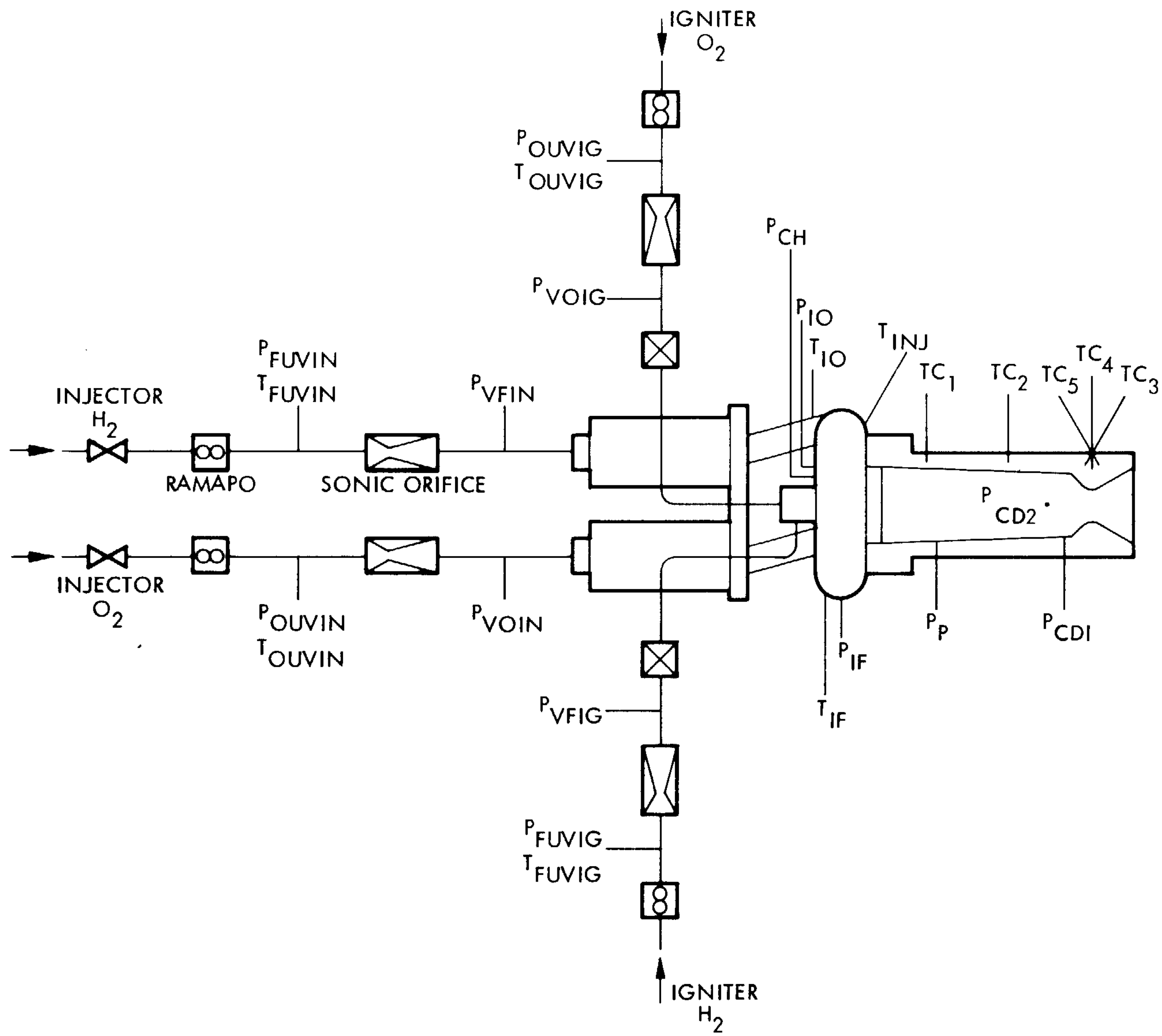

Figure 71. Instrumentation Location - Heat Sink Chamber Tests

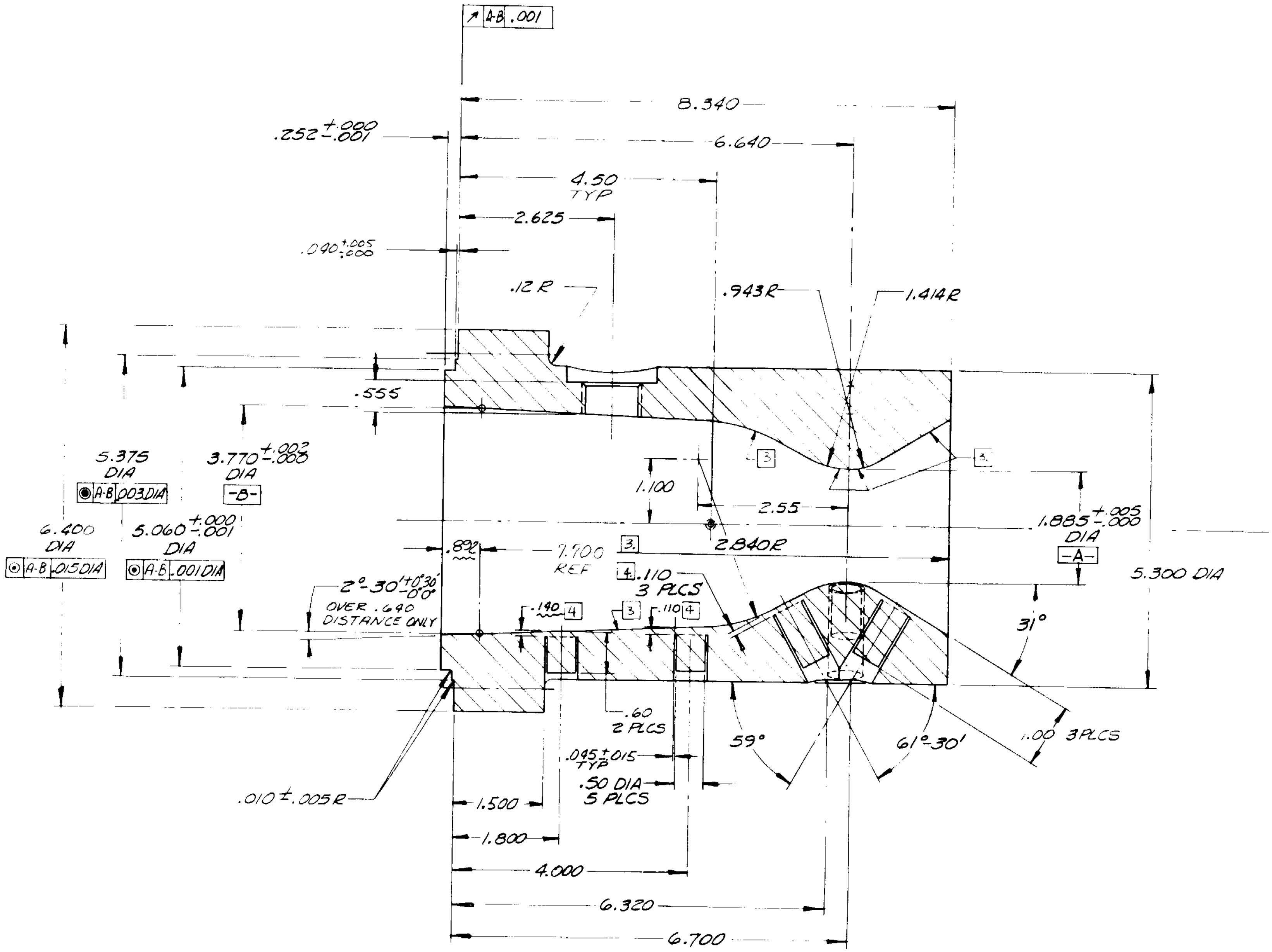

Figure 72. Heat Sink Chamber - P_c = 300 Psia

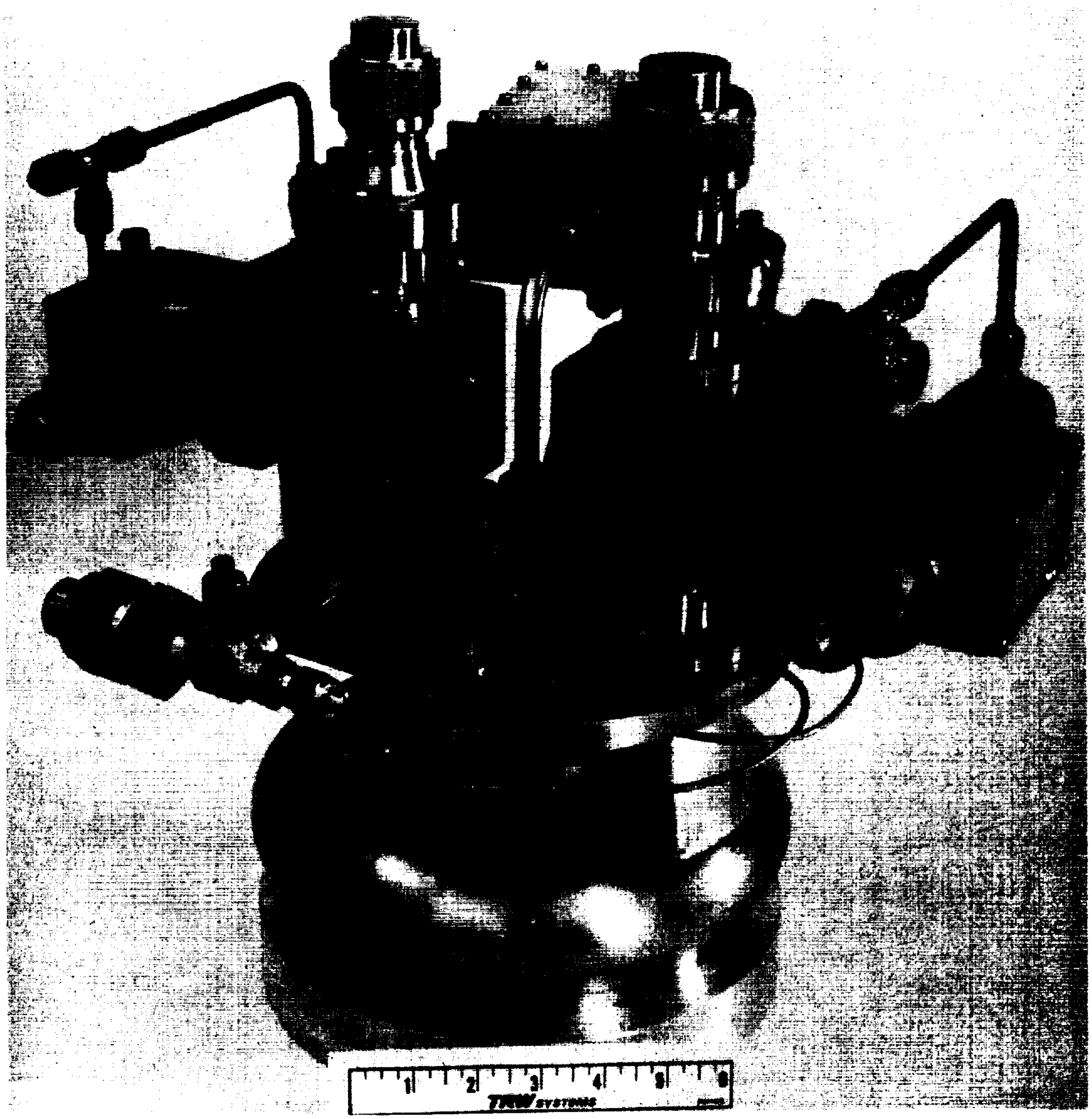

Figure 73. Head End Assembly, Electrical Ignition (TRW Supplied)

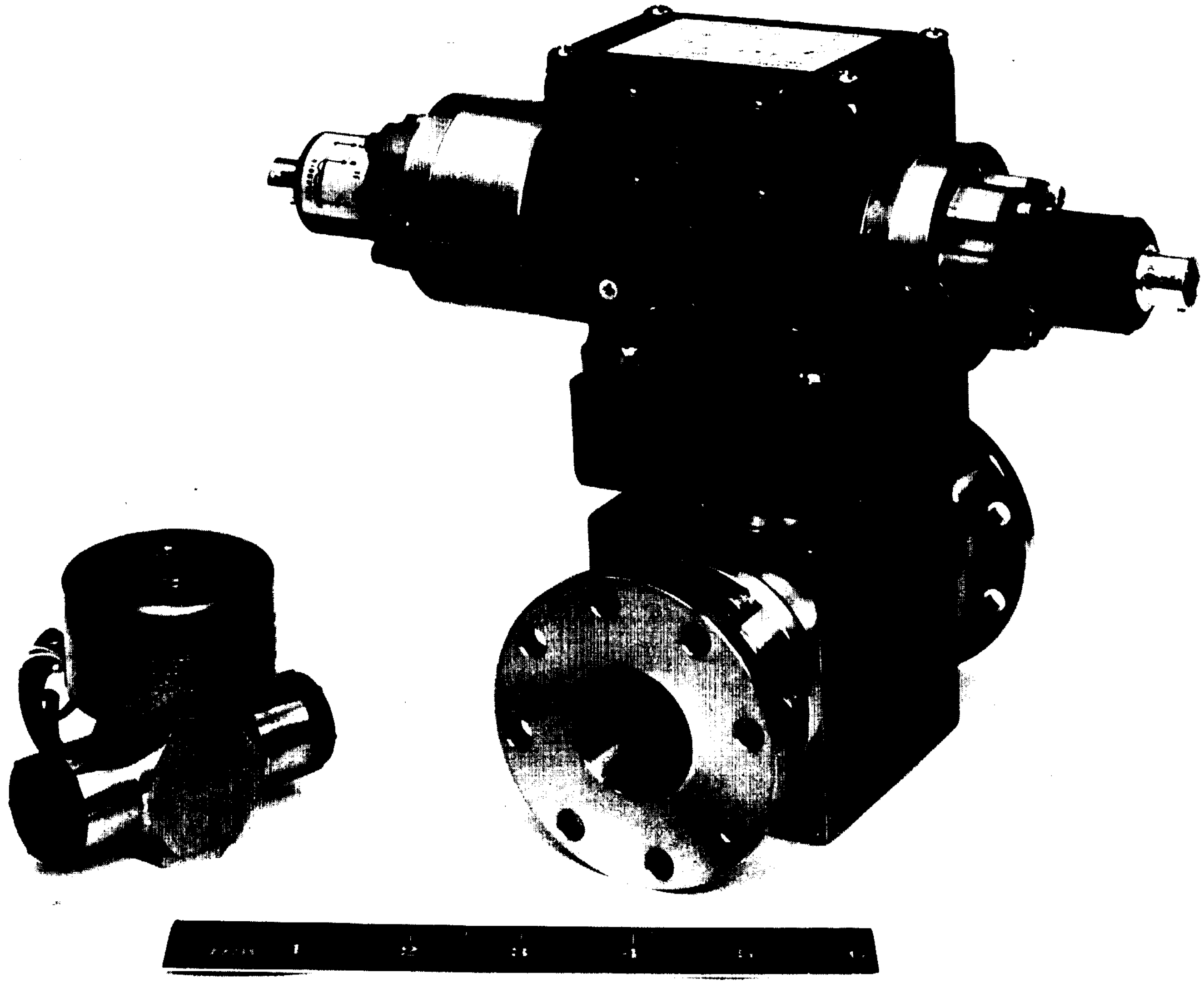

Figure 74. Flodyne and Circle Seal Valves

Prior to the hot firing tests the injector was water flowed to determine if internal manifolding was free of burrs, chips or braze material. A photograph of the water flow indicating the uniformity of the flow pattern is presented in Figure 75.

4.1.1.2 Test Summary

A summary of the performance data is presented in Table 9. Core mixture ratio was varied from 3.8 to 6.0 which would correspond to an overall mixture ratio of 2.9 to 4.5 with 25 percent duct cooling flow. Corrected core c* efficiency is essentially 100 percent over the mixture ratio range (Figure 76). (The calculation procedure is presented in Appendix A.) The chamber heat flux determined from the temperature measurements was consistent with chamber design values (Figure 77). The igniter flow was approximately 2 percent of the total propellant flow. A hydrogen flow of approximately 5 percent of the total hydrogen flow was injected along the chamber walls.

The rapid dynamic response of the thruster during start transients is indicated by the oscillograph traces presented in Figure 78. Chamber pressure overshoot was minimal as indicated by the photocon traces.

The short duration tests with the triplet injector indicated a recirculation of gas from the igniter occurred at the inner oxidizer ring. The recirculation was reduced by extending the steel sleeve of the igniter so that the tip extended 1/8 inch (.3175 cm) beyond the face (H_2 rings) of the injector. This reduced the hot gas recirculation, but the inner oxidizer ring required a clean up cut of 0.033 inches (.0838 cm) after the test series. A redesign was proven to be satisfactory in the longer firing duration test series with the duct cooled chamber, as described in the following section.

4.1.2 Cooled Thruster Performance Tests

4.1.2.1 Steady State Firings Installation

Sea level tests were conducted with a duct cooled stainless steel thrust chamber (ϵ = 12) to determine C* and thermal performance. The configuration allowed rapid visual inspection of the installed duct and injector face between firings. A photograph of the engine installation is presented in Figure 79. Flow and injector pressure instrumentation was essentially the same as for tests with the heat sink chamber. The hydrogen flow to the duct was calculated from measurement of the pressure differential across the replaceable duct flow control orifice ring. Chamber pressure was measured at the injector face.

4.1.2.2 Test Summary

The test results are summarized in Table 10. The C* efficiency is 94 to 95 percent at a ratio of duct cooling flow of 27 percent of the total hydrogen flow at a mixture ratio of 4.2 (Figure 80). The C* performance increases to 98 percent as duct flow is decreased to 16 percent of the total hydrogen flow. Once confidence had been established in the firing procedure, the catalytic igniter was substituted for the electrical igniter as indicated in Table 10.

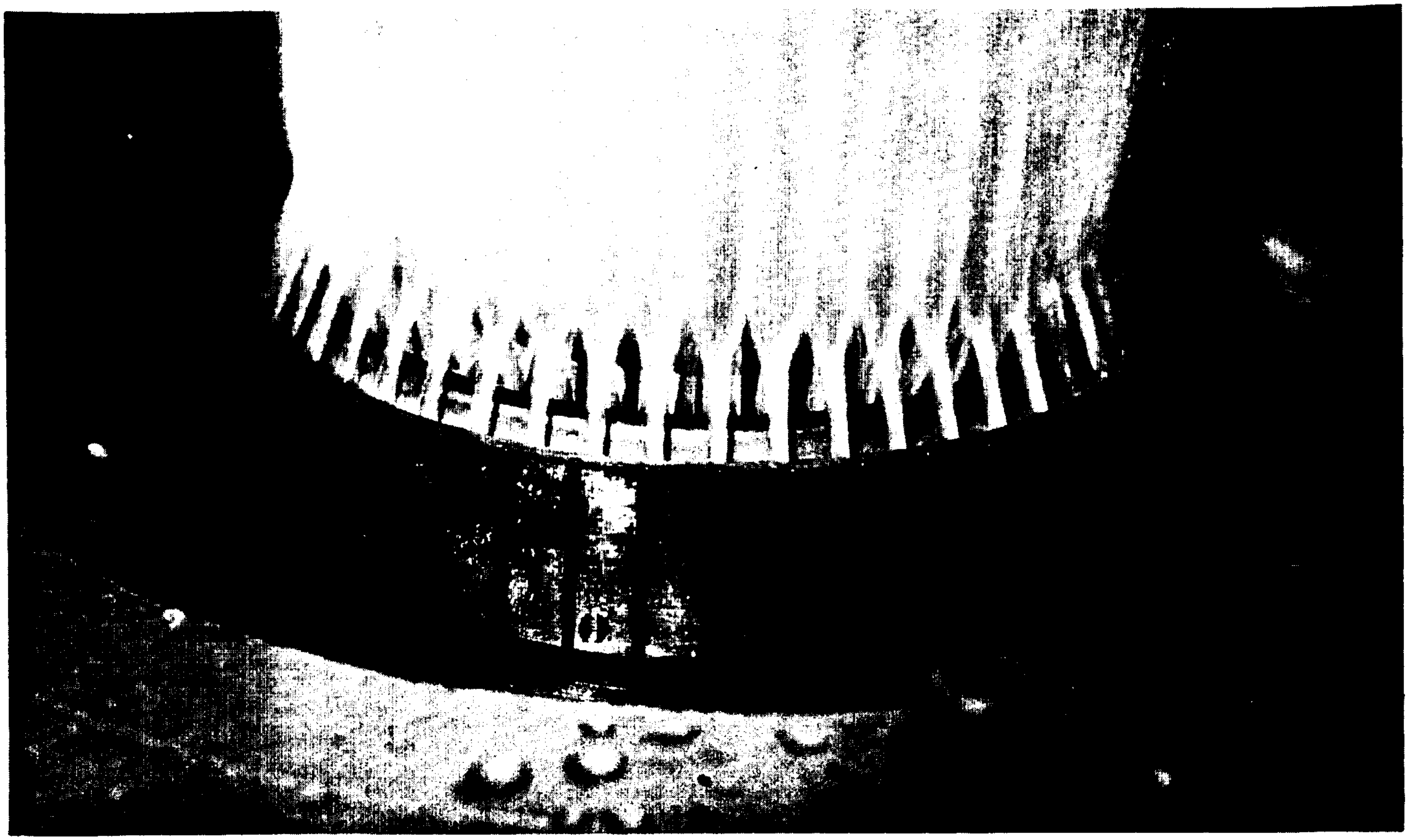

Figure 75. Water Flow of Injector - Oxidizer Side

Table 9. Triplet Injector Performance

Test No.	Test Duration (sec)	P_{CD} lb_f/in^2	P_{CD} kN/m^2	Injector Flow O_2 lb/sec	Injector Flow O_2 kg/sec	Injector Flow H_2 lb/sec	Injector Flow H_2 kg/sec	Igniter Flow O_2 lb/sec	Igniter Flow O_2 kg/sec	Igniter Flow H_2 lb/sec	Igniter Flow H_2 kg/sec	Mixture Ratio (O/F)	C^* corrected ft/sec	C^* corrected m/sec	$\eta_{c^*}P_c$ (%)	Comments
821	0.9	269.4	1857.5	2.340	1.061	.586	.266	.031	.014	.032		3.837	8145.6	2482.8	99.0	Igniter H_2 coolant recirculation burned igniter tip; extended igniter coolant tip 1/8" after Test 821
825	0.12 (1)															
826	0.35															
827	-															Firex triggered, no igniter operation because of wet stand
828	-															
829	0.7	262.3	1808.6	2.273	1.031	.524	.238	.031	.014	.032	.015	4.149	8115.7	2473.7	99.41	
830	-															Spark plug changed after Test 830
831	0.7	260.1	1793.4	2.258	1.024	.517	.235	.031	.014	.032	.015	4.173	8107.2	2471.1	99.38	
832		259.8	1791.3	2.258	1.024	.514	.233	.031	.014	.032	.015	4.190	8106.7	2470.9	99.42	
833		258.8	1784.4	2.254	1.022	.509	.231	.031	.014	.032	.015	4.228	8102.2	2469.6	99.48	
834																No digital tape
835																No digital tape
836		255.4	1761.0	2.325	1.055	.455	.206	.031	.014	.032	.015	4.839	7946.7	2422.1	99.57	
837		255.8	1763.7	2.376	1.078	.431	.196	.031	.014	.032	.015	5.203	7884.0	2403.0	100.1	
838		255.2	1759.6	2.373	1.076	.429	.195	.031	.014	.032	.015	5.214	7877.8	2401.2	100.1	
839		253.6	1748.6	2.367	1.074	.424	.192	.031	.014	.032	.015	5.258	7860.9	2396.0	100.0	
840		250.5	1727.2	2.360	1.071	.415	.188	.031	.014	.032	.015	5.345	7809.0	2380.2	99.7	
841		252.4	1740.3	2.422	1.099	.402	.182	.032	.015	.032	.015	5.652	7731.2	2356.5	99.9	
842		251.0	1730.6	2.418	1.097	.397	.180	.032	.015	.032	.015	5.713	7713.1	2347.9	99.9	
843		248.2	1711.3	2.404	1.090	.388	.176	.032	.015	.032	.015	5.799	7690.1	2343.9	100.0	
844		248.2	1711.3	2.427	1.101	.380	.172	.032	.015	.032	.015	5.967	7647.8	2331.0	100.1	
845	1.0	276.4	1905.8	2.294	1.041	.582	.264	.032	.015	.032	.015	3.791	8319.6	2535.6	100.9	
846		275.6	1900.3	2.291	1.039	.578	.262	.031	.014	.032	.015	3.807	8270.1	2520.7	100.6	
847		273.1	1883.0	2.293	1.040	.565	.256	.031	.014	.032	.015	3.921	8270.8	2520.9	100.6	Recirculation at inner oxidizer ring required cleanup cut of 0.033 inch after Test 848
848		271.4	1871.3	2.292	1.040	.550	.249	.031	.014	.032	.015	3.991	8265.2	2519.2	100.8	

(1) Tests for which data are not shown did not yield reliable steady state data

Test Configuration: X408170-3 Triplet Injector (ambient temperature)
X408258 Heat Sink Chamber
Flodyne Propellant Valves
Circle Seal Igniter Valves
X408322 Spark Igniter

Propellant Temperature: 80°F (300°K)

$$\eta_{C^*} = \frac{\left(\frac{P_{CD_1} + P_{CD_2}}{2}\right) \overbrace{A_t\, g_c f_P f_{TR} f_{DIS} f_{FR} f_{HL}}^{1.0075-1.0115}}{\dot{W}\, C^*_{ODK}}$$

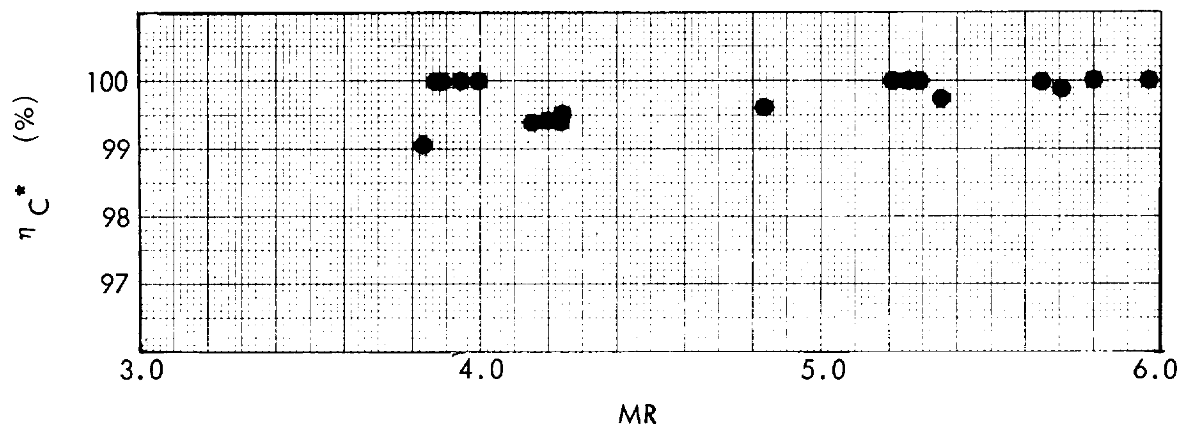

Figure 76. Triplet Injector Performance Summary

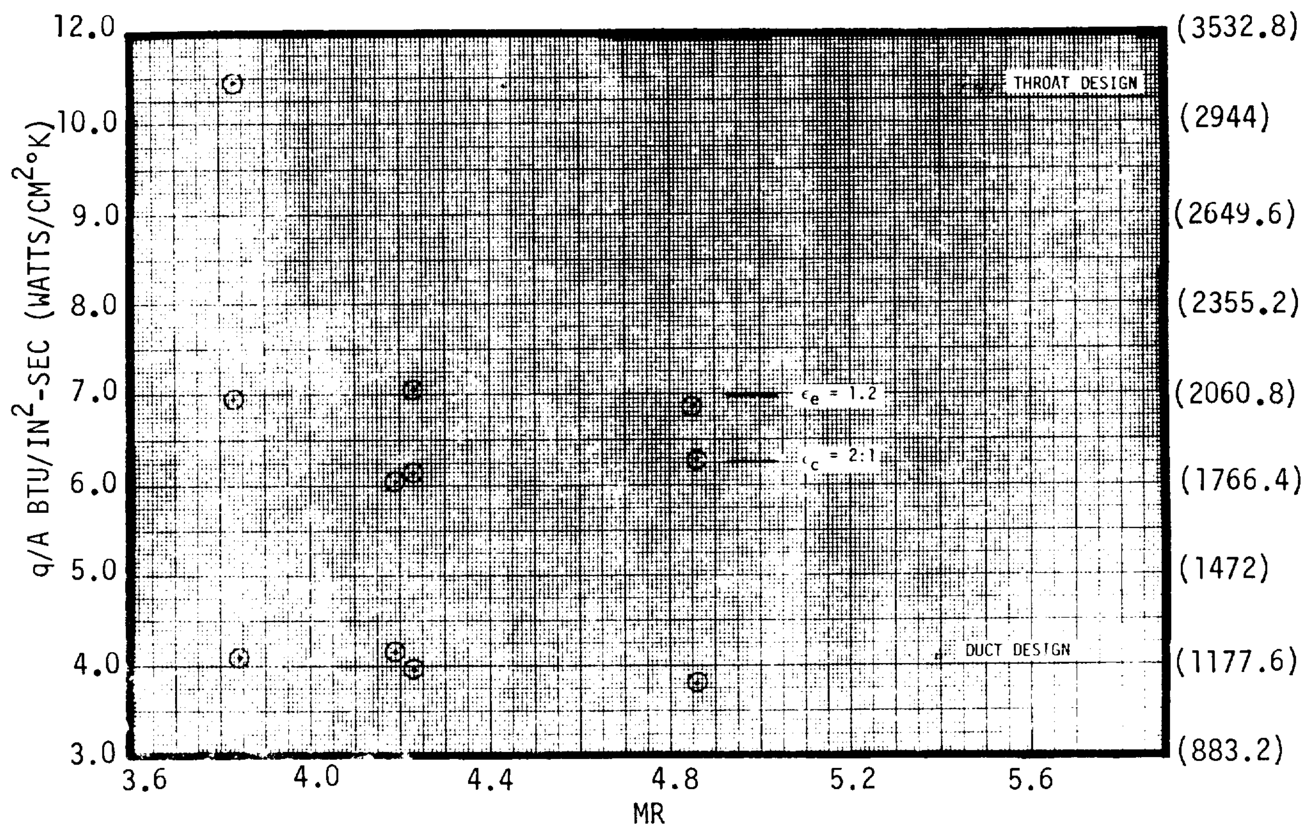

Figure 77. Preliminary Chamber Heat Flux — Triplet Injector

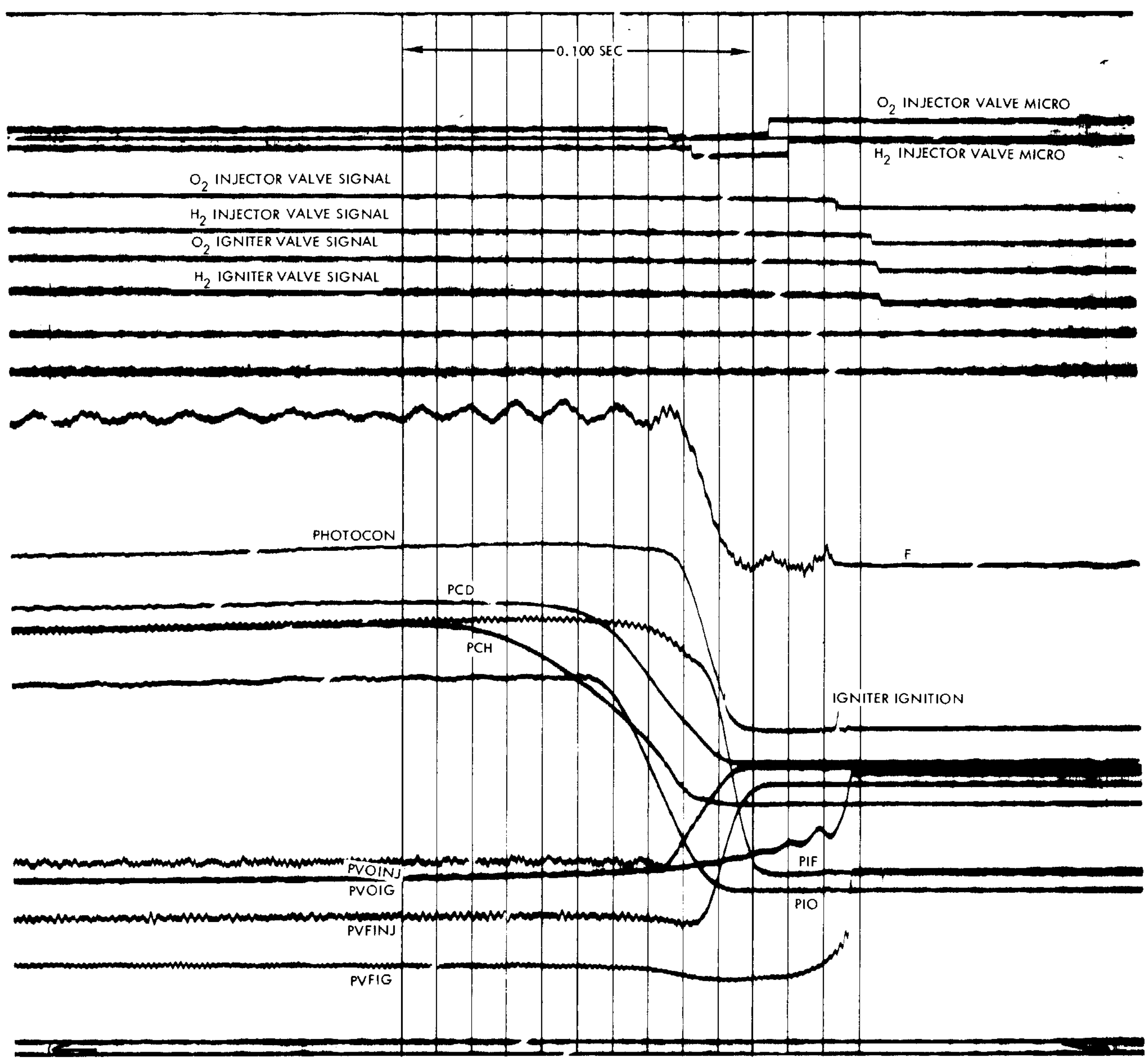

Figure 78, All Starts Were Virtually Identical

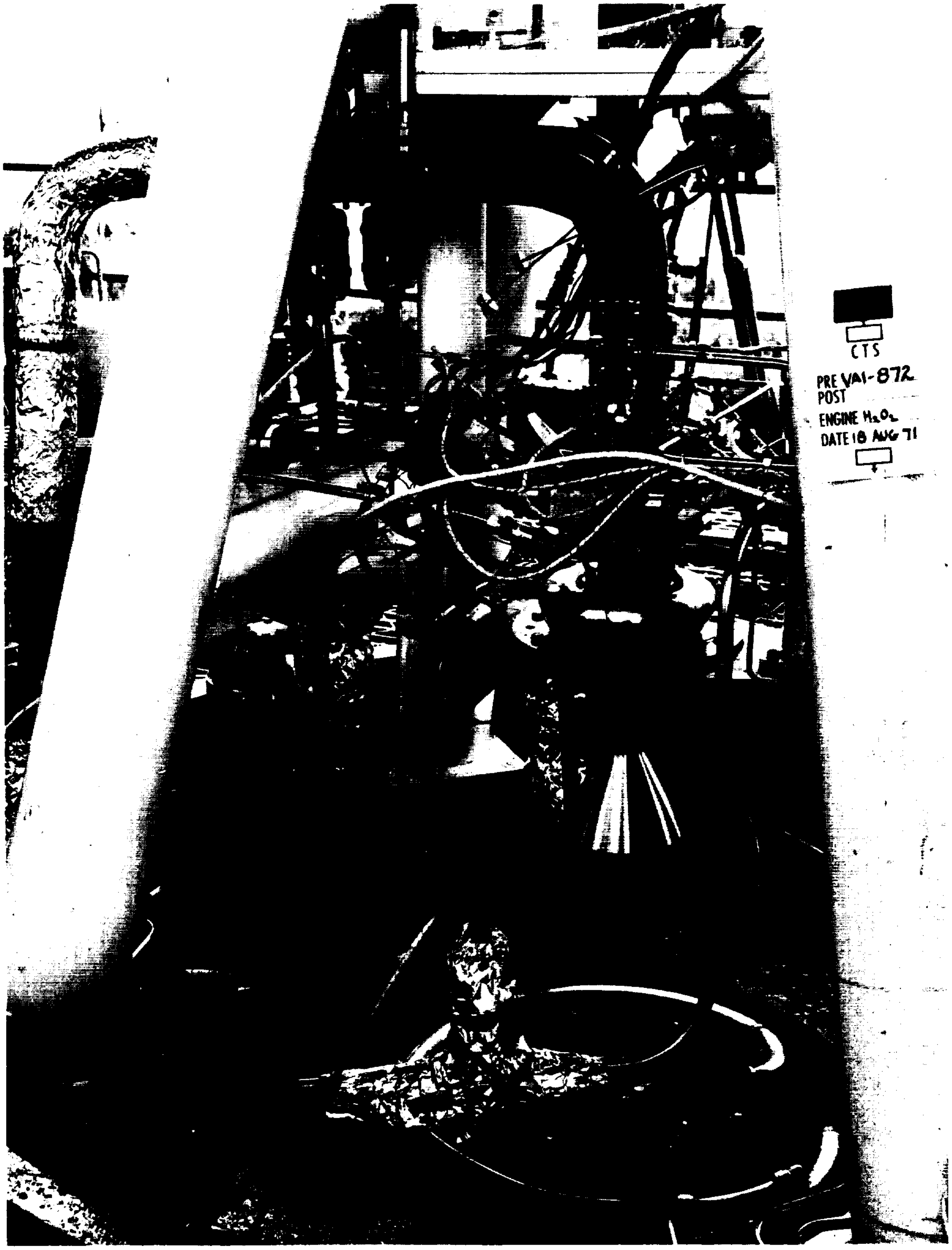

Figure 79. Duct Cooled Engine Installation with 12:1 Exit Area Nozzle

Table 10. Combustion Performance with Duct Cooled Chamber (Sea Level)

Test No.	Test[(1)] Duration (sec)	P_{CH} lb_f/sec	P_{CH} kN/m^2	Injector Flow O_2 lb/sec	Injector Flow O_2 kg/sec	Injector Flow H_2[(2)] lb/sec	Injector Flow H_2[(2)] kg/sec	Igniter Flow O_2 lb/sec	Igniter Flow O_2 kg/sec	Igniter Flow H_2 lb/sec	Igniter Flow H_2 kg/sec	Duct Coolant $\frac{W_{DC}}{W_{H_2}}$ X100	MR (O/F)	c^* (Overall) ft/sec	c^* (Overall) m/sec	η_{c^*} (Overall) (%)	Inj	Duct	Ign	Duct Flow Control Orifice Dia. in. (cm)	Comments
871	0.15											16					-3	-1(CU)	Spark	0.096 (0.244)	
872	0.50	277.9	1916.1	2.160	0.980	0.789	0.354	0.031	0.014	0.032	0.015		2.700	8288.3	2526.3	98.9					
873	1.0	284.0	1958.2	2.198	0.997	0.786	0.356	0.031	0.014	0.032	0.015		2.726	8343.9	2543.2	99.6					Copper duct collapsed on shutdown, repaired for Test 880
880	0.15																				
881	0.50																				
882	1.0	276.0	1903.0	2.336	1.060	0.631	0.286	0.031	0.014	0.031	0.014		3.575	8158.2	2486.6	98.5					
883	1.5	277.7	1914.7	2.372	1.076	0.625	0.284	0.031	0.014	0.031	0.014		3.659	8126.2	2476.9	98.3					
884	2.0	277.5	1913.4	2.362	1.071	0.631	0.286	0.031		0.032	0.015		3.612	8131.3	2478.4	98.3					Copper duct collapsed on shutdown
885	0.15											20						-1(Be-10)			
886	1.0	276.3	1905.1	2.358	1.070	0.636	0.289	0.031	0.014	0.032	0.015		3.580	8092.4	2466.6	97.7					
887	2.0	277.4	1912.7	2.372	1.076	0.639	0.290	0.031	0.014	0.033	0.015		3.578	8078.4	2462.3	97.5					
888	3.0	282.8	1949.9	2.431	1.103	0.640	0.290	0.031	0.014	0.032	0.015		3.665	8078.1	2462.2	97.7					
889	4.0	281.6	1941.6	2.431	1.103	0.632	0.287	0.031	0.014	0.032	0.015		3.712	8066.1	2458.5	97.7					
937	0.2																-4	-2	Cat	0.0785 (0.199)	
938	0.2																				
939	0.5						(To Be Completed)														
940	1.0																				
950	0.15											27					-3	-1		0.125 (0.317)	
953	0.50																				
954	1.0	287.5	1982.3	2.663	1.208	0.617	0.280	0.013	0.0059	0.013	0.0059		4.245	7691.6	2344.4	94.5					
955	0.15																				
956	0.15																				
957	1.0	292.7	2018.2	2.681	1.216	0.629	0.285	0.013	0.0059	0.013	0.0059		4.194	7759.7	2365.0	95.2					
958	2.0	292.8	2018.9	2.705	1.227	0.630	0.286	0.013	0.0059	0.013	0.0059		4.224	7704.8	2348.4	94.6					
959	3.0	292.8	2018.9	2.700	1.225	0.629	0.285	0.013	0.0059	0.013	0.0059		4.221	7718.8	2352.7	94.8					
960	0.15																				
961	1.0	290.9	2005.8	2.697	1.223	0.623	0.283	0.013	0.0059	0.013	0.0059		4.261	7689.2	2343.7	94.6					
962	2.0	283.4	1954.0	2.706	1.227	0.580	0.263	0.013	0.0059	0.013	0.0059		4.580	7577.9	2309.7	94.1					
963	4.0	291.8	2012.0	2.706	1.227	0.621	0.282	0.013	0.0059	0.013	0.0059		4.289	7717.9	2352.4	94.9					
964	6.0	292.0	2013.3	2.714	1.231	0.628	0.285	0.013	0.0059	0.013	0.0059		4.250	7668.2	2337.3	94.2					
968	0.15																				

(1) Tests for which data not shown did not yield reliable steady state performance data

Test Configuration: X408170 Triplet Injector (-3 ambient propellant temperature design, or -4 cold propellant temperature design, as noted)
X408169-3 Stainless Steel Chamber, A_c/A_t 12
X408163 Duct (-1 ambient propellant temperature design or -2 cold propellant temperature design, as noted)
Flodyne Propellant Valves
Circle Seal Igniter Valves
X408322 Spark Igniter or X408260 Catalytic Igniter, as noted.

(2) Includes duct flow.

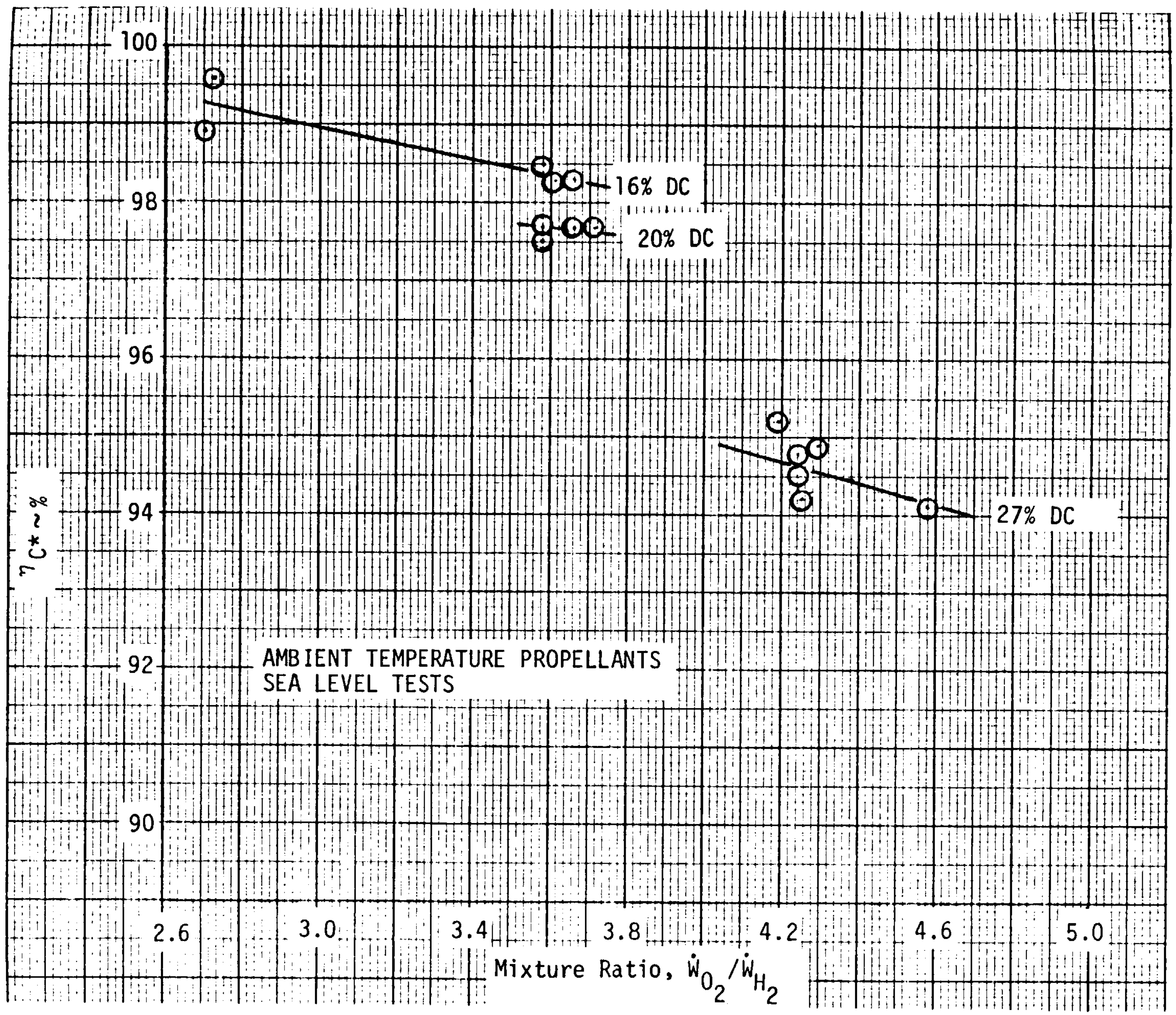

Figure 80. C* Efficiency with Duct Cooled Chamber

A duct fabricated from OFHC copper was used for the initial tests because the copper material was readily available for duct fabrication. The long lead time for delivery of the Berylco-10 material, for which the duct was designed, delayed fabrication of the design duct configuration. The much lower structural strength of the OFHC copper was evidenced by collapse of the duct during shutdown transients. The OFHC copper duct, reaching approximately 1000°F (811.18°K) within 1-2 seconds of engine operation, collapsed inwards because the chamber pressure decay was more rapid than the pressure decay in the duct. The copper duct was prepaired by rolling out the collapsed region and was used in subsequent tests. No structural problems resulting from pressure differentials were encountered with the higher strength Berylco-10 duct.

Hot gas recirculation across the face of the inner oxidizer ring during initial tests at sea level resulted in some melting in this region. The recirculation was eliminated by replacing the inner oxidizer ring with an oxidizer ring with the impingement angle, with respect to the axial H_2 orifices, reduced from 20° to 10°, setting back the face of the inner oxidizer ring by 0.050 inches (.127 cm) and decreasing the igniter flow from 2 percent to 0.8 percent.

4.1.2.3 Altitude Firing Installation

With the catalytic igniter, injector, and duct fully checked out, the testing activity turned to the altitude firings. Both ambient and reduced temperature propellants were used in their tests. A photograph of the test installation is presented in Figure 81. The thin steel wall chamber was instrumented with thermocouples fore and aft as well as three locations circumferentially.

4.1.2.4 Test Summary

The test results are summarized in Table 11. The experimentally determined specific impulse, corrected to vacuum, is 432 seconds at a mixture ratio of 4.0 with a duct coolant flow of 32 percent for ambient temperature propellants. The specific impulse and C* performance over a mixture ratio range from 3.0 to 4.8 is presented in Figure 82. The range of chamber pressures tested was limited because the initial test results at the nominal level of 300 psia (2068.5 KN/m^2) indicated that hot gas recirculation patterns were occurring at the outer rings of the injector causing higher heat transfer levels than anticipated. (The fixes described previously to the inner oxidizer ring resulted in no further overheating in this region.) During the latter tests, it was discovered that the protruding OFHC copper injection rings were imploded, resulting in some mixture ratio maldistribution. A transient negative pressure differential apparently occurred during startup across the injection rings for some of the ignition sequences which were used. Distortions of the internal flow passages may have been responsible for higher heat flux which occurred in local regions.

Numerous firings were conducted with the Berylco-10 duct with no difficulty. Figure 83 shows the duct after a 60-second firing and a total of 40 runs indicating its excellent condition. The corresponding nozzle temperature data are shown in Figure 84. All of this thermal data indicated strongly that excellent circumferential thermal control was being achieved

Figure 81. Test Installation of Altitude Thrust Chamber

Test No.	Test[1] Duration (sec)	P_C lb_f/in^2	P_C kN/m^2	Injector Flow O_2 lb/sec	Injector Flow O_2 kg/sec	Injector Flow H_2 lb/sec	Injector Flow H_2 kg/sec	Igniter F O_2 lb/sec	Igniter F O_2 kg/sec
944	0.2								
945	0.5	223.1	(1538)	1.823	(.8269)	0.576	(.261)	.0095	(.0043)
946	no ign								
947	1.0	213.9	(1474.84)	1.687	(.7652)	0.574	(.260)	.0085	(.0039)
948	no ign								
949	0.2								
950	1.0	216.5	(1492.77)	1.963	(.8904)	0.510	(.231)	.0069	(.0031)
951	1.0	201.3	(1387.96)	1.821	(.8260)	0.452	(.205)	.0076	(.0034)
965	0.15	-							
966	1.0	291.7	(2011.27)	2.728	(1.237)			0.013	(.0059)
967	6.0	295.0	(2034.03)	2.742	(1.244)	0.640	(.290)		
969	1.0								
970	6.0	291.1	(2007.13)	2.771	(1.257)	0.638	(.289)		
971	0.15								
972	0.15								
974	2.0	286.0	(1971.97)	2.644	(1.199)	0.635	(.288)		
975	1.0	277.1	(1910.60)	2.721	(1.234)	0.558	(.253)		
976	1.0	279.7	(1928.53)	2.654	(1.204)	0.592	(.269)	0.014	(.0064)
977	2.0	292.6	(2017.48)	2.413	(1.095)	0.803	(.364)		
978	2.0	300.6	(2072.64)	2.671	(1.212)	0.718	(.326)		
979	1.0	277.7	(1914.74)	2.711	(1.230)	0.571	(.259)		
980	2.0	290.6	(2003.69)	2.652	(1.203)	0.664	(.301)		
983	0.10								
984	0.075								
985	0.050								
986	0.050								
987	0.050								
988	2.0	295.7	(2038.85)	2.867	(1.300)	0.670	(.304)		
999	2.0	307.6	(2120.90)	2.698	(1.224)	0.732	(.332)		
1000	10.0	304.1	(2096.77)	2.697	(1.223)	0.724	(.328)		
1001	290								
	at 1.3	309.9	(2136.76)	2.727	(1.237)	0.737	(.334)		
	10	306.9	(2116.08)	2.729	(1.238)	0.731	(.332)		
	48	306.4	(2112.63)	2.737	(1.242)	0.728	(.330)		
	100	310.5	(2140.90)	2.826	(1.282)	0.724	(.328)		
	150	313.5	(2161.58)	2.896	(1.314)	0.720	(.327)		
	200	316.5	(2182.27)	2.938	(1.333)	0.724	(.328)		
	250	318.8	(2198.13)	2.969	(1.347)	0.730	(.331)		
	259	319.0	(2199.51)	2.975	(1.349)	0.712	(.323)		
	269	319.6	(2203.64)	2.978	(1.351)	0.697	(.316)		
	279	320.3	(2208.47)	2.984	(1.354)	0.682	(.309)		
	287	320.8	(2211.92)	2.990	(1.356)	0.670	(.304)		

(1) Tests for which data not shown did not yield reliable steady state performance

(2) Includes duct flow

(3) Specific impulse extrapolated to A_c/A_t = 40 for cold propellant tests with nozzle A_c/A_t = 12

Test Configuration: X408170 Triplet Injector (-3 ambient propellant temperature design; -4 co
temperature design used for tests with cold propellant
X408169 Thrust Chamber (A_c/A_t = 40, except A_c/A_t = 12 nozzle used for t
cold propellant)
X408163 Duct (-1 ambient propellant temperature design; -2 cold propellant
used for tests with cold propellant
Flodyne Propellant Valves
Circle Seal Igniter Valves
X408260 Catalytic Igniter

FOLDOUT FRAME /

Table 11. Altitude Test Summary

low H$_2$[(2)] lb/sec	H$_2$[(2)] kg/sec	Duct Coolant $\frac{W_{DC}}{W_{H_2}}$ X100	MR O/F	C* (Overall) ft/sec	C* (Overall) m/sec	F$_{Vacuum}$ lb$_f$	F$_{Vacuum}$ N	I$_{sp}$ Vacuum $\frac{lb_f sec}{lb_m}$	I$_{sp}$ Vacuum $\frac{Nsec}{kg}$	η_{c*} (Overall)	Comments
.0165	(.0075)	26	3.095	8237.7	(2511)	990.2	(4404)	443.8[(3)]	(4352)	98.4	Cold Propellant
.0161	(.0073)	25	2.873	8378.2	(2554)	954.3	(4245)	453.7	(4449)	99.7	
.0183	(.0083)	25	3.729	7796.2	(2376)	1006.6	(4477)	435.8	(4273)	94.3	
.0156	(.0071)	30	3.914	7850.3	(2393)	919.3	(4089)	435.2	(4268)	95.6	
0.014	(.0064)	37	4.308	7641.0	(2329)	1425.7	(6342)	422.2	(4140)	94.0	Ambient Temp.
			4.219	7657.3	(2334)	1453.7	(6466)	426.6	(4182)	94.0	
			4.271	7494.2	(2284)	1470.3	(6540)	427.9	(4196)	92.1	
		32									
			4.10	7654.5	(2333)	1424.5	(6336)	431.0	(4226)	93.6	
			4.781	7414.7	(2260)	1382.7	(6150)	418.2	(4101)	92.7	
			4.409	7560.5	(2304)	1383.1	(6152)	422.6	(4144)	93.4	
			2.973	7980.5	(2432)	1416.0	(6298)	436.6	(4281)	95.4	
			3.668	7782.4	(2372)	1478.1	(6575)	432.6	(4281)	94.2	
			4.659	7422.6	(2262)	1381.4	(6144)	417.4	(4093)	92.4	
			3.934	7689.9	(2344)	1459.1	(6490)	436.5	(4280)	93.6	Pulse Tests
			4.194	7368.3	(2246)	1478.7	(6577)	416.5	(4084)	90.4	
			3.619	7901.8	(2408)	1499.6	(6670)	435.4	(4270)	95.5	
			3.655	7833.1	(2388)	1496.6	(6657)	435.7	(4272)	94.7	
			3.631	7882.8	(2403)	1508.2	(6708)	433.6	(4252)	95.3	
			3.644	7816.5	(2383)	1518.8	(6756)	437.2	(4287)	94.6	
			3.690	7791.4	(2375)	1531.5	(6812)	440.2	(4317)	94.3	
			3.828	7708.2	(2349)	1562.5	(6950)	438.4	(4299)	93.6	
			3.944	7641.2	(2329)	1587.6	(7062)	437.4	(4289)	93.1	
			3.976	7616.7	(2322)	1603.6	(7133)	436.2	(4277)	92.9	
			3.987	7594.4	(2315)	1621.7	(7213)	436.7	(4282)	92.6	
			4.092	7623.0	(2324)	1613.7	(7178)	435.9	(4274)	93.2	
			4.185	7662.6	(2336)	1606.7	(7147)	435.4	(4270)	94.0	
			4.285	7699.3	(2347)	1597.7	(7107)	434.7	(4263)	94.7	
			4.368	7724.0	(2354)	1565.8	(6965)	426.1	(4178)	95.2	

ld propellant

ests with

temperature design

FOLDOUT FRAME 2

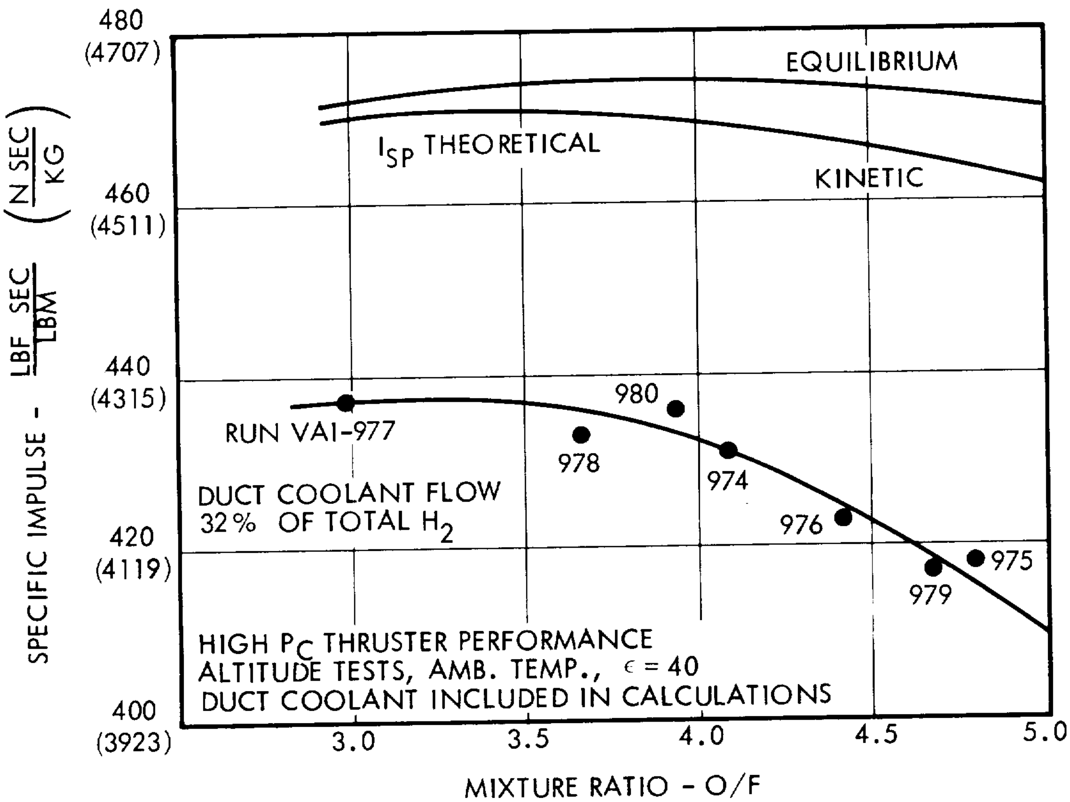

High Pressure Duct Cooled Thruster
Performance - Specific Impulse

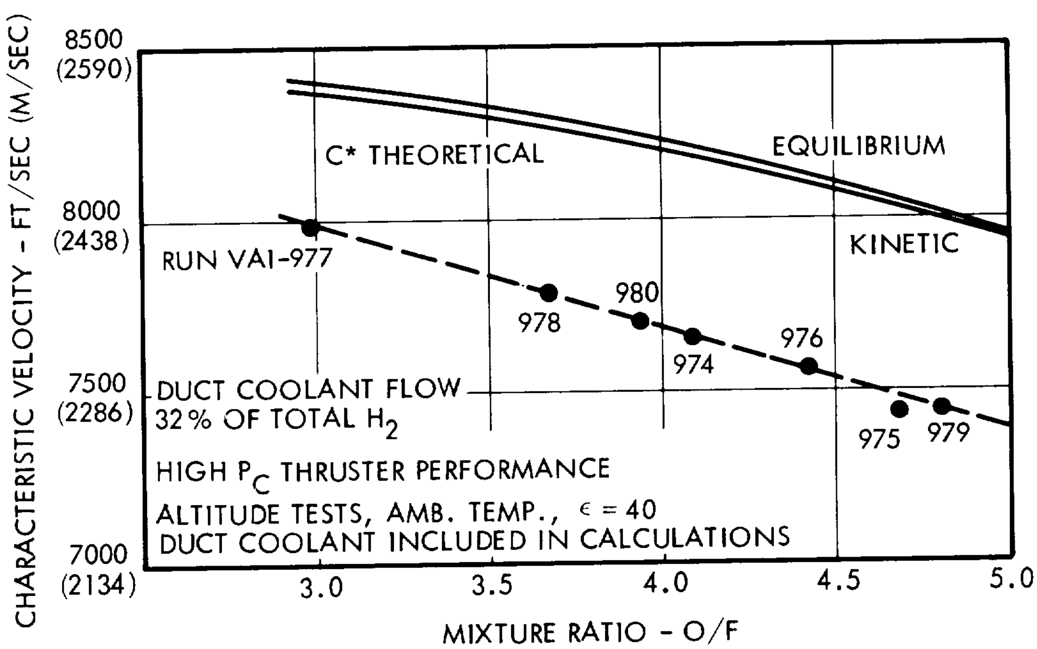

High Pressure Duct Cooled Thruster
Performance - Characteristic Velocity

Figure 82. Altitude Engine Performance

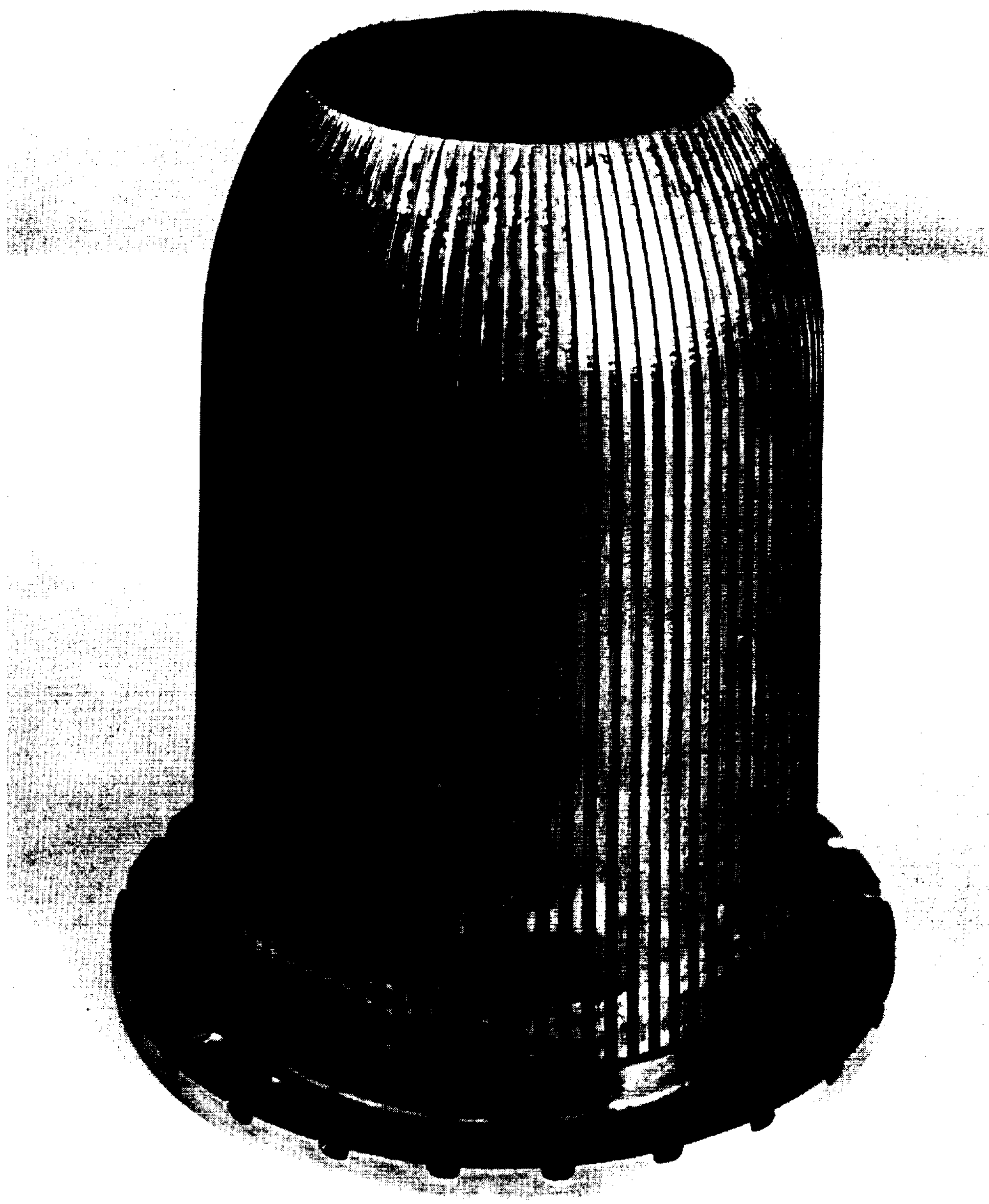

Figure 83. High Thrust Berylco-10 Duct After 60 Second Firings (40 Firings Total)

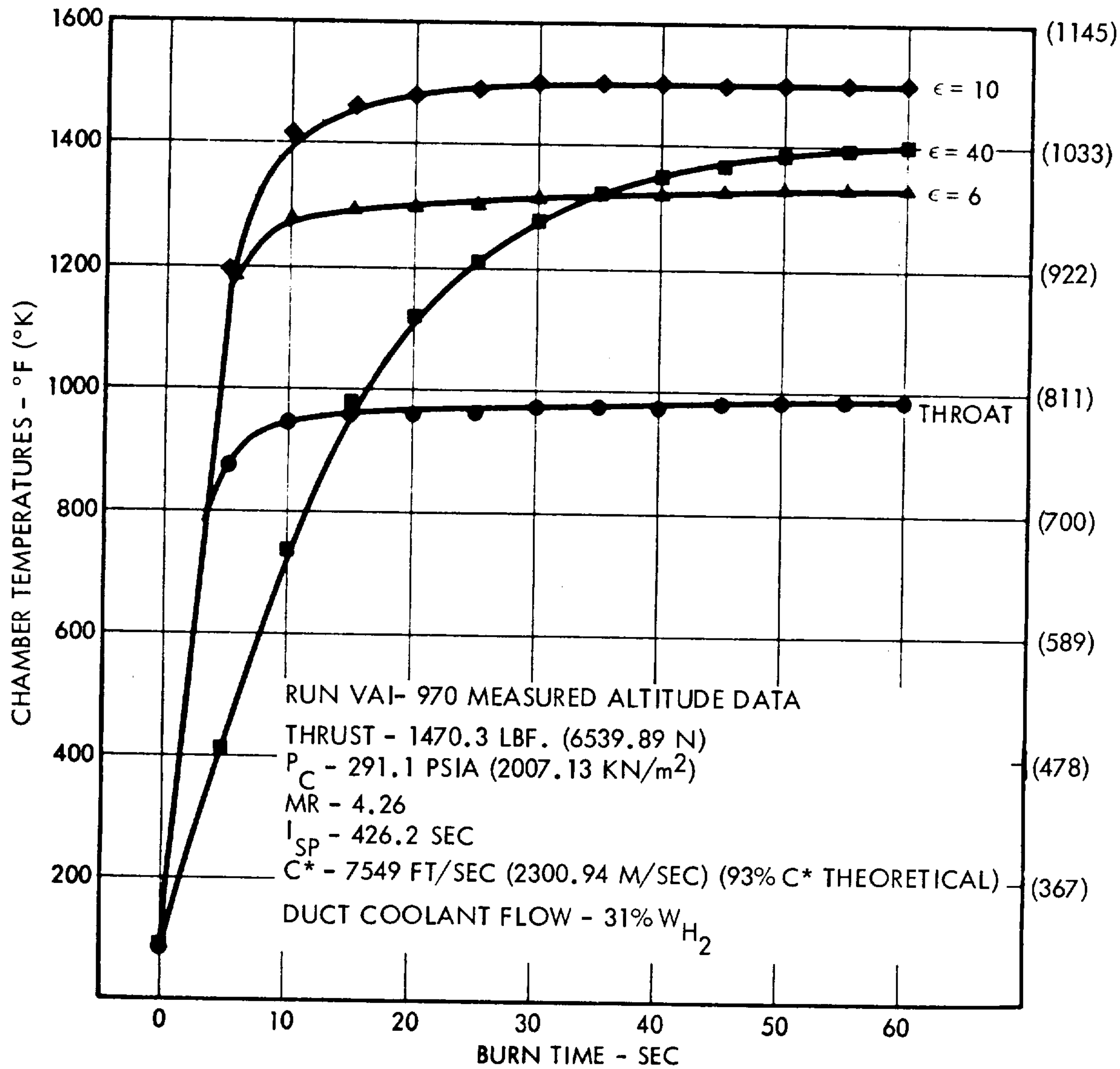

Figure 84. Thrust Chamber Temperatures for 60 Second Firing

with the duct concept. Following the 60 second data run, the analysis of the data indicated that the thruster could be run for the final duration run of the series, a 500 second test.

The 500 second duration test was to be made with ambient temperature propellants. Thrust chamber temperatures measured during the 290 second duration test with ambient temperature propellants are shown graphically in Figure 85. The highest temperatures of 1570°F (1128°K) occur at a nozzle area ratio of 10. Steady state throat wall temperatures are 1160°F (900°K). These data are significant in that they do prove the viability of the concept. The run was started purposely at a reduced mixture ratio. At 40 seconds the decision was made to increase the mixture ratio to its nominal value. At 250 seconds the automatic H_2 pressure control regulator began to bottom out because of an apparent loss of supply pressure. The mixture ratio suddenly increased and the run was terminated. Except for the unfortunate sudden rise in mixture ratio, there is every indication that the 500 seconds would have been completed.

The long duration test, scheduled for 500 seconds duration was terminated after 290 seconds because of H_2 supply pressure decay. The valve to the second H_2 trailer, required for the second half of the test was found to have been locked in the closed position. At the onset of rapid H_2 pressure decay and a nozzle throat temperature sudden rise in temperature the test was terminated. Examination of the hardware revealed localized surface melting damage to the outer oxidizer ring and a corresponding melt through of the duct.

The injector is shown in Figure 86 and 87 after the termination of the test. As is observed the injector proper is in very good condition. Damage occurred only on the outer oxidizer ring and fuel film coolant metering ring. The inner rings were in excellent condition as indicated.

The sudden rise in mixture ratio resulted in irreparable damage to the Berylco-10 duct, since the H_2 flow to the duct suddenly dropped by at least 25 percent. The duct is shown in Figures 88 and 89 post test the 290 second firing.

Experimental performance with cold propellants, with the X408170-4 triplet injector designed for cold propellants, compares closely with performance with ambient temperature propellants. The temperature conditions for the cold propellant tests are listed in Table 12. Propellant temperatures at the engine inlet were as low as 380°R (211°K) for the O_2 and 280°R ((155°K) for the H_2. Hydrogen flow to the chamber cooling duct ranged from 25-30 percent. The X408163-2 duct, designed with smaller groove flow areas, was used for the tests with cold propellant. Characteristic velocity and specific impulse performance for the cold propellant tests are presented in Figure 90. The measured characteristic velocity is somewhat higher than for the cold propellants. The nozzle area ratio for the cold propellant tests was 12. The measured specific impulse, corrected to vacuum, was extrapolated to that for a nozzle area of 40 by multiplying by the ratio of theoretical vacuum thrust coefficients and the nozzle divergence corrections for comparison to the ambient propellant temperature test results. (These corrections are 1.0517 and 1.0335, respectively.) The specific impulse compares closely

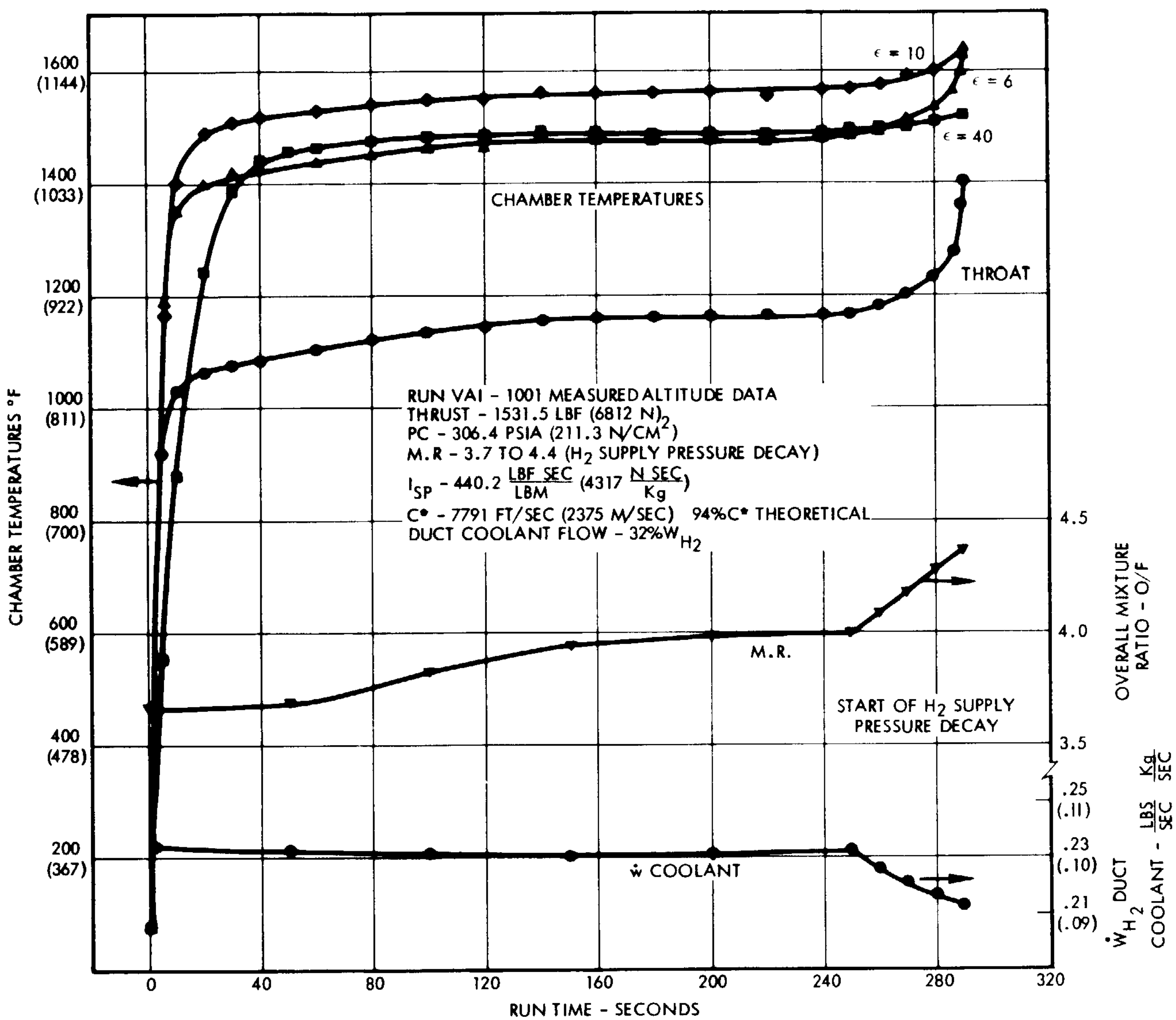

Figure 85. High Chamber Pressure Thruster Long Duration Test Data

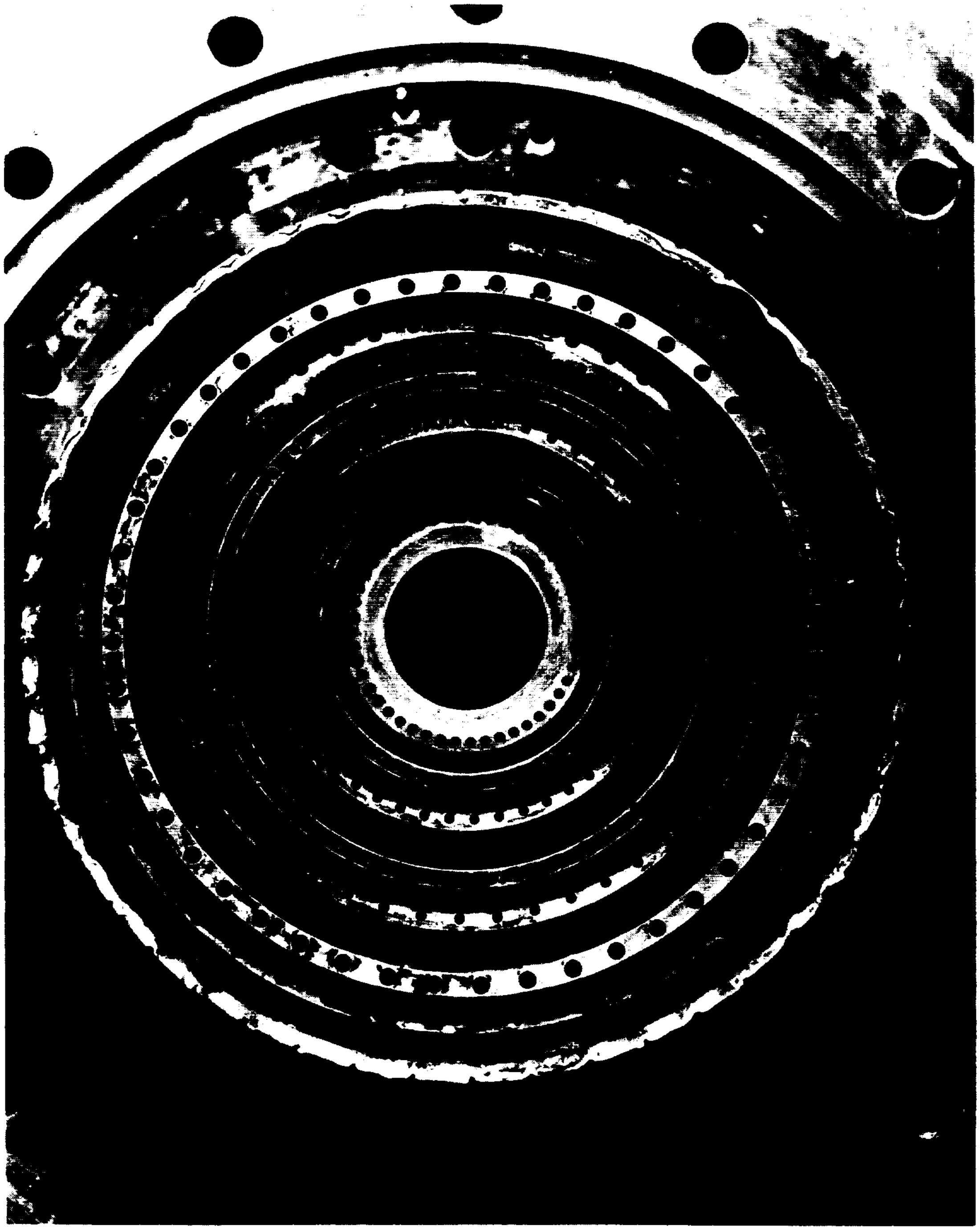

Figure 86. Injector Face After 290 Second Firing

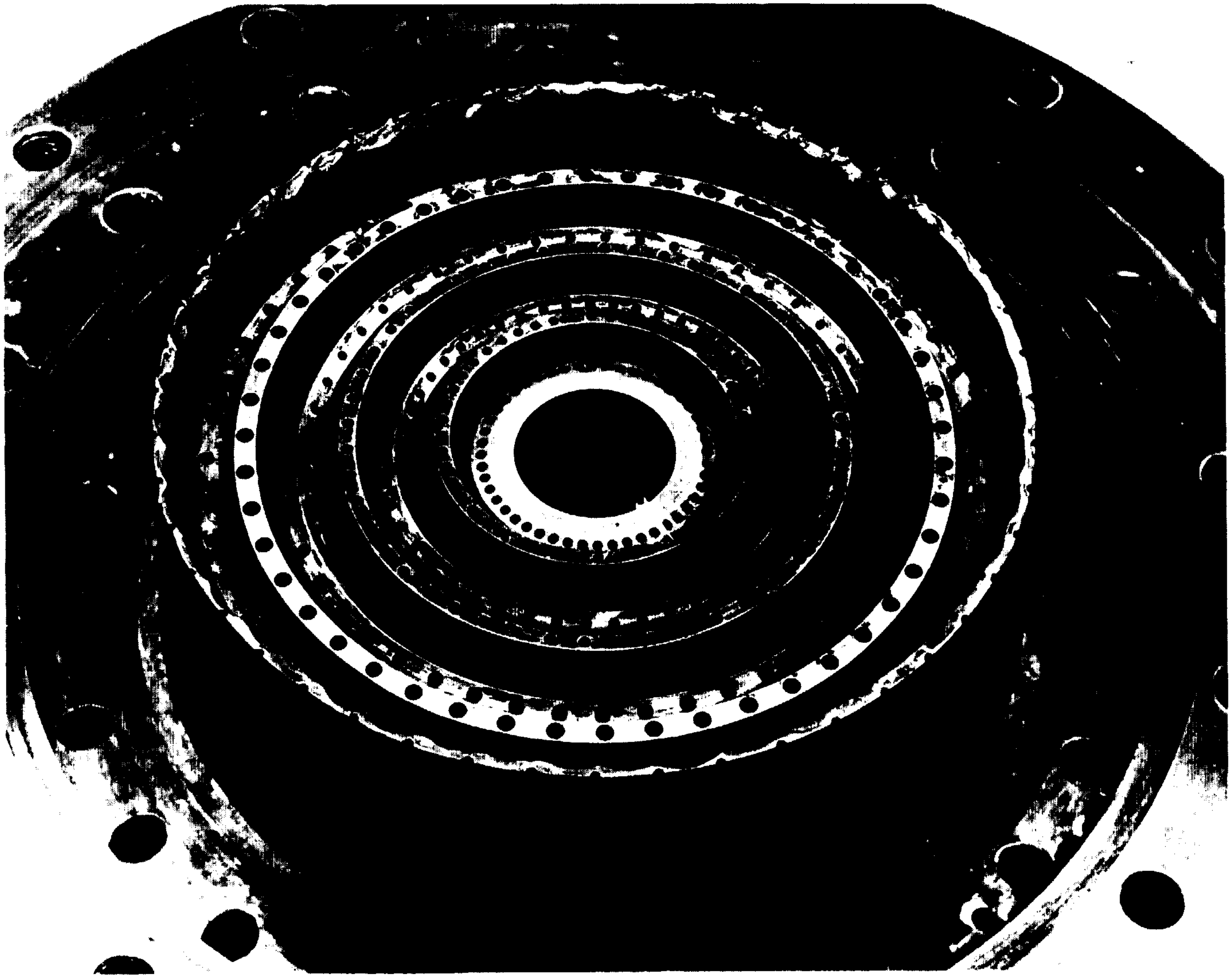

Figure 87. View of Injector After 290 Second Firing Showing Local Melting Adjacent to Outer Oxidizer Ring

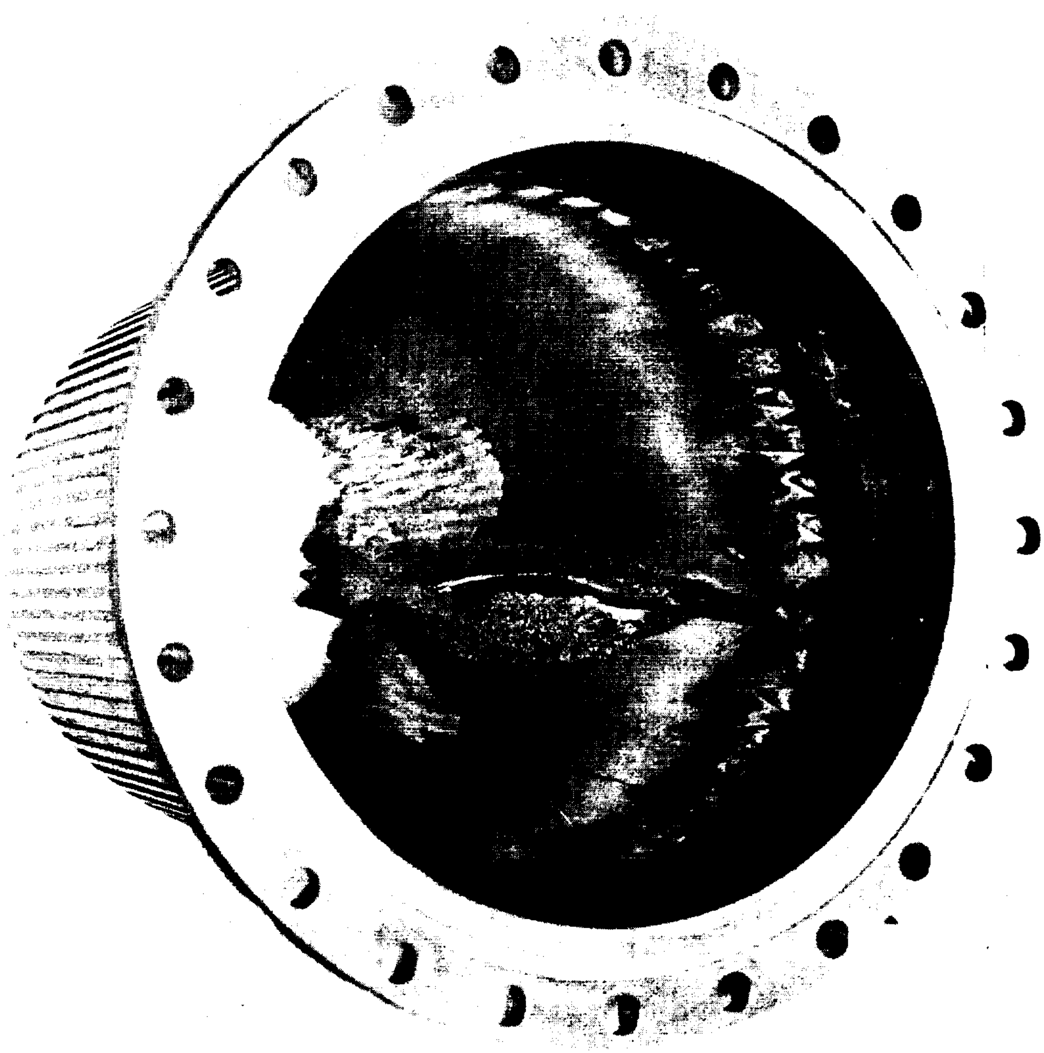

Figure 88. Internal View of Duct After 290 Second Firing

Figure 89. External View of Duct After 290 Second Firing

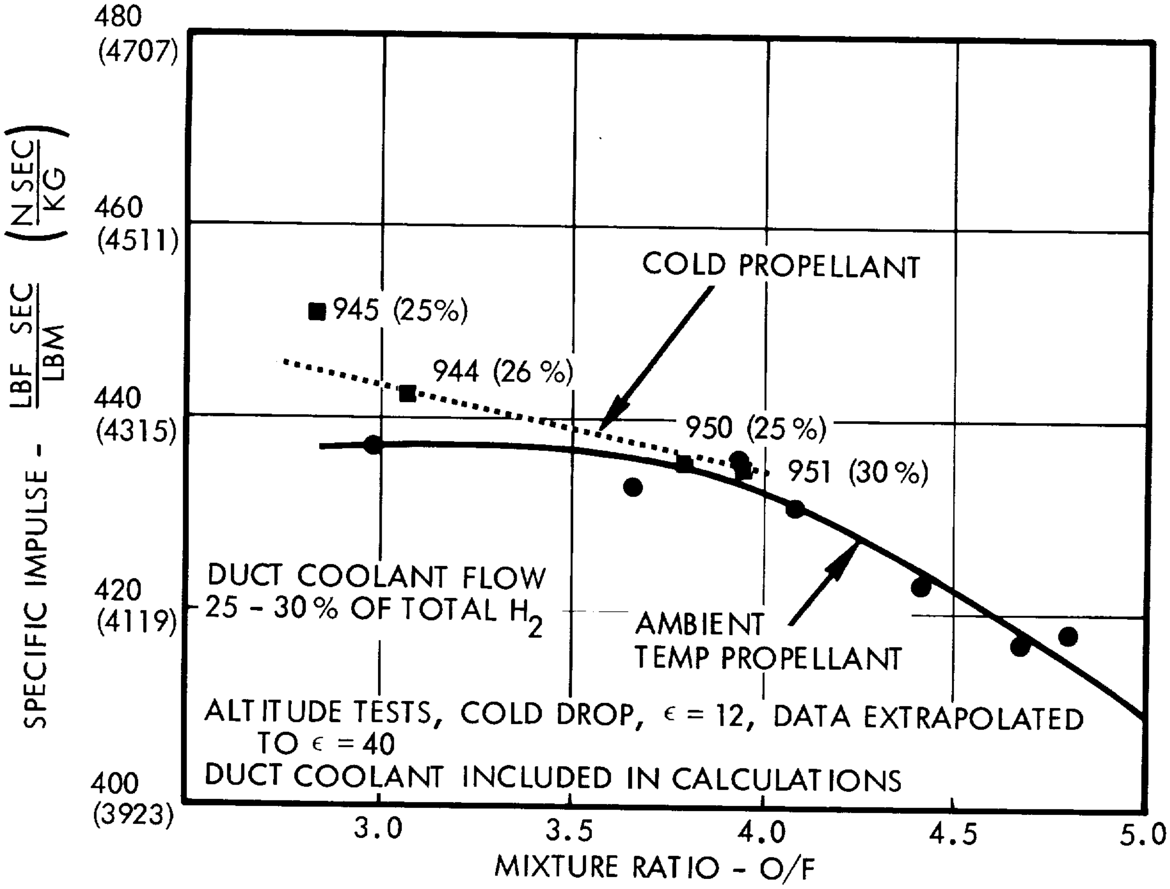

High Pressure Duct Cooled Thruster
Performance - Specific Impulse

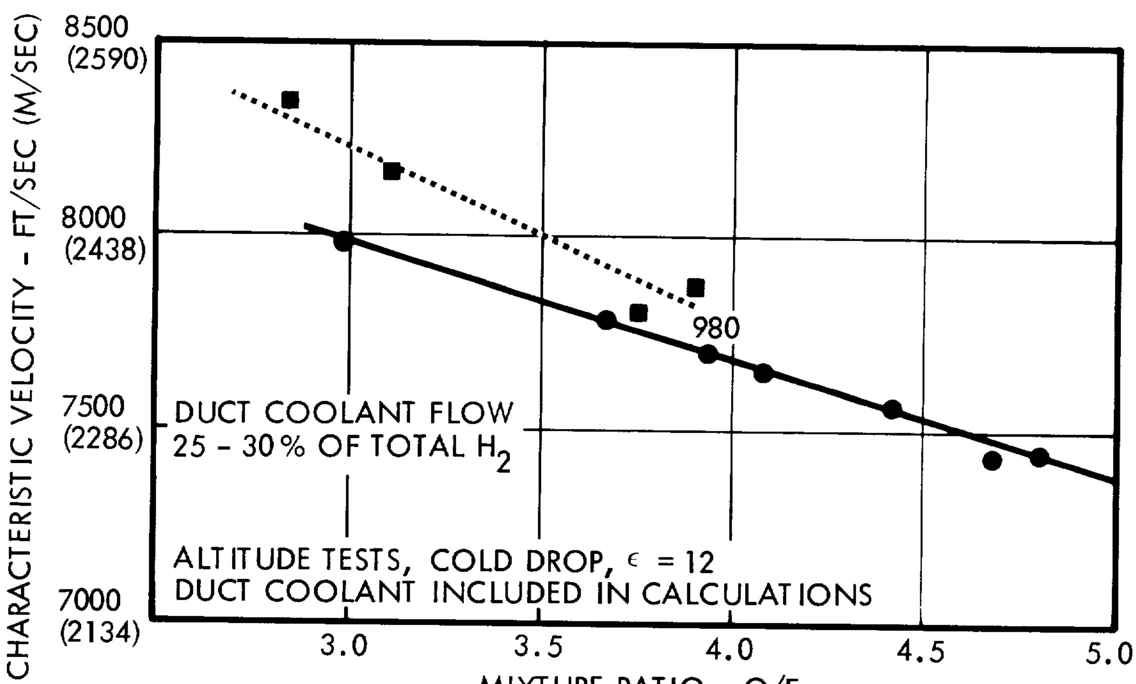

High Pressure Duct Cooled Thruster
Performance - Characteristic Velocity

Figure 90. Comparison of Altitude Performance With Cold Propellant and With Ambient Temperature Propellant

Table 12. Cold Propellant Test Temperature (°R)(°K)

Test	Injector[1] O_2	Injector[1] H_2	Igniter O_2	Igniter H_2
945	380 (211)	280 (156)	380 (211)	280 (156)
947	360 (200)	310 (172)	492 (273)	280 (156)
950	460 (256)	300 (167)	450 (250)	320 (178)
951	370 (206)	320 (178)	498 (277)	420 (233)

(1) Measured at inlet to subsonic flow control orifices

for the different temperature conditions, with the cold propellant data being slightly higher because of the lower percent duct cooling flow. Experimental specific impulse at an overall mixture ratio of 3.9 is 435 seconds with 320°R (178°K) H_2 and 370°R (206°K) O_2 injection propellant temperature.

In all of the tests, except for two no ignition tests, the high response catalytic igniter functioned quite well. The two no ignitions may have been due to sequencing valve delays. The exact cause is uncertain at this time. Figure 91 shows a typical start ignition transient. Following the igniter flow variables and signals, it is seen that the igniter response is extremely fast. The igniter ignition flow was programmed ahead of the main thruster valves by $\sim$ 25 ms. It would appear that the igniter could safely be overlapped into the starting sequence without difficulty.

4.1.2.5 Correlation with Predicted Modelling

The thermal data indicated, as a whole, a slightly higher temperature than was predicted by the design model. The overall trends were in near perfect agreement with the model. The minor discrepancies are felt to be associated with the duct gap not exactly matching the design valves.

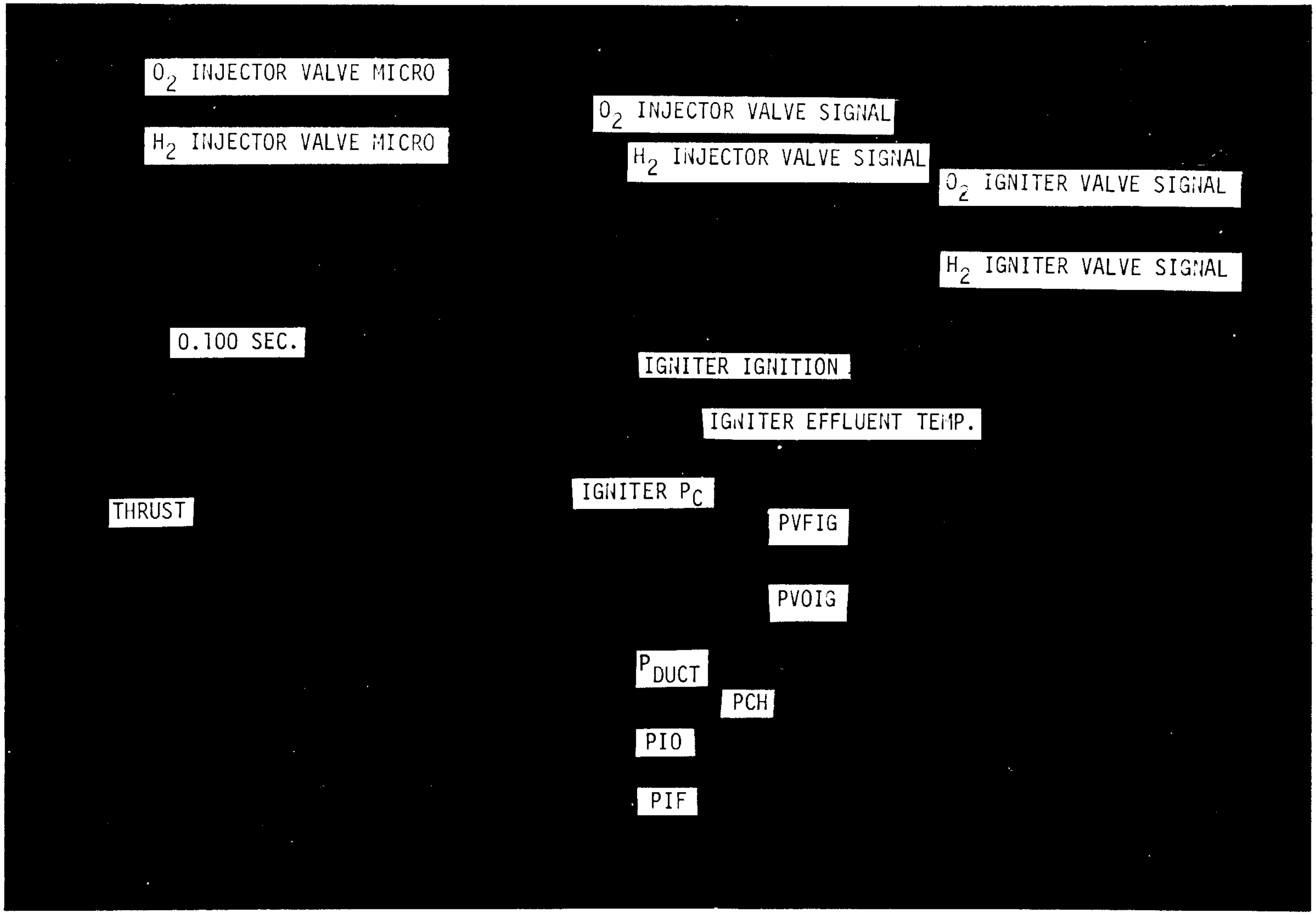

Figure 91. High Thrust Triplet Injector/Catalytic Igniter, Run VA1-961, MR4 - Start Transient

The performance correlation to the model proved to be outstanding as illustrated in Figure 92. The 32 percent coolant point is overlayed on the graph as originally derived from the MSFC data for the smaller TRW thruster. The 32 percent data from this program actually exceed the model predictions as shown. Of interest also is the fact that the original predicted roll-off at high MR did not actually turn out to be as severe.

4.1.3 Pulse Mode Tests

Runs 981 through 987 were conducted to partially investigate the pulse capability of the duct cooled thruster design. It should be kept in mind here that this program did not develop optimum valves for the thruster. The valves were TRW supplied and no effort was made to push these valves to their design limit. The igniter timing sequence was also not changed for these tests. The details of the pulse tests are summarized in Table 13.

Table 13. Pulse Mode Investigations

	Test Number	No. of Pulses	On-Time/ Off-Time	(lb-sec) (KG-sec) Impulse
VA1 Sea Level	981	1	0.100ms/ –	56.8 (2576.4)
VA1 Sea Level	982	1	0.100ms/ –	63.0 (2857.7)
Altitude	983	5	0.100ms/0.200ms	93.2 (1st pulse)(4227.6)
	984	5	0.075ms/0.100ms	68.4 (1st pulse)(3102.6)
	985	5	0.050ms/0.200ms	32.4,40.4,39.6,42.3,41.4(1469.7) (1832.5),(1796.3),(1918.7),(1877.9)
	986	5	0.050ms/0.100ms	35.3 (1st pulse) (1601.2)
	987	5	0.050ms/0.100ms	30.3 (1st pulse) (1374.4)

The approximate specific impulse for the initial 0.050 ms pulse of a pulse series, defined as the integrated thrust/integrated flow over the pulse, is approximately 328 seconds. During the 0.050 ms pulses, flow across the injection orifices is sonic. Following the P_c-c* dependance empirical data for both the low and high pressure performance data gives an average specific impulse result of 395 to 400 seconds for the 50 ms results.

Test number 988 was a 2.0 second test after the series of tests. This test showed a significant shift in overall fuel ΔP. Physical examination of the injector showed the fuel rings to be collapsed in several locations.

Figure 93 shows the beginning of the pulse train for run VA1-983 with nominally 100ms pulses. The pulses were quite reproducible as seen by visual comparison and F-t integrations. The long igniter P_c decay and rise times were found to be caused by a partially blocked instrumentation tube. The igniter temperature response is seen to be excellent on each startup.

Figure 94 shows typical data for the 50 ms pulse train of test VA1-985. The integrated impulse results show excellent reproducibility beyond the first pulse.

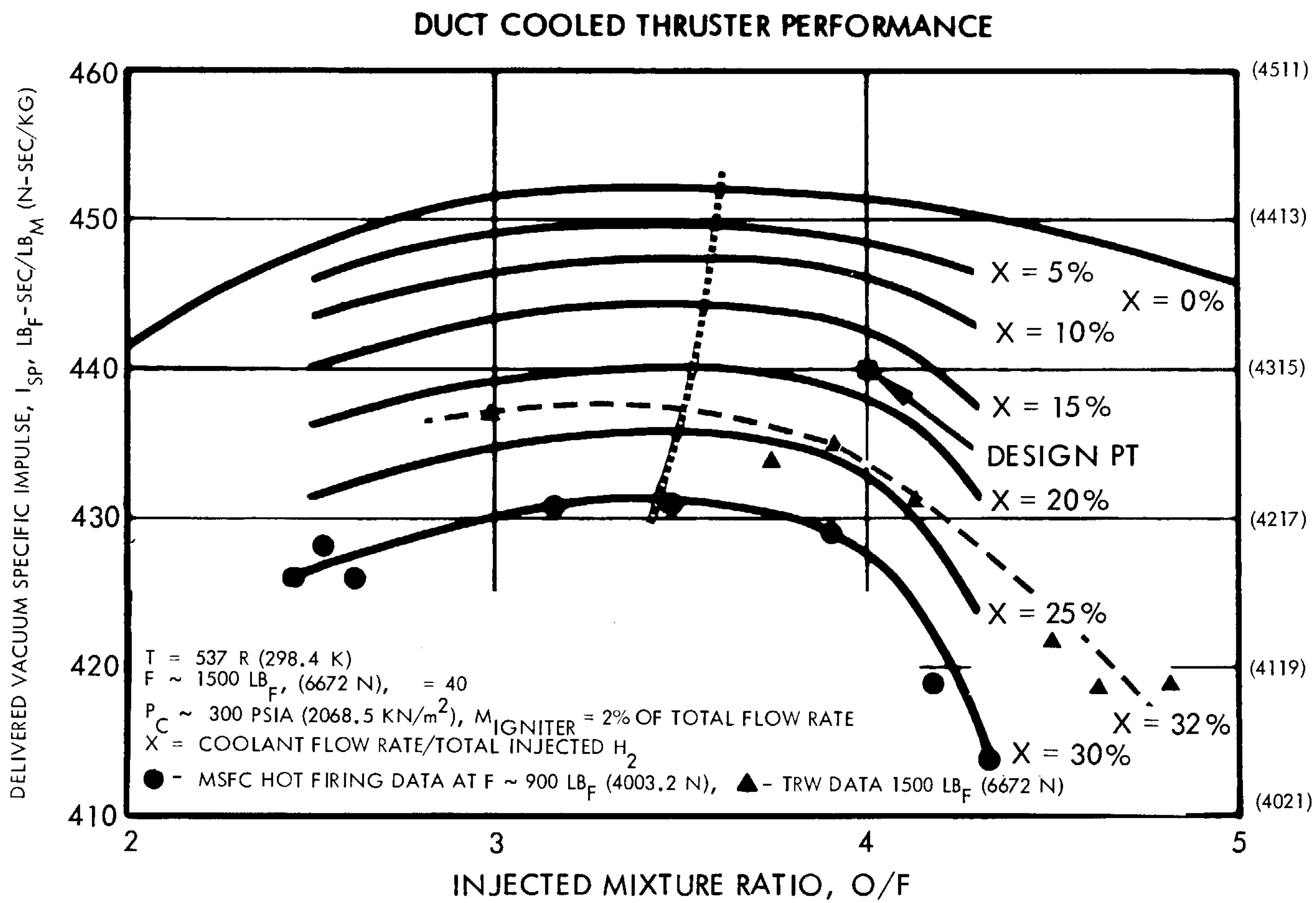

Figure 92. Performance Map - High Pressure Thruster Data Correlation With Original Model Predictions

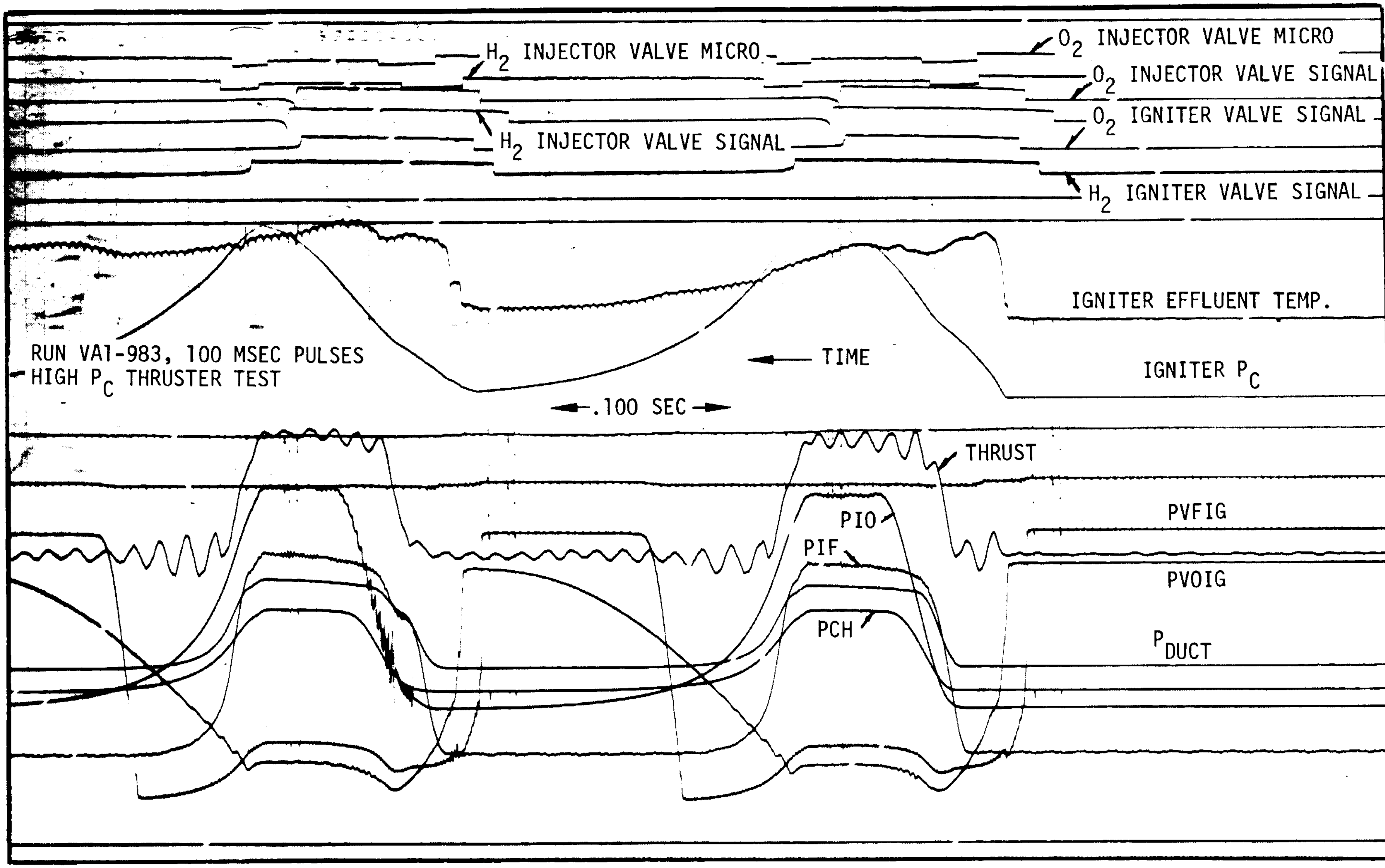

Figure 93. High Thrust Pulse Test VA1-983, 100 msec Pulses

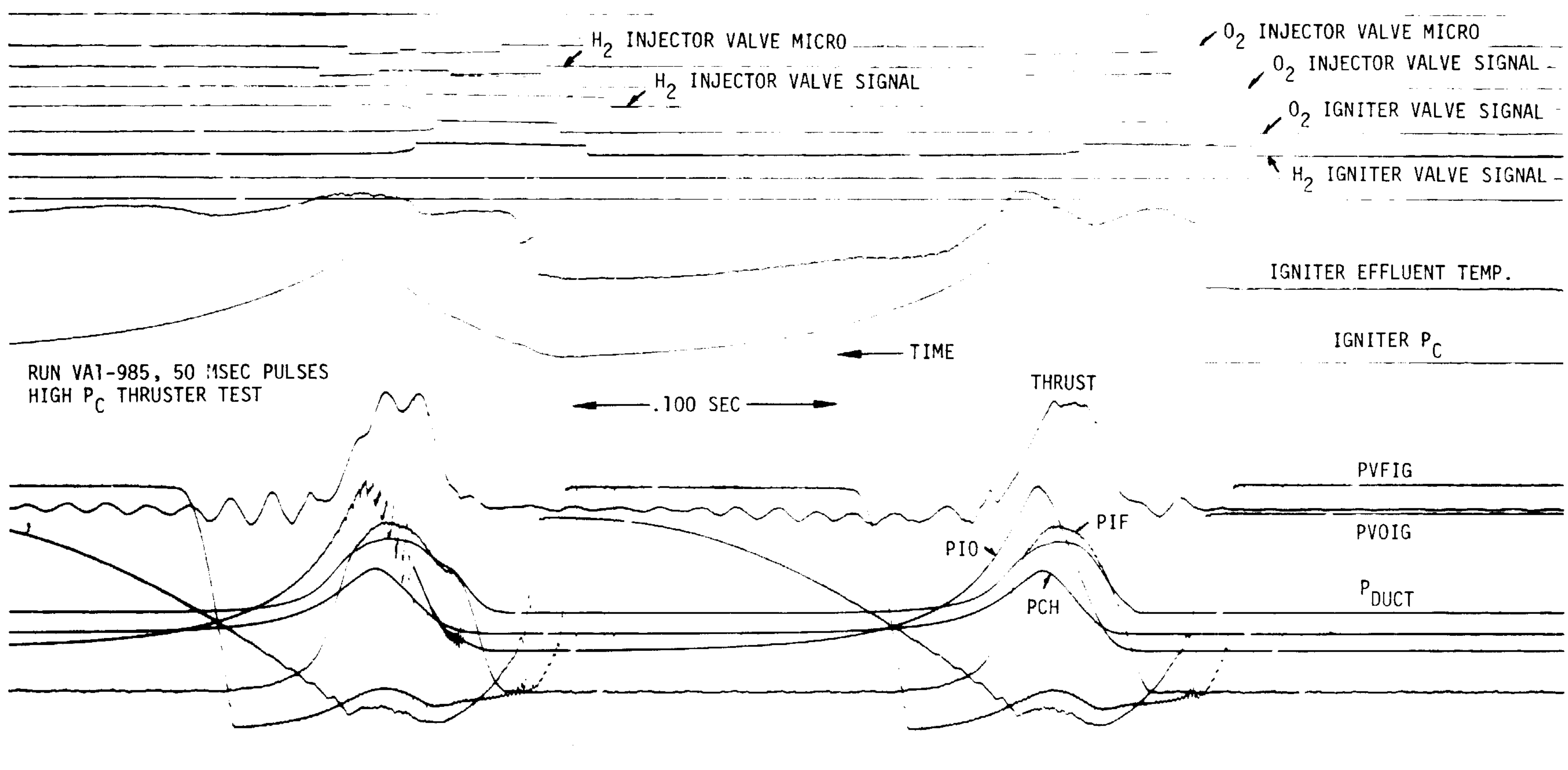

Figure 94. High Thrust Pulse Test VA1-985, 50 msec Pulses

Closer examination of Figures 93 and 94 provide a strong indication that the problem with the H_2 ring collapse is associated with a phenomena associated with pulsing. Note the pressure ringing in the second pulse on both sets of tests. Since it was not possible to place high frequency pressure response instrumentation in the thruster, the low frequency instrument outputs can only be received as an indicator of some difficulty. It appears that some reaction was taking place within the O_2 manifolding. It is speculated that there may have been popping occurring in the internal ring cavities also.

No damage was incurred in the O_2 side. The O_2 rings are shorter, stiff cylinders. The longer H_2 cylinders did not apparently have sufficient wall thickness to length ratio to withstand the magnitude of this hypothesized popping effect.

4.2 IGNITER-ONLY OPERATION

Firing tests of a catalytic pilot bed igniter mounted in a complete 1500 lbf (6672 N) thruster assembly were performed to determine the MIB capability and cooling requirements, if any, for igniter-only mode of operation. The previous results of the thruster/system MIB analysis (Section 3.4.1) had indicated the significant advantages of igniter-only operation in achieving extremely low MIB for precise attitude control with minimum propellant usage. These tests were conducted to identify any problems caused by firing of the igniter in a full thruster assembly without main propellant flow.

4.2.1 Test Description

The thruster igniter-only evaluation firings were performed with a full scale cooling duct and thrust chamber, except that a nozzle with an area ratio of 12:1 rather than a 40:1 nozzle was used to allow the use of the HA5 altitude test stand. This test position was used for the low pressure thruster tests (described in Volume I), and was equipped with a thrust measurement stand of suitable range for igniter-only firing of the high pressure thruster. The same catalytic igniter used for all of the full thruster tests was installed in a copper dummy high Pc injector instrumented for chamber pressure and face temperature measurements. The igniter, dummy injector, duct, and thrust chamber are shown in Figure 95. Installation of the thruster assembly on the HA5 thrust mount is shown in Figure 96. This photograph was taken during chill-down for an igniter-only test with the thruster at initial temperatures below 300°R (167°K).

4.2.2 Summary of Results

The data resulting from the high pressure thruster igniter-only tests are presented in Table 14 and summarized as follows:

Test 365T: A 1/2-second checkout firing was conducted to verify ignition with ambient temperature propellants.

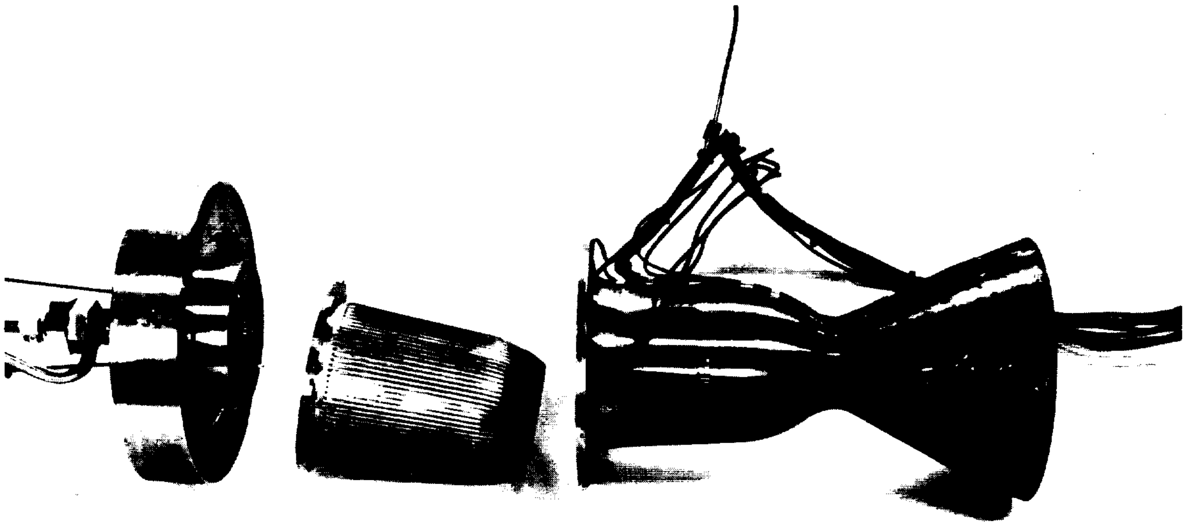

Figure 95. Igniter, Dummy Injector, Duct and Thrust Chamber

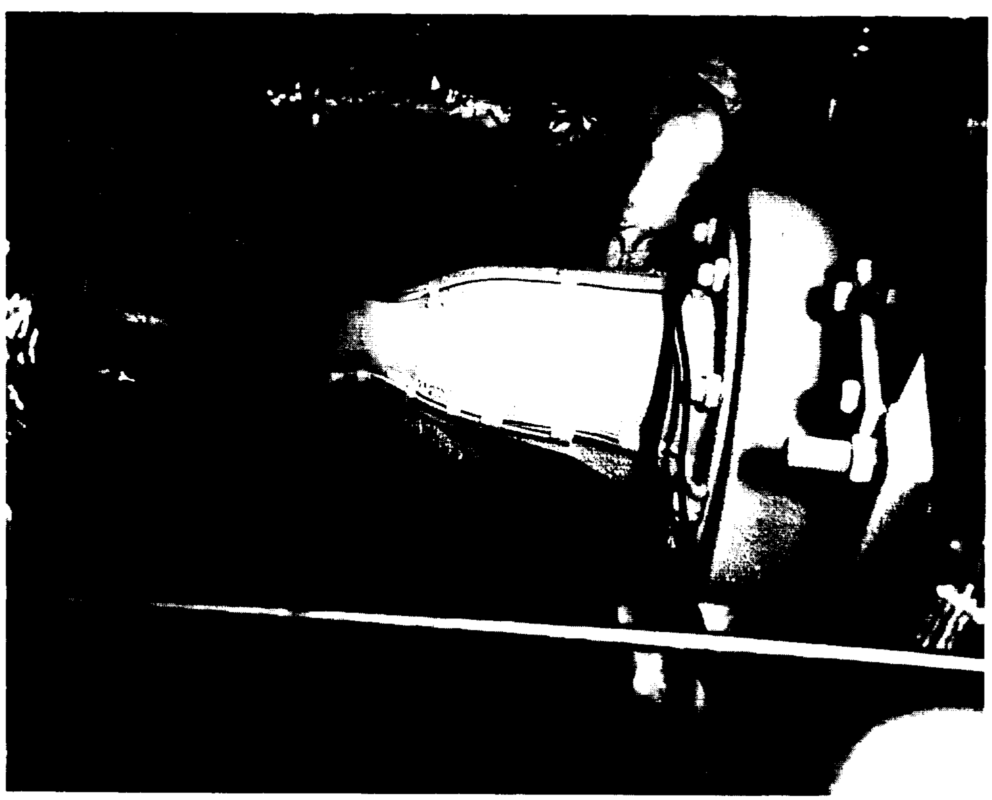

Figure 96. Installation of Thruster Assembly on HA5 Thrust Mount

Table 14. Igniter Only Pulse Tests

Test No. (HA5-)	P_{CH} (lbf/in^2)	P_{CH} (kN/m^2)	O_2 Temperature (°R)	O_2 Temperature (°K)	H_2 Temperature (°R)	H_2 Temperature (°K)	F_{Vaccum} (lbf)	F_{Vaccum} (N)	Run Duration (sec)	Comments
365T	2.69	18.5	529	294	530	294	26.9	120	0.5	Ambient temperature checkout
365Z	2.04	14.1	525	292	518	288	21.9	97.4	30	Extended duration test with duct coolant flow
365Z16	2.02	13.9	526	292	515	286	22.8	101	60	Evaluation test with no duct coolant flow
366K	0.66	4.55	525	292	523	291	8.29	36.9	1.0	Reduced igniter flow rates
366Z7	0.57	3.93	523	291	519	288	7.59	33.8	0.5	Five pulses fired in succession at reduced igniter flow
367K	1.78	12.3	363	202	151	83.9	18.0	80.1	0.5	Low temperature propellant ignition test
367R	2.67	18.4	335	186	143	79.4	22.5	100	1.0	Increased igniter flows with low temperature propellants
367S	3.10	21.4	330	183	143	79.4	24.2	108	0.5	Three pulses with low temperature propellants
367T	2.39	16.5	328	182	164	91.1	19.4	86.3	0.1	Five pulses of 100 msec duration each - low temperature propellants

Test 365Z: Duct coolant flow equal to one-half the total igniter flow rate was maintained during a 30-second duration igniter-only firing. Maximum chamber temperature was 446°F (503°K) measured at the thruster throat.

Test 365Z16: A 60-second igniter firing was performed without any duct coolant flow. Maximum chamber temperature was 482°F (523°K) and stabilized, indicating that continuous igniter firings of 60 seconds or longer could be made without duct flow or other cooling of the main thruster being required.

Test 366K: Igniter flow rates were reduced for this firing, resulting in a thrust level less than 10 lbf (44.5 N) and a thruster chamber pressure of less than 1 psia (6.9 kN/m^2).

Test 366Z7: A series of five pulses was conducted at reduced igniter flows to verify repeatability of ignitions.

Test 367K, R: Low temperature propellant tests were successfully performed with chilled thruster hardware. Igniter flows were increased for test 367R.

Test 367S: Low temperature pulses of 500 msec duration each were conducted with low temperature propellants and thruster hardware.

Test 367T: A series of five pulses was made with firing durations reduced to 100 msec on time. An oscillograph recording of this firing is reproduced in Figure 97, and indicates the repeatability of the pulses. No duct coolant was employed for any of the tests after 365Z, and the thruster and igniter hardware remained in excellent condition, as shown in Figures 98 and 99.

The results of the igniter-only high pressure thruster evaluations verified the previous analyses indicating that extremely low MIB values are feasible with this mode of operation. Test firings of up to 60-seconds steady-state operation without any chamber coolant required have indicated that igniter-only operation has many advantages for a reaction control thruster.

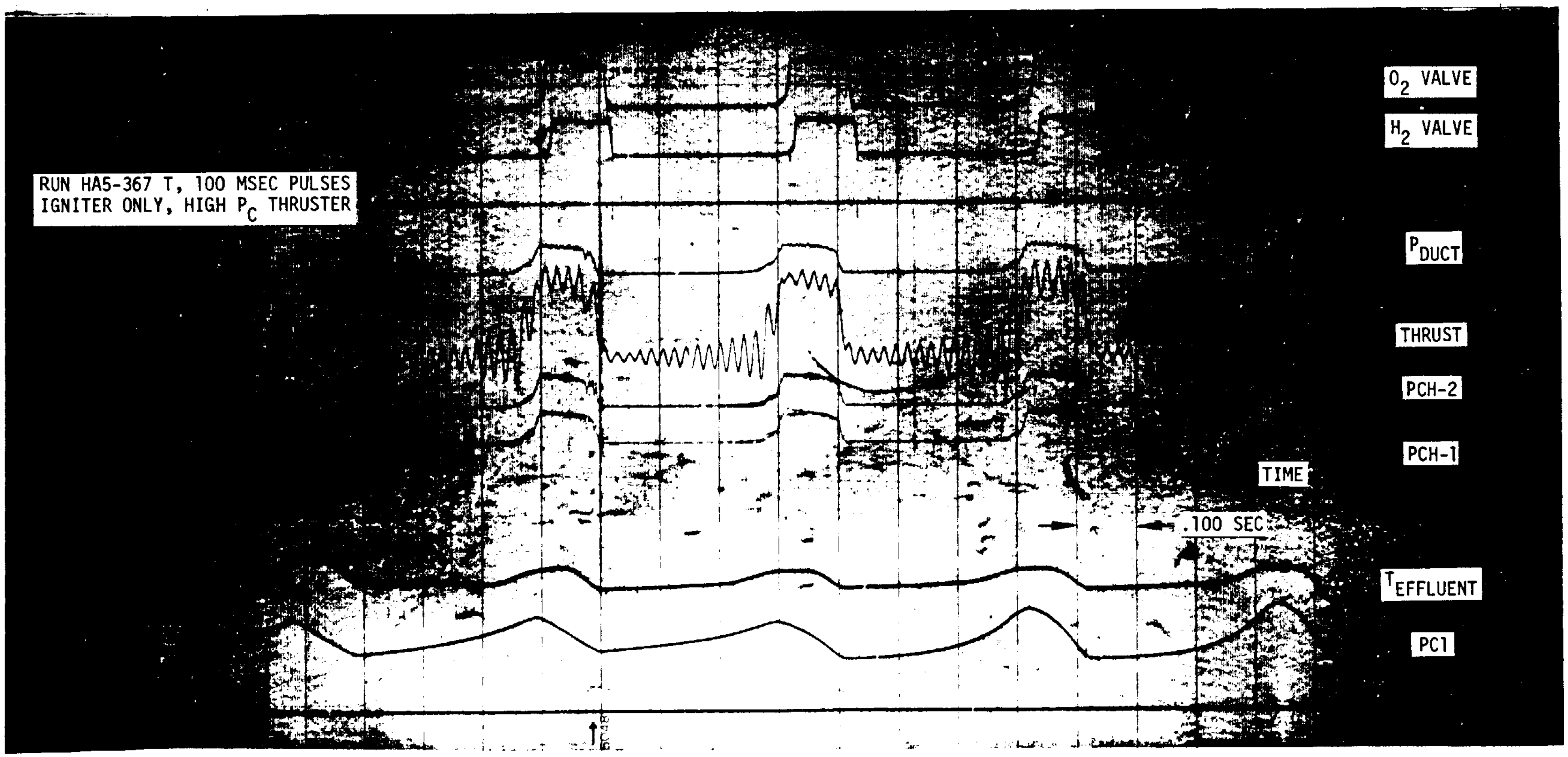

Figure 97. High Pc Thruster Test HA5-367T Igniter-Only Firings, 100 msec Pulses

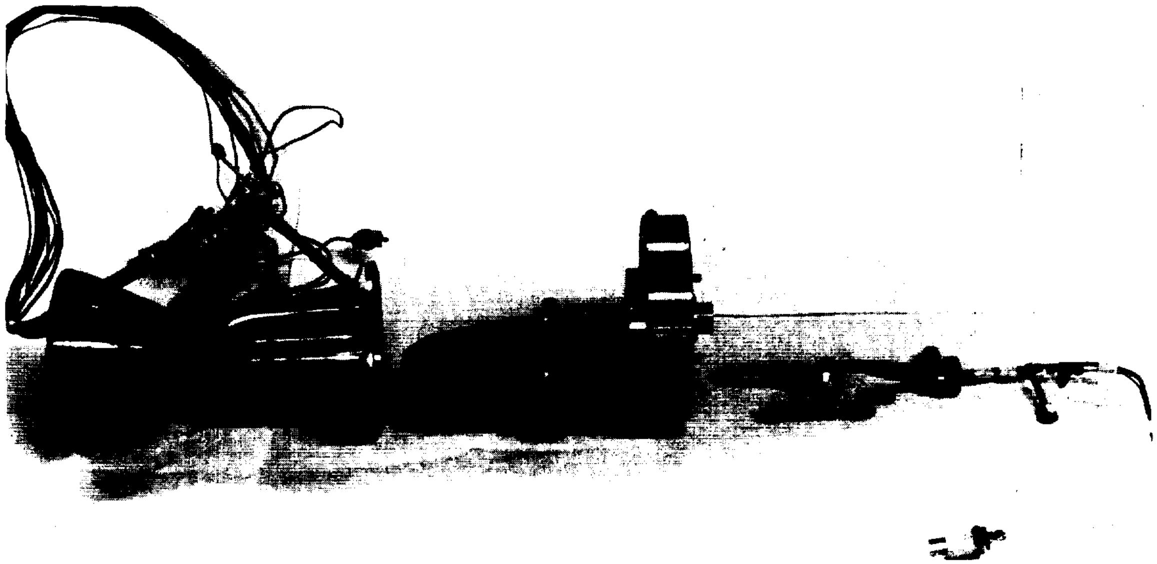

Figure 98. Thruster Hardware After Test

Figure 99. Igniter Hardware After Test 365Z

4.3 ENVIRONMENTAL EFFECTS ON THRUSTER OPERATION

A series of firing tests of the high pressure thruster/igniter assembly was conducted to evaluate the effects on thruster operation of potentially degrading environmental exposures. For these tests, the analytical and experimental results of catalytic igniter environmental effects investigations (described in Volume I of this contract report) were utilized in selecting test conditions. The environmental conditions evaluated during this task were saturated air exposure at thruster hardware temperatures as low as 200°R (111°K).

4.3.1 Test Description

The environmental effects evaluation tests were performed with the 40:1 exit area ratio, altitude thrust chamber and the high pressure triplet injector. The thruster assembly was installed in the altitude test cell and chilled with liquid nitrogen. Exposure of the subzero temperature thruster hardware to saturated air (100 percent relative humidity) resulted in significant frost formation on the thruster surfaces, as shown in Figure 100.

The photograph shown in Figure 101 was taken during saturated air soaking of the chilled thruster prior to test firing. Steam from the altitude system was utilized as a source of saturated air for these tests. The effects of soak times of up to 30 minutes in saturated air with thruster temperatures as low as 200°R (111°K) were evaluated during this test series.

4.3.2 Summary of Results

Data from the thruster environmental effects tests are presented in Table 15 and the results are summarized as follows:

Tests 989 - 990: Initial checkout tests were conducted with only ambient air, normal humidity exposure of the thruster to establish baseline ignition response before environmental soak exposure.

Test 991: The first exposure was 6 minutes saturated air at reduced propellant and initial thruster temperatures, as indicated in Table 4-VII. A trickle purge of gaseous nitrogen was maintained through the igniter to prevent catalyst bed icing. The igniter fired satisfactorily on this test, but main thruster valves did not open. Inspection of the test installation revealed that liquid nitrogen from the conditioning system was dripping on the main thruster valves, causing ice formation which physically prevented external movement of the valve. The thruster valves were shielded from LN_2 exposure for all subsequent tests.

Test 992: A 30-minute saturated air soak at initial thruster temperatures similar to test 991 resulted in normal main thruster ignition with the GN_2 igniter trickle purge on.

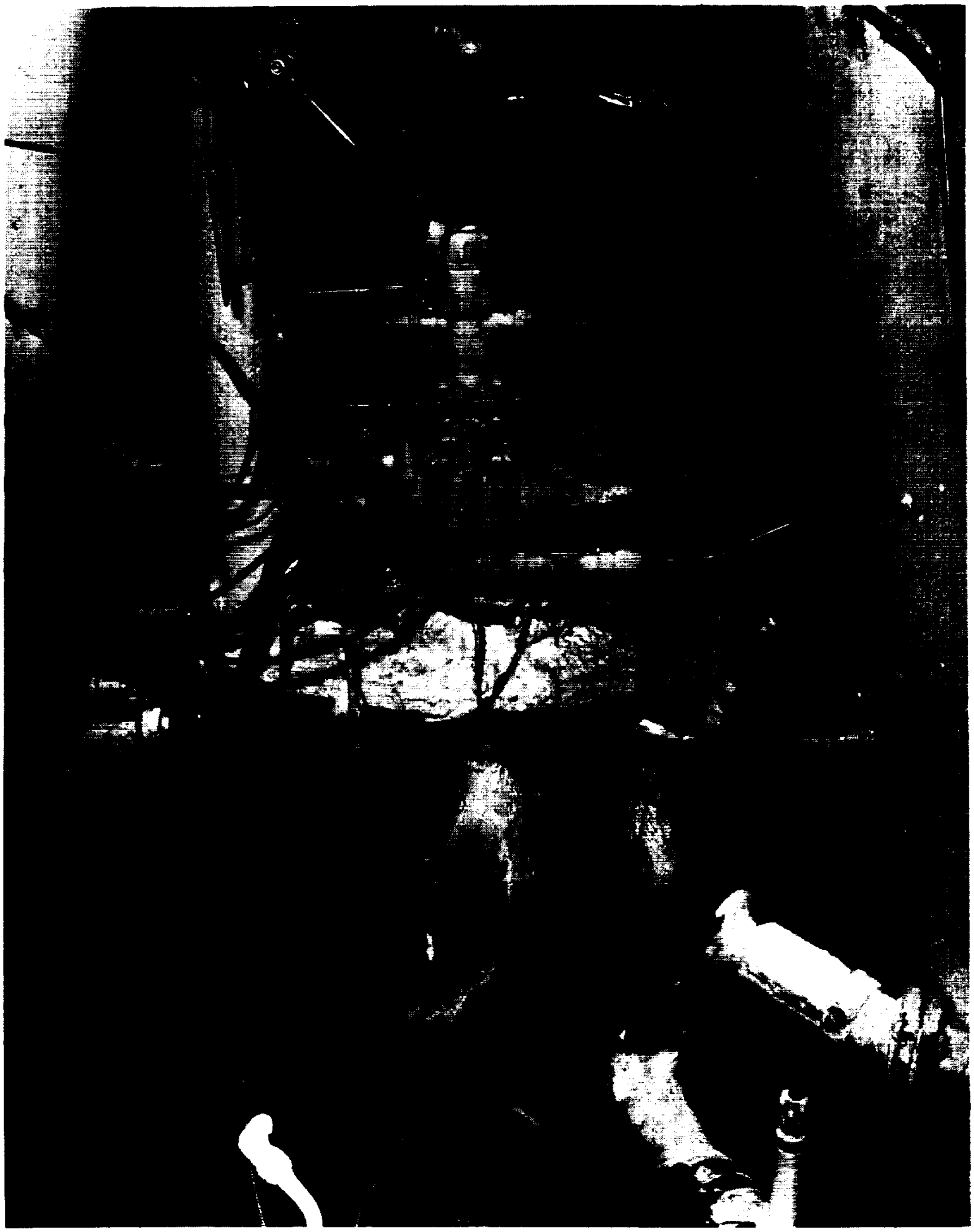

Figure 100. Chilled High P_c Thruster - Environmental Effects Tests

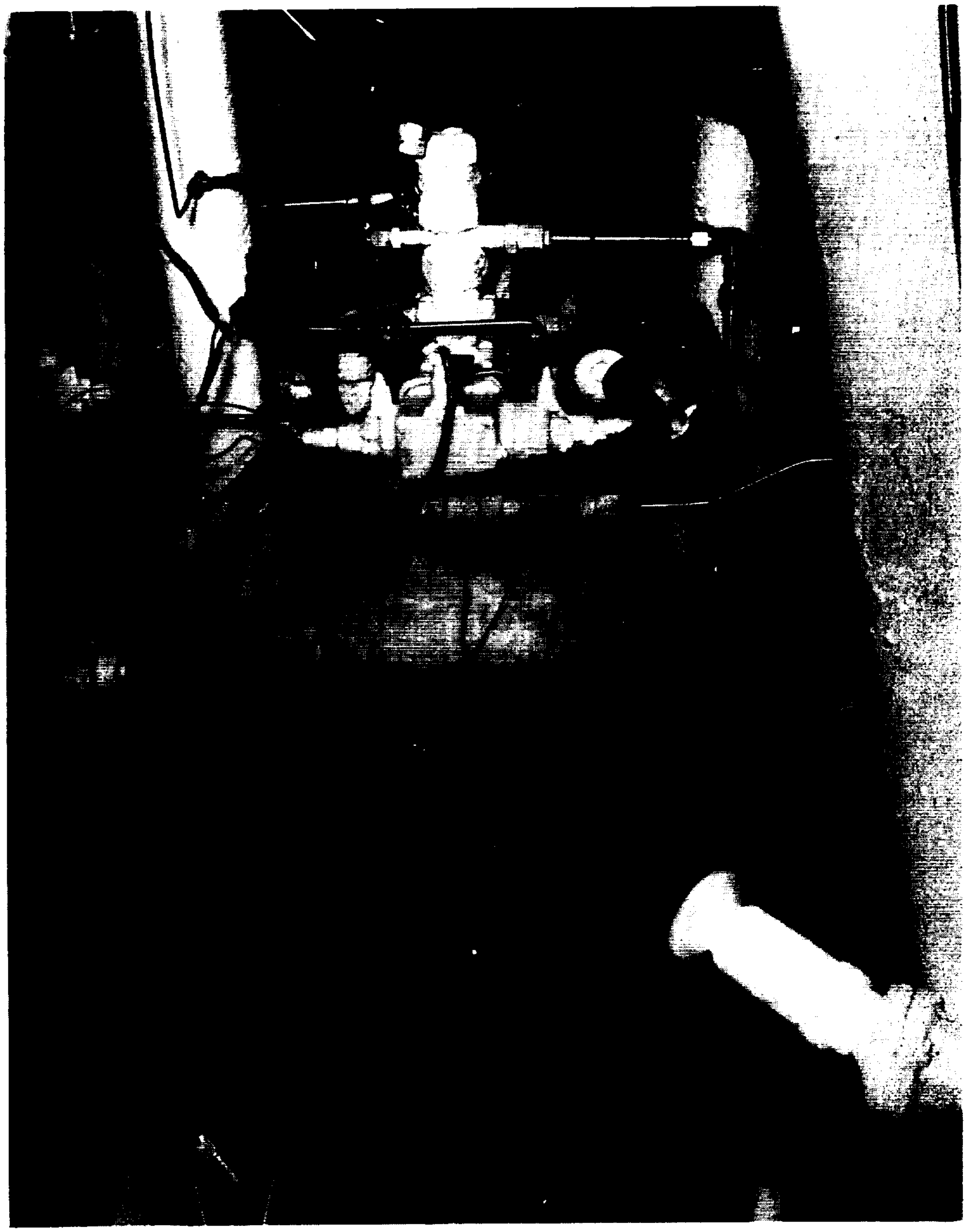

Figure 101. Saturated Air Soaking of Chilled Thruster Before Test Firing

Table 15. Environmental Effects on Thruster

Test No. (VAI-)	P_{CH} (lbf/in^2)	P_{CH} (kN/m^2)	O_2 Temperature (°R)	O_2 Temperature (°K)	H_2 Temperature (°R)	H_2 Temperature (°K)	Thruster Initial Temperature (°R)	Thruster Initial Temperature (°K)	Environmental Exposure	Comments
989	243.8	1681	512	284	508	282	509	283	ambient air, normal humidity	initial checkout, good ignition
990	252.7	1742	518	288	516	287	523	291	ambient air, normal humidity	**repeat** to verify ignition before cold propellant tests
991	no main ignition		285	158	262	146	356	198	6 minutes saturated air, GN_2 trickle purge on igniter	igniter fired, but main thruster valves did not open
992	250.3	1726	368	204	295	164	364	202	30 minutes saturated air. GN_2 trickle purge on igniter	main thruster ignition satisfactory after long soak
993	no main ignition		298	166	210	117	203	113	15 minutes saturated air, without igniter purge	igniter fired, but main O_2 valve did not open(2)
994	203.6	1404	521	289	518	288	521	289	ambient air, normal humidity	checkout firing, good ignition
995	(3)	-	519	288	517	287	217	121	28 minutes saturated air, GN_2 trickle purge on igniter	main thruster ignition, but no Pch(3)
996	no igniter ignition		516	287	514	286	201	112	27.5 minutes saturated air, without igniter purge	no reaction in igniter, catalyst bed iced

(1) Liquid nitrogen from the thruster conditioning system was dripping on the main fire valves, resulting in icing which physically prevented valve movement; the valves were shielded for subsequent runs.

(2) Icing **again** physically prevented valve movement; this time only the main O_2 valve.

(3) Main thruster ignition was attained, but Pch lines were frozen, verifying saturated air exposure at low hardware temperatures.

Test 993: Saturated air soak of 15 minutes duration without GN_2 igniter purge did not affect the operation of the catalytic igniter; however, main thruster ignition was not achieved because of ice formation externally preventing opening of the main oxygen valve.

Test 994: A checkout test was again performed at ambient temperatures and normal humidity to verify baseline ignition characteristics.

Test 995: Main thruster ignition was achieved after 28 minutes of saturated air soak at a thruster initial temperature of 217°R (121°K). No chamber pressure rise was measured because of ice formation within the Pc lines. The frozen chamber pressure line indicated that saturated air did reach the injector face during the soak period. The igniter purge was maintained for this test firing.

Test 996: Repeating test 995 without the GN_2 trickle purge through the catalyst bed resulted in no igniter reaction, and thus no main thruster ignition would occur. Normal igniter operation was most likely prevented by ice formation within the catalyst bed.

The results of the high pressure thruster environmental tests indicated that frost or ice formation on the thruster surfaces did not affect ignition characteristics, as long as the catalyst bed itself was not allowed to ice up. Purging and/or heating of the catalyst bed is therefore recommended to insure high response reaction after extreme environmental exposures. This same recommendation was also made after analysis of the igniter only environmental effects tests described in Volume I of this contract report.

5. CONCLUDING REMARKS

5. CONCLUDING REMARKS

The overall objectives of the high pressure thruster program tasks were to determine the delivered performance, operational requirements, and chamber cooling capability for a high performance, duct cooled, gaseous H_2/O_2 attitude control thruster. Specific task efforts included:

- Design and fabrication of 1500 lbf (6672 N) thruster assemblies, including detailed performance, thermal, stress, and life analyses.
- Demonstration of minimum response catalytic ignition of the thruster.
- Experimental evaluation of thruster altitude performance and minimum impulse bit, overall operating characteristics, and duct cooled thrust chamber cooling capability.
- Determination of environmental effects on thruster operation, including exposure to saturated air at thruster temperatures as low as 200°R (111°K), resulting in significant ice formation.

The major conclusions from the high pressure thruster evaluations were:

- The raised post triplet injector designed for this program delivered an Isp of 432 lbf-sec/lbm (4248 N-sec/kg) with a cooled, flightweight thrust chamber (ε= 40).
- Repeatable pulse mode impulse bits as low as 30 lb-sec (1361 kg-sec) were demonstrated.
- Consistent ignitions were attained at propellant temperatures as low as -280°F (156°K).
- A 25 to 40 ms ignition is possible with a catalytic ignitor.
- Cooling capability of the duct cooled thrust chamber was demonstrated by extended duration firings attaining steady-state thruster temperatures.

The experimental results of this program have demonstrated the high performance capability of gaseous hydrogen-oxygen thrusters. The effectiveness of the duct cooling concept was proven for the lightweight thruster design. The analytical cooling design techniques provide a workable, conservative engineering design approach for the concept. The same mixing model approach also predicts the performance with reasonable accuracy.

REFERENCES

REFERENCES

1. Bartz, D. R., "A Simple Equation for Rapid Estimation of Rocket Nozzle Convective Heat Transfer Coefficients," 49, Jet Propulsion, January 1957.

2. McCarthy, J. R. and Wolf, H., "The Heat Transfer Characteristics of Gaseous Hydrogen and Helium," RR 60-12, Rocketdyne, A Division of North American Rockwell, December 1960.

3. Carlson, L. W. and Talman, E., "Gaseous Film Cooling at Various Degrees of Hot Gas Acceleration and Turbulence Levels," Int. J. Heat Mass Transfer, Vol. II, 1695, 1968.

4. Librizzi, J. and Cresci, R. J., "Transpiration Cooling of a Turbulent Boundary Layer in an Axisymmetric Nozzle," AIAA Journal, Vol. 2, 617, 1964.

5. Chapman, G. T., "Total Boundary Layer Mass Flow With Mass Transfer at the Wall," AIAA Journal, Vol. 4, 1688, 1966.

6. Stollery, J. L. and El Ehwany, A.A.M., "A Note on the Use of a Boundary Layer Model for Correlating Film Cooling Data," Int. Jour. Heat Mass Transfer, Vol. 8, 55, 1965.

7. Krieth, F., Principle of Heat Transfer, International Textbook Company, 1958.

8. Kleinstein, G., "Mixing in Turbulent Axially Symmetric Free Jets," J. Spacecraft, Vol. 1, No. 4, July-August, 1964.

APPENDICES

APPENDIX A

CALCULATION OF C* EFFICIENCY

The index of injector performance used in the experimental program was the corrected C* efficiency. This parameter was calculated by two independent methods, one based on measurement of chamber pressure and the other on measurement of thrust. Details of the computational procedures and of the applied corrections are given in the following sections. The procedures and nomenclature format are essentially those as developed in NASA sponsored programs at Rocketdyne.

1.0 CHAMBER PRESSURE TECHNIQUE

Characteristic velocity efficiency based on chamber pressure is defined by the following:

$$\eta_{C^*} = \frac{(P_c)_o \, (A_t)_{eff} \, g_c}{(\dot{w}_T) \, (C^*)_{theo}} \tag{A-1}$$

where

$(P_c)_o$ = stagnation pressure at the throat

$(A_t)_{eff}$ = effective thermodynamic throat area

g_c = conversion factor (32.174 lbm-ft/lbf-sec^2)

$\dot{w}_T$ = total propellant weight flow rate

$(C^*)_{theo}$ = theoretical characteristic velocity based on shifting equilibrium

Values calculated from Equation (A-1) are referred to as "corrected" C* efficiencies, because the factors involved are obtained by application of suitable influence factor corrections to measured parameters. Stagnation pressure at the throat is obtained from measured static pressure at start of nozzle convergence by assumption of isentropic expansion, effective throat area is estimated from measured geometric area by allowing for geometrical radius changes during firing and for nonunity discharge coefficient, and chamber pressure is corrected to allow for energy losses from combustion gases to the chamber wall by heat transfer and friction. Equation (A-1) may therefore be written as follows:

$$\eta_{C^*} = \frac{P_c \, A_t \, g_c \, f_p \, f_{TR} \, f_{DIS} \, f_{FR} \, f_{HL} \, f_{KE}}{(\dot{w}_o + \dot{w}_f) \, (C^*)_{theo}} \qquad \text{(A-2)}$$

where

P_c = measured static pressure at start of nozzle convergence, psia

A_t = measured geometric throat area, in^2

g_c = conversion factor (32.174 $lbm\text{-}ft/lbf\text{-}sec^2$)

$\dot{w}_o$ = oxidizer weight flow rate, lb/sec

$\dot{w}_f$ = fuel weight flow rate, lb/sec

$(C^*)_{theo}$ = theoretical C* based on shifting equilibrium calculations, ft/sec

f_p = influence factor correcting observed static pressure to throat stagnation pressure

f_{TR} = influence factor correcting for change in throat radius during firing

f_{DIS} = influence factor correcting throat area for effective discharge coefficient

f_{FR} = influence factor correcting measured chamber pressure for frictional drag of combustion gases at chamber wall

f_{HL} = influence factor correcting measured chamber pressure for heat losses from combustion gases to chamber wall

f_{KE} = influence factor correcting C* values to account for finite chemical reaction rates

1.1 PRESSURE INFLUENCE FACTOR (f_p)

Measured static pressure at start of nozzle convergence is converted to stagnation pressure at the throat by assumption of effectively no combustion in the nozzle and application of the isentropic flow equations, with contraction ratio (A_c/A_t) and shifting-equilibrium specific heat ratios (γ). Frozen-equilibrium specific heat ratios usually make the influence correction factor about 1/2 percent larger. Hence the value employed with shifting-equilibrium is the more conservative. Figure A-1 shows the influence factor as a function of contraction ratio.

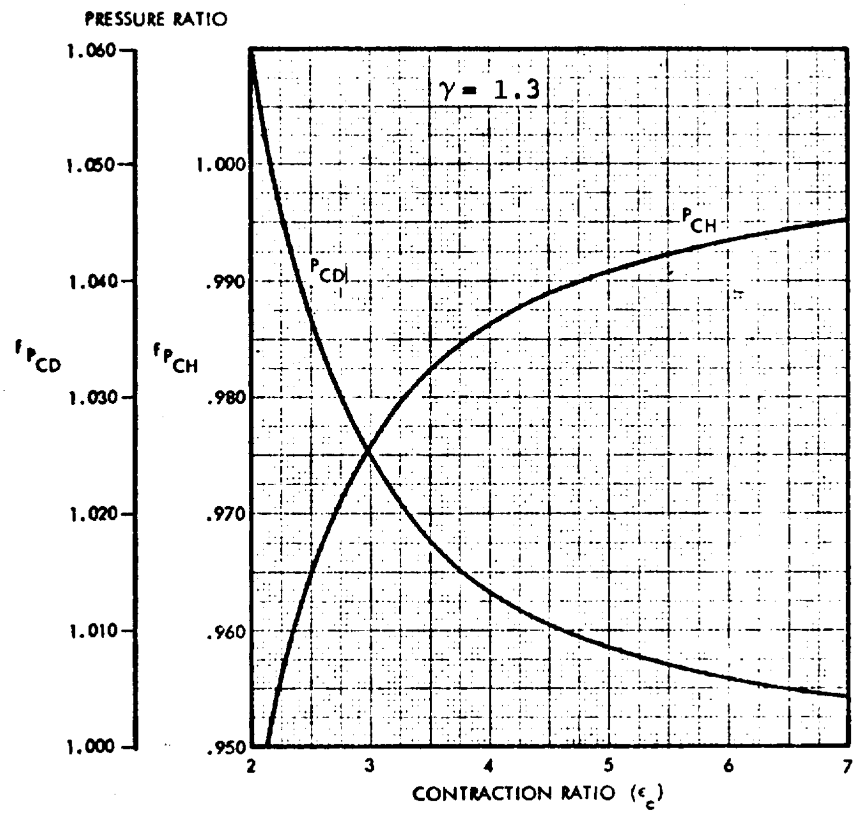

Figure A-1. Momentum Correction

1.2 THROAT RADIUS INFLUENCE FACTOR (f_{TR})

Temperature gradients produced in the solid metal nozzle wall result in thermal stresses which affect throat radius, with the result that the geometric throat diameter ambient measurement is not the same as that which exists during firing.

In the chamber type employed during the experimental effort (i.e. thin throat wall thickness), the throat area change is computed from the thermal growth of the throat based on temperature changes from ambient temperature. The change in throat area can be written as:

$$A_{th} = \frac{\pi}{4} (2 + \alpha \Delta T) \ (\alpha \Delta T) \ D^2 \qquad \text{(A-3)}$$

where

ΔA^* = change in throat area due to thermal growth

α = average thermal expansion coefficient

ΔT = temperature rise from ambient conditions

D = throat diameter at ambient conditions

The throat area correction factor is as follows:

$$f_{TR} = 1 + \frac{\Delta A_{th}}{A_{th}}$$

$$= [1 + \alpha \Delta T]^2 \qquad \text{(A-4)}$$

The thermal expansion coefficient for copper and CRES is $\alpha_{Cu} = 9.8 \times 10^{-6}$ in/in-°F, assuming an ambient temperature of 70°F, the throat area correction factor becomes

$$f_{TR} = [1 + 9.8 \times 10^{-6} (T_{th} - 70)]^2 \qquad \text{(A-5)}$$

This equation was used to generate the curve in Figure A-2.

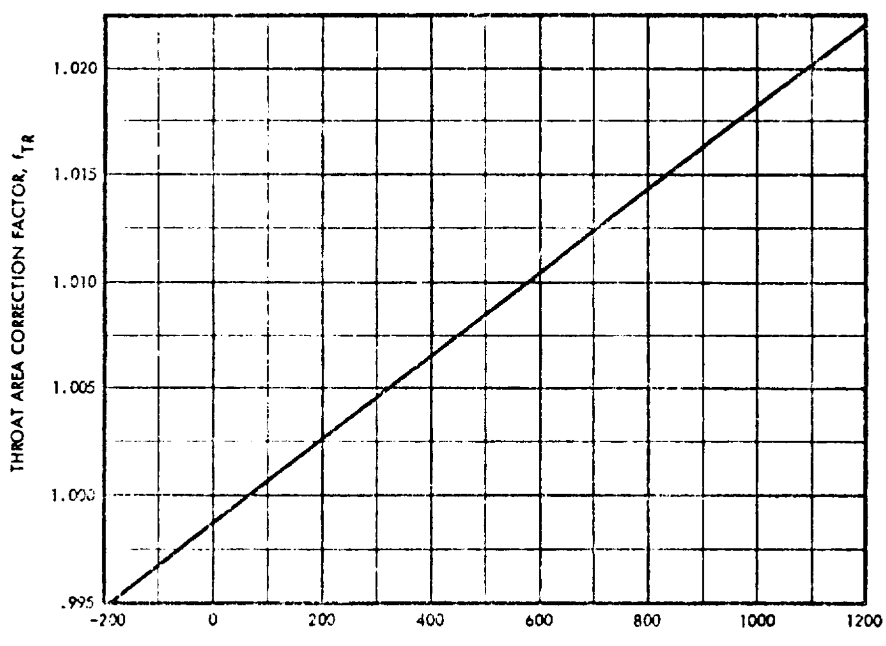

Figure A-2. Throat Area Correction Factor

1.3 THROAT DISCHARGE COEFFICIENT INFLUENCE FACTOR (f_{DIS})

The discharge coefficient is defined as the ratio of actual flow rate through the throat to the theoretical maximum, based on geometric throat area and ideal, uniform, one-dimensional flow with no boundary layer. The discharge influence coefficient may be estimated in two ways: one based on calculations made from a theoretical, inviscid flow model of combustion products, and the other based on a correlation of results obtained in various experimental study results of air flow through nozzles of similar geometry.

1.3.1 Theoretical Model

Total mass flow rate is given by

$$\dot{m} = \int_0^A \rho V \, dA \tag{A-6}$$

where:

ρ = gas density
V = gas velocity
A = cross-sectional area

Theoretical maximum flow rate at the throat is

$$\dot{m}_{max} = \int_0^{A_t} \rho^* V^* \, dA \tag{A-7}$$

where:

A_t = geometric area of the throat
ρ^* = sonic gas density
V^* = sonic gas velocity

For ideal, uniform, parallel flow, Equation (D-7) becomes

$$\dot{m}_{max} = \rho^* V^* A_t \tag{A-8}$$

The discharge coefficient is then

$$C_D = \frac{\dot{m}}{\dot{m}_{max}} = \int_0^A \left(\frac{\rho}{\rho^*}\right)\left(\frac{V}{V^*}\right)\left(\frac{dA}{A_t}\right) \tag{A-9}$$

1.3.2 Empirical Value

Experimental conical nozzle discharge coefficients obtained with air by various investigators are plotted in Figure A-3 against the indicated geometric parameter. Data sources also are listed in Figure A-3.

The values obtained by both methods are found to be in excellent agreement.

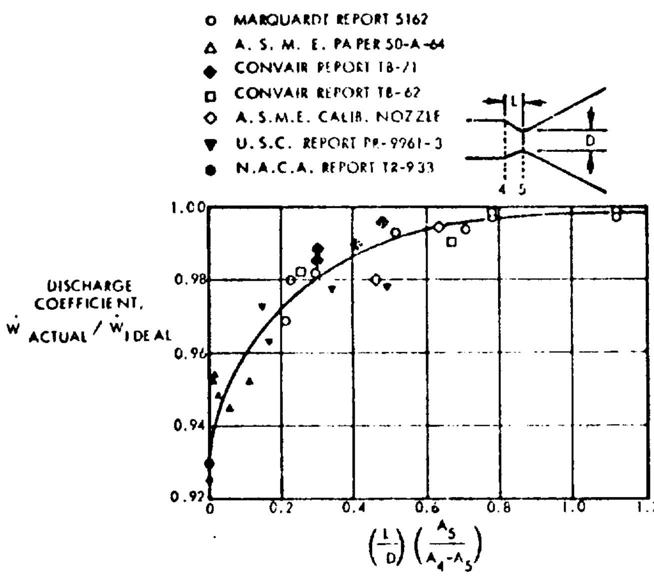

Figure A-3. Conical Nozzle Discharge Coefficient

1.4 FRICTIONAL DRAG INFLUENCE FACTOR (f_{FR})

Calculations of C* based on chamber pressure are concerned with chamber phenomena up to the nozzle throat. Drag forces to this point are small enough to be considered negligible, so that the factor f_{FR} may be taken to be unity.

1.5 ENERGY LOSS INFLUENCE FACTOR (f_{HL})

Chamber pressure and thrust are decreased by heat transfer from the combustion gases to the walls of a thrust chamber. This enthalpy loss is substantially reduced in ablative chambers and is effectively recovered in a regeneratively cooled chamber.

The effect on C* of enthalpy loss by heat transfer can be estimated from a loss of chamber enthalpy. This is determined from a two station energy balance, one at the start of nozzle convergence and the other at the throat.

$$1/2\ V_c^2 + H_c = 1/2\ V_t^2 + H_t + \dot{Q}_{conv} \qquad \text{(A-10)}$$

where:

V_c = gas velocity at chamber exit
V_t = gas velocity at nozzle throat
H_c = gas enthalpy at chamber exit
H_t = gas enthalpy at nozzle throat
$\dot{Q}_{conv}$ = heat loss in nozzle convergence

Velocity at the throat is given by:

$$V_t = [V_c^2 + 2(H_c - H_t - \dot{Q}_{conv})]^{1/2} \qquad \text{(A-11)}$$

With negligible nozzle inlet velocity

$$V_t = [2(H_c - H_t - \dot{Q}_{conv})]^{1/2} \qquad \text{(A-12)}$$

Logarithmic differentiation of Equation (A-12) gives

$$\frac{dV_t}{V_t} = 1/2\ \frac{d\ (H_c - H_t - \dot{Q}_{conv})}{(H_c - H_t - \dot{Q}_{conv})} = 1/2\left(\frac{d\ H_c - dH_t}{H_c - H_t - \dot{Q}_{conv}}\right) \qquad \text{(A-13)}$$

Substitution of enthalpy definition into Equation (A-13) gives:

$$\frac{dV_t}{V_t} = 1/2\left(\frac{c_{pc}\ dT_c - c_{pt}\ dT_t}{H_c - H_t - \dot{Q}_{conv}}\right) \qquad \text{(A-14)}$$

With constant $\dot{C}_p$ between the two stations,

$$\frac{dV_t}{V_t} = 1/2 \left(\frac{c_p \, dT_c}{H_c - H_t - \dot{Q}_{conv}} \right) \left(1 - \frac{dT_t}{dT_c} \right) \tag{A-15}$$

If the specific heat ratio, γ, is assumed constant,

$$\frac{dT_t}{dT_c} = \frac{T_t}{T_c} \tag{A-16}$$

Substituting Equation (A-16) into Equation (A-15), replacing differentials by incrementals, and noting that C* is proportional to gas velocity at the throat gives:

$$\frac{\Delta V_t}{V_t} = \frac{\Delta C^*}{C^*} = 1/2 \left(\frac{c_p \, \Delta T_c}{H_c - H_t - \dot{Q}_{conv}} \right) \left(1 - \frac{\Delta T_t}{T_c} \right) \tag{A-17}$$

Total heat loss to the chamber walls, in Btu per pound of propellant, is obtained by summation of observed heat fluxes over the appropriate areas:

$$\text{Heat loss} = \frac{\Sigma (q/A) \; A}{\dot{w}_T} \tag{A-18}$$

where:

q/A = experimentally observed heat flux

A = area applicable to each q/A value

$\dot{w}_T$ = total propellant flow rate

If this heat loss is equated to the change in enthalpy of the gas in the combustion chamber, $c_p \, \Delta T_c$, then substitution in Equation (B.19) gives:

$$\frac{\Delta C^*}{C^*} = 1/2 \left[\frac{\Sigma (q/A) A}{\dot{w}_T} \right] \left[\frac{1 - (T_t/T_c)}{H_c - H_t - \dot{Q}_{conv}} \right] \tag{A-19}$$

The applicable influence factor is:

$$f_{HL} = 1 + \frac{\Delta C^*}{C^*} = 1 + 1/2 \left[\frac{\Sigma (q/A) A}{\dot{w}_T} \right] \left[\frac{1 - (T_t/T_c)}{H_c - H_t - \dot{Q}_{conv}} \right] \tag{A-20}$$

An alternate expression can be obtained from the basic C* definition:

$$C^* = \frac{\sqrt{RT_c}}{\Gamma} \qquad \text{(A-21)}$$

Logarithmic differentiation of this yields:

$$\frac{dc^*}{c^*} = \frac{1}{2}\,\frac{dT_c}{T_c} \qquad \text{(A-22)}$$

Substituting incrementals from differentials in Equation (A-22) gives:

$$\frac{\Delta c^*}{c^*} = \frac{1}{2}\,\frac{\Delta T_c}{T_c} \qquad \text{(A-23)}$$

Equating ΔT_c with the heat loss from Equation (A-18) results in the following:

$$\frac{\Delta c^*}{c^*} = \frac{1}{2}\left[\frac{\Sigma(q/A)A}{\dot{w}_t}\right]\left[\frac{1}{c_p\,T_c}\right] \qquad \text{(A-24)}$$

The applicable influence factor is:

$$f_{HL} = 1 + \frac{1}{2}\left[\frac{\Sigma(q/A)A}{\dot{w}_t}\right]\left[\frac{1}{c_p\,T_c}\right] \qquad \text{(A-25)}$$

where

c_p = specific heat at constant pressure

Although derived independently it can be shown that these two expressions, Equations (A-20) and (A-25), are nearly equivalent.

1.6 INFLUENCE FACTOR FOR CHEMICAL KINETICS (f_{KE})

The effect of finite chemical reaction rates is to produce a C* less than the corresponding theoretical equilibrium values. A TRW Systems Group developed one-dimension nonequilibrium reacting gas computer program was employed with reaction rate constants selected for the propellant system. The fluid mechanical and chemical equations were integrated from the inlet section by an implicit technique.

2. CALCULATIONS BASED ON THRUST

The alternate determination of C* efficiency is based on thrust:

$$\eta_{C*} = \frac{F_{vac}\ g_c}{(C_F)_{vac}\ \dot{w}_T\ C^*_{theo}} \tag{A-26}$$

where:

F_{vac} = measured thrust corrected to vacuum conditions by the equation: $F_{vac} = F + P_a A_e$

F = measured thrust, lbf

P_a = ambient pressure, psia

A_e = area of nozzle exit, in^2

g_c = conversion factor (32.174 lbm-ft/lbf-sec^2)

$(C_F)_{vac}$ = theoretical shifting thrust coefficient (vacuum)

$\dot{w}_T$ = total propellant flow rate, lbm/sec

c^*_{theo} = theoretical shifting-equilibrium characteristic velocity, ft/sec

Values of vacuum thrust are obtained by applying corrections to sea-level measurements. With these values, which include allowances for all important departures from ideality, theoretical thrust coefficients may be used for calculation of C*. C_F efficiency is taken as 100 percent if there is no combustion in the nozzle, if chemical equilibrium is maintained in the nozzle expansion process, and if energy losses from the combustion gases are accounted for.

Applicable influence factors for measured thrust are specified in the following equation:

$$\eta_{C*} = \frac{(F + P_a A_e)\ g_c\ \phi_{FR}\ \phi_{DIV}\ \phi_{HL}\ \phi_{KE}}{(C_F)_{theo}\ (\dot{W}_o + \dot{w}_f)\ (C^*)_{theo}}, \tag{A-27}$$

where:

F = measured thrust, lb_f

P_a = ambient pressure, psia

A_e = area of nozzle exit, in^2

g_c = conversion factor (32.174 lbm-ft/lbf-sec^2)

$(C_F)_{theo}$	=	theoretical shifting thrust coefficient (vacuum)
$\dot{w}_o$	=	oxidizer weight flow rate, lbm/sec
$\dot{w}_f$	=	fuel weight flow rate, lbm/sec
$(C^*)_{theo}$	=	theoretical shifting equilibrium characteristic velocity, ft/sec
ϕ_{FR}	=	influence for frictional losses
ϕ_{DIV}	=	influence factor for nozzle divergence
ϕ_{HL}	=	influence factor for heat losses to chamber and nozzle walls
ϕ_{KE}	=	influence factor correcting C^* and C_F values to account for finite chemical reaction rates

The influence factors in Equation (A-27) are applied to vacuum thrust $(F + P_aA_e)$ instead of to measured site thrust (F) because, for convenience, the factors are readily calculated as changes in efficiency based on theoretical vacuum parameters. The total influence factor is then of the form $\Delta F/F_{vac}$.

Implicit in the use of theoretical C_F values are corrections to geometric throat area and to measured static chamber pressure at start of nozzle convergence. Therefore, calculation of corrected C* efficiency from thrust measurement includes all the previously described corrections plus an additional one to account for nonparallel nozzle exit flow. However, because $(C_F)_{theo}$ is essentially independent of small changes to chamber pressure and contraction ratio which are involved in corrections to P_c and A_t, these corrections are of no practical significance in calculation of C* from thrust measurements.

2.1 INFLUENCE FACTOR FOR FRICTIONAL DRAG (ϕ_{FR})

This factor corrects for energy losses caused by viscous drag forces on the thrust chamber walls. Its magnitude is estimated by a boundary layer analysis utilizing the integral momentum equation for turbulent flow, which accounts for boundary layer effects from the injector to the nozzle exit by suitable description of the boundary layer profile and local skin friction coefficient. A computer program is used to carry out a numerical integration of the equation, including effects of pressure gradient, heat transfer, and surface roughness. The program requires a potential nozzle flow solution obtained from variable-property, axisymmetric method of characteristics calculation of the flow field outside the boundary layer; corresponding properties for the subsonic combustion chamber flow field are also calculated.

2.2 INFLUENCE FACTOR FOR NOZZLE DIVERGENCE (φ_{DIV})

The one-dimensional theoretical performance calculations assume that flow at the nozzle exit is uniform and parallel to the nozzle axis. The influence factor, φ_{DIV}, allows for nozzle divergence (i.e., for nonaxial flow) and for nonuniformity across the nozzle exit plane. It is calculated by a computer program which utilizes the axisymmetric method of characteristics for a variable-property gas. Computation begins with a transonic input near Mach 1, providing a characteristic line for use in the analysis of the supersonic portion of the nozzle. The resulting pressures are integrated over the given geometry to give the geometric efficiency.

2.3 INFLUENCE FACTOR FOR HEAT LOSS (φ_{HL})

To obtain the heat loss influence factor from measured thrust the approach is identical to that taken previously from the pressure measurement, except that the nozzle losses must also be included. With constant specific heat and gamma from start of nozzle convergence to exit, Equation (A-20) becomes

$$\varphi_{HL} = 1 + \frac{1}{2}\left[\frac{\Sigma(\frac{q}{A})\ A}{\dot{w}_T}\right]\left[\frac{1 - T_e/T_c}{H_c - H_e - Q_{nozzle}}\right] \qquad \text{(A-28)}$$

when "e" corresponds to the exit condition, and the summation occurs over the entire combustion.

An alternate can also be derived as in Equation (D-25). This equation becomes

$$\varphi_{HL} = 1 + \frac{1}{2}\left[\frac{(q/A)A}{\dot{w}_T}\right]\left[\frac{1}{c_p\ T_e}\right] \qquad \text{(A-29)}$$

2.4 INFLUENCE FACTOR FOR CHEMICAL KINETICS (φ_{KE})

The effect of finite chemical reaction rates is to produce a C* and C_F less than the corresponding theoretical equilibrium values. A TRW Systems Group developed one dimensional nonequilibrium reacting gas computer program was employed with reaction rate constants selected for the FLOX methane-ethane blend propellant system. The fluid mechanical and chemical equations were integrated from the inlet section by an implicit technique.

APPENDIX B

DISTRIBUTION LIST

REPORT COPIES R D	RECIPIENT	DESIGNEE
	National Aeronautics & Space Administration Lewis Research Center 21000 Brookpark Road Cleveland, Ohio 44135	
1	Attn: Contracting Officer, MS 500-313	
5	E. A. Bourke, MS 500-203	
1	Technical Report Control Office, MS 5-5	
1	Technology Utilization Office, MS 3-16	
2	AFSC Liaison Office, 501-3	
2	Library	
1	Office of Reliability & Quality Assurance, MS 500-111	
1	J. W. Gregory Chief, MS 500-203	
3	P. N. Herr Project Manager, MS 500-209	
1	Director, Shuttle Technology Office, RS Office of Aeronautics & Space Technology NASA Headquarters Washington, D. C. 20546	

REPORT COPIES R	D	RECIPIENT	DESIGNEE
2		Director Space Prop. and Power, RP Office of Aeronautics & Space Technology NASA Headquarters Washington, D.C. 20546	
1		Director, Launch Vehicles & Propulsion, SV Office of Space Science NASA Headquarters Washington, D.C. 20546	
1		Director, Materials & Structures Div, RW Office of Aeronautics & Space Technology NASA Headquarters Washington, D. C. 20546	
1		Director, Advanced Manned Missions, MT Office of Manned Space Flight NASA Headquarters Washington, D.C. 20546	
3?		National Technical Information Service Springfield, Virginia 22151	
1		National Aeronautics & Space Administration Ames Research Center Moffett Field, California 94035 Attn.: Library	Hans M. Mark Mission Analysis Division
1		National Aeronautics & Space Administration Flight Research Center P.O. Box 273 Edwards, California 93523 Attn: Library	
1		Director, Technology Utilization Division Office of Technology Utilization NASA Headquarters Washington, D. C. 20546	
1		Office of the Director of Defense Research & Engineering Washington, D. C. 20301 Attn: Office of Asst. Dir. (Chem Technology)	

REPORT COPIES R	D	RECIPIENT	DESIGNEE
2		NASA Scientific and Technical Information Facility P. O. Box 33 College Park, Maryland 20740 Attn: NASA Representative	
1		Nation Aeronautics & Space Administration Goddard Space Flight Center Greenbelt, Maryland 20771 Attn: Library	Merland L. Moseson, Code 620
1		National Aeronautics & Space Administration John F. Kennedy Space Center Cocoa Beach, Florida 32931 Attn: Library	Dr. Kurt H. Debus
1		National Aeronautics & Space Administration Langley Research Center Langley Station Hampton, Virginia 23365 Attn: Library	E. Cortwright Director
1	1	National Aeronautics & Space Administration Manned Spacecraft Center Houston, Texas 77001	J. G. Thiobodaux, Jr. Chief, Propulsion & Power Division
	1	Attn: Library	C. A. Vaughan
1	1 1	National Aeronautics & Space Administration George C. Marshall Space Flight Center Huntsville, Alabama 35912 Attn: Library	Hans G. Paul Keith Coates
1		Jet Propulsion Laboratory 4800 Oak Grove Drive Pasadena, California 91103 Attn: Library	Henry Burlage, Jr. Duane Dipprey
1		Defense Documentation Center Cameron Station Building 5 5010 Duke Street Alexandria, Virginia 22314 Attn: TISIA	

REPORT COPIES R	REPORT COPIES C	RECIPIENT	DESIGNEE
1		Arnold Engineering Development Center Air Force Systems Command Tullahoma, Tennessee 37389 Attn: Library	Dr. H. K. Doetsch
1		Aeronautical Systems Division Air Force Systems Command Wright-Patterson Air Force Base, Dayton, Ohio Attn: Library	D. L. Schmidt Code ARSCNC-2
1		Air Force Missile Test Center Patrick Air Force Base, Florida Attn: Library	L. J. Ullian
1		Air Force Systems Command Andrews Air Force Base Washington, D.C. 20332 Attn: Library	Capt. S. W. Bowen SCLT
1	1 1	Air Force Rocket Propulsion Laboratory (LKDS) Edwards, California 93523 Attn: Library	R. L. Wiswell W. Lawrence
1		Air Force Rocket Propulsion Laboratory(RPM) Edwards, California 93523 Attn: Library	
1		Air Force FTC (FTAT-2) Edwards Air Force Base, California 93523 Attn: Library	Donald Ross
1		Air Force Office of Scientific Research Washington, D.C. 20333 Attn: Library	SREP, Dr. J. F. Masi

REPORT COPIES R	D	RECIPIENT	DESIGNEE
1		Space & Missile Systems Organization Air Force Unit Post Office Los Angeles, California 90045 Attn: Technical Data Center	**Lt. Col. J. L. Fisher** **Code XRZE**
1		Office of Research Analyses (OAR) Holloman Air Force Base, New Mexico 88330 Attn: Library RRRD	
1		U. S. Air Force Washington, D.C. Attn: Library	Col. C. K. Stambaugh, Code AFRST
1		Commanding Officer U. S. Army Research Office (Durham) Box CM, Duke Station Durham, North Carolina 27706 Attn: Library	
1		U. S. Army Missile Command Redstone Scientific Information Center Redstone Arsenal, Alabama 35808 Attn: Document Section	Dr. W. Wharton
1		Bureau of Naval Weapons Department of the Navy Washington, D.C. Attn: Library	J. Kay, Code RTMS-41
1		Commander U. S. Naval Missile Center Point Mugu, California 93041 Attn: Technical Library	
1		Commander U. S. Naval Weapons Center China Lake, California 93557 Attn: Library	
1		Commanding Officer Naval Research Branch Office 1030 E. Green Street Pasadena, California 91101 Attn: Library	

REPORT COPIES R	D	RECIPIENT	DESIGNEE
1		Director (Code 6130) U. S. Naval Research Laboratory Washington, D.C. 20390 Attn: Library	H. W. Carhart J. M. Krafft
1		Picatinny Arsenal Dover, New Jersey 07801 Attn: Library	I. Forsten
1		Air Force Aero Propulsion Laboratory Research & Technology Division Air Force Systems Command United States Air Force Wright-Patterson AFB, Ohio 45433 Attn: APRP (Library)	R. Quigley C. M. Donaldson
1		Space Division Aerojet-General Corporation 9200 East Flair Drive El Monte, California 91734 Attn: Library	S. Machlawski
1	1	Aerojet Liquid Rocket Company P. O. Box 15847 Sacramento, California 95813 Attn: Technical Library 2484-2015A	R. Stiff R. L. LaBotz
1		Aeronutronic Division of Philco Ford Corp. Ford Road Newport Beach, California 92663 Attn: Technical Information Department	Dr. L. H. Linder

REPORT COPIES R	C	RECIPIENT	DESIGNEE
1		Aerospace Corporation 2400 E. El Segundo Blvd. Los Angeles, California 90045 Attn: Library-Documents	J. G. Wilcer
1		Astropower Laboratory McDonnell-Douglas Aircraft Company 2121 Paularino Newport Beach, California 92163 Attn: Library	
1		ARO, Incorporated Arnold Engineering Development Center Arnold AF Station, Tennessee 37389 Attn: Library	
1		Susquehanna Corporation Atlantic Research Division Shirley Highway & Edsall Road Alexandria, Virginia 22314 Attn: Library	
1		Beech Aircraft Corporation Boulder Facility Box 631 Boulder, Colorado Attn: Library	Douglas Pope
1	1	Bell Aerosystems, Inc. Box 1 Buffalo, New York 14240 Attn: Library	T. Reinhardt W. M. Smith J. Flanagan

REPORT COPIES R	D	RECIPIENT	DESIGNEE
1		Instruments & Life Support Division Bendix Corporation P.O. Box 4508 Davenport, Iowa 52808 Attention: Library	W. M. Carlson
1		Boeing Company Space Division P.O. Box 868 Seattle, Washington 98124 Attn: Library	J. D. Alexander C. F. Tiffany
1		Boeing Company P.O. Box 1680 Huntsville, Alabama 35801	Ted Snow
1		Chemical Propulsion Information Agency Applied Physics Laboratory 8621 Georgia Avenue Silver Spring, Maryland 20910	Tom Reedy
1		Chrysler Corporation Missile Division P.O. Box 2628 Detroit, Michigan Attn: Library	John Gates
1		Chrysler Corporation Space Division P.O. Box 29200 New Orleans, Louisiana 70129 Attn: Librarian	

REPORT COPIES R	D	RECIPIENT	DESIGNEE
1		Curtiss-Wright Corporation Wright Aeronautical Division Woodridge, New Jersey Attn: Library	G. Kelley
1		Fairchild Stratos Corporation Aircraft Missiles Division Hagerstown, Maryland Attention: Library	
1		Research Center Fairchild Hiller Corporation Germantown, Maryland Attn: Library	Ralph Hall
1		Republic Aviation Fairchild Hiller Corporation Farmington, Long Island New York	
1		General Dynamics/Convair P. O. Box 1128 San Diego, California 92112 Attn: Library	Frank Dore
1		Missiles and Space Systems Center General Electric Company Valley Forge Space Technology Center P. O. Box 8555 Philadelphia, Pa. 19101 Attn: Library	A. Cohen G. E. DeSalle
1		General Electric Company Flight Propulsion Lab. Department Cincinnati, Ohio Attn: Library	D. Suichu Leroy Smith

REPORT COPIES R	D	RECIPIENT	DESIGNEE
1		Grumman Aircraft Engineering Corporation Bethpage, Long Island, New York Attn: Library	Joseph Gavin
1		Honeywell Inc. Aerospace Division 2600 Ridgeway Road Minneapolis, Minnesota Attn: Library	
1		IIT Research Institute Technology Center Chicago, Illinois 60616 Attn: Library	C. K. Hersh
1		Kidde Aer-Space Division Walter Kidde & Company, Inc. 567 Main Street	R. J. Hanville
1		Ling-Temco-Vought Corporation P. O. Box 5907 Dallas, Texas 75222 Attn: Library	
1		Lockheed Missiles and Space Company P. O. Box 504 Sunnyvale, California 94087 Attn: Library	
1		Lockheed Propulsion Company P. O. Box 111 Redlands, California 92374 Attn: Library, Thackwell	H. L. Thackwell
1		Marquardt Corporation 16555 Saticoy Street Box 2013 - South Annex Van Nuys, California 91409	Tom Hudson

REPORT COPIES R	D	RECIPIENT	DESIGNEE
1		Martin-Marietta Corporation (Baltimore Division) Baltimore, Maryland 21203 Attn: Library	
1		Denver Division Martin-Marietta Corporation P. O. Box 179 Denver, Colorado 80201 Attn: Library	Dr. Morgenthaler F. R. Schwartzberg
1		Western Division McDonnell Douglas Astronautics 5301 Bolsa Ave Huntington Beach, California 92647 Attention: Library	R. W. Hallet G. W. Burge P. Klevatt
1	1	McDonnell Douglas Aircraft Corporation P. O. Box 516 Lambert Field, Missouri 63166 Attn: Library	R. A. Herzmark L. Koars
		Rocketdyne Division North American Rockwell Inc. 6633 Canoga Avenue Canoga Park, California 91304 Attn: Library, Department 596-306	Dr. R. J. Thompson S. F. Iacobellis
1	2	Space & Information Systems Division North American Rockwell 12214 Lakewood Blvd. Downey, California Attn: Library	R. E. Field
1		Northrop Space Laboratories 3401 West Broadway Hawthorne, California Attn: Library	Dr. William Howard

REPORT COPIES R D	RECIPIENT	DESIGNEE
1	Radio Corporation of America Astro-Electronics Products Princeton, New Jersey Attn: Library	
1	Rocket Research Corporation Willows Road at 116th Street Redmond, Washington 98052 Attn: Library	F. McCullough, Jr.
1	Thiokol Chemical Corporation Redstone Division Huntsville, Alabama Attn: Library	John Goodloe
1	TRW Systems Inc. 1 Space Park Redondo Beach, California 90278 Attn: Tech. Lib. Doc. Acquisitions	D. H. Lee E. Burge
1	United Aircraft Corporation Corporation Library 400 Main Street East Hartford, Connecticut 06108 Attn: Library	Dr. David Rix
1	United Aircraft Corporation Pratt & Whitney Division Florida Research & Development Center P. O. Box 2691 West Palm Beach, Florida 33402 Attn: Library	R. J. Coar Dr. Schmitke

REPORT COPIES R	D	RECIPIENT	DESIGNEE
1		B. F. Goodrich Company Aerospace & Defense Products 500 South Main Street Akron, Ohio 44311	
1	1	Goodyear Aerospace Corporation 1210 Massilon Road Akron, Ohio 44306	L. Romick
1		Vought Astronautics Box 5907 Dallas, Texas Attn: Library	